

# Charge generation and recombination in solid-state dye-sensitized solar cells

Dissertation zur Erlangung des Grades  
“Doktor der Naturwissenschaften”  
im Promotionsfach Chemie  
am Fachbereich Chemie, Pharmazie und Geowissenschaften  
der Johannes Gutenberg-Universität  
in Mainz

**Yoojin Kim**

Mainz, 2014



This dissertation contains work of my own carried out at the Max Planck Institute for Polymer Research (Max Planck Institut für Polymerforschung) in Mainz. I hereby declare that I wrote this dissertation without any unauthorized external assistance and I used only results acknowledged in the work. I complied with the rules of standard scientific practice as formulated in the statutes of the Johannes Gutenberg-University Mainz to insure standard scientific practice. This dissertation has not been submitted in whole or in part for the award of a degree at this or any other university.

Yoojin Kim



## SUMMARY

This dissertation deals with charge generation and recombination in solid-state dye-sensitized solar cells that use spiro-OMeTAD as a hole conductor. It is divided into three case studies: i.) core-enlarged rylene dyes, ii.) a perylene monoimide dye, and iii.) donor –  $\pi$  spacer (cyclopentadithiophene) – acceptor dyes. Despite high molar extinction coefficients and high absorbance of sensitized films, some of those dye molecules did not show high photovoltaic efficiencies. In order to understand the origin of the poor device performance, broadband ultrafast transient absorption spectroscopy was carried out on solar cell devices.

Specifically, the effect of anchor groups, dipole moments, photoluminescence lifetimes, Li cation-sensitivity, and carrier dynamics, which have a significant influence on the power conversion efficiency are investigated. In the first case study, the shortest core-enlarged rylene dye exhibited the highest power conversion efficiency among the other dye molecules due to much longer lifetimes of excited states than the core-extended rylene dye did. The lifetimes further decreased when the maleic acid anchor group underwent ring opening during adsorption onto a mesoporous metal oxide semiconductor surface. This was due to changes in dipole moment between the ground and excited state as calculated by density functional theory (DFT, B3LYP) supporting unfavorable injection upon ring opening of the anhydride anchoring groups by a changed direction of dipole moments. In the second study, a perylene monoimide derivative dye, ID889, showed an efficiency of 4.5% in a solid-state dye-sensitized device. ID889 could generate long-lived dye cations even without the help of an additive; however, after Li cation use, stabilized charge generation and regeneration processes were observed. Furthermore, reductive quenching was not observed in an ID889-sensitized device when a soft-modelling technique, multivariate curve resolution (MCR), was used to determine the dynamics of excitons based on TA data. Last, in cyclopentadithiophene (CPDT) building block dyes with a typical D- $\pi$ -A molecular structure, FPH224 and 233 showed better power conversion efficiencies in devices than FPH231 and 303 due to high injection efficiency (IE) and long lifetime of the excited state. This appeared to originate from a reductive quenching of FPH231 and 303, whereas FPH224 and 233 exhibited moderate rates of spiro cation decay dynamics.



## ZUSAMMENFASSUNG

Diese Doktorarbeit befasst sich mit Ladungsgeneration und – rekombination in Feststoff-Farbstoffsolarzellen, die spiro-OMeTAD als Lochleiter verwenden. Die vorliegende Arbeit ist in drei Fallstudien unterteilt: i.) Kern-erweiterte Rylene-Farbstoffe, ii.) ein Perylenmonoimid-Farbstoff und iii.) Donor- $\pi$  verbrückte (Cyclopentadithiophen)-Akzeptor-Farbstoffe. Trotz ihres hohen molaren Extinktionskoeffizienten und der hohen Absorbanz der sensibilisierten Filme, zeigen einige dieser Farbstoffmoleküle nur geringe photovoltaischen Effizienzen. Um den Ursprung des geringen Wirkungsgrades herauszufinden, wurde breitbandige, ultraschnelle transiente Absorptionsspektroskopie an Solarzellen durchgeführt.

Insbesondere die Auswirkungen verschiedener Ankergruppen, Dipolmomente, Photolumineszenzlebenszeiten, Lithium-Kationensensitivität und Ladungsträgerdynamik, die alle einen großen Einfluss auf den Wirkungsgrad der Solarzelle besitzen, wurden untersucht. In der ersten Fallstudie zeigte ein kurzer Rylene-Farbstoff aufgrund deutlich verlängerter Lebenszeiten die beste Effizienz im Vergleich zu größeren Kern-erweiterten Rylene-Farbstoffen. Die Lebenszeit wurde weiter reduziert, wenn Maleinsäure als Ankergruppe unter einer Ringöffnungsreaktion an die mesoporöse Oberfläche des Metalloxid-Halbleiters adsorbierte. Dies konnte mit Hilfe von Berechnungen mittels der Dichtefunktionaltheorie (DFT, B3LYP) auf die Differenz des Dipolmoments zwischen Grundzustand und angeregtem Zustand zurückgeführt werden. Die Berechnungen bekräftigen die unvorteilhafte Injektion von Ladungen durch die Änderung der Richtung des Dipolmoments, wenn eine Ringöffnung der Anhydridgruppe stattfindet. In der zweiten Studie zeigte das Perylenmonoimid-Derivat ID889 einen Wirkungsgrad von 4.5% in Feststoff-Farbstoffsolarzellen, wobei ID889 sogar ohne Zuhilfenahme eines Additivs in der Lage ist langlebige Farbstoffkationen zu bilden. Die Verwendung von Lithium-Kationen stabilisiert jedoch sowohl den Prozess der Ladungsgeneration als auch den der Ladungsregeneration. Des Weiteren wurde in ID889-sensitivierten Bauteilen kein reduktives Löschen beobachtet. Dabei wurde die Dynamik der Exzitonen mittels einer *soft-modelling* Methode Kurvenanalyse aus den Daten der transienten Absorptionsspektroskopie gewonnen. Zuletzt wurden Strukturen mit Cyclopentadithiophen(CPDT)-Baustein untersucht, die eine typische D- $\pi$ -A Molekülstruktur bilden. FPH224 und 233 zeigten dabei eine bessere Effizienz als FPH231 und 303 aufgrund einer großen Injektionseffizienz (IE) und längerer Lebenszeit der angeregten Zustände. Dies kann auf reduktives Löschen in FPH231 und 303 zurückgeführt werden, wohingegen FPH224 und 233 einen moderaten Zerfall des Spirokationensignals zeigten.





# CONTENTS

1. INTRODUCTION.....	07
2. BACKGROUND.....	11
2.1 Interaction between electromagnetic radiation and conjugated organic molecules.....	11
2.1.1 Electronic states and configuration of organic molecules	
2.1.2 Jablonski diagram	
2.1.3 Absorption	
Conditions for absorption	
Transition probability for absorption and the Franck-Condon principle	
Absorption related to Einstein coefficients	
2.1.4. Stark effect	
2.1.5 Emission	
Einstein coefficients	
Decay rates and quantum yield	
2.1.6 Solvent polarity (Solvatochromism)	
2.1.7. Metal complexes	
2.2 Transfer process.....	20
2.2.1. Electron transfer: semi-classical Marcus theory	
2.2.2. Energy transfer	
2.3 Laser spectroscopy.....	23
2.3.1. Transient absorption spectroscopy (TAS)	
2.3.2. Generation of femtosecond laser pulses	
Creation	

Amplification	
2.3.3. Supercontinuum generation	
2.4 Dye-sensitized solar cells (DSCs).....	28
2.4.1 Excitons	
2.4.2 Working principle of DSCs	
Dye-sensitized solar cells using metal oxide semiconductors	
2.4.3. Dyes	
2.4.3.1. Ruthenium complex dyes	
2.4.3.2. Organic dyes	
Rylene related dyes	
Cyclopentadithiophene (CPDT) related dyes	
2.4.4. Crucial factors affecting injection of electron	
Anchoring group	
Dipole moment and interfacial environment	
2.4.5. Solid-state DSCs	
Additives	
Solid-state hole transporter: Spiro-OMeTAD	
Reductive quenching in solid-state DSCs	
2.5 Multivariate curve resolution (MCR).....	36
3. EXPERIMENTAL TECHNIQUES.....	37
3.1 Sample preparation.....	37
3.1.1. Device fabrication	
3.1.2. Samples for spectroscopy	
3.2. Steady-state measurements.....	40
3.2.1. J-V characteristics	

3.2.2. External quantum efficiency	
3.2.3. UV-Vis absorption	
3.2.4. Photoinduced absorption spectroscopy	
3.3. Time-resolved measurements.....	45
3.3.1. Photoluminescence spectroscopy	
3.3.2. Transient absorption spectroscopy	
3.4. Materials.....	47
3.4.1. Naphthalene core-enlarged rylene family dyes	
3.4.2. Perylene derivative dye	
3.4.3. Cyclopentadithiophene building block dye	
3.4.4. Z907	
4. RYLENEANHYDRIDE SENSITIZERS.....	51
4.1. Materials.....	51
4.2. Dyes in solution.....	54
4.2.1. Absorption and emission spectra of dye solutions	
4.2.2. PL decay transients of dye solutions	
4.3. Dipole moment of dyes in solution.....	57
4.4. Dye-sensitized metal oxide nanoparticle films.....	59
4.5. Dipole moments calculated by density functional theory.....	63
4.6. Detection of long-lived species .....	64
4.6.1. Detection of dye and hole conductor cations	
4.6.2. Quasi-steady-state photoinduced absorption spectroscopy	
4.7. J-V curves and external quantum efficiency (EQE).....	67
4.8. Ryleneanhydrides sensitizers: Conclusions.....	69

5. PERYLENE MONOIMIDE DERIVATIVE SENSITIZER, ID889.....	71
5.1. Materials and samples used.....	71
5.2. Absorption/Emission spectra.....	72
5.2.1. Dye solutions	
5.2.2. Dye-sensitized nanoparticle films	
5.2.3. Dye cation and anion absorption	
5.3. Device characteristics and photoinduced absorption measurement .....	74
5.3.1. J-V characteristics	
5.3.2. Quasi-steady-state photoinduced absorption (PIA) measurements	
5.4 Measurement of dye solutions.....	77
5.4.1. Photoluminescence (PL) Streak Camera measurements	
5.4.2. Transient Absorption (TA) measurements	
5.5. Time-resolved Photoluminescence (PL) of dye-sensitized films.....	80
5.6. Transient absorption spectroscopy on films.....	83
5.6.1. Main species observed	
5.6.2. Charge Transfer (CT) states on alumina	
5.6.3. Generation of free charge carriers after addition of Li-TFSI on titania surface	
5.6.4. Regeneration using Spiro-OMeTAD and the critical role of Li-TFSI	
5.7. Reductive quenching.....	94
5.8. ID889: Conclusions.....	99
6. CYCLOPENTADITHIOPHENE (CPDT) BUILDING BLOCK DYES.....	102
6.1. Materials and samples.....	102
6.2. Dyes in solution.....	104
6.2.1. Absorption and emission spectra	

6.2.2. Decay dynamics	
6.3. Films.....	107
6.3.1. Absorption and Emission spectra	
6.3.2. PL dynamics	
6.3.3. Injection Efficiency (IE)	
6.4. Device characteristics and photoinduced absorption experiments.....	113
6.4.1. J-V curves and EQE	
6.4.2. Quasi-steady-state photoinduced absorption experiments	
6.5. Transient Absorption Spectroscopy.....	117
6.5.1. FPH224	
6.5.2. FPH233	
6.5.3. FPH231	
6.5.4. FPH303	
6.6. Comparison of charge generation and recombination of all four dyes.....	131
6.7. CPDT building block sensitizers: Conclusions.....	132
7. DISCUSSION.....	135
7.1 Energy levels.....	135
7.2 Anchoring groups.....	136
7.3 Dipole moments and Use of Li-TFSI.....	137
7.4 Long-lived charges.....	139
7.5 Conclusion.....	139
8. REFERENCES.....	141

9. LIST OF ACRONYMS.....149

10. LIST OF FIGURES.....153

# 1. INTRODUCTION

The International Energy Outlook 2013 (IEO2013) estimates that energy consumption will increase by over 50% from 524 quadrillion British thermal units (Btu, joule) in 2013 to 630 quadrillion Btu in 2040 <sup>[1]</sup>. In this outlook, renewable and nuclear power are projected to be the fastest growing energy sources, increasing by 2.5% per year, and renewable energy is anticipated to constitute almost 20% of the total energy capacity in 2040. Photovoltaic and wind energy are expected to occupy the majority of renewable energy capacity growth and photovoltaic energy may increase at a rate of 9.8% each year.

The sun radiates about 120-170 PW of energy to the earth and a massive demand for energy can be resolved if even a small fraction of this solar energy can be converted. A.E. Becquerel discovered electricity conversion using sunlight and built the first photovoltaic cell in 1839. For the first solid-state solar cell, C. Fritts made a solar cell using selenium in 1883 after W. Smith and W.G.Adams studied the photovoltaic effect in selenium in 1873 and 1876. Silicon solar cells became widely used after G. Pearson reported a higher efficiency in silicon photovoltaics than in selenium cells in 1970. During the cold war era, the space race pushed forward the study of photovoltaics and development of practical uses due to the need to power satellites. Since then, various materials, such as silicon, cadmium telluride or copper indium selenide, or compound-semiconductors from the III-V family, i.e. Ga-As, Ga-P, or InGa-As, have achieved high performance and have been used as industrial photovoltaic solar cells.

Against these expensive inorganic materials, emerging organic photovoltaic cells using polymers, quantum dot technology, perovskite, and light absorbing dye-sensitized cells were proposed and studied due to their low production cost potential and since they may be more environmentally friendly. However, a main difference between inorganic and organic solar cells is how they respond to absorption of a photon. Light absorption leads to direct creation of free electron-hole pairs in most conventional (inorganic) semiconductor cells, whilst it generates a strongly bound electron-hole pair in excitonic (organic) semiconductors due to different dielectric constants. Consequently, the efficiencies of these cells and modules of organic photovoltaic devices remain between 8 and 16% <sup>[2][3][4]</sup> and their stabilities are not yet as good as those of inorganic devices. Therefore, efficiencies and long-term stabilities have to be further improved to reach a broad market share and study of large-scale energy generation is necessary.

Polymer-polymer or polymer-fullerene solar cells have exhibited gradual increases in efficiency through development of new materials and changes in device architecture. Particularly, application of the bulk heterojunction (BHJ) concept <sup>[5]</sup> has significantly improved the efficiencies of devices compared to a planar heterojunction (HJ) bilayer, as reported by Tang in 1986 <sup>[6]</sup>. The BHJ device is used to increase the contact area between donor and acceptor materials for enhanced charge generation when a blend of donor and acceptor materials in a solution is casted onto a substrate. The morphology

in BHJ cells is closely related to the charge collection rate and this is further determined by the ratio of donor and acceptor materials used, the drying process depending on the kind of solvent, the annealing process, etc. However, a critical hindrance in polymer solar cells is the large Columbic interaction due to the low dielectric constant of the materials, leading to difficult charge separation. In addition, a low charge mobility causes charge recombination, due to slow charge collection. Although devices using polymers are projected to one day exhibit efficiencies of about 20-22% in a single cell <sup>[7-9]</sup> and 20-24% in a tandem cell <sup>[10, 11]</sup> when a Shockley–Queisser thermodynamic model <sup>[12]</sup> is used, the maximum efficiency of polymer-polymer single cell still remains at 9% <sup>[13]</sup> due to the limited (internal) quantum efficiency.

Quantum dots reduced below the size of the exciton Bohr radius were initially proposed to replace expensive GaAs materials in inorganic tandem cells. GaAs devices show high absorption and a bandgap tunable by elemental composition. Quantum dots are theoretically able to achieve comparable efficiencies because the energy band gap of quantum dots can be easily tuned by changing the dot size. Also, similar to GaAs, quantum dots can enhance optical absorbance by harvesting photons in the near infrared region. Quantum dots are used not only in inorganic solar cells but also in hybrid solar cells such as in dye-sensitized solar cells, replacing light absorbing dyes <sup>[14, 15]</sup>. However, liquid electrolytes used as a redox couple in the dye-sensitized solar cells cause photo-corrosion problems of quantum dots. For better stability, a solid-state dye sensitized solar cell can be another solution <sup>[16]</sup>, but the efficiencies are still pretty low. The performance of quantum dot photovoltaic devices has markedly increased in the last five years and one report has shown an efficiency of 5.2 % <sup>[17]</sup> owing to the quantum dots' ultrafast exciton dissociation and charge transfer.

Perovskite solar cells, another type of hybrid solar cell, consist of an extremely thin absorber layer of perovskite with a thickness of less than 10 nm on top of mesoporous metal oxide particles such as titania or alumina. The electrons are extracted from a fluorinated tin oxide (FTO) electrode and the holes are collected from a counter-electrode after a hole-transfer process occurs with the liquid electrolyte or solid-state hole conductor. Performance of perovskite solar cells has increased significantly to 19.3 % at present <sup>[3, 18]</sup>, from the 3% of its first report in 2009 <sup>[19]</sup>, and it is expected to increase further. The high performance is attributed to the long diffusion length of electron-hole pairs, ranging from 100 nm <sup>[20]</sup> to almost 1  $\mu\text{m}$ , and optimized geometry of perovskites for better charge collection <sup>[21]</sup>. However, the material itself needs to be closely studied since its chemical composition and crystal structure can differ, as can its photophysical properties.

Another hybrid solar cell, namely dye-sensitized solar cells (DSC), as studied in this dissertation, uses dyes as a light harvesting photosensitizer, entering an excited state upon photon absorption followed by injection of an electron into the conduction band of a metal oxide particle layer such as  $\text{TiO}_2$ ,  $\text{ZnO}$  and  $\text{SnO}_2$ . The oxidized dye generated after injection of electrons is regenerated by a liquid-state electrolyte or by transfer of holes to a solid-state hole conductor. The electrons and holes are then



collected by a transparent conductive oxide (TCO) electrode and a counter-electrode such as platinum or silver, respectively. DSCs have shown a gradual increase in performance since first introduced in 1991 <sup>[22]</sup>, due to the development of dyes, redox mediators, hole conductors, and additives. Due to this increased understanding and exploration, devices have reached efficiencies exceeding 12% at lab scale in liquid-state DSCs <sup>[23]</sup> and 6% in solid-state DSCs <sup>[24]</sup>.

The critical benefits of DSCs in the market include easier manufacturing, device transparency, selective light absorption properties, and mechanical flexibility. With these advantages, applications of DSCs extend from powering small electronics such as mobiles (MKE Technology, Taiwan) and tablets (G24 Innovation and Logitech) to large-area solar panels for building-integrated photovoltaics (Dyesol Italian BIPV Company and Fraunhofer). Flexible dye sensitized solar cells (G24 Innovation, NGK Laboratories, KIST) are expected to increase the applications of solar cells further, perhaps to clothes or other flexible materials.

All these organic and hybrid solar cells go through 5 photovoltaic conversion steps: photon harvesting by the absorbing system, excited state generation, charge separation, charge transport and charge collection. In DSCs, a light absorbing dye, an electron donor, creates the excited state, whereupon an electron is injected into the conduction band to a semiconducting layer, an electron acceptor. The charges are separated after overcoming the strong Coulomb interaction of an electron and a hole. Here, the electron injection yield is close to unity since the electron injection process takes place on the ultrafast timescale, below a few hundred femtoseconds <sup>[25-29]</sup>. The oxidized dye, after electron injection, goes through a redox process with liquid-state electrolytes or regeneration by a solid-state hole conductor, depending on the type of reducing agent, to be ready for the next photo-excitation process.

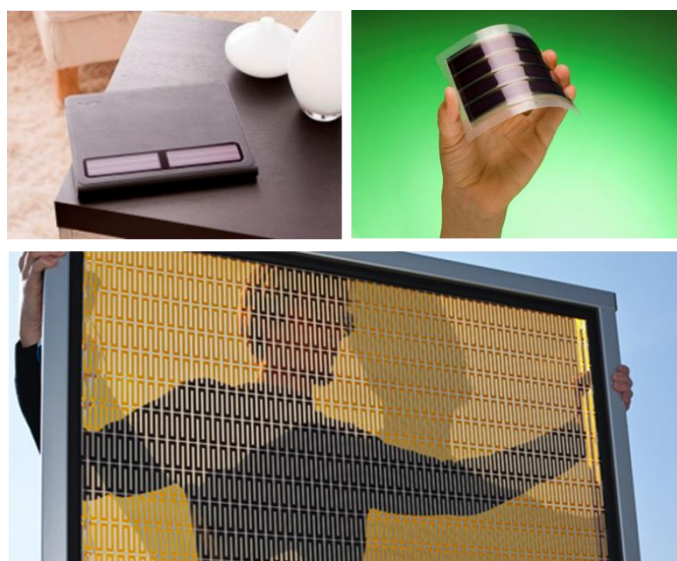


Figure 1-1. A variety of applications of dye-sensitized solar cells in electronics and building: tablet manufactured by G24 Innovation and Logitech (top left), flexible dye-sensitized solar cells by G24 innovation (top right), and building-integrated photovoltaics by Fraunhofer (bottom).

Injected electrons in the metal oxide layer can recombine with oxidized dye molecules on the nano- to milli-seconds timescale, thus regeneration needs to take place prior to recombination in a time range of sub-milliseconds for liquid state<sup>[30, 31]</sup> and nano- to microseconds for solid state DSCs<sup>[32-34]</sup>. Finally, even if recombination is avoided, the electron and hole have to diffuse to each electrode to be collected. In this dissertation, the charge generation and recombination processes in solid-state DSCs are reported with three case studies using organic dye molecules. A detailed description of the light conversion processes will be given in theory section, Chapter 2.

This study has two primary objectives. The first is to understand how charge generation and regeneration processes contribute to PCE in solid-state DSCs when new dye molecules are employed. The second is to find out which physical properties and how the environment of the sensitizer molecules is correlated with charge generation and regeneration or recombination. Three case studies are introduced: rylene dyes, novel perylene dyes, and CPDT  $\pi$ -conjugated building block dyes with different donor moieties and anchoring groups.

In rylene dyes, perylene, terrylene, and quaterrylene derivatives are investigated as the core size of the rylene dyes is increased. The different efficiencies of these dyes are explained experimentally, with optical absorbance, electron injection rates, and excited state lifetimes. Density functional theory (DFT) is employed to relate the varying performances to changes of dipole moments when the acid anhydride rylene dyes open on interaction with a mesoporous titania surface.

In the second case study a novel perylene imide derivative, containing a fused dibenzothiophene as spacer and triarylamine moieties as an electron donor, is studied. Devices using this dye exhibited very good EQE values, up to 70 %, leading to a high short circuit current and ultimately to an efficiency of 4.5 % in solid-state DSCs. The high photocurrent can be explained by long excited state lifetimes determined by time-resolved photoluminescence, a favorable electron density in the HOMO/LUMO level by DFT, facilitated injection/regeneration by the use of Li additive, and fast electron injection without reductive quenching by transient absorption pump-probe spectroscopy and soft-modelling using multivariate curve resolution (MCR).

In the last study, four dyes are investigated: three dyes have the structure A (carboxylic acid anchoring group) -  $\pi$  (cyclopentadithiophene, CPDT) - D (different electron-rich donor moieties such as triarylamine moiety and two novel moieties) and one dye has the structure A (rhodanine-3-acetic acid and carboxylic acid anchoring group) -  $\pi$  (CPDT) - D (electron rich donor moiety). High performing dyes have long-living TA signals due to efficient regeneration, whereas poor performing dyes show less long-living signals of oxidized hole-transporting material.

The theory is described in Chapter 2 and the experimental methods and materials are described in Chapter 3. We discuss the case studies using different molecules in Chapter 4, 5, and 6. Finally, conclusions are presented in Chapter 7.

## 2. BACKGROUND

### 2.1 Interaction between electromagnetic radiation and conjugated organic molecules

Conjugated organic molecules that have a bandgap in the visible enter an excited state by gaining energy from photon absorption with a photon energy corresponding to the bandgap. In this chapter, interaction of a light-absorbing organic system with electromagnetic radiation is described by the processes of photon absorption and emission.

#### 2.1.1 Electronic states and configuration of organic molecules

A conjugation system has a sequence of alternating single and double bonds, with  $sp^2$  hybridization at each participating carbon atom. In a conjugated system, the p-orbitals of each carbon atom combine to form a large molecular orbital over the length of the system. This means that the system does not really consist of alternating single and double bonds, as the electrons are delocalized over the conjugated system. Hence, the bond lengths between each atom within the system are the same, shorter and stronger than a single  $\sigma$  bond, but with a bond length greater than that of a non-delocalized  $\pi$  bond.

A typical example of a conjugated system is a benzene ring, which shows very good stability due to delocalization of electrons from 6 p-orbitals. The  $\sigma$  bonds are formed when a pair of atomic orbitals overlaps end-on, whereas  $\pi$  bonds are formed when a pair of atomic orbitals overlaps side-on. Figure 2-1 shows schematically the  $\sigma$  and  $\pi$  bonds in a benzene ring.

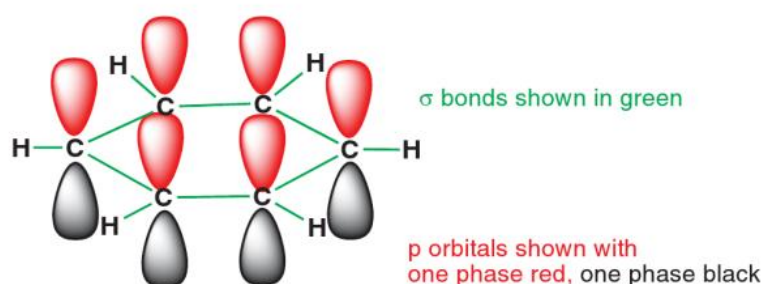


Figure 2- 1.  $\sigma$  and  $\pi$  bonds in a benzene ring <sup>[35]</sup>.

#### 2.1.2 Jablonski diagram

The Jablonski diagram shown in Figure 2-2 shows the electronic states ( $S_n$  or  $T_n$ ) and their vibrational energy levels for a typical organic molecule. The molecule can be excited from the ground state ( $S_0$ ) to the singlet excited states ( $S_n$ ,  $n \geq 1$ ) by an absorption of a photon having an energy corresponding to  $E=h\nu$  ( $h$ : Planck's constant,  $\nu$ : frequency of the absorbed light).

After excitation, the excited state undergoes vibrational relaxation (vr) by dissipation of energy to the surrounding environment. Internal conversion (IC) is a transition between states having the same spin multiplicity ( $S_n \rightarrow S_1$ ,  $T_n \rightarrow T_1$ ) and takes place on femtosecond timescale. Intersystem crossing (ISC) is a transition of an electronically excited state to a different spin multiplicity ( $S_1 \rightarrow T_1$ ) and competes with fluorescence. ISC is spin-forbidden, but it is enhanced by heavy atoms due to spin-orbit coupling.

Kasha's empirical rule explains why absorption and emission spectra show mirror-symmetry at room temperature. The absorption process takes place from the zero vibrational level of the ground state to the zero or higher vibrational levels in the excited state. Emission most likely occurs from the lowest vibrational excited state of the first electronically excited state to either the zero or a higher vibrational state of the electronic ground state, because vr and IC are faster than fluorescence. Therefore, radiative deactivation processes will most likely occur from the lowest vibrational level of the excited state.

The radiative decay process from  $S_1$  to  $S_0$  is called fluorescence, and has a relatively fast decay time, ranging from  $10^{-10}$  to  $10^{-7}$  seconds in the visible range. It is generally observed at lower energy than the absorption, due to energy loss processes such as vibrational relaxation. The spin-forbidden phosphorescence spectrum ( $T_1 \rightarrow S_0$ ) is observed at longer wavelengths compared to the fluorescence with a slow decay rate of  $10^{-6} - 1$  s. The redder emission of phosphorescence is attributed to the lower energy level of the triplet state than the singlet state.

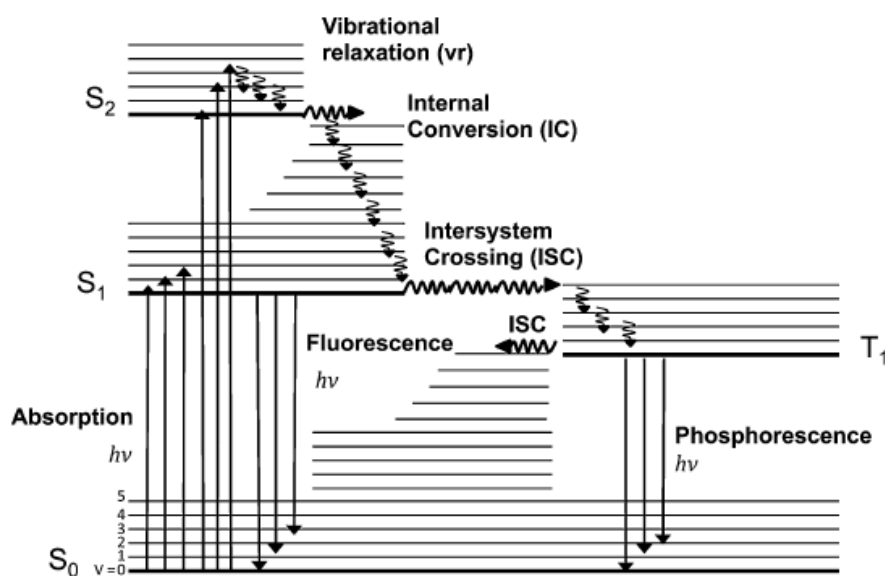


Figure 2- 2. Jablonski diagram illustrating electronic states of a molecule (singlet excited states  $S_n$  or triplet states  $T_n$ ) and transitions between those states. This panel is adapted from <sup>[36]</sup>.

### 2.1.3 Absorption

#### *Conditions for absorption*

Electrons fill the lowest lying orbitals of the molecules and the highest energy orbital filled with electrons is called the highest occupied molecular orbital (HOMO). Electrons are promoted into unoccupied molecular orbitals (which are typically non-bonding or anti-bonding) by excitation, with the lowest energy unoccupied molecular orbital referred to as the LUMO. When a light-absorbing system such as a molecule or an atom obtains energy from absorption of photons corresponding to the energy of the bandgap between the HOMO and LUMO, then an electronically excited state is created. However, if the energy is not matched with the bandgap then, the photons will not be absorbed but just scattered, reflected, or transmitted.

Light absorption by a molecule can be described by interaction of the molecule's transition dipole moment with the photon. The photon is a discrete quantum of electromagnetic radiation (EMR) that has electric and magnetic field components. Oscillation of the dipole, induced by EMR, leads to perturbation of the electronic wavefunctions. If this electromagnetic field perturbs the electronic wavefunction effectively, then the electrons will be pushed away to the position and the momenta of a higher energy state; therefore, an electronic transition finally takes place.

#### *Transition probability for absorption and the Franck-Condon principle*

As described above, an electronic transition occurs due to the interaction of an electromagnetic field with a molecule's dipole moment. The transition probability of an electron for an absorption process is calculated from the integral of the two wavefunctions of the initial electronic state,  $\psi_i$ , and the final state,  $\psi_f$ .

$$M_{if} = \langle \psi_i | \vec{\mu} | \psi_f \rangle \quad (2.1)$$

$\vec{\mu}$  is a dipole moment operator that is defined as  $\sum e\vec{r}_j$  for a single electron, where  $e$  and  $\vec{r}_j$  indicate the electron charge and a vector position with respect to a nucleus, respectively. The transition dipole moment,  $M_{if}$ , is related to the electronic transition between two states and the transition probability for an absorption process is proportional to the square of the transition dipole moment,  $|\vec{M}_{if}|^2$ . The transition dipole moment is defined by a product of three terms as shown in equation (2.2) using the Born-Oppenheimer (BO) approximation, where the wavefunction of a system can be described by electronic and nuclear (vibrational, rotational) components due to the difference in the mass of separated electron and nuclei. Therefore, the total molecular energy is the same as the product of the electronic, vibrational, and rotational energies of the molecule in the solid state,  $\psi = \phi \cdot S \cdot X$ ;

$$M_{if} = \langle \phi_i | \vec{\mu} | \phi_f \rangle \langle S_i | S_f \rangle \sum_n \langle X_{i,0} | X_{f,n} \rangle \quad (\text{vibrational transition : } 0 \rightarrow n) \quad (2.2)$$

$M_{if}$  describes if the transition will be forbidden (zero-resultant) or allowed (non-zero-resultant) based on selection rules. The first term on the right side is an integral containing the orbitals of the two states and a dipole moment operator. This term, describing transition symmetry, needs to be an even function for the integral to be a non-zero resultant (symmetry allowed), because integration of any odd function will yield zero. Strong transitions such as  $\pi \rightarrow \pi^*$  and  $\sigma \rightarrow \sigma^*$  transitions show large spatial overlap between the two states, and so the integral is large in these cases. The second term is a non-zero resultant integral when the two states have the same spin multiplicity. In a spin forbidden transition, i.e. from singlet to triplet, the integral will be 0. However, heavy atoms, such as palladium or platinum, will also show spin-forbidden transition, due to spin-orbit coupling.

The first two terms in equation (2. 2) are related to an electronic property, while the third term relates to a nuclear property. The third term is called the Franck-Condon factor, and refers to the degree of overlap between the vibrational levels of the two states. Figure 2-3 shows a schematic diagram of the Franck-Condon principle consisting of the potential energy graphs of the ground ( $\psi$ ) and excited states ( $^*\psi$ ), as a function of the internuclear separation distance ( $Q$ ). The Franck-Condon principle states that an electronic transition is fast compared to a nuclear motion due to the difference in mass of electron and nuclei, based on the BO approximation; hence the distance between the nuclei in the molecule does not change during the electronic transition of an electron, and fast electronic transitions are drawn vertically between two potential energy curves as shown in Figure 2-3. One vibrational level where the vertical line ends shows the highest degree of overlap, hence the Franck-Condon factor is largest and electronic transition between the states will be fastest.

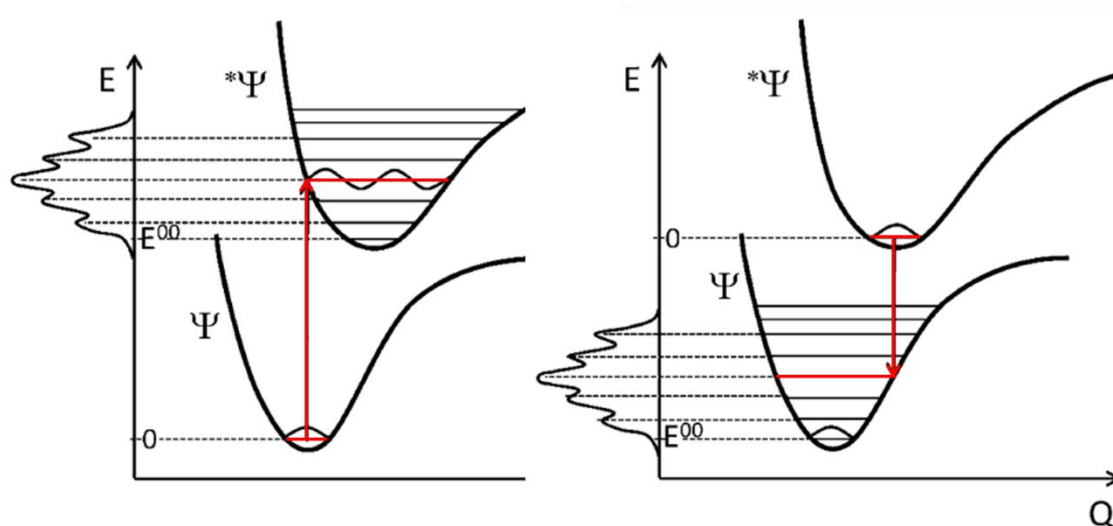


Figure 2- 3. Electronic transition represented as vertical line between two potential energy diagrams of ground ( $\psi$ ) and excited state ( $^*\psi$ ) as a function of the internuclear separation distance ( $Q$ ). The Franck-Condon principle states that an electronic transition is faster than a nuclear transition due to the difference in mass of electron and nuclei. This panel is adapted from <sup>[37]</sup>.

As a result of the selection rules, an electronic transition probability will be high when the two orbitals are largely overlapped, the two states have the same spin multiplicity, and the Franck-Condon factor is largest. However, no transition occurs when the transition probability is 0.

#### Absorption related to Einstein coefficients

The probability of a transition  $|M_{if}|^2$  has a linear relation to the absorption,  $\varepsilon(\tilde{\nu})d\tilde{\nu}$ , where  $\tilde{\nu}$  is the wavenumber and  $\varepsilon$  is the molar extinction coefficient. The integrated absorption coefficient (IAC) can be experimentally obtained and is proportional to the photon harvesting process.

$$IAC = \int_0^\infty \varepsilon(\tilde{\nu})d\tilde{\nu} = B_{12} \cdot h\nu \cdot N_A / \ln 10 \quad (2.3)$$

The IAC can be also expressed by the Einstein coefficient.  $B_{12}$ , the Einstein coefficient, defines the rate of transition of an electron upon induced absorption in a two-discrete energy level system, with  $E_1$  the ground state and  $E_2$  the excited state, as shown in Figure 2-4. The Einstein coefficient  $B_{12}$  is defined as follows:

$$B_{12} = \frac{4\pi^2 e^2}{m_e h \nu c} \cdot f_{12} \quad (2.4)$$

where  $e$  is the electron charge,  $m_e$  is the electron mass,  $c$  is the speed of light,  $\nu$  is the frequency of the light,  $h$  is the Planck constant, and  $f_{12}$  is the oscillator strength. The oscillator strength is a dimensionless quantity and obtained experimentally by integrating over the cross section  $\sigma$  as a function of the wavelength  $\lambda$  as shown in Equation (2.5). It is also directly related to the transition dipole moment. Therefore, the oscillator strength is a direct measure of how strongly the molecule absorbs the light at a given wavelength and thus the extinction coefficient can be used instead of the cross section term according to Equation 2.14.

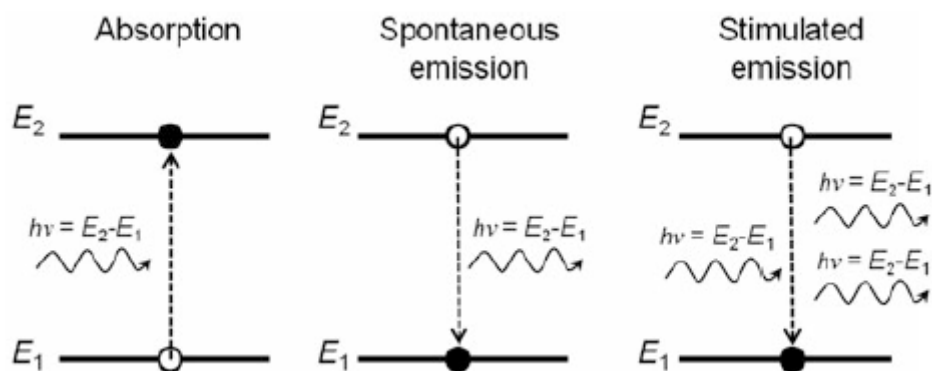


Figure 2- 4. Transitions in a two discrete energy level system, namely induced absorption, spontaneous emission, and stimulated (induced) emission. Adapted from <sup>[36]</sup>.

$$f_{12} = \frac{4m_e c_0 \epsilon_0}{e^2} \int_{\max}^{\min} \frac{1}{\lambda^2} \sigma(\lambda) d\lambda \quad (2.5)$$

The oscillator strength is also used to determine if the transition is allowed or forbidden depending on its value, i.e.  $f \geq 1$  for allowed transitions and  $f \ll 1$  for forbidden transitions.

Different Einstein coefficients are used to define rates of electronic transitions such as induced absorption, and spontaneous and induced (stimulated) emission. The Einstein coefficients  $A_{21}$  and  $B_{21}$  will be explained in Chapter 1.1.5.

#### 2.1.4. Stark effect

The Zeeman effect splits up atomic nuclear spin levels into sublevels under a magnetic field, while the Stark effect introduced by Johannes Stark in 1913 splits electronic levels under an external electric field.

$$\Delta E = E - E(0) = \underbrace{-\Delta\vec{\mu} \cdot \vec{F}}_{\substack{\text{permanent} \\ \text{dipole} \\ \text{moment}}} - \frac{1}{2} \underbrace{\Delta\alpha \cdot \vec{F} \cdot \vec{F}}_{\substack{\text{dipole} \\ \text{moment} \\ \text{induced by} \\ \text{polarizability}}$$

Linear term    Quadratic term

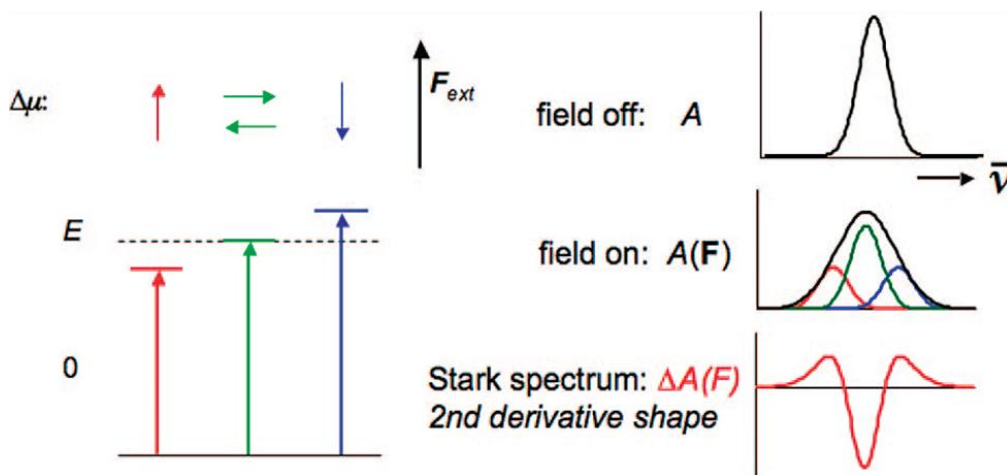


Figure 2- 5. The Stark effect on different energy levels due to interaction of dipole moments with an external electric field. This panel is adapted from <sup>[38]</sup>.



The Stark effect explains how an electric field induces energy level shifts on atoms or molecules. The Stark effect can be divided into a linear and a quadratic term. The linear part is related to the change of the dipole moment when the electronic transition takes place from the ground state to the excited state, whereas the quadratic part relates to the change of the dipole moment induced by polarizability. We only consider the linear Stark effect in this dissertation when observing molecules with a permanent dipole moment caused by their donor-acceptor dye molecular structures. Therefore, changes in position of the band maxima and the shape of absorption occur when the electric field affects electronic transitions or transition dipole moments of the system.

As shown in Figure 2-5, energy levels of an atom or a molecule shift downward, if the electric field and dipole moments are parallel (red arrow). This shift is energetically favorable, leading to red-shifted absorption spectra, while the Stark spectrum shows a positive first derivative shape due to the differences in absorption. However, when the electric field is antiparallel (blue arrow), the energy level will shift upward and absorption spectra will be blue-shifted. When the direction of the dipole moment is random, there is no net effect on the energy levels. Hence, when an electric field exists in a system, the absorption spectra will be broadened and then transient absorption spectroscopy measurements will be also affected.

The Stark effect is often observed in the region of the ground state absorption of the dye in the bleach signal if local electric fields exist. Therefore, derivative shape signals in the visible region where the dyes absorb light can be often assigned to the Stark effect. The local electric field in solid-state DSCs can be caused by photoinduced charges.

### 2.1.5 Emission

Emission spectra are normally observed at lower energy than absorption spectra due to the relaxation processes as shown in the Jablonski diagram above. This difference in energy between absorption and emission spectra is called Stokes shift.

#### *Einstein coefficients*

Radiative deactivation occurs via emission of a photon, while a radiationless deactivation will dissipate most energy as heat and/or vibration rather than by photon emission. Deactivation means that a molecule in the excited state returns to the ground state and thereby loses energy.

Radiative decay can be divided into two processes: spontaneous emission and stimulated (induced) emission. The main difference between them is whether or not the decaying process is related to an electromagnetic radiation (EMR) field. Spontaneous emission is a natural and intrinsic decay process where an excited state (E2) spontaneously decays to a ground state (E1) by releasing energy as a photon. Spontaneous emission is known as photoluminescence.

Stimulated emission, the prerequisite for lasing, becomes dominant when the population in the excited state is larger than that in the initial state. This process is stimulated by the interaction of an excited state (E2) with an electromagnetic wave. As a result, the state decays into the lower level (E1) by emitting a photon. The emitted photons have the same characteristics as the incident EMR that is frequency, phase, and direction.

The rate of spontaneous emission is proportional to the induced emission rates multiplied with the radiation energy density of the two states ( $A_{21} \propto B_{21} \cdot 8\pi h\nu^3 / c^3$ ) whereas the rate of stimulated emission ( $B_{21}$ ) is the same as that of induced absorption ( $B_{21} = B_{12}$ ). For a schematic diagram, see Figure 2-4.

### *Decay rates and quantum yield*

In a molecule, all deactivation processes, such as radiative deactivation, non-radiative deactivation, and intersystem crossing, are competing with each other. Thus, the total decay rate of an excited state is equal to the sum of the decay rates of all processes:

$$k_{\text{total}}[S_1] = (k_f + k_{IC} + k_{ISC})[S_1] \quad (2.6)$$

where  $S_1$  is the population of the excited state and  $k_f$ ,  $k_{IC}$ ,  $k_{ISC}$  are the transition rate constants for fluorescence, internal conversion, and intersystem crossing, respectively. With the deactivation rate constants, a photoluminescence (PL) quantum yield can be calculated. For example, the quantum yield for fluorescence can be derived from the radiative decay rate divided by the sum of the decay rates of the excited state.

$$\Phi_f = k_f / (k_f + k_{IC} + k_{ISC}) \quad (2.7)$$

The population of excited states  $[S_1]$  is time-dependent after photoexcitation and the decay can be described as follows:

$$[S_1]_t = [S_1]_0 \exp\left(-\frac{t}{\tau}\right). \quad (2.8)$$

$[S_1]_t$  is the population of the excited state at the time after excitation and  $t$  denotes the time elapsed after the excitation pulse.  $\tau$  indicates the excited state lifetime taking into account all decay channels, according to:

$$\tau = \frac{1}{k_f + k_{IC} + k_{ISC}} = \frac{1}{k_{\text{total}}}. \quad (2.9)$$

For radiative decay,  $\tau$  is defined simply by  $1/k_f$ . In this case, the equation (2.8) represents monoexponential decay under the assumption that there is only one decay channel.

In this dissertation, most dynamics follow the stretched exponential decay:  $[S_1]_t = [S_1]_0 \cdot \exp(-(t/\tau)^\beta) + c$ . The exponent  $\beta$  denotes a dispersion of relaxation times and  $c$  is a constant. This is known as the Kohlrausch-Williams-Watts function, and is often used to describe relaxation in disordered materials. In a dye-sensitized solar cell, the excited states of the dyes do not decay by just one simple decay channel. They undergo an electron injection process, intra-/intermolecular charge transfer state formation, or exhibit different lifetimes caused by the random orientation of dye molecules on the titania metal oxide nanoparticles. Hence, the stretched exponential decay is used here which accounts for the distribution of transfer rates.

To extract the mean excited state lifetime, the gamma function is used as shown in Equation (2.10). Since the gamma function is mathematically an extension of the factorial function and can be used for all complex numbers, an exponent from the stretched exponential decay function having a form of a real number can be used in the gamma function to derive a mean relaxation time as shown in Equation (2.10) and (2.11).

$$\tau = \left(\frac{\tau_{str.exp.}}{\beta}\right) \Gamma\left(\frac{1}{\beta}\right) \quad (2.10)$$

$$\Gamma\left(\frac{1}{\beta}\right) = \int_0^\infty x^{\left(\frac{1}{\beta}-1\right)} e^{-x} dx \quad (2.11)$$

### 2.1.6 Solvent polarity (Solvatochromism)

The absorption and emission of a dye in solution can change if the solvent polarity is varied, since each solvent has a different dielectric constant and dipole moment. This phenomenon is called solvatochromism. The interaction between solvent-solute will be considered in this section.

Negative solvatochromic properties result in blue-shifted (hypsochromic shift) absorption/emission spectra of the dye molecules as the polarity of the solvent increases. This is due to the decrease of the dipole moment of the dye on excitation, leading to greater stabilization of the ground state. An increase in the dipole moment of the dye leads to a stabilization of the excited state as the polarity of the solvent increases and absorption/emission spectra show a red-shift (bathochromic shift), termed positive solvachromism.

Therefore, the disparity and directions of the ground/excited state dipole moments of a dye determine the type of solvatochromism and also ultimately affect the electronic charge distribution.

In this dissertation different solvents were used to approximate the magnitudes of dipole moments and to compare the different environments affecting CT states of dye molecules when Li cation additives were used on dye-sensitized films.

### 2.1.7. Metal complexes

In contrast to organic molecules, electronic transitions in metal complexes are as follows: metal-centered (MC) transition, ligand-centered (LC) transition, ligand-to-metal charge transfer (LMCT), and metal-to-ligand charge transfer (MLCT). The MC and LC transition can be observed from the first-row transition metals of the periodic table and from metal complexes with aromatic ligands, respectively. The LMCT and MLCT transitions depend on which part is easier to oxidize or reduce.

Octahedral complexes of which Ru(II), i.e. Z907 (cis-Bis(isothiocyanato)(2,2'-bipyridyl-4,4'-dicarboxylato)(4,4'-di-nonyl-2'-bipyridyl)ruthenium(II)), is a typical example show MLCT transitions. In this complex, the metal center plays the role of an electron donating group and the ligand acts as an electron withdrawing group leading to charge transfer  $M(II)^+ - L^-$  from the metal center to the ligand (MLCT). This transition can be observed from complexes with low oxidation potentials of the metal center and a localized low-lying vacant MO in the ligand. The Z907 dye which goes through MLCT transition is used as a reference dye in this dissertation and its molecular structure is shown in Figure 3-12.

## 2.2 Transfer processes

In a donor-acceptor system, generation of an excited state in one molecule will be caused by either (photoexcited) electron transfer or an energy transfer process. In the following sections, the rate constants and conditions of electron and energy transfer are explained.

### 2.2.1. Electron transfer: semi-classical Marcus theory

Marcus theory is a semi-classical model in that it uses the Boltzmann distribution of energies to determine the electron transfer rates of a system in equilibrium, and makes use of Fermi's golden rule to describe the nuclear motion. In Figure 2-6 (a), the potential energy curves of an electron transfer reaction are represented as harmonic oscillators as a function of the nuclear coordinate. States before and after electron transfer are denoted as the initial state (i) and the final state (f), respectively.

The electron transfer rate in Marcus' theory is influenced by two factors: the Franck-Condon Principle and the First Law of thermodynamics. There is no change in nuclear configuration during instantaneous electron transfer according to the Franck-Condon principle. For conservation of total energy, electron transfer should be an isoenergetic process. In order to fulfil these requirements, electron transfer takes place at an intersection of two parabolas having the same curvatures, and it is here where the transfer rate is determined. The rate constant for an electron transfer process in Marcus theory is given by

$$k_{ET} = \frac{|V_{DA}|^2}{\hbar} \sqrt{\frac{\pi}{kT\lambda}} \exp\left(-\frac{\Delta G^\ddagger}{RT}\right) \quad (2.12)$$

where  $|V_{DA}|^2$  is the electronic coupling strength between the initial and the final state,  $\hbar$  is the Planck constant,  $\lambda$  is the reorganization energy, and  $\Delta G^\ddagger$  is the activation energy. Non-adiabatic electron transfer reactions in Marcus theory show a small electronic coupling value of  $|V_{DA}|^2$  compared to the reorganization energy, as shown in Figure 2-6 (a), while donor and acceptor do not change their properties.

For the electron transfer process, the energy barrier that must be overcome is called activation energy,  $\Delta G^\ddagger$ . From a simple mathematical consideration of two parabolas,  $\Delta G^\ddagger$  is defined as  $(\lambda + \Delta G^0)^2/4\lambda$  and  $\Delta G^0$  is the Gibbs free energy change between the neutral and the charged state.  $\lambda$  is the reorganization energy and forces the final state to have the same nuclear configuration as the initial state. Therefore, the electron transfer rate in Marcus theory shows a quadratic dependence on the Gibbs energy. A schematic mechanism of electron transfer is shown in Figure 2-6 (a).

The electron transfer rate varies with changes in the activation energy  $\Delta G^\ddagger$  and the magnitude of  $\Delta G^0$  and  $\lambda$ . In the range of  $0 < \Delta G^0 < \lambda$ , only small driving forces are required for electron transfer and the electron transfer is somewhat favored. The electron transfer rate increases until  $\Delta G^0$  becomes equal to the reorganization energy,  $\lambda$ . The fastest electron transfer occurs at  $\Delta G^0 = \lambda$  since there is no barrier to overcome. If  $\Delta G^0 > \lambda$ , a barrier for the reaction returns, leading to a lower electron transfer rate with increased driving force required. This is called the Marcus inverted region. When the relationship between  $\ln k_{ET}$  and  $\Delta G^0$  is plotted from equation (2.12), the graph will show a bell-shape, with  $\ln k_{ET}$  having a maximum value at  $\Delta G^0 = \lambda$ .

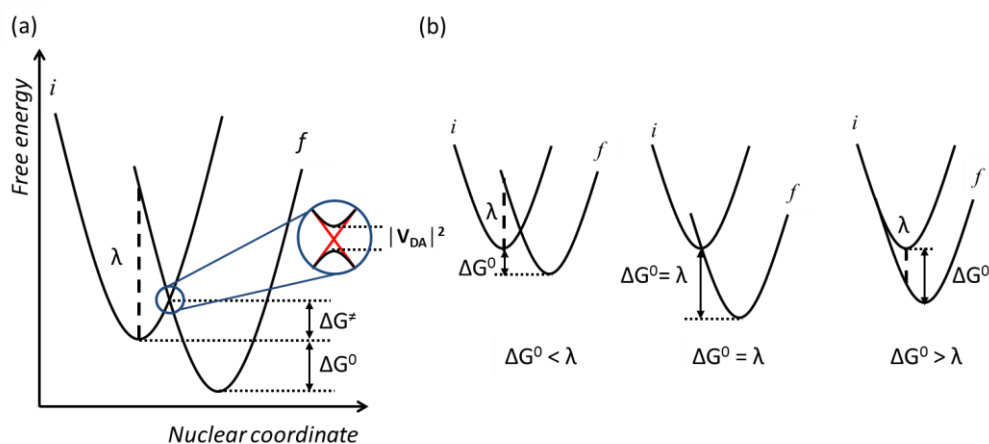


Figure 2- 6. Marcus theory: the potential energy curves of an electron transfer reaction are represented as harmonic oscillators as a function of nuclear coordinate. *i* and *f* stand for initial state and final state, respectively. A small electronic coupling value of  $|V_{DA}|^2$  compared to the reorganization energy in

non-adiabatic electron transfer reactions (a), and different electronic situation depending on the relation between the energy barrier and activation energy,  $\Delta G^\ddagger$  (b).

### 2.2.2. Energy transfer

Fermi's golden rule can be also applied to energy transfer processes since they are regarded as a non-radiative transition between initial and final states.

$$k_{ET} = \left(\frac{4\pi}{h}\right)^2 \cdot |V_{DA}|^2 \cdot FC^{ET} \quad (2.13)$$

$FC^{ET}$  is the Franck Condon factor described above and  $|V_{DA}|^2$  is the electronic coupling between the donor and acceptor states. This  $|V_{DA}|^2$  term can be explained by two different energy transfer mechanisms: Förster and Dexter energy transfer.

Dexter energy transfer is an electron-exchange mechanism. The electron in the excited state of the donor molecule is transferred to the excited state of the acceptor molecule, while an electron in the ground state of the acceptor molecule transfers to the ground state of the donor molecule. This will only occur at short distances, approximately 5-20 Å, which is shorter than Förster resonance energy transfer because it needs strong spatial overlap of wavefunctions of the donor and acceptor.

Förster resonance energy transfer (FRET) originates from an electric field or transition dipole (caused by relaxation processes of the donor molecule) that stimulates formation of the excited state of the acceptor molecule. Relaxation processes of the acceptor species generate different transition dipoles that stimulate deactivation processes of the excited donor molecule. This is why FRET is often called non-radiative dipole-dipole coupling or a Coulombic mechanism. The rate constant for FRET has a  $1/r^6$  distance dependence between the donor and acceptor molecules and the transfer distance is up to 10 nm in this energy transfer process.

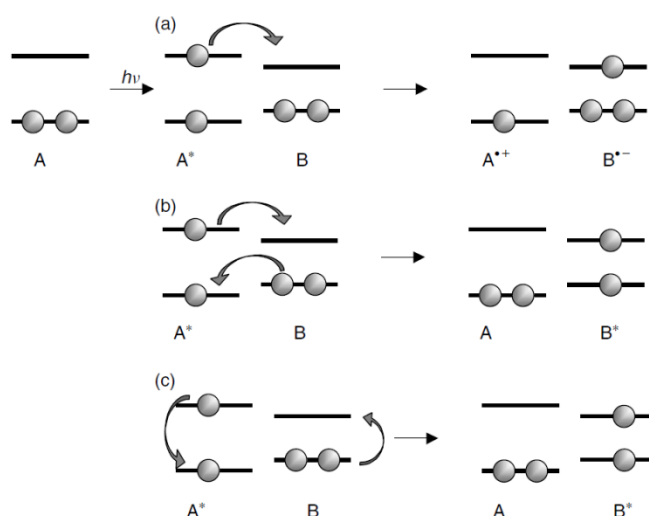


Figure 2-7. Schematic diagram of (a) electron transfer, (b) Dexter and (c) Förster energy transfer <sup>[39]</sup>.

## 2.3 Laser spectroscopy

Norrish and Porter, who were awarded the Nobel Prize in Chemistry in 1967, developed flash photolysis for detecting electronic absorption of excited species that were generated by gas-filled discharge lamps. This achievement enabled studies of transient species such as excited states and radical ions. With the introduction of pulsed lasers and selective excitation using monochromatic light, transient absorption spectroscopy (TAS) allowed detection of the excited state dynamics of different transient species on a time scale which can vary by more than 10 orders of magnitude.

Most photophysical processes in dye-sensitized solar cells, such as charge generation, relaxation, recombination, and regeneration processes, generally take place on the femto- to milliseconds timescale. To identify the processes in femto- to pico- timescales, TAS measurements using ultrafast pulsed laser systems can be employed. In this chapter, the working principles of TAS and the generation of ultrashort pulses will be briefly introduced.

### 2.3.1. Transient absorption spectroscopy (TAS)

The Beer-Lambert law describes how transmittance of light through matter varies with the absorption coefficient and thickness of the material. According to this law, transmission is given by

$$\mathbf{T} = \frac{I}{I_0} = e^{-\alpha d}, \quad (2. 14)$$

where  $I$  is the intensity of transmitted light after passing through the sample,  $I_0$  is the intensity of the incident light,  $\alpha$  is a frequency-dependent absorption coefficient, and  $d$  is the thickness of the sample.  $\alpha$  is a measure of how strongly a system absorbs photons that consists of the molar concentration and the molar extinction coefficient.

The absorbance,  $A$ , is given by the change in population between initial state,  $N_i$ , and final state,  $N_f$ , and the cross-section,  $\sigma$ , when molecules experience electronic transitions.

$$\mathbf{A} = \sum_{if} \sigma_{if}(\lambda)(N_i - N_f). \quad (2. 15)$$

Detection of transient absorption signals is based on changes in concentration of photoinduced species over time. Transient absorption spectroscopy is a pump-probe technique. The first step of the experiment is the excitation of the system with a short ‘pump’ laser pulse. The system is then allowed to evolve for a given delay time, where it will undergo relaxation, recombination, or charge transfer.

First, a probe pulse absorption spectrum of the system in the ground state is taken. Then a pump pulse is used to excite the system, and the system is allowed to evolve for a given delay. Another probe pulse absorption spectrum is then taken, and the difference between this spectrum and the first

provides insights into the transitions of excited states. This is repeated multiple times whilst varying the delay time between pump and probe.

Changes in the excited state population with respect to time evolution,  $t$ , are observed according to:

$$\frac{\Delta T}{T}(\omega, t) = \sum_{if} \sigma_{if}(\lambda) \Delta N_i(t) d. \quad (2. 16)$$

If there is no absorption in the final state  $f$  ( $f=0$ ), then  $\Delta N_0(t)$  reflects the depleted population in the ground-state leading to increased transmission. Therefore, this yields positive  $\Delta T$  signals and is called ground state bleaching (GSB). When transitions to the ground state or to higher-lying excited states occur ( $f>0$ ) then stimulated emission (SE) and photoinduced absorption (PIA) can be observed, and they result in positive and negative  $\Delta T$  signals, respectively. The SE signals are induced by the probe pulse when the excited species that have been created by the pump pulse shows an emissive transition. Hence, SE signals can be generally observed in the photoluminescence wavelength range. PIA is revealed by a negative  $\Delta T$  signal due to additional absorption of an excited state generated by the pump pulse to a higher excited state, ultimately leading to a smaller transmission signal after the pump pulse compared to the transmission signal before the pump pulse. A schematic diagram of TA spectra is shown in Figure 2-8.

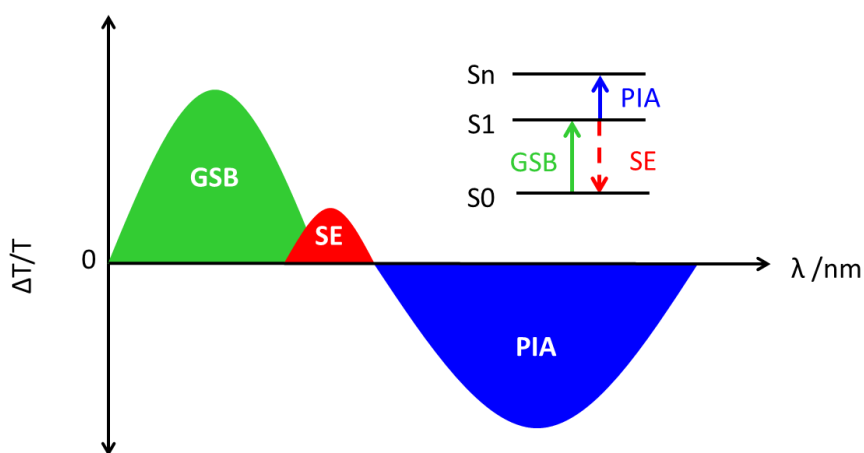


Figure 2- 8. A schematic diagram of signals obtained from transient absorption spectroscopy.

### 2.3.2. Generation of femtosecond laser pulses

#### *Creation*

In order to study the dynamics of excited species on the sub-nanosecond timescale it is necessary to generate the fs laser pulses with mode-locking techniques. Generation of mode-locked pulses is attained via constructive interference of laser beam modes having different frequencies as shown in Figure 2-9 (a). Mode-locking builds short and intense pulses in a resonant cavity from uncoupled modes having different frequencies. The cavity sustains the laser action by using two highly reflective



mirrors, an output coupler (R1) and a high reflector (R2). The cavity round trip time,  $T$ , is determined by the cavity roundtrip length,  $2L$ , between R1 and R2 ( $T = 2Ln/c$  where  $n$  is refractive index and  $c$  is speed of light). The laser repetition rate  $\Delta f$  is defined as the inverse of  $T$  ( $\Delta f = 1/T$ ). A wider spectral bandwidth contains a larger number of longitudinal cavity modes and is able to achieve shorter pulses, based on the uncertainty principle,  $\Delta t \propto \frac{1}{\Delta\omega}$ . Schematic diagrams of the generation of mode-locked pulses and cavity modes are depicted in Figure 2-9.

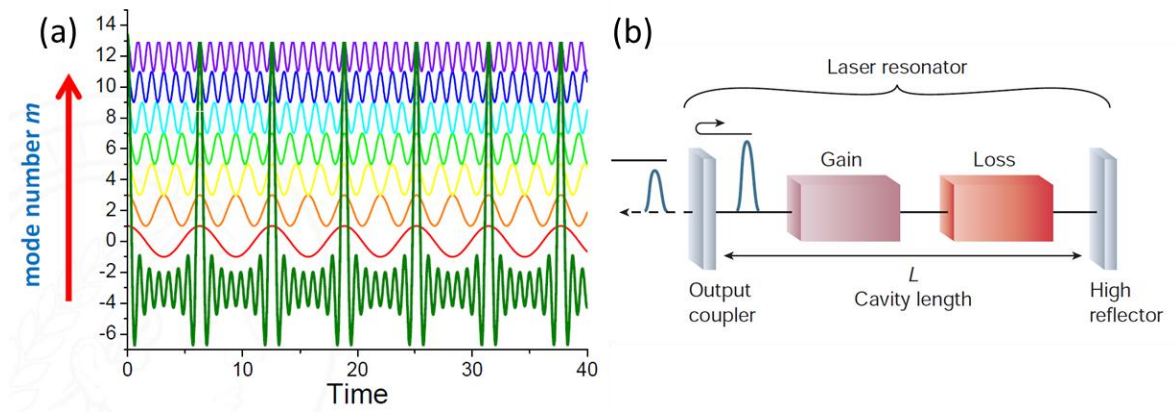


Figure 2- 9. A schematic diagram of generation of mode-locked pulses having different frequencies (a) and a laser resonator using gain and loss medium in a cavity mode (b). The panel is adapted from <sup>[40]</sup>.

Mode-locking is classified as active or passive. Active mode-locking uses an external signal to modulate the loss in the laser resonator in synchronization with the round-trip time. It is a very good method for initiating mode-locking but it needs an extra modulator. For passive mode-locking, a saturable absorber can control the loss modulation. A widely used technique is Kerr lens mode-locking (KLM). The Kerr lens (e.g. Ti:Sapphire) is a nonlinear medium and shows nonlinear intensity dependent properties. This causes a self-focusing of the incident beam, leading to an increase in light intensity. The aperture behind the Kerr lens allows only focused light to pass through and blocks unfocused and low intensity light, resulting in a focused, high intensity beam.

A Ti:Sapphire oscillator is often used as a fs laser in ultrafast measurements due to its wide gain spectrum and high saturation of absorption.

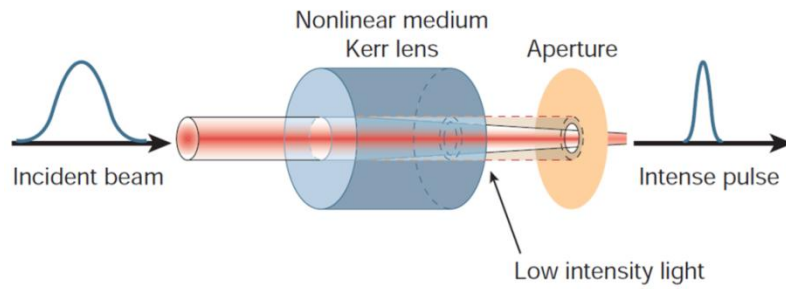


Figure 2- 10. Passive mode-locking using a Kerr lens to allow only focused light to pass through. The panel is adapted from <sup>[40]</sup>.

### *Amplification*

Regular oscillators cannot provide peak powers above a few gigawatts per square centimeter and at this high intensity spectral and temporal pulse distortion and thermal breakdown damage can occur. Therefore, the peak power needs to be reduced by temporal stretching at the laser pulse before amplification.

In chirped pulse amplification (CPA), an initial short (fs) pulse generated from a mode-locked Ti:Sa oscillator has typically a pulse duration of 100 fs, an energy of 1 nJ and an intensity of 1 MW/cm<sup>2</sup>. A pair of gratings spreads the beam into its frequency components, and the laser pulse is temporally stretched by a factor of 10<sup>3</sup> to 10<sup>5</sup>. The stretched pulse therefore shows a longer pulse duration of approximately 100 ps and a decreased intensity of 1 KW/cm<sup>2</sup>. Amplification of this low intensity, stretched pulse is carried out by a power amplifier by a factor of 10<sup>4</sup> or more, i.e. the intensity of the amplified pulse is approximately 10 MW/cm<sup>2</sup> compared to that of the stretched pulse of 1 kW/cm<sup>2</sup>. The amplified laser pulse is then compressed again to the same pulse width as the original pulse (100 fs) and its pulse energy and intensity finally reach 1 mJ and 10 GW/cm<sup>2</sup>, respectively. The chirped pulsed amplification process is schematically shown in Figure 2-11.

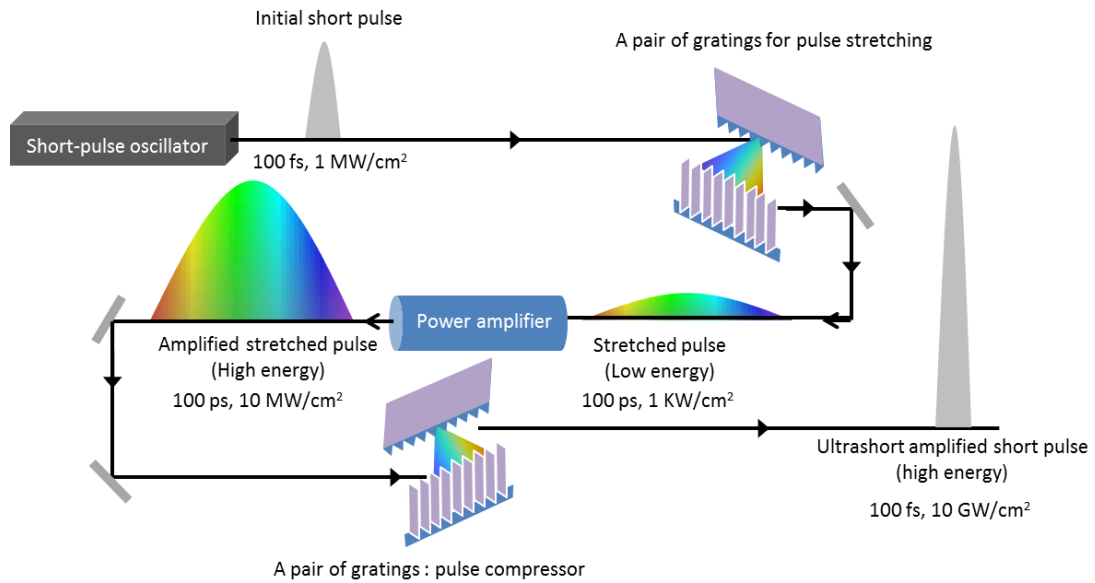


Figure 2- 11. Process of chirped pulse amplification of a femtosecond laser pulse.

### 2.3.3. Supercontinuum generation

A broad spectrum of light can be created in a nonlinear medium such as a sapphire plate. As shown in Figure 2-12, an 800 nm-centered excitation pulse generated from a Ti:Sapphire laser passes through lens L1, and in a sapphire plate generates a continuum of light ranging from 400 to 1800 nm. This broadened pulse, used as a probe in a pump-probe experiment, is then collimated by lens L2.

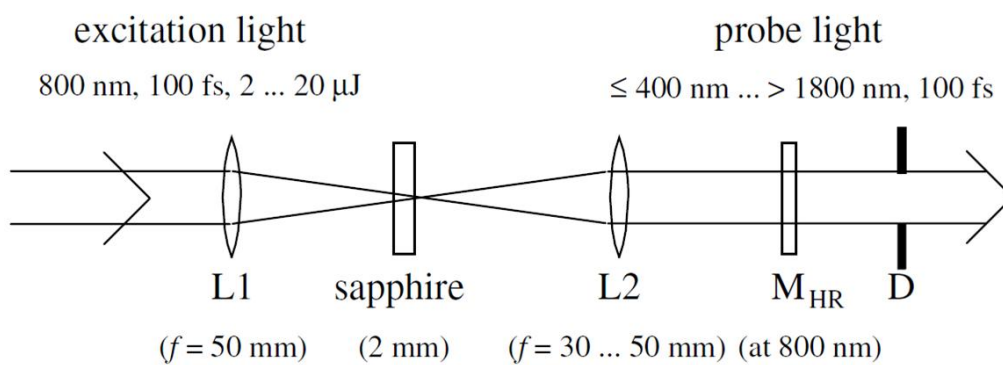


Figure 2- 12. A schematic diagram of supercontinuum white light generation. The panel is adapted from <sup>[41]</sup>.

## 2.4 Dye-sensitized solar cells (DSCs)

### 2.4.1 Excitons

Inorganic materials have different excited state characteristics compared to organic materials due to their larger dielectric constant resulting in a different kind of excitons. Excitons are quasi-particles without charge, namely electron-hole pairs generated by absorption of photons. The type of exciton affects the photophysics of the systems.

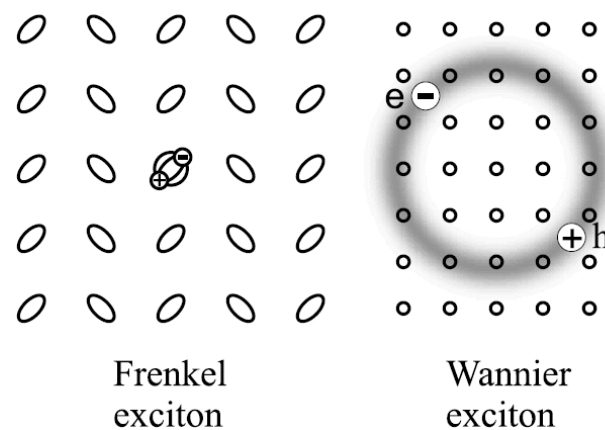


Figure 2- 13. Different exciton radii of Wannier and Frenkel excitons due to the different dielectric permittivity of the material. The panel is adapted from <sup>[42]</sup>.

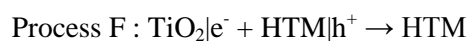
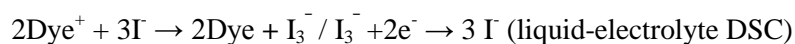
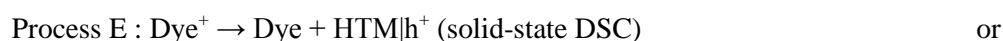
In inorganic materials, a large dielectric constant ( $\epsilon \approx 12$ ) causes effective screening of the Coulombic interaction between electron and hole, called Wannier excitons <sup>[43]</sup>. The generated excitons are only weakly bound in inorganic materials, having a binding energy of about 0.015 eV, and thus a larger exciton radius ( $\leq 100 \text{ \AA}$ ) than lattice distance. Free charge can be generated from these excitons, as their binding energy is comparable to  $k_b T$ .

In organic materials, the excitons are Frenkel type excitons, having a relatively small radius of less than  $10 \text{ \AA}$ . This is due to the stronger Coulombic interaction, which itself is due to the smaller dielectric permittivity ( $\epsilon \approx 4$ ) of organic materials. Excitons are localized on a molecule due to the stronger binding energy of 0.3-1 eV, as shown in Figure 2-14. In solids, the Frenkel exciton moves by a hopping process that is described by an energy transfer mechanism, as depicted above. For a schematic diagram, see Figure 2-13.

### 2.4.2 Working principle of DSCs

#### *Dye-sensitized solar cells using metal oxide semiconductors*

Excitonic solar cells, such as a polymer and dye-sensitized solar cell, are governed by majority charge carriers, in contrast to conventional inorganic solar cells. When it comes to dye-sensitized solar cells, metal oxide semiconductors, such as TiO<sub>2</sub> and ZnO, act as electron acceptors, and photosensitizers (dyes) work as electron donors. The Fermi energy level of the semiconducting nanoparticle layer is initially determined by the type of materials, but is additionally shifted by the trap density, inclusion of mobile charges (electrons) from sensitizers, and changes in the surface environment of the metal oxide layer caused by additives. The open circuit voltage in devices is given by the difference between the Fermi energy level of the metal oxide layer and the HOMO level of the solid-state hole transporter material (HTM); therefore, V<sub>OC</sub> in devices varies with the properties of the dye sensitizer and hole transport material. A schematic diagram to explain the working principle of dye-sensitized solar cells is given in Figure 2-14.



Upon absorption of a photon (process A), an electronically excited state is created on the dye. The dye's excited state decays in less than a hundred nanoseconds<sup>[44]</sup> (process B) in a radiative deactivation process or it emits thermal energy in a radiationless deactivation process. The dye can also undergo an oxidation process by injection of electrons into the metal oxide layer (process C), which transfers an electron from the LUMO level of the dye's excited state to the conduction band of the mesoporous nanoparticle semiconducting layer. Injected electrons then diffuse by hopping to the fluorinated tin oxide (FTO) electrode. Process C generally takes place on an ultrafast time scale, a few tens of fs for Ru dyes<sup>[25-29]</sup> and a few picoseconds for organic dyes<sup>[45]</sup>, but slower injection originating from triplet states in Ru dyes<sup>[46]</sup> is observed too. The reduction process of a dye's oxidised state is carried out by a redox mediator or a hole transporting material (process E). For an efficient device, this regeneration process needs to be much faster than the recombination (process D and F). Regeneration of solid-state DSCs occurs on a timescale of pico- to a few nano-seconds<sup>[47]</sup>, which is several orders of magnitude faster than in liquid-state devices, where regeneration generally proceeds on a nano- to milliseconds<sup>[41,44,45]</sup> timescale. This fast regeneration process in solid-state DSCs is attributed to direct hole transfer (via an energy gradient) into the HOMO level of a solid-state hole transporter from the

oxidized state of the dye molecule <sup>[47]</sup>, whereas the redox reaction in a liquid-state system is diffusion-limited <sup>[48]</sup>. Injected electrons can recombine with either an oxidized dye molecule (process D) or a hole conductor carrying holes (process F). The former is normally called a back-electron transfer and this process takes place on a timescale between nano- and milliseconds <sup>[49-56]</sup>, while the latter process is in the range of a few tens of milliseconds for liquid-state DSCs <sup>[30, 31]</sup> and of nano- to microseconds for solid-state DSCs <sup>[32-34]</sup>.

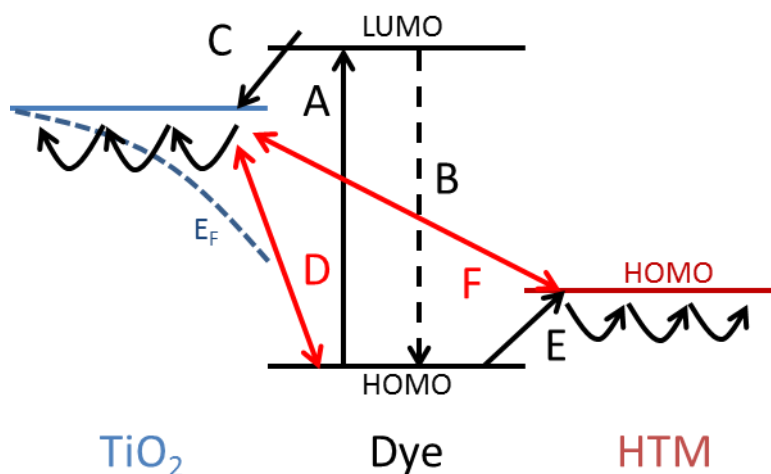


Figure 2- 14. Working principle of solid-state dye-sensitized solar cells. A: absorption of a photon, B: excited state decay, C: injection of electrons, D: recombination between injected electrons and oxidized dye molecule, E: reduction process of a dyes' oxidized state, and F: recombination between injected electrons and an oxidized hole conductor.

Electrons and holes in solid-state DSCs are finally extracted by a transparent conductive oxide layer (TCO) anode such as FTO and a counter-electrode such as silver, respectively. In addition, to prevent another recombination path due to the direct contact between the TCO and the hole conducting material, a compact titania layer on top of the TCO film is necessary.

### 2.4.3. Dyes

Studies of photosensitizers such as the dye molecules had significant influence on the development of DSC performance. A sensitizer should possess an absorption band in the visible range or up to the near-infrared range due to the high photon flux of the sun in these wavelength regions. Dye molecule design enables not only to selectively change absorption bands of the dye but also to modify energy levels, namely the HOMO/LUMO energies.

#### 2.4.3.1. Ruthenium complex dyes

Among the many different dyes, ruthenium (Ru(II)) complexes have attracted a lot of attention due to their outstanding characteristics, such as wide absorption bands, high external quantum efficiencies,

favorable energy levels and relatively long excited state lifetimes. Among several Ru complexes, Ru complexes with carboxylated bi- or poly-pyridine ligands such as N3<sup>[57]</sup>, N719<sup>[58]</sup>, CYC-B11<sup>[59]</sup>, Z907<sup>[60, 61]</sup>, and Z910<sup>[62]</sup> were extensively studied due to their higher conversion efficiencies, ranging from 6 to 11%. Especially, N3, N719, and Z907 are widely used as reference dyes when comparing device performance. The N3 dye, having two bipyridyl moieties connected to four carboxylate anchoring groups, exhibited an efficiency of about 10 % owing to a long excited state lifetime and strong electronic coupling between the LUMO level of the dye and the conduction band of the metal oxide layer<sup>[57]</sup>. The N719 dye, modified from N3 to have a double protonated structure, showed improved  $J_{SC}$  and  $V_{OC}$  in devices<sup>[63]</sup> due to changes in the metal oxide surface environment. The hydrophobic dye Z907 showed increased molar extinction coefficients<sup>[64, 65]</sup> compared to N3 and N719, and extended absorption up to 750nm. Devices using Z907 exhibited efficiencies of 7% in liquid state<sup>[65]</sup> and 4% in solid state<sup>[66]</sup>. In this dissertation, Z907 was used as a reference dye to compare the device performance of each batch and it generally exhibited efficiencies of 1.5 – 2.3% in solid-state DSCs. The rather low efficiencies of these cells compared to those of other research groups are probably due to different fabrication conditions and the materials used such as titania oxide layers and compact titania layers.

The high efficiencies of these dyes reported in the literature are mainly attributed to slow recombination of injected electrons with oxidized dye molecules and fast regeneration processes; however, the devices still suffer from rather low photocurrents. To solve this problem, studies adding coadsorbents<sup>[65]</sup>, increasing ligand length by extension of the conjugated system<sup>[62, 67, 68]</sup>, cosensitization<sup>[23]</sup>, and the use of a near-IR absorbing dye, known as black dye<sup>[69-72]</sup>, were reported. Some reports demonstrated higher power conversion efficiency by an increase of light absorption, but overall efficiencies did not change significantly and still remained at around 7-10%.

#### 2.4.3.2. Organic dyes

Ruthenium complex dye molecules are rare and expensive; therefore, despite their high efficiencies, all organic alternatives were developed. Organic dyes have advantages such as high molecular extinction coefficients, cost effectiveness, environmental cleanliness, relatively easy synthesis and the possibility of molecular design of their chemical and physical properties. Generally, organic dye molecules employ the Donor- $\pi$ -Acceptor structure, so called 'push-pull' dyes. One can design a variety of dye molecules, selectively change the absorption spectrum, and modify energy levels by using this structure. Many dyes having different donor moieties such as coumarin<sup>[73]</sup>, indoline<sup>[74-76]</sup>, carbazole<sup>[77-79]</sup>, triarylamine<sup>[80-83]</sup> and perylene<sup>[84, 85]</sup>, one of the rylene family dyes, have been used in this D- $\pi$ -A arrangement. On illumination, the dye molecule absorbs the photons and the electron-rich donor moiety transfers electron density through the  $\pi$ -conjugated segments to the acceptor.

#### ***Rylene related dyes***

Rylene dyes show high molecular extinction coefficients, excellent thermal and photo-stability, and strong absorption in the visible range. Devices using perylene dyes exhibit efficiencies of 3 – 6 % in liquid-state <sup>[84, 86-89]</sup>, and 2% in solid-state <sup>[84]</sup>, largely owing to the long excited state lifetimes <sup>[90-92]</sup>. For core-enlarged rylene molecules, T. Edvinsson et al. measured energy levels of the TMIMA dye experimentally and computationally. They found that delocalized orbitals in the HOMO and LUMO levels showed no changes in their charge transfer properties, regardless of the conformation of the ring opened anchoring group <sup>[93]</sup>. Y. Geerts et al. reported that quaterrylene diimide (QDI) showed a low quantum yield compared to perylene and terrylene diimide (PDI and TDI) due to increased radiationless deactivation caused by vibrational torsion <sup>[92]</sup>. To further enhance the electron injection of these molecules, studies of alteration of energy levels <sup>[89]</sup>, changes in the donating or conjugated  $\pi$ -moiety <sup>[88, 94-96]</sup>, prevention of dye aggregation <sup>[87]</sup>, and UV radiation exposure to cause band shifts of the conduction band <sup>[85]</sup> were reported; however, the PCE of the devices are generally rather low, since the rylene sensitizer has poor electron donating properties <sup>[97]</sup>. In Chapter 4, the rylene dyes are presented, which exhibited a rather low efficiency of 0.3 % due to unfavorable electron injection properties, however, the novel perylene dye reported in Chapter 5 showed an efficiency of 4.5% in solid-state DSC owing to high photocurrents.

### *Cyclopentadithiophene (CPDT) related dyes*

Triarylamine moieties known as electron rich units were used in both metal complex dyes and organic dyes. They were used in bipyridyl ligands in Ru(II) complex sensitizers to spatially retard recombination between injected electrons and holes in a regeneration medium and as a result, they ultimately increased efficiencies in both liquid- and solid-states DSCs <sup>[98-100]</sup>.

In D- $\pi$ -A type organic dyes, devices using triarylamine moieties as a donor and cyclopentadithiophene (CPDT) moieties as a bridging unit have shown good efficiencies, up to 10 %, when they are used with cobalt (II/III) as a redox electrolyte <sup>[101, 102]</sup> and efficiencies of 3 % <sup>[103]</sup> in solid-state DSCs were reached. Wang et al., compared the kinetics of dye cation recombination and regeneration using transient absorption spectroscopy in several D- $\pi$ (CPDT)-A(Triarylamine) dye molecules. They used a gamma function to derive the meantime for the excited state kinetics <sup>[94, 104]</sup>, whereas other groups used a monoexponential function <sup>[102]</sup> or simply take the time at 50% of the signal decay <sup>[105]</sup>. This gamma function uses an exponent,  $\beta$ , and a lifetime,  $\tau$ , obtained from a stretched exponential decay function to determine the excited state lifetime components in various time dependent distribution functions.

In this dissertation, a stretched exponential decay function is generally used, especially for samples using metal oxide layers, but the lifetime determined using a gamma function is also introduced in Chapter 6 to compare the mean lifetime of four different dyes consisting of triarylamine-based donor building blocks and cyclopentadithiophene (CPDT) moieties as a  $\pi$ -conjugated spacer.



#### 2.4.4. Crucial factors affecting injection of electron

In this section, different type of dye molecules will be reviewed to understand several factors affecting injection of electrons, such as electronic coupling via anchoring group, dipole moment, and surface environment.

##### ***Anchoring group***

More than one anchoring group on the sensitizer is necessary not only to adsorb to the surface of a semiconducting oxide layer, but also to be a channel for electron injection from the dye molecule. In addition, the anchoring group determines the electronic coupling properties and it has been found to be an important factor in device performance, since the LUMO level of the dye is generally governed by the acceptor and an anchoring moiety that substantially affects electron injection into the conduction band.

Carboxylic acid anchor groups are most widely used because of their stability, easy synthesis, and strong electronic coupling leading to efficient electron injection rates <sup>[54, 106, 107]</sup>. As derivatives of carboxylic acids, acid chlorides, esters, carboxylate salts, and maleic acid anhydrides have also been used and their binding modes also affect the efficiency of devices <sup>[106]</sup>.

Anhydrides can be used to form carboxylic acid anchoring groups <sup>[88, 108]</sup> but when maleic anhydride groups undergo ring opening, the absorption and emission is blue-shifted. Völker et al. studied the slower adsorption rates of anhydride groups relative to other acid groups <sup>[109]</sup> due to the ring opening process and Johansson et al. reported that dyes with anhydride groups adsorb only to specific sites on the metal oxide film <sup>[108]</sup>. Therefore, depending on the kind of anchoring group, changes in adsorption rate and intramolecular interaction can take place.

An indoline donor dye molecule has shown a very good efficiency of 9.5% in liquid-state DSCs <sup>[75]</sup> due to its high open circuit voltage caused by chenodeoxycholic acid when it owns rhodanine-3-acetic acid as the acceptor and anchoring moiety. However, another report showed rather low photocurrents due to a localized electron density in the LUMO of the rhodanine unit, leading to unfavorable electron injection <sup>[110]</sup>. In Chapter 6, one of the CPDT building block dyes consisting of a rhodanine-3-acetic acid anchoring group will be discussed in comparison to a carboxylate acid anchoring group that has a different electron density.

##### ***Dipole moment and interfacial environment***

The dipole moment of the dye can influence the device performance due to changes in dipole moment between ground state and excited state. Generally, dyes showing big changes in dipole moment between two states have excellent injection properties owing to the fairly localized electron density in the HOMO and LUMO levels. Different magnitude of the dye's dipole moment can lead to different

absorption spectra due to changes in the density of states in the metal oxide layers<sup>[111]</sup> or due to the Stark effect.

Aside from internal changes in the dye molecules through redistribution of electron density, changes in the metal oxide surface environment, i.e. local electric fields, near the dye molecules also have an influence on electron injection. Changes in the local electric field can be caused by insertion of Li-TFSI<sup>[112]</sup> or a dipolar coadsorbent, leading to a facilitated injection process. Perylene derivatives used with a dipolar coadsorbent show slow injection rates due to band shifts of the conduction band<sup>[113]</sup>. The research in this area demonstrates how  $J_{SC}$  and  $V_{OC}$  are correlated and determine device performance due to shifts of the conduction band.

In the first case study in Chapter 4, the small photocurrents due to the changes in dipole moment of rylene dyes are explored, when the anhydride anchoring group opens due to the adsorption process. In Chapter 5, insertion of Li cations causes a change in the environment around the dye molecules, leading to enhancement of injection rates.

#### 2.4.5. Solid-state DSCs

##### *Additives*

The photocurrents and voltages of devices determine the PCE and these two factors are highly influenced by band shifts of the conduction band and changes of the Fermi energy level due to a shift of the conduction band. Modification of band positions can be achieved with additives such as lithium bis (trifluoromethanesulphonyl) imide (Li-TFSI) salts and 4-tert-butylpyridine (tBP). The role of Li-TFSI is not fully understood yet; however, insertion of ionic salts prevents charge recombination and stabilizes the dye cation. These changes appear to arise from lowering the conduction band by screening the charges from the TiO<sub>2</sub> surface, which facilitates electron injection but decreases the voltage of the device. However, the pyridine unit in tBP gives rise to a negative shift in the conduction band of TiO<sub>2</sub>, increasing  $V_{OC}$ , by giving a negative charge to and removing protons from the surface. Consequently, the use of both tBP and Li cation influences device performance by slowing down the recombination rate<sup>[114]</sup>. Durrant et al., reported a dependence of electron injection dynamics on the concentration of both tBP and Li ions, and this dependence is closely related to the shift of the conduction band<sup>[115]</sup>.

##### *Solid-state hole transporter: Spiro-OMeTAD*

Despite the high efficiency of liquid-state DSCs, a need for alternative materials for dye regeneration occurred due to the corrosive properties and leakage problems of liquid-state electrolytes. As a result, studies on polymer semiconductors (PEDOT or P3HT) and small molecules (spiro-OMeTAD) began. These materials can be spin-cast on top of the dye surface from solution to interpenetrate into the mesoporous semiconducting layer. With the use of polymer materials, pore-filling rates seemed low

due to the long polymer chains, leading to poor efficiency, despite their advantages such as additional absorption and moderate charge mobilities. With the use of spiro-OMeTAD, devices exhibited increasing efficiencies, up to 7 %<sup>[24]</sup>, owing to fast hole-mobility<sup>[116]</sup>, better infiltration, and geometric structure of the hole transporter<sup>[117]</sup>. This solid hole conductor accepts holes from the oxidized dye and transports the holes to the counter electrodes, demonstrating that fast hole mobility is an important key to solid-state DSCs. The HOMO level of hole conductors needs to be less negative than the HOMO level of the dye to allow dye regeneration. The dye regeneration process takes place in sub-nanoseconds, several orders of magnitude faster than the redox process in liquid-state DSCs<sup>[47]</sup>. J. Bisquert et al., reported that the energy gap between the HOMO level of spiro-OMeTAD and that of the dye needs only to be 0.2 V at minimum for the dye regeneration<sup>[118]</sup>. However, charge screening in the solid-state DSCs is not as effective as that in liquid-state DSCs because the population of the holes in the hole transporter layer is dense, causing fast recombination between injected electrons and holes residing in the transporter. This process is in the range of few tens of milliseconds for the liquid state<sup>[30, 31]</sup> and nano- to microseconds for the solid state devices<sup>[32-34]</sup>.

Despite the advantages of easy manufacturing and excellent stability in solid-state DSCs even in air, devices still suffer from incomplete pore filling<sup>[119]</sup>, leading to short diffusion lengths of holes and therefore, lower efficiencies. Pore filling seems to be optimized at a titania thickness of 2  $\mu\text{m}$ <sup>[120]</sup>. However, it causes lower IPCE in solid-state devices due to less light scattering and insufficient light trapping, whereas liquid-state DSCs often achieve an IPCE of 100 % owing to 10  $\mu\text{m}$  thick titania layer.

### ***Reductive quenching in solid-state DSCs***

Aside from low photocurrents, there is one more distinguishing characteristic, only observed in solid-state devices. This is another charge creation channel called reductive quenching or preceding hole transfer. Normally, charges are injected from an excited state after photon absorption by the dye, whereas reductive quenching contributes to charge generation by formation of a dye anion prior to electron injection<sup>[121]</sup>. This reductive quenching process is considered less efficient than the ordinary generation channel<sup>[45]</sup>. In Chapter 5, the possibility of reductive quenching will be discussed based on transient absorption data and a multivariate curve resolution analysis is used to probe its existence.

## 2.5 Multivariate curve resolution (MCR)

Multivariate curve resolution (MCR) developed by a group in the Universitat de Barcelona <sup>[122]</sup> is a soft-modelling method for extracting undetermined species or chemical constituents qualitatively from the experimental measurements showing species-associated profiles such as spectra and dynamics.

To begin with, one starts with an initial guess for the concentration profile based on a data matrix from TAS measurements. This initial guess is generated by using evolving factor analysis (EFA) under a supposition of how many species will be needed. Resolved spectra and concentration profiles are obtained from a data optimization process using spectral and concentration constraints, such as non-negativity of concentrations.

Initially UV-vis absorption spectra were employed in this modelling, but now transient absorption spectroscopy has also been used to identify transient species <sup>[123]</sup>. However, the data set used in previous MCR analyses is all from measurements in solution and there has been no prior study reporting MCR analysis on solid-state dye-sensitized solar cells to the best of our knowledge. In Chapter 5, we used MCR analysis on a novel perylene monoimide dye to discover whether or not there is a reductive quenching process. Detailed information will be given in Chapter 5.6.

### 3. EXPERIMENTAL TECHNIQUES

#### 3.1 Sample preparation

##### 3.1.1. Device fabrication

24×24×3.1 mm fluorinated tin oxide (FTO) coated glass substrates (Pilkington, TEC-15) were used to fabricate solar cells. 11.2 mm-wide polyimide tape containing silicone adhesive (Kapton™) was used to define the active layer in the middle of the substrate. Zinc powder and 4M hydrochloric acid (1:2 v/v, 37% HCl:H<sub>2</sub>O) solution were used to etch away the fluorine doped tin oxide (FTO) layer left uncovered by the tape. The tape was detached from the substrate after etching. The substrates were rinsed with distilled water and then treated in an ultrasonic bath with detergent (Hellmanex III, Hellma), ethanol or 2-propanol, then acetone, in that order, for 15 minutes each. In order to remove all organic contaminants, argon plasma cleaning was carried out under 0.2 mbar argon at 300 W for 15 minutes.

An insulating compact oxide layer was deposited by spray pyrolysis to prevent direct contact of electrons in the metal oxide layer with holes in a hole conductor. The solution for the compact layer consisted of a titania precursor of diisopropoxytitanium bis(acetylacetonate) (Sigma-Aldrich, CAS 17927-72-9) and ethanol in a ratio of 1:10 v/v. During spray pyrolysis, a hot plate was required to keep the temperature at 450 °C, and each spray was pumped out using an atomizer (Glaskeller Art Nr. 12.159.603) every 10 seconds to give enough time to the samples to sinter the nanoparticles and to recover the set temperature. The total thickness of this compact layer was about 80-100 nm. After the samples were cooled down to room temperature, a 2 μm-thick mesoporous TiO<sub>2</sub> layer was applied using the doctor blade coating method with titania paste (Dyesol, DSL-18NR-T). The paste was diluted with ethanol at a ratio of 1:1.3 wt%. 40 μL of the diluted paste was spread out on top of the titania compact layer and doctor blade coating was carried out. For uniform thickness, the substrates were temporarily stored in a petri dish for 60 seconds to evaporate the solvents and then placed on a hot plate set to 70 °C. The sintering stage of the metal oxide nanoparticles is shown in Figure 3-1.

For better light collection and scattering the substrates were heated in a titanium (IV) chloride (Sigma-Aldrich ReagentPlus®, 99.9%, trace metals basis, CAS 7550-45-0, 208566) solution at 70°C for 1 hour after doctor blade coating. This solution consisted of a 1 mL hydrochloride solution, 200 g TiCl<sub>4</sub>, and 350 mL distilled water. This solution was diluted further with additional distilled water at a ratio of 1:10 v/v. About 7 – 8 samples were dipped in this solution and were placed on a hot plate set to 70 °C for one hour. After the TiCl<sub>4</sub> treatment the substrates were rinsed with distilled water and then sintered at 500 °C for 45 minutes. The samples were finally dipped in the dye solution for the sensitization. For dye staining in different dye solutions, see section 1.4.

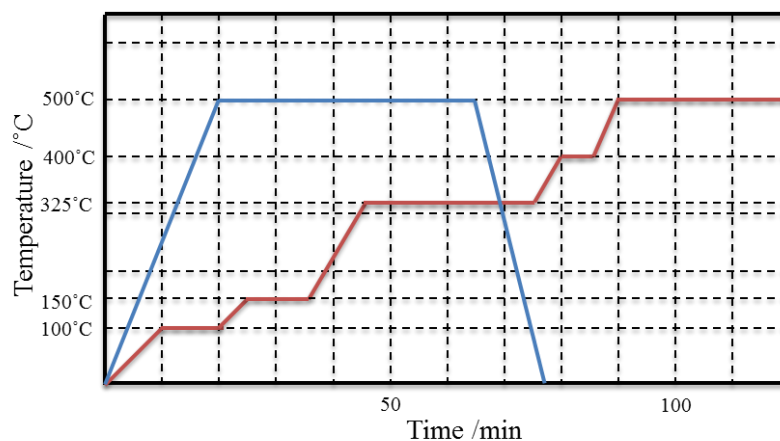


Figure 3-1. Time-temperature profile of the sintering process for two layers. A mesoporous titania layer after doctor blade coating in red, and an insulating metal oxide layer in blue.

To regenerate oxidized dyes spiro-OMeTAD (2,2',7,7'-tetrakis-(N,N-di-p-methoxyphenyl-amine)-9,9'-spirobifluorene, Merck, SHT-263 Livlux) was employed in this dissertation. 121.9 mM spiro-OMeTAD solution in chlorobenzene was prepared and heated up to 60-80 °C to dissolve all material. 97 mM *t*BP (4-*tert*-butylpyridine, Aldrich, 3978-81-2) and 18.2 mM Li-TFSI solution (lithium bis (trifluoromethanesulfonyl) imide salt, Aldrich, 900-76-65-6) were added into the dissolved spiro-OMeTAD solution. The molecular structures of these three chemicals are shown in Figure 3-2. A Li cation additive solution was prepared in advance at a concentration of 0.59 mM in acetonitrile and stored under nitrogen. Approximately 65  $\mu$ L of spiro-OMeTAD solution was used to spin coat each sample. The spin-coating procedure was as follows: wait for the evaporation of solvents for pore filling for 1 min and then spin-cast at a speed of 1000 rpm for 5 seconds followed by a speed of 1500 rpm for 30 seconds.

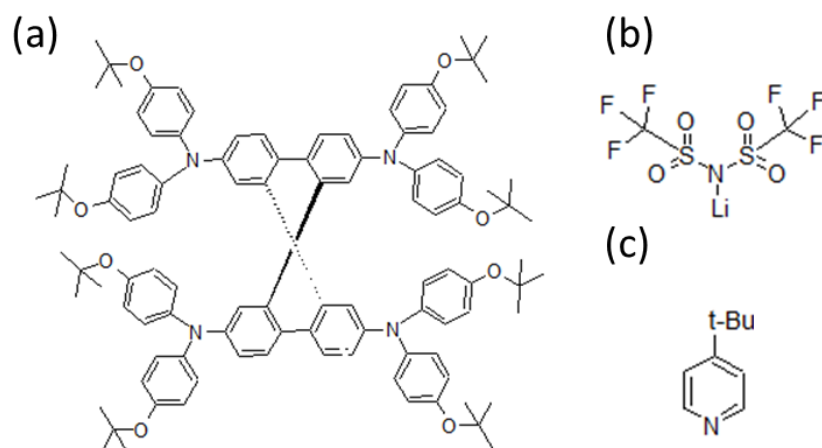


Figure 3-2. Molecular structure of spiro-OMeTAD (a), Li additive ion salt (b), and *tert*-butylpyridine (*t*BP) (c).

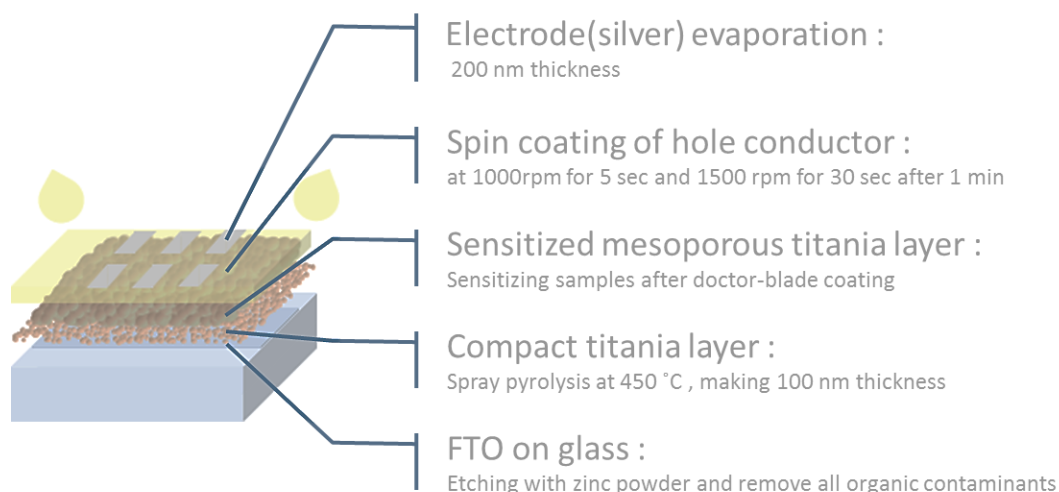


Figure 3-3. Schematic structure of a solid-state dye-sensitized solar cell: FTO as an anode, compact titania layer, mesoporous metal oxide layer as an electron acceptor, sensitized dye as a photon harvesting system, hole conductor for dye regeneration, and silver as a cathode.

For the formation of counter electrodes, thermal evaporation deposition was carried out (Edwards FL400, AUTO 306 CRYO). A tungsten boat was used to melt the silver and a shadow mask with the exact dimensions of the active area of the cell was used for evaporation. The silver electrode showed good confinement of the light and good electronic contact with a hole conductor material <sup>[120]</sup>. The deposition rate was controlled at a rate below 2.5 Å/s: 1 Å/s for the first 100 nm thickness and 2Å/s for the next 100 nm, for a total thickness of 200 nm. The FTO area for electron extraction was covered by the titania layer from the pyrolysis deposition and by the hole conductor, thus, to make a better contact, those layers needed to be scratched. After scratching, silver paste was used on top of the anode and cathode points. A simplified structure diagram of the solid-state dye-sensitized solar cells is given in Figure 3-3.

### 3.1.2. Samples for spectroscopy

For time-resolved photoluminescence spectroscopy, photoinduced absorption spectroscopy, and transient absorption spectroscopy measurements, both titania and alumina film substrates were used in order to measure the excited state dynamics of the dyes.

For the alumina (Al<sub>2</sub>O<sub>3</sub>) samples, 300 mg terpeneol, 1250 μL ethanol, and 50 mg ethyl cellulose solution <sup>[124]</sup> were added to 500 μL of an alumina dispersion (Sigma Aldrich, 702129, CAS 1344-28-1). The ethyl cellulose solution was prepared with both 0.75 mg ethyl cellulose (Sigma-Aldrich, 9004-57-3) of viscosity 46 cP and 0.75 mg ethyl cellulose of viscosity 10 cP in 15 mL ethanol. The alumina solution was coated using the doctor blade coating method on quartz substrates and the samples were sintered using the same sintering procedure as for sintering the mesoporous titania layer. The samples

using titania nanoparticles were prepared using the same procedure as the general device preparation described above, except for the etching and evaporation process.

The samples were prepared under 3 different conditions on both titania and alumina layers to be able to distinguish the absorption spectra of a variety of excited species: the dye alone, the dye with a Li cation additive, and the complete device structure (dye plus spiro-OMeTAD, Li cation, and *t*BP).

### 3.2. Steady-state measurements

#### 3.2.1. J-V characteristics

The power conversion efficiency of the solar cell devices was measured using a solar simulator (LOT-Oriel, LSE 340/850.27B) with an incident illumination power density of  $100 \text{ mW/cm}^2$ . The solar simulator uses a xenon arc lamp calibrated by a silicon photodiode and it has a photon spectrum similar to air mass (AM) 1.5 global solar conditions at room temperature and in the air. The AM 1.5G solar spectrum shown in Figure 3-4 is used as a standard reference spectrum to compare the performance of the devices since the spectrum of incident light depends on factors such as latitude and cloud coverage. In our system, one solar cell device consists of 6 pixels with an active area of  $0.1403 \text{ cm}^2$  each and the performance of the devices discussed in this dissertation is obtained by taking the average value of all 6 cells.

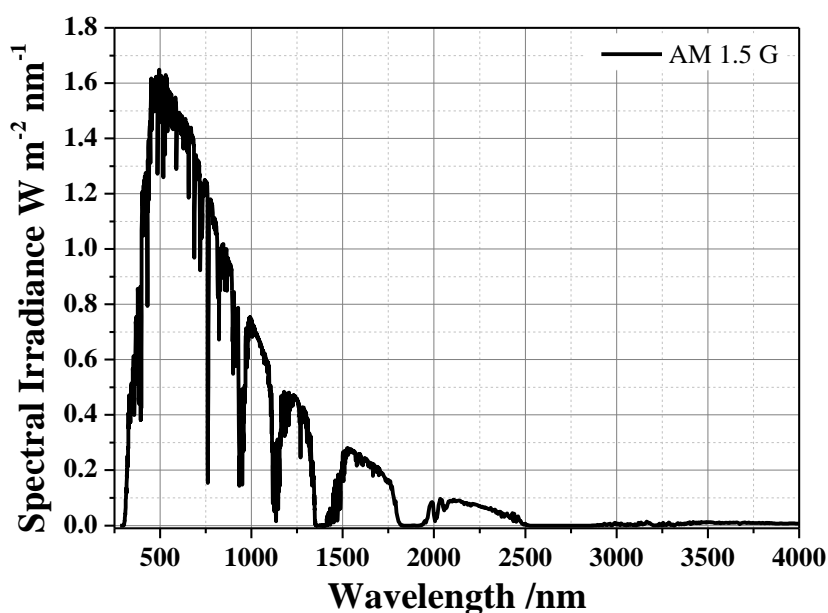


Figure 3-4. Spectral irradiance at air mass (AM) 1.5 global solar conditions.



A Keithley 2400 digital source meter was used to apply the voltages and to measure the currents under light. The parameters for the Keithly were set using a Labview software programme (National Instruments). Figure 3-5 shows how the currents from the devices were obtained when the applied voltage changes. Reverse bias set the voltage at the counter electrode (Ag) higher than that at the electrode (FTO) as shown in Figure 3-5 (a), therefore, only slight leakage current will flow due to an injection barrier. When the applied bias is 0 the work function of the two electrodes becomes the same and here only the forward drift current is observed, as in Figure 3-4 (b). This is the short circuit current density ( $J_{SC}$  when  $V_{app}=0$ ) when the surface area of the cell is taken into account. There is no current flow when the applied voltage and built-in potential (voltage) of the device are the same and this is defined as the open circuit voltage ( $V_{OC}$ ). The J-V curve will be a square (like the blue box line) between these two points ( $V_{OC}$  and  $J_{SC}$ ) if there is no recombination of electrons and holes. If the built-in potential becomes smaller than the applied voltage, forward bias is observed and it changes are injected from the electrodes.

The performance of the device was assessed using the short circuit current density ( $J_{SC}$ ), the open circuit voltage ( $V_{OC}$ ), the fill factor (FF), and incident light irradiance  $P_{inc}$ , according to:

$$\eta = \frac{J_{SC} \cdot V_{OC} \cdot FF}{P_{inc}}$$

As shown in Figure 3-5,  $J_{SC}$  and  $V_{OC}$  measurements were obtained by sweeping the devices with an externally applied voltage. The FF is calculated according to the following formula:

$$FF = \frac{V_{MPP} \cdot J(I)_{MPP}}{V_{OC} \cdot J(I)_{SC}}$$

where  $I_{MPP}$  is the current at maximum power point, and  $V_{MPP}$  is the voltage where the maximum power point is reached.

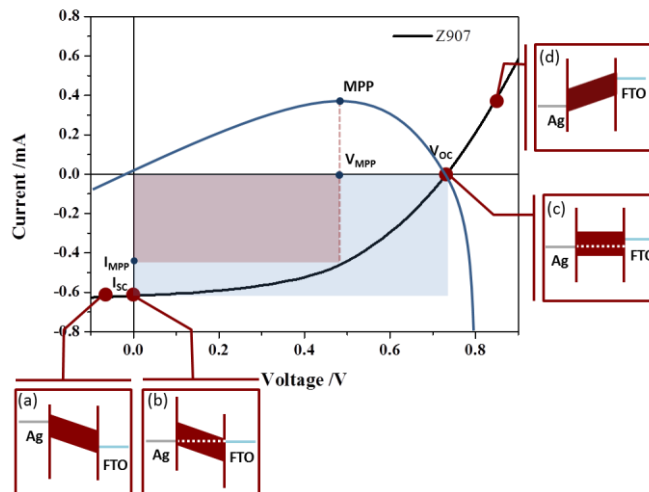


Figure 3-5. Schematic diagram showing how the band positions shift according to the applied voltage.

### 3.2.2. External quantum efficiency

External quantum efficiency (EQE) is the number of electrons that contribute to the current divided by the number of incident photons. The EQE measurement was carried out with a home-built instrument and the EQE values were calculated by the equation

$$EQE = \frac{I_{SC}^{s.c.}}{I_{SC}^{ref}} \cdot EQE_{ref}.$$

Therefore, the ratio of a sample cell's currents ( $I_{SC}^{s.c.}$ ) and the reference photodiode's current ( $I_{SC}^{ref}$ ) multiplied by the number of incident photons for each wavelength ( $EQE_{ref}$ ) leads to the sample cell's EQE. With the EQE values, the short circuit current ( $J_{SC}$ ) of the sample can be obtained from the integral of the EQE values and the number of incident photons across the wavelength range measured:

$$J_{sc} = \frac{q}{h} \int_{\lambda_{min}}^{\lambda_{max}} EQE P_{in}(\lambda) \lambda d\lambda$$

Where  $q$  is the elementary charge,  $h$  is Plank's constant,  $P_{in}$  is the light intensity at a certain wavelength, and  $\lambda$  is the wavelength measured. However, the EQE does not take into account how many photons are absorbed. This is taken into account by the internal quantum efficiency (IQE). IQE is defined as the ratio of the number of electrons that contribute to the current over the number of absorbed photons and can be expressed as follows:

$$IQE(\lambda) = \frac{EQE(\lambda)}{1 - 10^{-A(\lambda)}}$$

### 3.2.3. UV-Vis absorption measurements

Absorption measurements were carried out using a Perkin Elmer Lambda 25 UV-Vis absorption spectrometer and absorbance is measured based on changes in transmission (see the section 2.3.1.) with and without an inserted sample.

Most samples with a titania or an alumina coating were dipped in 0.3 mM dye solution overnight. For dye solution measurements, the concentration was kept at 0.1 mM to exclude aggregation, intermolecular reactions and reabsorption of light.

To measure the absorption of cationic species, 5 mM anhydrous iron(III) chloride solution was mixed with the dye solution, acting as a Lewis acid. For example, one of the cyclopentadithiophene dyes, coded FPH303, investigated here and shown in Figure 3-6 (a), shows an additional dye cation absorbance peak at 760 nm after the addition of  $FeCl_3$ .

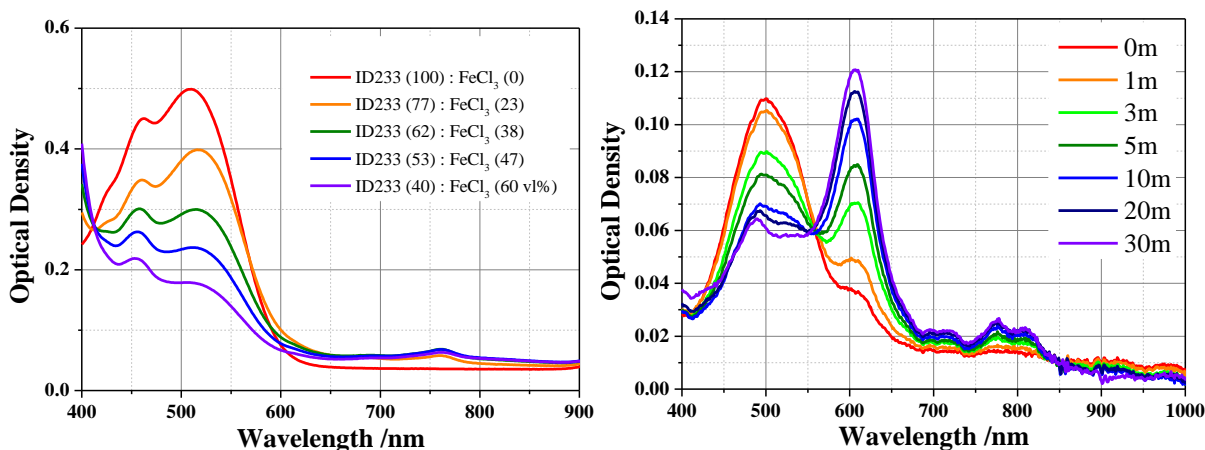


Figure 3-6. (a) Changes in absorption of oxidized dye FPH303 created by adding 5 mM anhydrous iron(III) chloride solution. Ratios are based on volume percent; (b) Changes in absorption of ID889 due to anion formation under Lupasol and UV illumination treatment.

For the absorption measurements of anionic species, 20 mg of polyethylenimine molecules (Lupasol<sup>®</sup>, BASF) and 20  $\mu$ L of 0.3 mM dye solution were mixed and sandwiched between two slide glasses. Lupasol helps to form anionic species of the dye under UV illumination. The perylene dye ID889 studied here shows absorption peaks due to the anionic species at 600, 700, and around 800 nm, not seen in the films or dye solution in Figure 3-6(b).

#### 3.2.4. Photoinduced absorption spectroscopy

Photoinduced absorption spectroscopy (PIA) is a quasi-steady-state pump-probe measurement to detect excited species living up to microseconds, such as charged species or triplet states. In order to excite the dye molecules, a 100W tungsten halogen lamp (Müller Elektronik Optik DUO150) was used as a probe light and the white probe light was passed through a pre-monochromator. Two monochromators (Lot Oriel omni- $\lambda$  300) allow only a single wavelength of light to be passed and the transmission/absorption of the sample was detected from 500 nm to 4500 nm. After passing through the first monochromator the probe light was chopped by an electronically-controlled chopper, and the light was focused on the sample. The post-monochromator ensures that only light of the same wavelength as set by the first monochromator passes to the detector. The photoinduced absorption (PIA) signal of the sample was recorded by changes in transmission of the probe pulse with and without excitation. The detected photoluminescence signal in the visible range was deducted from the PIA signals in the visible range.

The probe light transmitted by the sample before and after excitation was collected by 3 different detectors, depending on the wavelength region. Silicon (Thorlabs PDA 100A), germanium (Thorlabs PDA 50B), and indium antimonide detectors (Teledyne-Judson J10D) were used to detect the signals in the wavelength regions of 500-1100 nm, 900-1700 nm, and 1700-4500 nm, respectively. For

excitation, 3 different light sources were used depending on the absorption bands of the materials: a purple LED (Hamamatsu LC-L2,  $\lambda=365$  nm), a green LED (Newport LED-527-HP,  $\lambda=530$  nm), and a red laser (HeNe cw-laser, JDSU,  $\lambda=633$  nm).

The pump light was modulated by a function generator (Kontron Messtechnik Model 8201) at a fixed frequency of 317 Hz and a synchronization output signal from the function generator was sent to a lock-in amplifier (EG&G Princeton Applied Research Model 5210). The  $\Delta T/T$  signals in the PIA measurement have an order of  $10^{-4}$  to  $10^{-5}$ , hence use of the lock-in technique is necessary to increase the signal-to-noise ratio. The lock-in amplifier takes a square modulated reference signal that is used for the excitation source and then measures the accurate transmission signal of the samples. This records changes in transmission,  $\Delta T$ , by subtraction of the transmission of the sample without a pump pulse from the transmission with a pump pulse. Finally, changes in transmission are divided by transmission in the absence of excitation.

Since the samples create different species upon excitation,  $\Delta T/T$  signals normalized to the photon flux,  $(= \frac{P \cdot \lambda_{exc}}{h \cdot c} \cdot (1 - 10^{-A}))$ , were required for the data processing.  $P$ ,  $h$ ,  $c$ , and  $A$  represent power density, Planck's constant, the speed of light, and the absorbance at the excitation wavelength of the samples, respectively. As described above, to exclude a contribution/perturbation by PL emission to the PIA signal, signals in the visible range were obtained by subtraction of PL signals from the PIA signals :  $\frac{\Delta T}{T} = \frac{\Delta T_{PIA} - \Delta T_{PL}}{T}$ .

During the measurement, the sample was placed in an optical cryostat (Oxford Instruments Optistat CF) at a  $45^\circ$  angle to optimize the overlap at the sample area with the pump and probe light. The sample was measured at a pressure below  $10^{-5}$  mbar. A schematic of the PIA set-up is shown in Figure 3-7.

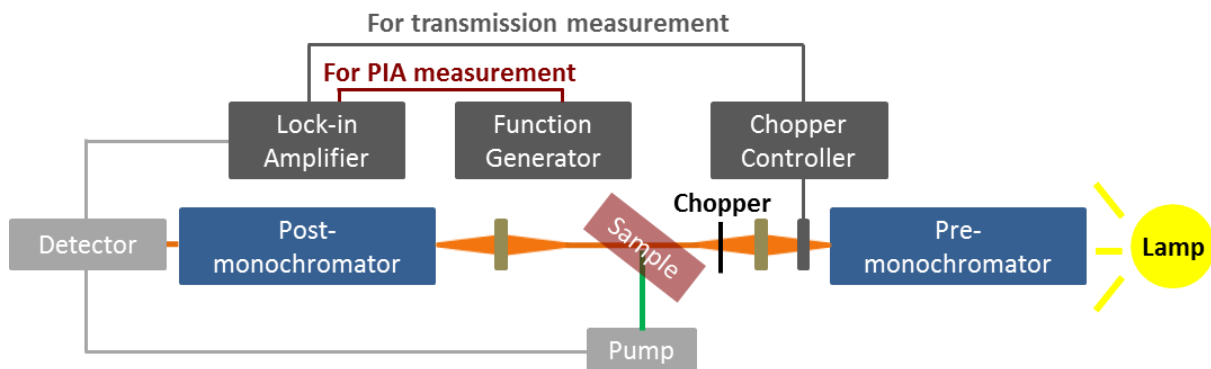


Figure 3-7. Schematic illustration of photoinduced absorption spectroscopy.

### 3.3. Time-resolved measurements

#### 3.3.1. Photoluminescence spectroscopy

Time-resolved photoluminescence (PL) spectroscopy using a streak camera system probes the emission of excited states and the time-dependent radiative decay. Two modes for PL spectroscopy were used depending on the excited species lifetime range: fast sweep (a couple of picoseconds to 2 nanoseconds) and slow sweep (hundreds of picoseconds to milliseconds).

For fast sweep measurements, the output from a Ti:Sapphire ultrafast laser system (Coherent Mira 900-Dual fs-ps-Oscillator) was used to excite the light absorbing system. The 800 nm centered pulsed excitation has a repetition rate of 80 MHz with a pulse width of 200 fs. This excitation goes through a BBO crystal to double the frequency and generates output at 370-430 nm (3.35-2.88 eV). For longer excited state lifetimes, a supercontinuum fiber laser (Fianium, SC450-2,  $450 \text{ nm} < \lambda < 2200 \text{ nm}$ ) was used. It has a repetition rate of 20 MHz and generates 200 mW of power.

The photons emitted from the samples were spectrally resolved by a spectrograph, and sequentially converted into electrons at a photocathode. The released electrons were accelerated in a time-dependent electric field in the y axis (Hamamatsu Streak Camera system), and swept by the applied voltage time-synchronized with the incident pulsed excitation. Electrons multiplied by the microchannel plate were converted back into photons on a phosphorescent screen at a different time and space position. A two dimensional CCD camera was used to record the number of photons and to obtain an image of the PL with both spectral (x-axis) and temporal (y-axis) distributions.

A schematic diagram of the streak camera is shown in Figure 3-8. All films were measured at a pressure of  $10^{-5}$  mbar.

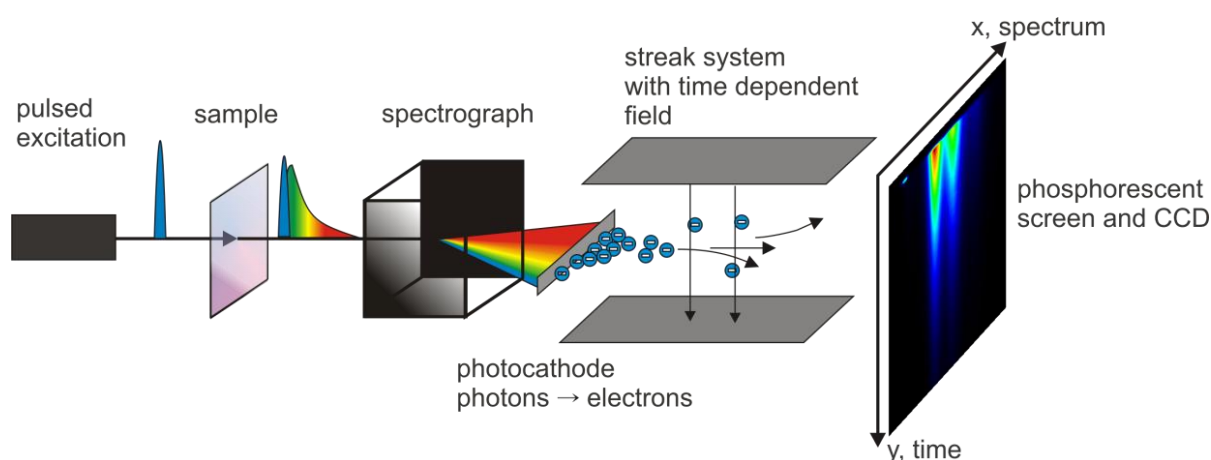


Figure 3-8. Operating principle of a streak camera system.

### 3.3.2. Transient absorption spectroscopy

Analyzing the dynamics of excited state populations, such as exciton/charge generation and recombination, gives insights into device performance constraints. Transient absorption spectroscopy (TAS) is a useful method for observing excited state population changes over time. TAS is also known as pump-probe spectroscopy. It uses a monochromatic pulsed excitation as a pump and a broad supercontinuum white-light as a probe.

The Ti-Sapphire laser system (Coherent Libra-HE) generates laser pulses (800 nm centered, length of 100 fs) with a repetition rate of 1 kHz. The amplified laser output is split and sent into two optical parametrical amplifiers, OPA, (Coherent OPerA Solo Topas System) by beam splitters. Topas 1 converts the laser pulse to a pump pulse ranging from 285 nm to 2600 nm. The excitation wavelength can be obtained by different nonlinear process such as the sum frequency of signal (470-535 nm), of idler (533-613 nm), second harmonic of signal (565-810 nm) or of idler (793-1130 nm). The pump pulse is delayed by simply changing the laser propagation path with a translation stage (Newport, 600 mm travel range), allowing monitoring the time evolution of excited species on a femto- to nanoseconds time scale. To obtain  $\Delta T/T$ , the repetition rate of the pump pulse is reduced to 500 Hz from 1 kHz by a rotating disk (chopper) to block every second excitation pulse corresponding to pump on or pump off.

Topas 2 creates a seed wavelength that is focused to generate a white light supercontinuum probe beam (450-2000 nm) in sapphire, yttrium-aluminium-garnet (YAG) or yttrium vanadate (YVO<sub>4</sub>). This probe beam is superimposed on the pump beam on the sample, but the probe beam spot size has to be smaller than the pump beam to maintain overlap. The probe beam is then detected by a CCD spectrograph. Two configurations are available for long time delay (up to 1ms with a time resolution of 600 ps) and for short time delay (up to 4 ns with a time resolution of 100 fs). In the long time delay configuration, a Q-switched Nd:YVO<sub>4</sub> laser (AOT Ltd. MOPA) is used as an excitation source operated at 532 nm and triggered by an external trigger. The delay between the pump and probe beam is controlled by an electronic delay generator (Stanford Research Systems DG535) rather than a delay stage.

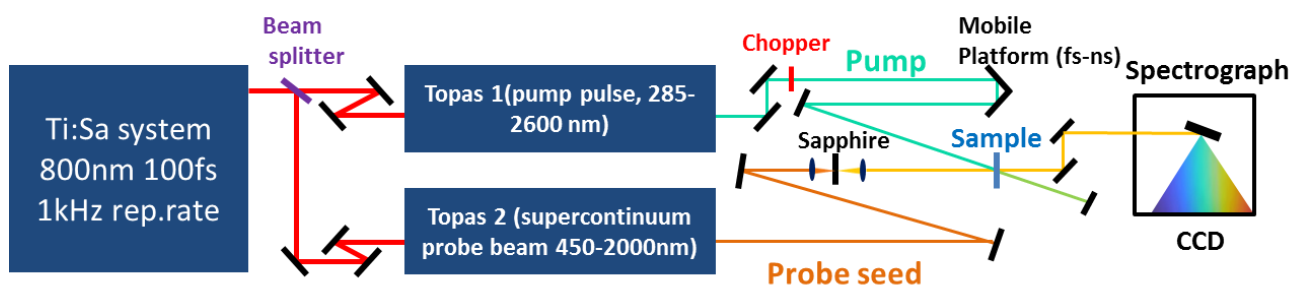


Figure 3-9. Schematic of the transient absorption spectroscopy setup. This panel is adapted from <sup>[125]</sup>.

To maintain a homogeneous excitation density, the size of the pump spot was set to be larger than that of the probe spot, as described above. After finding the overlap of the pump and probe pulse, a polarizer was placed along the pump pulse to rotate the polarization to magic angle,  $54.7^\circ$ , with respect to the polarization of the probe light, to null effects from light polarization of the pump and probe pulse.

$\Delta T$  signals were detected by a grating spectrometer (Princeton Instruments Acton SP2150) with a photodiode array detector (silicon photodiode NMOS array with 256 and 512 pixels, a Hamamatsu NMOS linear image sensor S3901-25/512 for the visible range and an InGaAs array detector with 512 pixels, Entwicklungsbuero Stresing, for the NIR/IR range). All signals shown in this dissertation were averaged for better signal-to-noise ratio by one thousand shots of the pump on/off pulses and kinetics were extracted at chosen wavelengths from the averaged data.

TA measurements were carried out at room temperature in high vacuum at  $10^{-5}$  mbar.

### 3.4. Materials

In this dissertation, 3 different push-pull type dye groups were investigated. The first group consisted of rylene family dyes, from perylene to quaterylene derivatives. In the second case study, the sensitizer was a perylene derivative as  $\pi$ -conjugated system with fused dibenzothiophene as a bridge and triphenylamine as donor. The third case study concerned a set of CPDT building units as  $\pi$ -conjugated systems and varying donor structures.

Sensitization times varied depending on the different dye adsorption rates. Concentration of dye solutions were kept at 0.3 mM for all dyes. For solution measurements, concentration was kept at 0.1 mM to prevent reabsorption of light and aggregation of dye molecules.

#### 3.4.1. Naphthalene core-enlarged rylene family dyes (PMIMA, TMIMA, and QMIMA)

The materials studied in Chapter 4 belong to the family of rylene dyes. Three different dyes were investigated, namely a perylene, terylene and quaterylene derivative (perylene mono-imid mono-anhydride PMIMA, TMIMA, and QMIMA). All dyes are substituted at the bay-position of the rylene core to improve the solubility and prevent aggregation and bear an imide and an anhydride group at the terminal positions. The latter group functions as anchor group during the adsorption of the dye molecules on the metal nanoparticle surface, as it undergoes hydrolyses in situ to the di-carboxylic-acid, which in turn can attach to the metal oxide nanoparticle surface. Since the ryleneanhydride dyes exhibit a change in molecular structure on adsorption to a semiconducting film, the dyes are treated with potassium hydroxide (KOH) aqueous solution to study the ring opening. Figure 3-10 shows the chemical structures of the investigated rylene dye molecules.





### 3.4.3. Cyclopentadithiophene building block dye (FPH224, 231, 233, and 303)

The materials studied in Chapter 6 are push-pull dyes using a cyclopentadithiophene (CPDT) building block as a conjugated bridging unit. FPH224, 231, and 233 dyes have several novel donor blocks and FH303 has a different acceptor moiety, compared to FPH224, but with the same bridge and donor moiety.

FPH224, 231, and 233 comprise of the CPDT bridging moiety with 2-butyl-groups and a cyanoacrylic acid as an anchoring group. FPH231 has a dendrimer-like electron donating group made of triphenylamine units. FPH303 has shown red-shifted absorption when compared to FPH224 because of its rhodanine-3-acetic acid group. The samples were left in 0.3 mM THF at 25°C overnight. The molecular structures are shown in Figure 3-12.

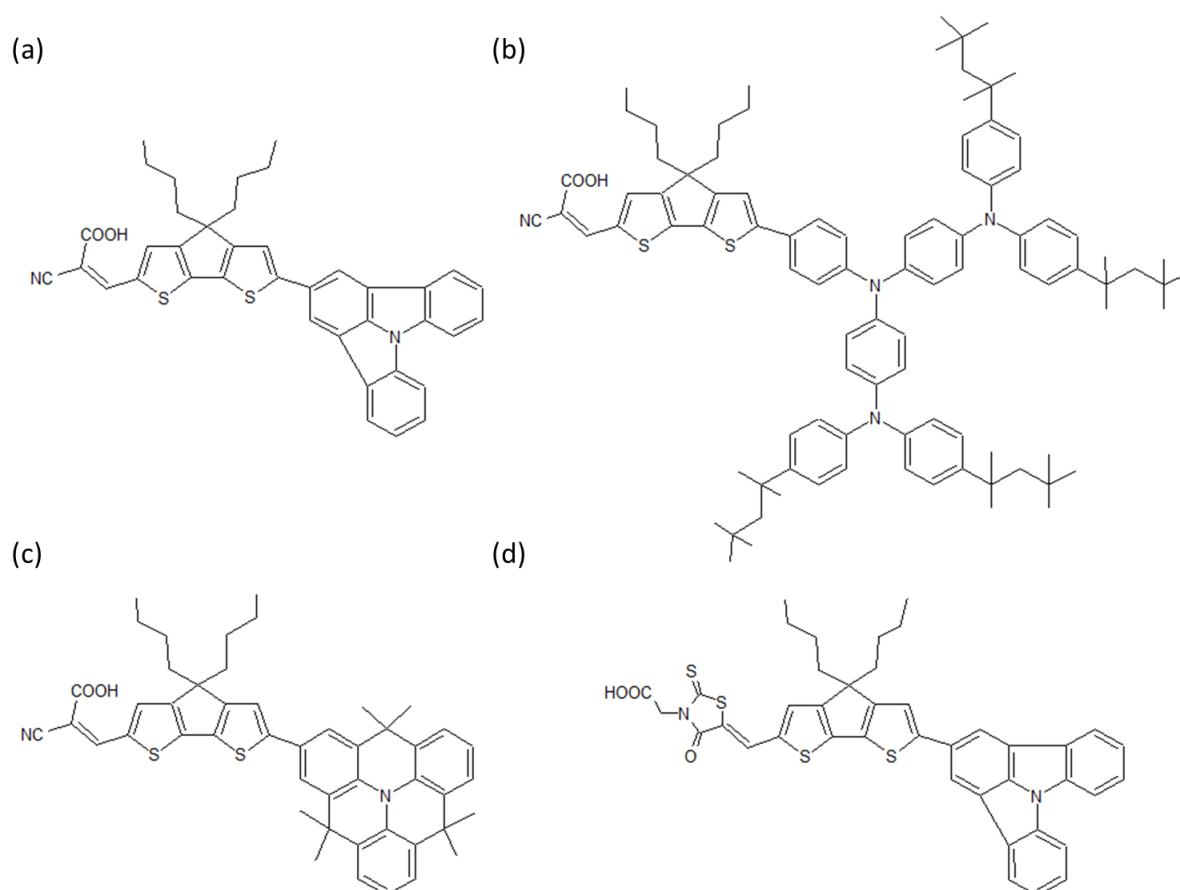


Figure 3-12. Molecular structures of the series of CPDT building block dyes, FH224 (a), FH231 (b), FH233 (c), and FH303 (d).

### 3.4.4. Z907

One of the ruthenium complexes, Z907, is a standard dye for dye-sensitized solar cells and Z907 was used here as a reference. A 0.3 mM dye solution was prepared in tert-butanol and acetonitrile with a

ratio of 1 to 1 and stirred overnight in air. The preparation of devices was considered to be appropriate, when the Z907-based device demonstrated an efficiency of  $2\% \pm 0.3\%$ .

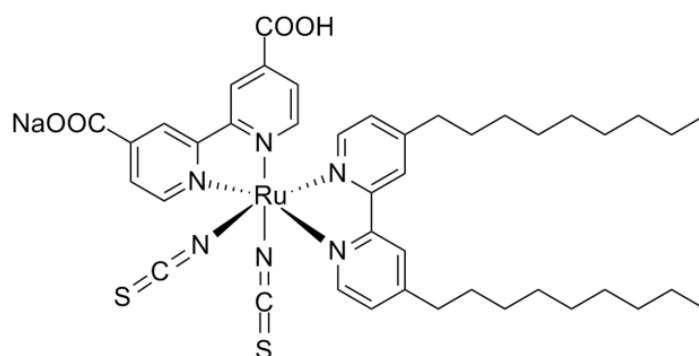


Figure 3-13. Molecular structure of the ruthenium complex Z907.

## 4. RYLENEANHYDRIDE SENSITIZERS

Rylene dyes are considered promising candidates for efficient dye-sensitized solar cell (DSC) devices due to their high molar extinction coefficients, photo-stability, and tunable energy levels. Despite these good prerequisites, solid-state dye-sensitized solar cell devices using rylene dye molecules suffer from low photocurrents. In this chapter, we are going to investigate changes in photophysical properties of perylene, terylene, and quaterylene mono-imide mono anhydride dye molecules as the length of the rylene core is increased and as the maleic acid anhydride anchoring group experiences ring opening. Low short-circuit currents in devices will be assigned to changes in dipole moments as determined by density functional theory calculations.

### 4.1. Materials

The materials studied here belong to the family of rylene dyes. Three different rylene dyes were investigated, namely a perylene, terylene and quaterylene derivative. If one or two naphthalene units are added to PMIMA (perylene mono-imide-mono-anhydride,  $n=0$ ), dye molecules will be named TMIMA ( $n=1$ ) and QMIMA ( $n=2$ ) as shown in Figure 4-1. All dyes are substituted at the bay-position of the rylene core to improve the solubility, prevent aggregation and they bear an imide and a maleic acid anhydride group at the terminal positions. Because of the maleic acid anhydride groups, these dye molecules can be adsorbed on metal oxide surfaces.

Titanium dioxide has three mineral forms, namely anatase, brookite, and rutile. A widely used  $\text{TiO}_2$  structure in DSCs is anatase due to its higher short-circuit photocurrent in a device as it provides more adsorption sites for dye molecules and a better electron transport property due to more conductive channels in the interparticle network. Hence, for device fabrication and spectroscopy, anatase  $\text{TiO}_2$  is used in this dissertation.

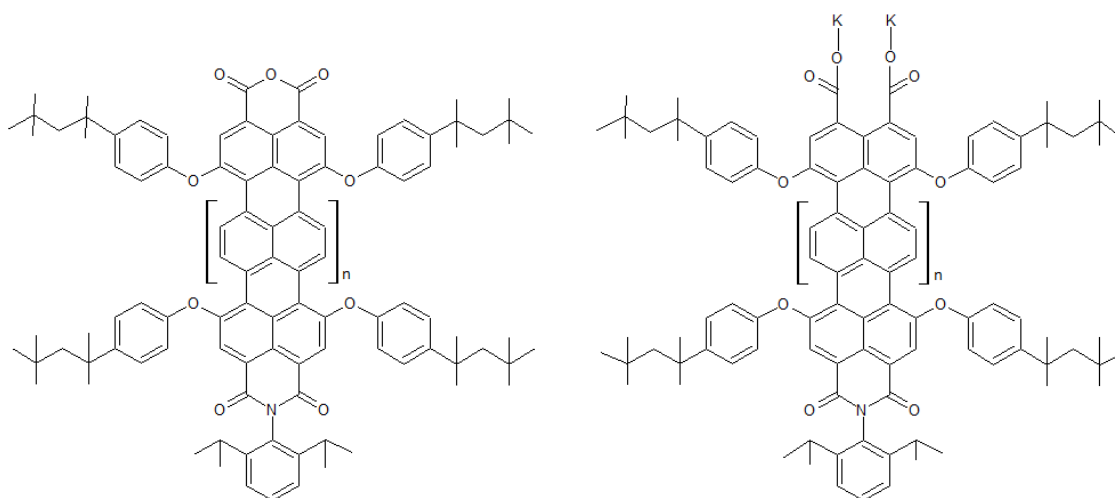


Figure 4-1. Chemical structures of PMIMA ( $n=0$ ), TMIMA ( $n=1$ ), and QMIMA ( $n=2$ ) with anhydride group (left) and as potassium salts of the di-carboxylic acids (right) used in solution measurements.

The binding of a maleic acid anchoring group to a titanium dioxide surface has been investigated by many research groups. Do et al. confirmed that maleic acid anhydride undergoes ring-opening during adsorption on  $\text{Al}_2\text{O}_3$  and  $\text{TiO}_2$  by IR spectroscopy <sup>[126]</sup> and Wilson et al. found that maleic acid anhydride binds with one oxygen to one Ti atom of the rutile (001) surface by formation of a monodentate bridging configuration <sup>[127]</sup>. Other research groups studied bidentate bridging modes on titania: sodium formate tends to form dissociated bridging bidentate geometry on hydrated anatase (101)  $\text{TiO}_2$  surfaces, which was calculated by DFT <sup>[128]</sup>. In addition, the dissociative adsorption of acetic anhydride took place on a (110)  $\text{TiO}_2$  surface and two acetate ions are bound with a bidentate coordination with the 5-fold coordinated Ti sites <sup>[129]</sup>. Johansson et al. reported that maleic acid anhydride undergoes ring opening by adsorption at the (100) and (101) anatase surfaces due to a dissociative binding mode forming bidentate fashion, but adsorption at (001) surface shows different geometry by carboxylates involving one oxygen atom from a titania surface <sup>[108]</sup>.

Therefore, maleic acid anhydride undergoes ring opening either through bidentated bridging as suggested by Ashima and Johansson or through monodentate coordination due to  $-\text{CO}^+$  and  $-\text{COO}^-$  that are rather strongly bound to rylene core <sup>[130]</sup>. Figure 4-2 shows two binding configurations of maleic acid anhydride upon adsorption at a  $\text{TiO}_2$  surface.

Since the ryleneanhydride dyes are undergoing a change in molecular structure upon adsorption on a semiconducting metal oxide film, the dyes are treated with potassium hydroxide (KOH) in aqueous solution to study the ring-opened anhydride moiety as shown in the right panel of Figure 4-1.

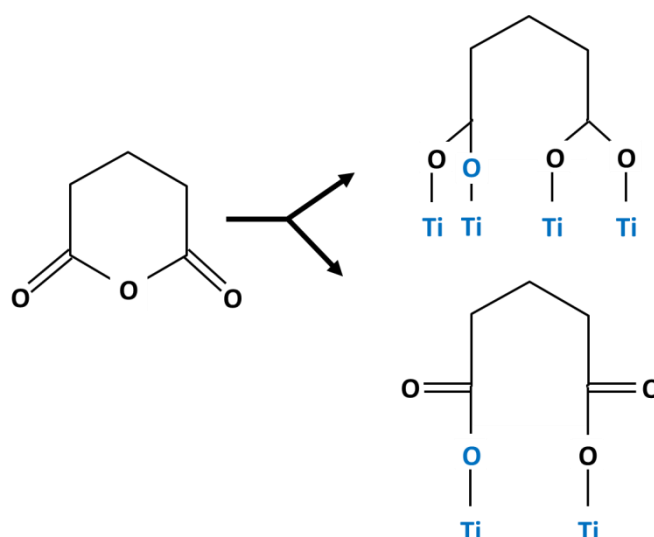


Figure 4-2. Potential binding configurations of maleic acids on  $\text{TiO}$  surface: (a) bidentate bridging and (b) monodentate mode. Atoms in blue originate from titanium dioxide surface and atoms in black come from maleic acid anhydride.

The energy levels of the dye molecules are expected to change by increasing the rylene core lengths. Figure 4-3 shows the HOMO/LUMO levels of the dye molecules that are obtained from density functional theory (DFT) calculation. The HOMO and LUMO levels of PMIMA are changed from -5.50 eV and -3.20 eV to -5.28 eV and -3.35 eV in TMIMA, and to -5.01 eV and -3.41 eV in QMIMA, respectively. Significant changes in both the HOMO and LUMO levels are due to delocalized charge densities across acceptor and donor moieties. These energy levels appear to be favorable enough to inject electrons into the conduction band of the TiO<sub>2</sub> layer and to regenerate the dye cation. The HOMO and LUMO levels of the anhydride-rylene dyes (solid lines) shown in Figure 4-3 are obtained from density functional theory (DFT) calculations.

The samples for device fabrication and for optical spectroscopy were prepared as described in the experimental section, Chapter 3.1. For solution measurements, a 0.1 mM dye solution was prepared with solvents of different polarity. The sensitization of metal oxide films was carried out at 25 – 30 °C for 15 hours in toluene.

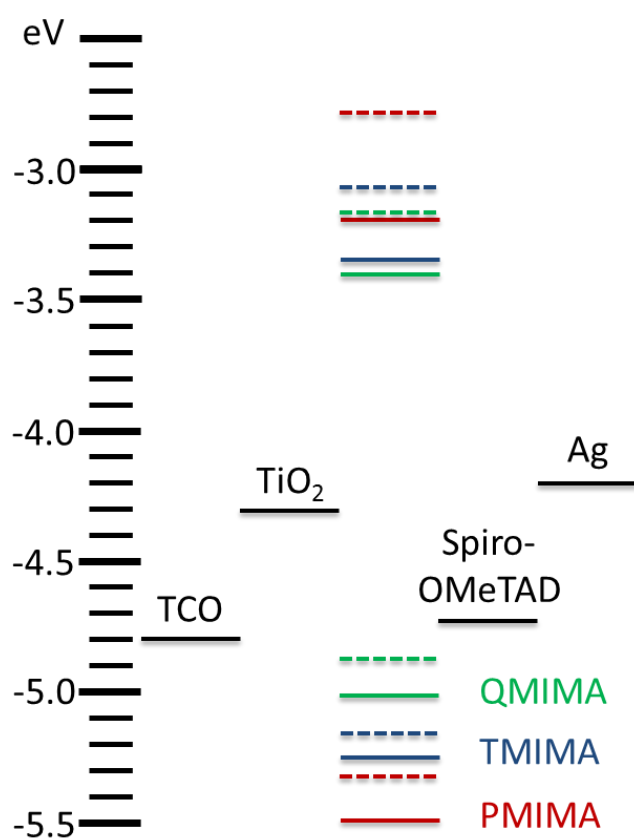


Figure 4-3. The HOMO and LUMO energy levels of anhydride-PMIMA (black solid), TMIMA (red solid), and QMIMA (blue solid) and of di-carboxylic acids of the dye molecules (dotted) calculated by density functional theory calculation

## 4.2. Dyes in solution

In this section, changes in absorption/emission spectra and in excited state lifetimes of the dyes in solution are investigated. These observations give insight into the dynamics of excited states that play an important role for electron injection. For detection of spectra and excited state lifetimes of dye solutions, time-resolved photoluminescence (PL) measurements are carried out and the detailed experimental setup is introduced in Chapter 3.3.1.

### 4.2.1. Absorption and emission spectra of dye solutions

In Figure 4-4, normalized absorption/emission spectra of each anhydride dye molecule in a 0.1 mM solution in toluene (TLN) (a) are presented along with the absorption spectra of the potassium salts of the di-carboxylic acids created by hydrolysis of the anhydride moieties (b).

In panel (a), the absorption/emission spectra of the P-, T-, Q-MIMA rylene dye solutions are represented as solid/dotted black, red, and blue lines, respectively. Each dye solution shows distinct vibronic progressions in the absorption spectra, peaking at 579 nm for the PMIMA, 673 nm for the TMIMA and at 782 nm for the QMIMA. As expected, the absorption of the dye molecules clearly red-shifts when going from a perylene to a terylene and a quarterylene core due to increased conjugation [92, 131]

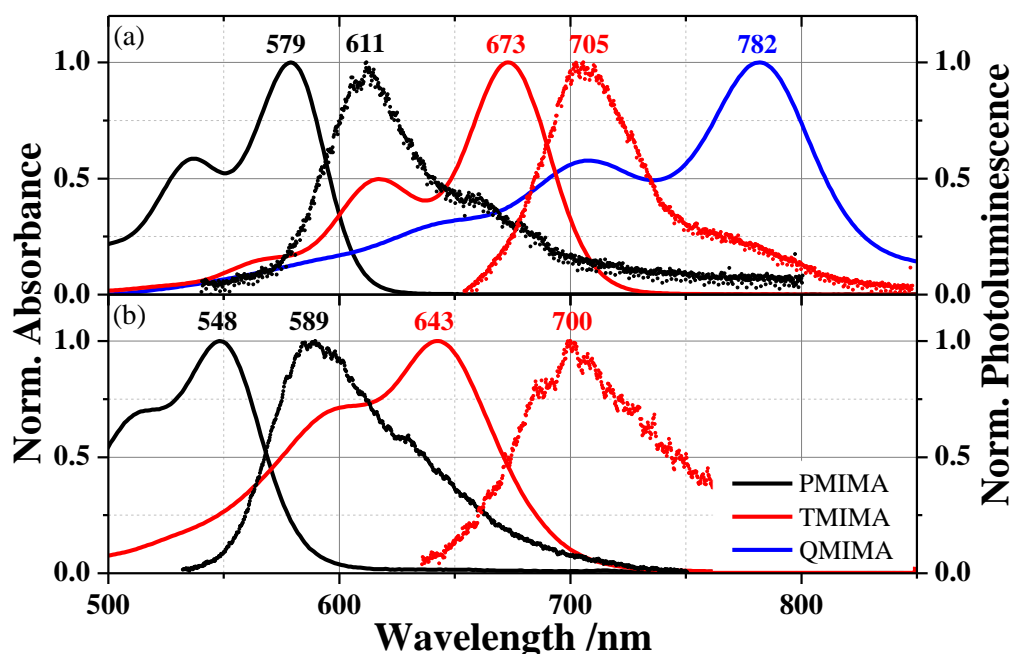


Figure 4-4. Normalized absorption/emission spectra of 0.1 mM PMIMA (black), TMIMA (red), and QMIMA (blue) dyes in toluene solution as anhydrides (a) and after ring opening (b).

Table 4-1. Molar extinction coefficients of anhydride and di-carboxylic acid dye solutions.

	Formation of anhydride moiety	Molar extinction Coeff. $M^{-1}cm^{-1}$
PMIMA	Open	12432 at 579 nm
	Closed	51274 at 579 nm
TMIMA	Open	34659 at 673 nm
	Closed	87801 at 673 nm
QMIMA	Open	-
	Closed	117279 at 785 nm

The emission spectra of these rylene dyes show to some extent mirror-image symmetry of the absorption spectra with the vibronic features, peaking at 611 and 705 nm for PMIMA and TMIMA, respectively. From the onset of absorption in solution, the LUMO levels of the PMIMA and TMIMA can be calculated, resulting in -3.4 and -3.48 eV, respectively. These levels are lower than the LUMO levels obtained from DFT calculation. This is because hydrogen atoms are used to open the rings in DFT calculation since potassium shows very strong electron pulling properties in the molecule which can cause significant changes in the HOMO (-4.46 – -4.63 eV) and LUMO (-2.07 – -2.65 eV) energy levels.

In comparison to the anhydrides, the di-carboxylic acids of the dye molecules shown in panel (b) exhibit a clear hypsochromic shift peaking from 579 nm to 548 nm for the PMIMA and from 673 nm to 643 nm for the TMIMA due to ring opening. They show larger Stokes shifts than the anhydride dyes shown in panel (a), due to considerable energy losses through structural relaxation. Increased non-radiative decay is confirmed by highly reduced photoluminescence quantum efficiency (PLQE) in di-carboxylic acid dyes. Unfortunately, we could not measure the emission spectra of the QMIMA, since the emission spectrum lies outside the detection limit of our experimental setup. The energy levels of di-carboxylic acids of the dye molecules are shown as dotted lines in Figure 4-3.

The absorption coefficient, i.e. the molar extinction coefficient, increases with increasing length of the ryleneanhydride dye molecules as a consequence of the extended  $\pi$ -system as shown in Table 4-1. The molecular extinction coefficients of the P-, T-, QMIMA are three, five, and ten times higher than that of the Ru (II) complex dye Z907, showing only  $13000 M^{-1}cm^{-1}$ . The higher absorption of these rylene dyes is expected to yield higher photocurrents in devices. Upon ring opening of the maleic acid anhydride, the molar extinction coefficients are, however, significantly reduced which is in line with the lower absorbance of the di-carboxylic acid dye solutions. Table 4-1 summarizes the molar extinction coefficients of anhydrides and di-carboxylic acid dye solutions.

#### 4.2.2. PL decay transients of dye solutions

Given the results shown above from the absorption/emission spectra and molar extinction coefficients, we assumed that there will be a change in the excited state upon opening of the anhydride rings. Figure 4-5 shows the nanosecond fluorescence decay transients of the anhydrides and potassium salts of the dicarboxylic acids of the PMIMA and the TMIMA in solution. The decay transients of the anhydrides PMIMA and TMIMA solution can be reasonably well fit with single exponentials, exhibiting lifetimes of 8.3 ns for the anhydride PMIMA (black) and 3.5 ns for the anhydride TMIMA (red). The decays of the PMIMA and TMIMA potassium salts follow single exponentials with a lifetime of 6.9 ns (gray) and 1.2 ns (orange), respectively. The reduced fluorescence lifetimes of the open ring dyes reflect enhanced non-radiative processes (confirmed by the decreased photoluminescence quantum efficiency (PLQE)) compared to the parent molecules.

The fluorescence lifetimes of the solutions are still long enough to ensure efficient injection when the dyes are attached on titania, as the injection is expected to occur on a femto- to picosecond timescale. However, the fluorescence lifetime in films needs to be studied, since the direction of adsorption, interaction between dye molecules, and aggregation can influence the lifetime of the excited states. Unfortunately, the fluorescence lifetime of the QMIMA could not be determined for the same reason as mentioned above.

For all dye solutions, the solid lines correspond to fits where amplitude and offsets are set to 1 and 0, respectively.

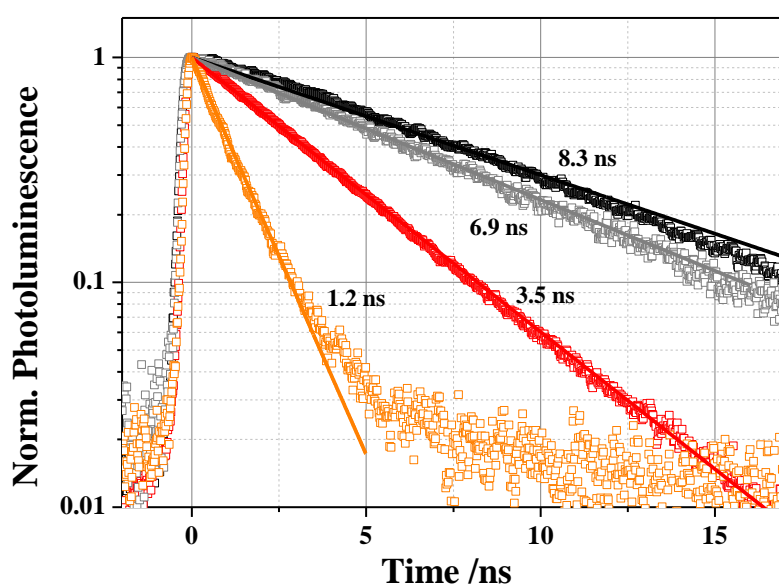


Figure 4-5. Normalized fluorescence decay of PMIMA (black) and TMIMA (red) in toluene solution. Di-carboxylic acid PMIMA and TMIMA dye solutions are represented as gray and orange,



respectively. The decays (solid lines) of anhydride and di-carboxylic dye solutions follow a single exponential.

#### 4.3. Dipole moment of dyes in solution

Measurements in different polarity solvents give insight into changes in the dipole moment between excited and ground state of the dye and allow us to analogize to the change of the surrounding of the dye molecules in films, i.e. after addition of Li cations. Figure 4-6 (a) shows the steady-state absorption and time-resolved PL spectra of 0.1 mM anhydride PMIMA solutions in toluene (TLN) and dichlorobenzene (DCB). TLN and DCB were chosen due to their difference in polarity: 0.099 for TLN and 0.188 for DCB when the relative polarity of water is set to 1.

When dye molecules are dissolved in solvents, the dipoles of dye and solvents interact with each other: the dipoles of the solvent molecule orient around the excited state of dye molecules. The internal relaxation of energetically high vibrational states generated upon excitation of the dye molecules occurs on a fs timescale. Therefore, the Stokes shift in a non-polar solvent is determined by the energy difference of the vibrational states involved in absorption and emission. In a more polar solvent, a larger Stokes shift is observed due to the larger orientation polarizability of the solvent that consists of both solvent reorientation and electronic redistribution of the solvent molecules. Electronic transitions are much faster than the solvent orientation around dye molecules, which leads to spectral shifts in a more polar solvent. Therefore, the dye showing a larger Stokes shift in more polar solvents is expected to have a larger dipole moment in the excited state than in the ground state.

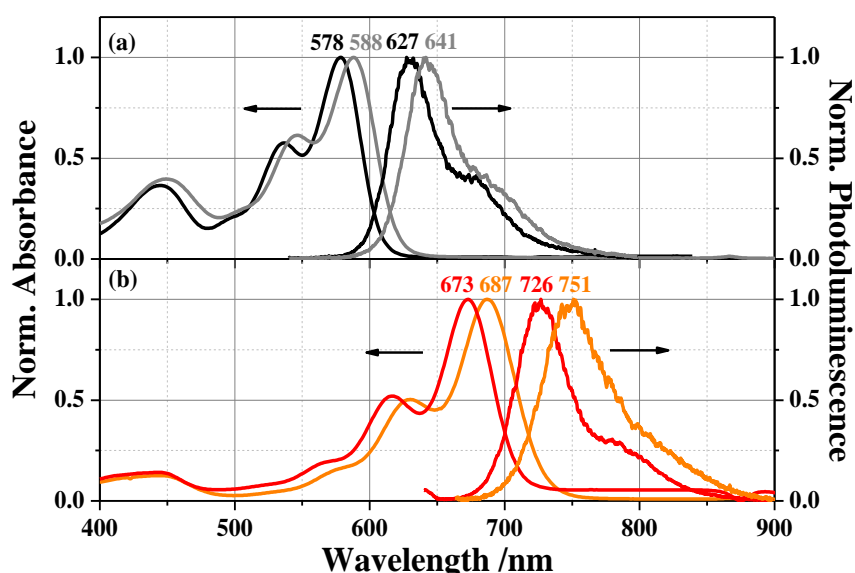


Figure 4-6. Normalized absorption and emission spectra of 0.1 mM solutions of anhydride (a) PMIMA and (b) TMIMA in toluene (TLN) and dichlorobenzene (DCB). Black and red lines represent anhydride PMIMA and TMIMA in TLN and gray and orange lines show anhydride PMIMA and TMIMA in DCB, respectively.

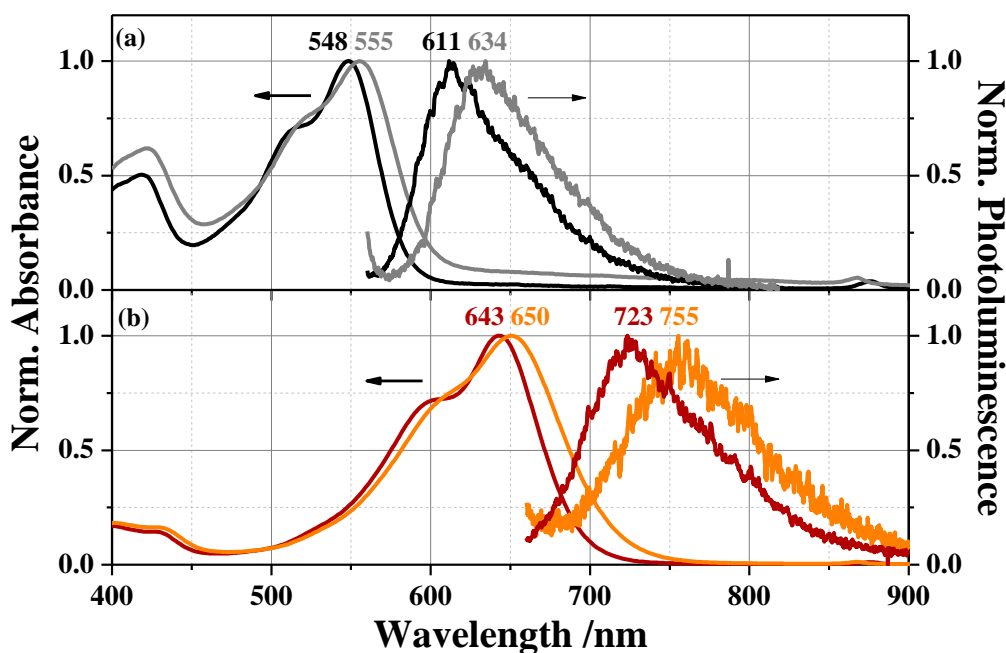


Figure 4-7. Normalized absorption and photoluminescence spectra of (a) di-carboxylic acids PMIMA dye solution in TLN (black) and DCB (gray), and of (b) di-carboxylic acids TMIMA dye solution in TLN (red) and DCB (orange)

The anhydride PMIMA dye solution shows small positive solvatochromism in absorption. The spectra shift from 578 nm in TLN to 588 nm in DCB, while similar shifts in emission spectra are observed from 627 nm in TLN to 641 nm in DCB. The similar shifts between absorption and emission spectra in two solvents of different polarity indicate that the dipole moment in the excited state is not significantly larger than that in the ground state. This implies that injection may not be facilitated in this dye.

Similarly, the anhydride TMIMA solution shows a similar Stokes shift, if a more polar solvent is used, shifting to 687 nm from 751 nm in DCB and from 673 nm to 726 nm in TLN. It indicates that the anhydride TMIMA dye molecule shows similar changes in dipole moment between the excited and ground state as PMIMA. Considering all experimental data, it appears that QMIMA may also show a similar Stokes shift and we can conclude that injection properties may be rather similar even if the  $\pi$ -extension is increased.

Since the injection takes place from the dye molecules after ring opening, we carried out the absorption/emission measurements of the potassium salts of di-carboxylic acid dye solutions. Figure 4-7 (a) shows the normalized absorption and PL spectra of di-carboxylic acid PMIMA in TLN (black) and DCB (gray). Interestingly, the shift at the absorption spectra is only 7 nm, whereas the shift in the PL spectra is 22 nm. However, this cannot be a clear indication of facilitated electron injection for this dye molecule. In addition, TMIMA shows a similar Stokes shift compared to PMIMA, indicating similar injection properties.

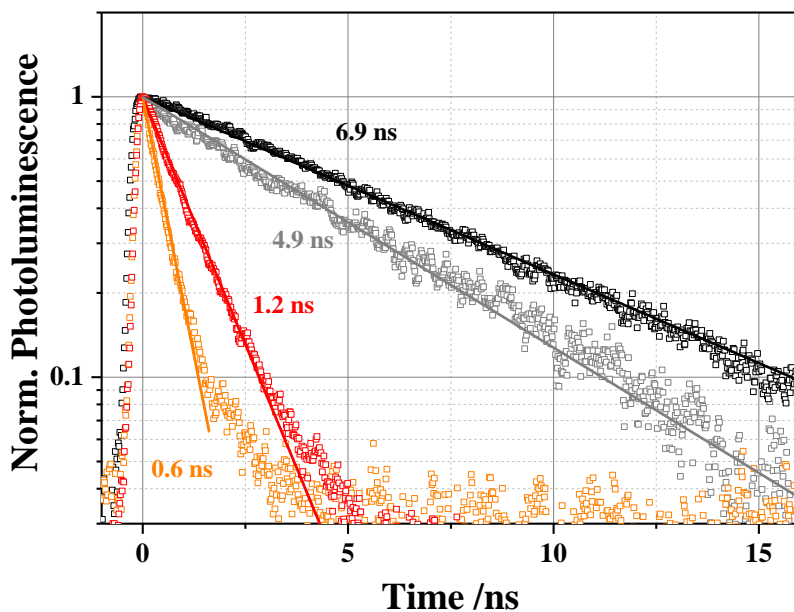


Figure 4-8. Normalized photoluminescence decays of 0.1 mM di-carboxylic acid PMIMA in TLN (black) and DCB (gray), and of 0.1 mM di-carboxylic acid TMIMA in TLN (red) and DCB (orange). The solid lines correspond to mono-exponential fits.

Figure 4-8 shows the decay of the excited states of two dye solutions using solvents of different polarity. The PL lifetime of the di-carboxylic acids dye solutions is further decreased compared to those of the anhydride: from 8.3 ns to 6.9 ns in PMIMA TLN, from 8.1 ns to 4.9 ns in PMIMA DCB, from 3.5 ns to 1.2 ns in TMIMA TLN, and from 1.4 ns to 0.6 ns in TMIMA DCB. This is likely due to different excited states of the open forms.

Furthermore, the ring opening of the anhydride moiety seems to cause enhanced non-radiative decay or a different interaction of dipole moments with the solvent shell. All lifetimes shown in Figure 4-8 are obtained from mono-exponential fits with an amplitude of 1 and an offset of 0.

#### 4.4. Dye-sensitized metal oxide nanoparticle films

Upon ring opening of the maleic acid anhydride by hydrolyses a decreased molar extinction coefficient, enhanced non-radiative decay, blue-shifted absorption/emission and shortened excited state lifetimes were observed along with changes of the dipole moments. In this section, changes in absorption/emission spectra and lifetimes after addition of Li cations will be investigated in dye molecules adsorbed onto metal oxide nanoparticle layers.

Titania, a metal oxide semiconductor with a bandgap of about 3.2 eV <sup>[132]</sup>, is widely used as an electron acceptor in dye-sensitized solar cells. The dye molecules adsorb on the titania surface by an

anchor group and they are able to inject electrons if the LUMO of the dye molecules is higher than the conduction band of titanium dioxide.

Figure 4-9 shows the absorption spectra of the dye molecules adsorbed on titania nanoparticles as used for the preparation of dye-sensitized solar cells. Compared to the solution spectra as shown in Figure 4-4 (b), the absorption of the adsorbed dye molecules is further blue-shifted, i.e. peaking at 527 nm from 548 nm for PMIMA and peaking at 633 nm from 643 nm for TMIMA. However, the absorption spectra still resemble the spectral features of the potassium salts of the dicarboxylic acids as measured in solution, indicating that it is the di-carboxylic acid that attaches to the surface of the metal oxide nanoparticles. The absorbance of the dyed titania films increases significantly from the perylene derivative to the quarterylene derivative most probably as a consequence of the increased molar absorption coefficient of the dye molecules as shown in Table 4-1. Hence, from a first glance, the quarterylene dye appears to be particularly promising for applications in dye-sensitized solar cells. The maximum short circuit current that can be expected from the dye-sensitized titania films when assuming unity internal quantum efficiency is calculated and the maximum photocurrents are 12.6, 18.4, 23.0 mA·cm<sup>-2</sup> for PMIMA, TMIMA, and QMIMA, respectively.

As stated in Chapter 3.1.1, several additives are typically used for the fabrication of DSCs to optimize power conversion efficiencies. One of the important additives in solid-state DSCs is Li-TFSI that is a commonly used additive and increases the driving force for electron injection by changing the surface potential or shifting the conduction band of titania<sup>[133-135]</sup>. Li cations can intercalate in the metal oxide nanoparticles or reside at the interface, leading to changes in absorption and emission spectra of the dye molecules due to the Stark effect.

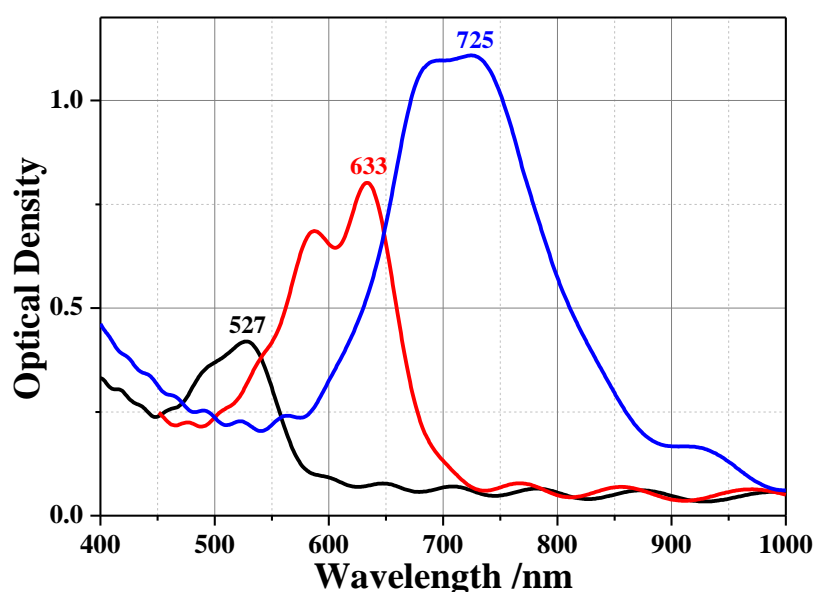


Figure 4-9. Steady-state absorption spectra of PMIMA-(black), TMIMA-(red), and QMIMA-(blue) sensitized titania films.

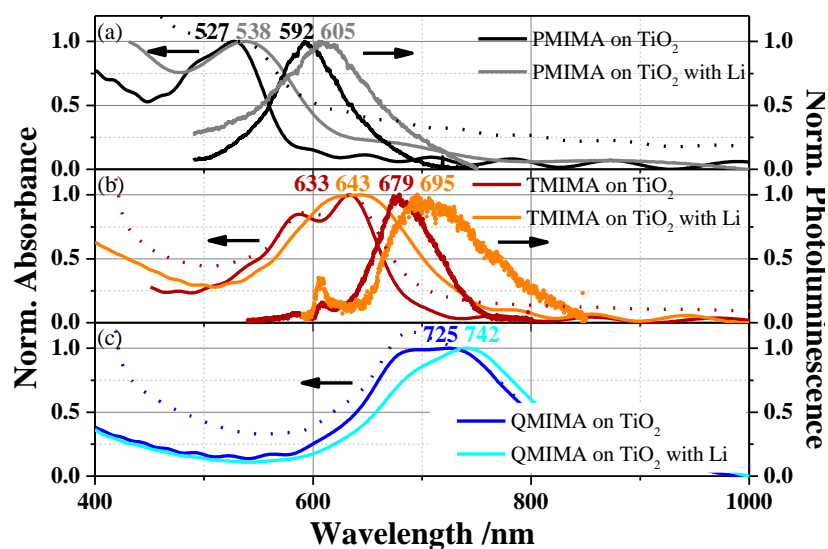


Figure 4-10. Normalized absorption and emission spectra of dye molecules adsorbed on titania in the presence and absence of Li salts. (a) PMIMA on titania (black) and after application of Li cation (gray); (b) TMIMA on titania (red) and with Li cation (orange); (c) QMIMA on titania (blue) and with Li cation (light blue).

The Stark effect has a strong influence on the dye's energy levels due to the interaction of local electric fields with the dyes dipole moment. The local electric field changes the ground state absorption of the dye molecules by interacting with the permanent dipole moment of the dye molecules. Therefore, the direction of the two components, namely the local electric field and the dipole moment, determines the energy levels and the absorption spectra.

Figure 4-10 shows the normalized absorption and emission spectra of the rylene dyes adsorbed on titania under different conditions: dyes on  $\text{TiO}_2$ , dyes on  $\text{TiO}_2$  with Li cations, and in a device-like sample.

In panel (a), the PMIMA-sensitized  $\text{TiO}_2$  film (black) shows a similar absorption as the PMIMA solution shown in Figure 4-7, but slightly blue-shifted due to the adsorption. The PMIMA on titania with Li cations (gray) shows less vibronic features than the PMIMA dye adsorbed on titania (black) and a strongly red-shifted absorption peaking at 538 nm. This red-shift is considered to be due to the local electric field interacting with the dye's dipole moment. We note that the Stokes shift in PMIMA-sensitized samples, from 527 nm to 592 nm (65 nm), is fairly similar to that of the sample with Li, from 538 nm to 605 nm (67 nm), meaning that there is no significant change of the dipole moment between the excited state and the ground state in these rylene dyes. This can be attributed to a uniform charge distribution over the molecules even after excitation.

For TMIMA, the absorption and emission spectra red-shift compared to the PMIMA dye molecules, but exhibit similar characteristics as PMIMA. Upon the addition of Li cations, the absorption and emission spectra shift to 643 nm from 633 nm and to 695 nm from 679 nm, respectively. The emission

spectrum of the QMIMA is expected to show a similar trend as PMIMA and TMIMA, although it could not be measured.

Figure 4-11 shows the fluorescence decay transients of PMIMA and TMIMA adsorbed on titania in the presence and absence of Li cations. The fluorescence decays of these samples are observed on the picosecond timescale, which is significantly faster than the nanosecond timescale in solution. The lifetimes of PMIMA (black) and TMIMA (red) adsorbed on  $\text{TiO}_2$  are determined to be 149 ps and 80 ps, respectively, by using stretched-exponential fits with an amplitude of 1. This multi-exponential fluorescence decay could originate from several possible decay channels of the dye molecules such as differences in adsorption, aggregation and tilted binding modes.

As explained above, addition of Li-TFSI ions creates a local electric field due to intercalation of Li cations. In addition, Li-TFSI is an electron-withdrawing agent, causing a surface potential build up at the interface, which can attract electrons from the anchoring/acceptor groups close to the  $\text{TiO}_2$  nanoparticles. Theoretically, the injection yield can be increased by the use of Li cations and thus a further reduced PL lifetime is observed from most dye molecules after addition of Li cations.

After application of Li cations, PMIMA and TMIMA show significantly decreased PL lifetimes from 149 ps to 39 ps and from 80 ps to 24 ps, respectively. These highly reduced PL lifetimes were also observed in solutions of different polarity which gives insight into the properties of dye molecules in polar environments.

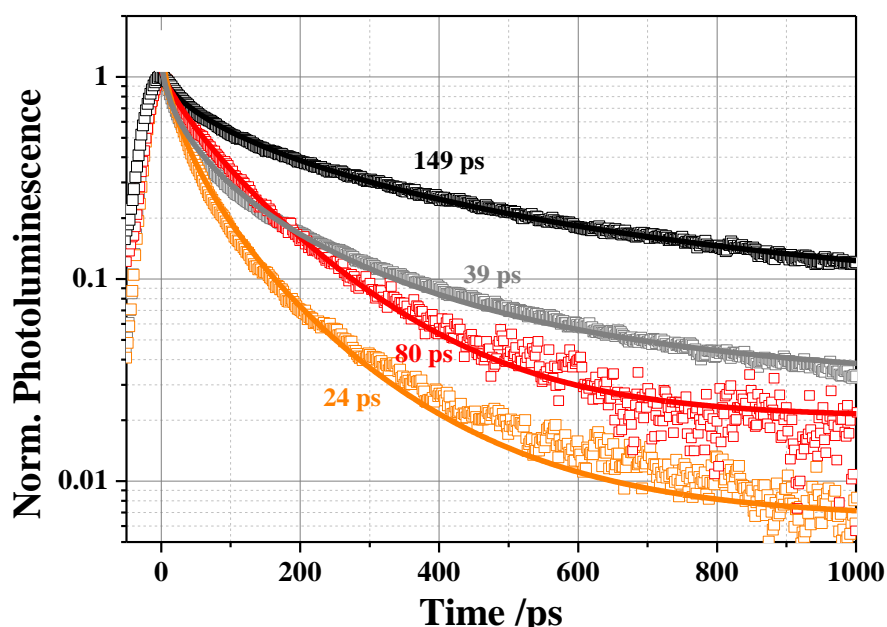


Figure 4-11. Normalized PL decays of PMIMA (black) and TMIMA (red) on titania, and the decays of PMIMA (gray) and TMIMA (orange) after application of Li cations. Solid lines represent stretched-exponential fits.

For QMIMA, the lifetime is expected to be much shorter than the P- and T-MIMA sensitized-films, which is unfavorable for electron injection. The lifetimes obtained by using stretched exponential fits are short to ensure quantitative electron-injection into the conduction band of TiO<sub>2</sub> as the molecules become longer, indicating TMIMA and QMIMA dyes may have difficulties to generate charges.

#### 4.5. Dipole moments calculated by density functional theory (DFT)

The dye molecules' properties undergo significant changes upon ring opening of the anhydride groups. For instance, the di-carboxylic acid dyes exhibit different energy levels, blue-shifted absorption and emission spectra, reduced molar extinction coefficients and PL lifetimes as shown in the previous sections. However, the dye molecules showed almost no solvatochromism and thus no changes of dipole moments in absorption and emission when two solvents of different polarity were used to analogize the changed surrounding of the dye molecules in the presence of Li-cations.

In this section, the dipole moments of the anhydride-rylene dye molecules are compared to those of the di-carboxylic acids to investigate the effect ring opening has on the electron injection at the dye:metal oxide interface. Molecular geometries were optimized using the B3LYP functional and 6-311g (d,p) basis set and all calculations were performed using the Gaussian 09 package. The first singlet excited states were calculated by time dependent density functional theory (TD-DFT). Generally, the first singlet excited states exhibited the highest transition probability upon excitation (Table 4-2) and the corresponding calculated energy levels are in good agreement with experimental absorption spectra as shown in Figure 4-6 and 4-7.

Table 4-2. The energies of the first excited singlet state of the rylene dyes as anhydrides (closed structure) and dicarboxylic acids (open structure) as calculated by TD-DFT. *f* denotes oscillator strength .

	Anhydrides (closed structure)	Dicarboxylic acids (open structure)
PMIMA	2.14 eV (577 nm) f=0.5388	2.25 eV (552 nm) f=0.4902
TMIMA	1.85 eV (670 nm) f=1.1035	1.93 eV (636 nm) f=1.0486
QMIMA	1.57 eV (787 nm) f=1.6807	1.63 eV (762 nm) f=1.6154

Table 4-3. Calculated dipole moments of the rylene dyes with closed and open ring.

Dipole moment (Debye)	Anhydrides (closed structure)	Dicarboxylic acids (open structure)
PMIMA	4.3 D	-3.1 D
TMIMA	4.6 D	-1.8 D
QMIMA	5.2 D	-2.1 D

Table 4-3 shows the calculated dipole moments of the rylene dyes as anhydrides (closed structure) and dicarboxylic acids (open structure). As expected from previous sections, anhydride-PMIMA and TMIMA dye molecules show fairly similar dipole moments with 4.3 and 4.6 Debye, respectively, indicating that electron density is localized at the anchoring group (acceptor moiety). Hence, the dipole moment points to the terminal group, which is favorable for electron injection. This means that the anchor group (acceptor moiety) shows electron withdrawing properties, whereas the imide group exhibits weak electron donating properties.

On the contrary, the dipole moments of the dicarboxylic acids of P-, T-, Q-MIMA dyes are changed to -3.1, -1.8, and -2.1 Debye, respectively. Hence, the direction and magnitude of the dipole moments are significantly changed upon opening of the anhydride groups and adsorption at the metal oxide surface, implying that the electron injection becomes unfavorable. In fact, the negative dipole moment values indicate that the dipole moment of the dye molecules points to the anchor group rather than away from it.

#### 4.6. Detection of long-lived species

##### 4.6.1. Detection of dye and hole conductor cations

The presence of long-lived charges is important for efficient dye-sensitized solar cells (DSCs) and was investigated by quasi-steady-state photoinduced absorption (PIA) spectroscopy. The charges are created as a consequence of injection and regeneration, and PIA signals in different spectral ranges indicate charges. Prior to quasi-steady-state PIA measurements, the absorption of dye cations and hole transporter cations was examined by the use of a Lewis acid, namely  $\text{FeCl}_3$ , which can oxidize dye and spiro-OMeTAD molecules to determine the absorption of dye cations and spiro cations.



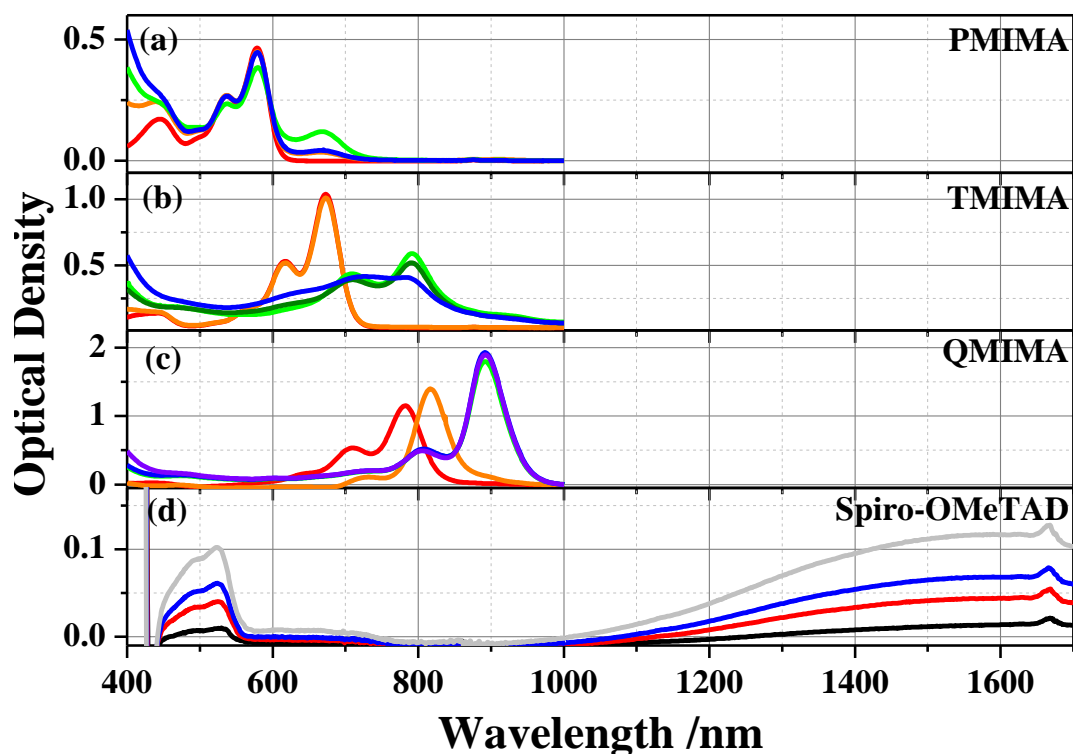


Figure 4-12. Steady-state absorption spectra of (a) PMIMA, (b) TMIMA, (c) QMIMA dye cations, and (d) spiro-OMeTAD cations after addition of a 10 mM  $\text{FeCl}_3$  solution.

Figure 4-12 (a-c) shows steady-state absorption spectra of 0.1 mM solution of anhydride P-, T-, Q-MIMA dyes in TLN mixed with 10 mM  $\text{FeCl}_3$  in TLN. In panel (a-c), red, orange, green, blue, and purple lines represent 0.1 mM dye solution mixed with 0, 2, 5, 10, and 20 v1% of 10 mM  $\text{FeCl}_3$  solution in TLN, respectively. It is clear that the absorption spectra of dye cations red-shift compared to those of the neutral dyes and peak at 670 nm, 790 nm, and 890 nm for the cationic P-, T-, and Q-MIMA, respectively.

Figure 4-12 (d) shows the steady-state absorption of a 0.12 M spiro-OMeTAD solution in chlorobenzene (CB) after addition of 10 mM  $\text{FeCl}_3$  in TLN. The absorption of hole conductor cations can be seen in three spectral regions between 440 – 550 nm, 550 – 760 nm, and 950 – 1600 nm, while the strongest absorption is observed in the near infrared, peaking at 1625 nm. Black, red, blue, and gray lines present 0.12 M spiro-OMeTAD mixed with 2, 5, 10, and 20 v1 % of 10 mM  $\text{FeCl}_3$  solution in CB, respectively. These absorption spectra of dye cations and spiro cations can be used as a fingerprint of injection and regeneration processes in photoinduced absorption experiment.

#### 4.6.2. Quasi-steady-state Photoinduced Absorption (PIA) spectroscopy

Photoinduced absorption (PIA) spectroscopy allows probing the presence of ( $\mu\text{s}$  –  $\text{ms}$ ) long-lived excited states such as charges in dye-sensitized solar cells by monitoring the excited state absorption. Therefore, this measurement can be used as an indication of the device performance.

Figure 4-13 shows the quasi-steady-state PIA spectra obtained for all dyes on titania (panel a), in the presence of Li-ions (panel b) and in a device-like sample (with a structure of titania/dye/spiro-OMeTAD + Li-TFSI + *t*BP, panel c). Here, the PMIMA, TMIMA, and QMIMA dyes were excited at 530 nm, 700 nm and 800 nm, respectively, and the data were normalized to the same excitation density calculated from the photon flux and absorption cross-section at the respective excitation wavelength.

In general, positive features correspond to bleaching of the ground state absorption, while negative features can be assigned to the photoinduced absorption of cations created by electron transfer processes. These features can be seen for all dyes on titania as presented in Figure 4-13 (a), however, the spectral position and signal amplitude significantly differs between the various rylene dyes as observed from Figure 4-12. The cation-induced absorption spectra are close to the ground state bleaching of dye molecules as observed from Figure 4-12 (a-c) and peak at 598 nm for the PMIMA, 768 nm for the TMIMA and 931 nm for the QMIMA as shown in Figure 4-13 (a), respectively. The difference between Figure 4-12 and 4-13 originates from whether or not the dye molecules are in the open form. Clearly, the QMIMA shows the weakest bleaching and cation-induced absorption signal among the series of rylene dyes, implying that there is only little electron injection from the excited state of the dye into titania.

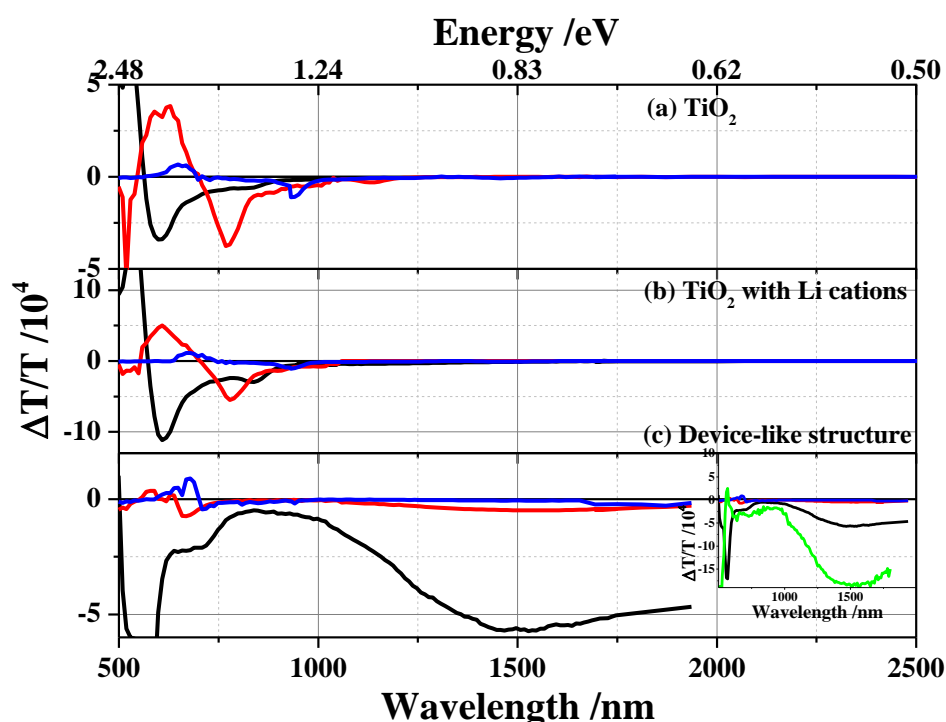


Figure 4-13. Quasi-steady-state PIA absorption spectra (a) of the dyes adsorbed on titania, (b) of the dyes on titania after application of Li-TFSI, and (c) of a device-like sample when PMIMA (black), TMIMA (red), and QMIMA (blue) dyes are used. The inset: PIA spectra of a device-like sample using Z907 (green) compared to the rylene dyes.

In the presence of Li cations, the amplitudes of the cation-induced absorption of the PMIMA and the TMIMA dyes are increased as shown in panel (b) indicating that for both dyes Li-ions facilitate the electron injection process. This observation is in good agreement with the fluorescence decay dynamics presented above, which demonstrated faster fluorescence decay in the presence of Li-ions for both dyes. On the other hand, virtually no effect is seen for the QMIMA indicating that the dye is unable to inject electrons into the titania conduction band even in the presence of the Li cations. We note, however, that a weak photoinduced absorption signal can be observed which may be attributed to injection into low-lying sub-bandgap states of titania.

If the solid-state hole transporter Spiro-OMeTAD is used on the sensitized films, no PMIMA cation-induced absorption can be seen anymore and instead a broad photoinduced absorption signal peaking at around 1530 nm is observed. This signal has previously been assigned to the absorption of the hole conductor-cations as shown in Figure 4-12 (d) exhibiting a peak at 1668 nm, and the difference of the absorption spectral ranges originates from sample preparation, i.e. solution and film. This broad PIA signal of the hole conductor demonstrates efficient regeneration of the dye's oxidized state. In case of the PMIMA, the second and third higher energy absorptions of hole conductor-cations can be observed between 500 – 638 and 620 – 780 nm, respectively. These features are also observed from Figure 4-13 (442 - 570 and 570 - 760 nm) and where reported elsewhere <sup>[136]</sup>. In fact, the PMIMA-sensitized device-like sample shows the strongest hole-transporting spiro-OMeTAD cation signal; however, the amplitude of this signal is one order of magnitude lower than for Z907 as shown in the inset, and this is directly related to the device performance as shown in the next section. The QMIMA sample exhibits only a very weak spiro cation signal, which supports our previous statement that electron injection from the QMIMA into titania is impeded and thus no dye regeneration occurs as indicated by the absence of the photoinduced absorption from hole conductor cations.

We note that the Stark effect in these dye molecules is also observed in the visible range. Edvinsson et al. described that a negative signal from TMIMA, looking like a PIA signal in the range between 580 - 700 nm (which is not observed from our data), cannot reliably be considered a dye-cation signal. We consider this signal to originate from the Stark effect.

#### 4.7. J-V curves and external quantum efficiency (EQE)

In the previous sections, changes in lifetimes and absorption/emission spectra upon adsorption of dye molecules on titania and the charge generation were investigated. This section shows how these photophysical characteristics ultimately affect the power conversion efficiency and external quantum efficiencies (EQE) of the devices when the rylene dyes are used as sensitizers.

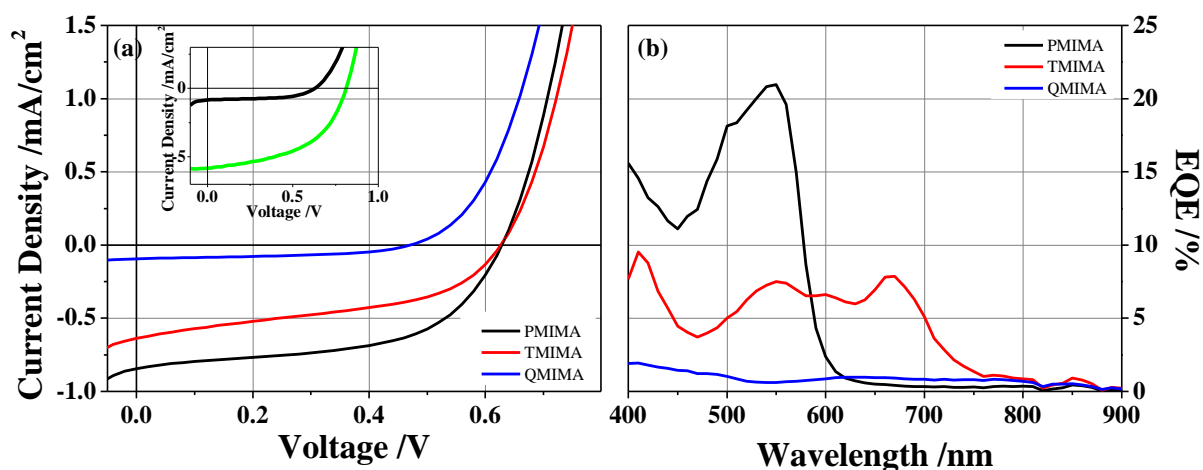


Figure 4-14. J-V curves of the dye-sensitized solar cells measured under AM1.5G solar illumination (a) and corresponding EQE spectra (b) using PMIMA (black), TMIMA (red), and QMIMA (blue) dyes.

Figure 4-14 shows the J-V curves of solid-state dye-sensitized solar cells under AM1.5G solar illumination using the different rylene dyes and the ruthenium dye Z907 as sensitizer along with the external quantum efficiency (EQE) of the respective devices.

Among the rylene dyes, PMIMA exhibits the highest power conversion efficiency in solid-state DSCs with a total PCE of 0.3 % which is well in line with the longest lifetime of the dye's excited state and the strongest spiro-OMeTAD cation signal. For the TMIMA, we obtained a PCE of 0.18 % whereas QMIMA exhibited almost no meaningful photovoltaic performance in line with little cation-induced absorption signals observed in PIA measurements.

Table 4-3. Photovoltaic parameters of the devices obtained from their J-V curves.

	$V_{OC}/V$	$J_{SC}/mA/cm^2$	FF	Eff./%	Expected $J_{SC}/mA/cm^2$
PMIMA	0.62	0.84	55.69	0.29	12.6
TMIMA	0.62	0.64	45.47	0.18	18.4
QMIMA	0.46	0.09	48.66	0.02	23.0
Z907	0.82	5.82	49.96	2.38	-

The low efficiencies of the rylene-sensitized solar cells are mainly due to the low short-circuit currents, as indicated by the low charge generation signals of spiro cations. The reason for the low short-circuit currents can be found in Figure 4-14(b) that shows the external quantum efficiency (EQE) as a function of excitation wavelength for the rylene devices. The EQE levels of P-, T-, and Q-MIMA only reach up to 20, 7, and 1 % at 550, 670, and 680 nm, respectively.

The current densities in the devices correspond to only 0.3 – 6 % of the maximum photocurrents that can be calculated from the absorbance of the dye-sensitized solar cells under the assumption of unity internal quantum efficiency. This large difference may mainly originate from poor charge generation properties of rylene-sensitized films, which was expected from not only low  $\Delta T/T$  signals in PIA measurements, but also short lifetimes of the excited states.

The inset of Figure 4-14 (a) shows the J-V curves of the devices using PMIMA (black) and Z907 (green) dyes. Z907-sensitized solar cells exhibit an efficiency of 2.38 % with a short circuit current of  $5.82 \text{ mA}\cdot\text{cm}^{-2}$ , an open circuit voltage of 820 mV, and a fill factor of 0.49, whereas the PMIMA-sensitized solar cell shows a power conversion efficiency of 0.3 %. The large difference in the PCE between the two samples is mainly due to the low photocurrents that are a consequence of the injection properties observed in PIA measurement. The PCEs of each device are averaged and summarized in Table 4-3.

#### 4.8. Ryleneanhydrides as sensitizers: Conclusions

The materials studied in this chapter belong to the family of rylene dyes, namely a perylene, terylene and quaterylene derivative, bearing an imide and a maleic acid anhydride group at the terminal positions. Each dye solution shows distinct vibronic progressions in the absorption and emission spectra and clear red-shifts when going from a perylene to a terylene and a quaterylene core due to increased conjugation.

The di-carboxylic acids of the dye molecules exhibit altered spectroscopic properties due to a change in the excited state energies upon opening of the anhydride rings. They exhibit a clear hypsochromic shift and highly reduced photoluminescence quantum efficiency caused by an increased non-radiative decay resulting also in reduced fluorescence lifetimes.

The anhydride rylene dye solutions show small positive solvatochromism in absorption and emission spectra when toluene and dichlorobenzene were used to change the polarity of the dye solution, indicating that the dipole moment in the excited state is not significantly larger than that in the ground state. This implies that injection may not be facilitated in these dyes since the measurements in different polarity solvents give insight into changes in the dipole moment between excited and ground

state of the dye and allow us to analogize these changes to those that occur in the surrounding of the dye molecules in films upon treatment with Li cations.

The maximum short circuit currents that can be expected from the rylene dye-sensitized films when assuming unity internal quantum efficiency are calculated and range between 12.6 and 23.0 mA·cm<sup>-2</sup>, since rylene dyes generally exhibit high molar extinction coefficients. However, solid-state P-, T-, Q-MIMA-sensitized DSCs exhibit power conversion efficiencies of only 0.3, 0.2, and 0.02 %, with low short circuit currents of 0.84, 0.64, and 0.09 mA·cm<sup>-2</sup>, respectively. The low efficiencies of the rylene-sensitized solar cells are mainly due to the low short-circuit currents. This is supported by result from photoinduced absorption spectroscopy showing that the electron injection properties of these dye molecules are very poor. Furthermore, the amplitude of the spiro cation signal of the PMIMA-sensitized device-like sample is one order of magnitude lower than for the reference dye Z907 and this appears to be directly related to the device performance. However, the PMIMA-sensitized device-like sample showed the strongest spiro-OMeTAD cation signal of all rylene dyes in line with the best device efficiency.

The unfavorable charge generation was found to be a result of changes in the dipole moment as calculated by density functional theory. The anhydride-rylene dyes show small but favorable dipole moment for electron injection, however, the dipole moment direction changes and points to the anchor group, which is unfavorable for electron injection. upon ring opening of the anhydride moiety.

In summary, for efficient photovoltaic devices, high molar extinction coefficients are important to absorb more photons as well as high energy levels to ensure injection and to generate more charges. However, these are not the only prerequisites for a high power conversion efficiency of devices. In fact, the influence of anchor groups and changes in dipole moments need to be thoroughly considered when designing novel dye structures for dye-sensitized solar cells.

## 5. Perylene monoimide derivative dye, ID889

### 5.1. Materials and samples used

The material investigated in this chapter is a perylene monoimide derivative dye named ID889. It consists of a carboxylic acid anchoring group, a perylene monoimide as an acceptor, and a fused dibenzothiophene with a triarylamine as a  $\pi$ -conjugated bridge and donor moiety. The carboxylic acid anchoring group is used to increase adsorption on the semiconducting oxide layer in a device. The dibenzothiophene moiety not only plays the role of a spacer, but also increases pi-conjugation to absorb photons at lower energies. ID889 dye has been designed to have a localized electron distribution in the HOMO and LUMO levels with the addition of the electron donating triarylamine moiety in order to improve electron injection properties since perylene derivative dyes are known to be poor electron donors. Alkyl groups on the triarylamine moiety are attached to increase the solubility of the dye. The molecular structure of ID889 is shown in Figure 5-1.

The HOMO and LUMO levels shown in Figure 5-1 (b) are obtained from time-dependent density functional theory (TD-DFT) calculations. The HOMO level of ID889 is lower than the HOMO level of spiro-OMeTAD, thus, regeneration of the dye cation is energetically favorable. The LUMO level is -3.5 eV by DFT calculation, but the LUMO level obtained from absorption/emission experiments is -3.0 eV. These two values are high enough to inject electrons into the conduction band of the TiO<sub>2</sub> layer. The energy levels of transparent conductive oxide (TCO), TiO<sub>2</sub>, spiro-OMeTAD, and the silver electrode are adapted from elsewhere<sup>[137-142]</sup>.

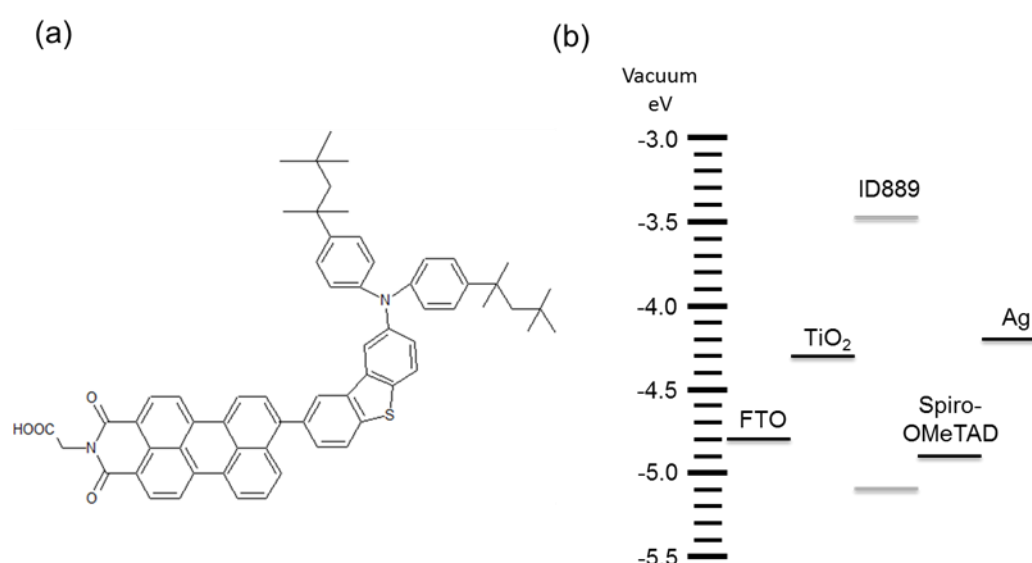


Figure 5-1. Molecular structure of the perylene monoimide derivative dye ID889 and the HOMO/LUMO energy levels of the dye.

Table 5-1. List of investigated sample structures.

Number of sample	Description
<b>Sample 1</b>	ID889 on alumina
<b>Sample 2</b>	ID889 on alumina with addition of Li-TFSI
<b>Sample 3</b>	ID889 on alumina with spiro-OMeTAD and all additives (Li-TFSI and (DSC structure on Al <sub>2</sub> O <sub>3</sub> ) <i>t</i> BP)
<b>Sample 4</b>	ID889 on titania
<b>Sample 5</b>	ID889 on titania with addition of Li-TFSI
<b>Sample 6</b>	ID889 on titania with spiro-OMeTAD and all additives (Li-TFSI and <i>t</i> BP) (DSC structure on TiO <sub>2</sub> )
<b>Sample 7</b>	ID889 on titania with spiro-OMeTAD and with <i>t</i> BP but without Li-TFSI
<b>Sample 8</b>	ID889 with spiro-OMeTAD on quartz

The samples for device fabrication and for optical spectroscopy were prepared as described in the experimental section 3.1. For solution measurements, a 0.1 mM dye solution was prepared. The sensitization of metal oxide films was carried out at 25°C for 3-5 hours in toluene. Table 1 shows seven sample structures that are studied in this chapter. The dyes in **Samples 1-3** and in **Samples 4-7** were adsorbed on alumina surfaces and on titania surfaces, respectively. **Sample 8** was prepared by spin-coating a blend of ID889 and a molecular hole conductor, namely spiro-OMeTAD.

## 5.2. Absorption/Emission spectra

### 5.2.1. Dye solutions

ID889 shows a molar extinction coefficient of 28,382 M<sup>-1</sup>cm<sup>-1</sup> at 512 nm in dichloromethane, which is much higher than Z907, a Ru(II) complex dye, with 13,000 M<sup>-1</sup>cm<sup>-1</sup> at 520 nm<sup>[98]</sup>. Figure 5-2 (a) shows the steady-state absorption and emission spectra of a 0.1 mM ID889 dye solution in toluene. The absorption spectrum does not show pronounced vibronic features but shows a gentle peak between 495 nm and 520 nm. Excitation at 450 nm gives rise to a broad emission between 500 and 750 nm. The emission spectrum shows a Stokes shift of 50 nm and is peaking at 570 nm, with a shoulder around 600 nm.

The LUMO level is determined to -3.0 eV, obtained from the onset of absorption in solution as shown in Figure 5-2 (a). This energy level is located further up compared to the DFT calculated LUMO level of 3.5 eV, and thus is energetically favorable for electron injection.



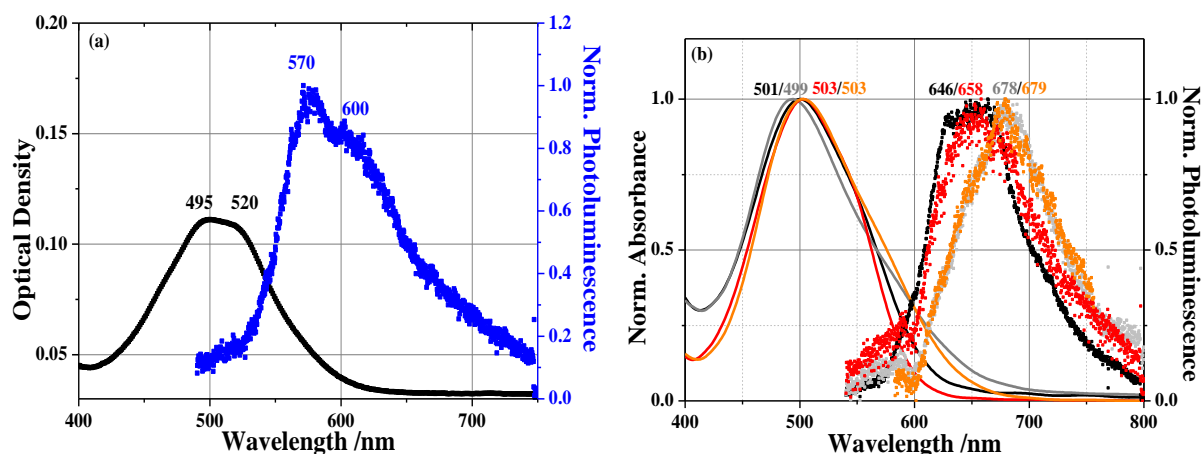


Figure 5-2. Absorption and emission spectra of (a) 0.1 mM ID889 in toluene and (b) of **Sample 1** (red), **2** (orange), **4** (black), and **5** (gray).

### 5.2.2. Dye-sensitized nanoparticle films

Figure 5-2 (b) shows the absorption and emission spectra of dye-sensitized TiO<sub>2</sub> and Al<sub>2</sub>O<sub>3</sub> nanoparticle films in the presence and absence of Li-TFSI salts. In ID889-sensitized alumina (**Sample 1**, red) and ID889-sensitized titania samples (**Sample 4**, black), the films show similar absorption spectra, peaking at 503 nm and 501 nm, respectively. With application of Li cations, the tail of the absorption spectra of sensitized alumina (**Sample 2**, orange) and sensitized titania samples (**Sample 5**, gray) shows a red-shift. The red-shift is due to accumulation of Li ion on the metal oxide surface, or the intercalation of Li ions into the mesoporous metal oxide nanoparticles. TD-DFT calculations support the idea that the change in the dye's ground state absorption is caused by a Stark effect of a local electric field<sup>[125, 133]</sup> caused by addition of Li cations. A detailed description is given in Chapter 4.3.

Photoluminescence (PL) of **Sample 2** and **5** shows also a red-shift, indicating an increase in dipole moment of the dye's excited state, which will be confirmed in section 5.4.

### 5.2.3. Dye cation and anion absorption

Detecting the absorption spectra of charged molecules is useful when analysing TAS because it allows distinguishing each species' contribution to the transient absorption spectrum. When Lupasol<sup>®</sup> is used in a 0.1 mM ID889 dye solution, the sample shows distinct anionic charge-induced absorption (red) peaks at around 607, 718, 776 and 813 nm (Figure 5-3) that are not observable from either the sensitized films or the dye solution. The absorption spectrum of the dye cation (blue) obtained by oxidation with iron(III) chloride solution is also different to that of the neutral dye, showing a peak around 840 nm. These features can be used to analyze the spectra and kinetics of each species in TA measurements.

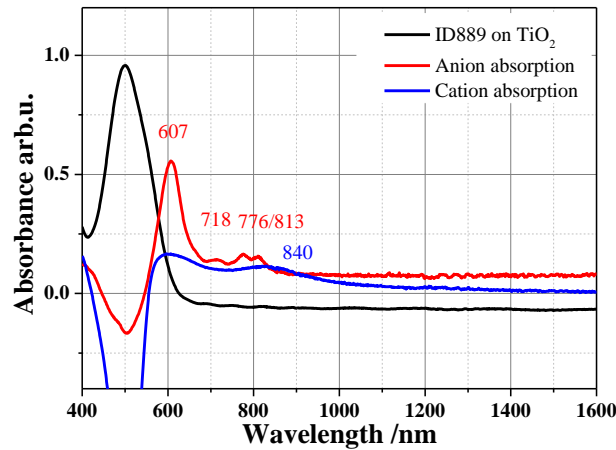


Figure 5-3. Absorbance spectrum of dye-sensitized titania film (black), dye anion (red), and dye cation (blue) with an arbitrary offset.

For detailed sample preparation procedures, see Chapter 3.1.

### 5.3. Device characteristics and photoinduced absorption measurements

#### 5.3.1. J-V characteristics

Figure 5-4 (a) shows the J-V characteristics of a solid-state dye-sensitized solar cell (DSC) using ID889 under solar illumination of AM 1.5G. The best device exhibited a power conversion efficiency of 4.5 % with a short circuit current of  $7.47 \text{ mA}\cdot\text{cm}^{-2}$ , an open circuit voltage of 860 mV, and a fill factor of 69 %. The high efficiency of the ID889 device is mainly due to the high short circuit current, as a consequence of the good charge separation and collection that will be demonstrated in section 5.5.

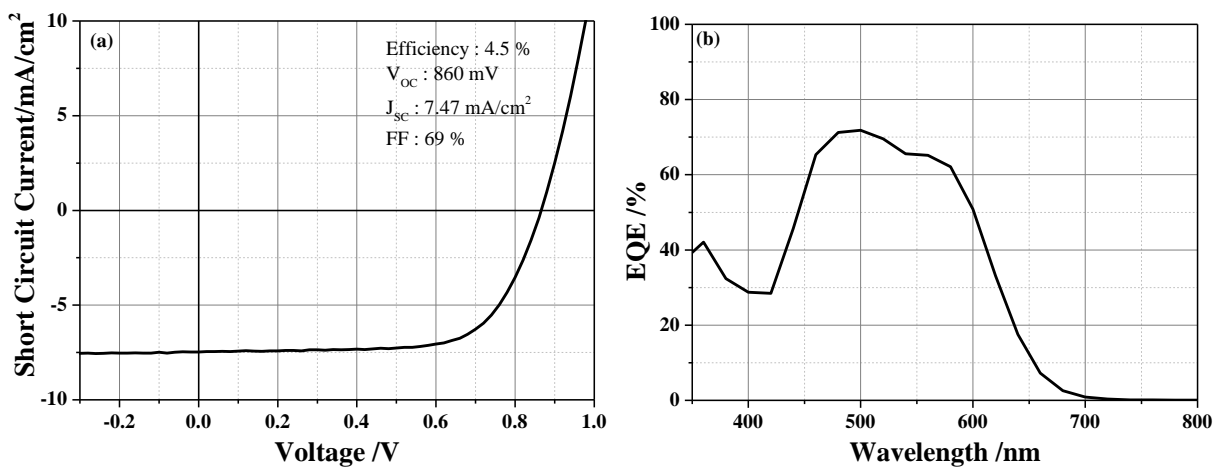


Figure 5-4. J-V characteristics of ID889-sensitized solid-state DSC measured under  $100 \text{ mW}\cdot\text{cm}^{-2}$  AM 1.5 G solar intensity and (b) corresponding EQE spectrum as a function of wavelength.

The maximum short circuit current can be predicted from the absorbance spectrum of the dye-sensitized titania film under the condition of unity internal quantum efficiency and was calculated to  $12.6 \text{ mA}\cdot\text{cm}^{-2}$  for ID889. However, we obtained a short circuit current of  $7.47 \text{ mA}\cdot\text{cm}^{-2}$  only corresponding to about 60 % of the total expected short circuit current, indicating significant losses - presumably loss channels such as incomplete pore filling and recombination between injected electrons and oxidized dye molecules/holes in the molecular hole transporter.

Figure 5-4(b) shows the external quantum efficiency (EQE) as a function of excitation wavelength for the ID889 device. The EQE reaches up to 75% at 500 nm which is comparable to the 80 % EQE in solid-state DSCs using spiro-OMeTAD exhibiting record efficiencies of 7.2 %<sup>[24]</sup>. This high EQE allows reasonable short-circuit currents in the device.

Although perylene dyes show very strong absorbance and long excited state lifetimes, the poor injection properties of the perylene moiety limit the photocurrent, and the best reported efficiency using perylene dyes in solid-state DSCs remains at 3.2% with a photocurrent of  $8.7 \text{ mA}/\text{cm}^2$  to dates<sup>[86]</sup>. We note that the performance of devices using ID889 surpasses the efficiencies of previously reported solid-state DSCs using perylene derivatives.

### 5.3.2. Quasi-steady-state photoinduced absorption (PIA) measurements

Tailored energy levels of the dye photosensitizer as shown in Figure 5-1 are important for high device efficiency. The LUMO level of ID889 is high enough to inject electrons into the conduction band of the metal oxide layer and the HOMO level of ID889 is lower than the HOMO level of the spiro-OMeTAD, which allows dye regeneration.

Figure 5-5 shows quasi-steady-state photoinduced absorption (PIA) spectra obtained from ID889 (black, **Sample 4**), ID889 with Li cation additive (blue, **Sample 5**), and a complete device-like structure using titania (orange, **Sample 6**). The samples were excited with a 530 nm LED to investigate long-lived excited states such as charges.

As described in section 2.3.1, positive and negative features are assigned to ground-state bleaching (GSB) and photoinduced absorption (PIA), respectively. All three samples show a GSB signal below 650 nm, where ID889 strongly absorbs photons, and PIA of the dye cation extending further into the near-infrared spectral range.

Strongly modulated signals are observed below 590 nm as shown in Figure 5-5 caused by a Stark effect. The Stark effect is observed due to the electric field between injected electrons and oxidized dye molecules, and oxidized hole conductor molecules, and it interferes with the ground state absorption of non-excited dyes that have already recombined or did not participate in charge generation<sup>[143]</sup>. Therefore, one should be careful to compare kinetics taken from the visible spectral region, since they can be highly influenced by the Stark Effect.

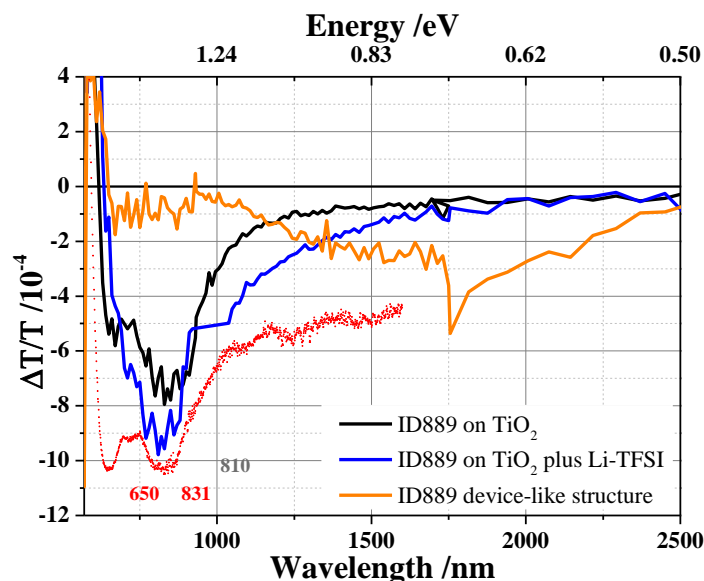


Figure 5-5. Quasi-steady-state photoinduced absorption (PIA) spectra of ID889 on titania excited with a 530 nm LED: ID889 on TiO<sub>2</sub> (black, **Sample 4**), ID889 on TiO<sub>2</sub> with Li salt (blue, **Sample 5**), and ID889 on TiO<sub>2</sub> with all additives and a hole conductor, having a complete device-like structure (orange, **Sample 6**). Red-dotted line represents the absorption of dye cations obtained from steady-state absorption measurements.

**Sample 4** (black) shows broad PIA signals from the visible wavelength range to the NIR spectral region even at room temperature, which implies that ID889 creates long-lived charge carriers without the help of additives. However, it seems that not all dye molecules in **Sample 4** contribute to the injection process because **Sample 5** (blue) which contains Li cation shows a slightly stronger signal amplitude due to more efficient charge generation.

The stronger PIA signal of **Sample 5** reveals more charge generation, perhaps owing to suppressed recombination or facilitated injection originating from an increased driving force for electron injection. In **Sample 5**, a positive signal up to 630 nm is followed by a broad PIA signal peaking at 810 nm. The shape of the PIA is similar to the absorption spectrum of the dye cation (red dotted line in Figure 5-5, taken from Figure 5-3) peaking at 650 and 831 nm. Despite a spectral mismatch between these two spectra, presumably originating from the different environment (i.e. solution and film), it seems that the broad PIA signal of **Sample 5** can be assigned to dye cation absorption and thus is a direct indication of injection from the dye molecule. Furthermore, the addition of Li cations appears to lead to more efficient charge generation.

For a DSC device-like sample (orange, **Sample 6**), the strong absorption feature of the dye cation is no longer observed and instead a broad PIA spectrum at lower energy is found. This broad PIA between 1000 and 2500 nm is assigned to the absorption of spiro-OMeTAD cations, due to efficient regeneration of the dye cation, since this feature is the same as the absorption of oxidized spiro-

OMeTAD as shown in Chapter 4.5 and in the literature <sup>[144]</sup>. Therefore, the high photocurrent of the DSC using ID889 is attributed to an efficient injection and regeneration process.

The PIA data were normalized to the absorbance of each sample at the excitation wavelength to allow a direct comparison of the signal amplitudes.

#### 5.4 Measurement of dye solutions

PL measurements of the dye in solvents of different polarity give insight into the dipole moment change of the dye and the surrounding of dye molecules in films that can affect the injection rate when Li-TFSI salt is used to facilitate the injection process. Here, steady-state absorption and time-resolved photoluminescence (PL) Streak Camera measurements are carried out to estimate changes in the dipole moment between the excited state and ground state, and broadband transient absorption spectroscopy (TAS) is used to investigate the excited-state dynamics.

##### 5.4.1 Photoluminescence (PL) Streak Camera measurements

Figure 5-6 (a) shows the steady-state absorption and time-resolved photoluminescence (PL) spectra of two 0.1 mM dye solutions in toluene (TLN) and dimethylsulfoxide (DMSO). TLN and DMSO solvents were deliberately chosen due to their large difference in relative polarity: 0.099 for toluene and 0.444 for DMSO, when the relative polarity of water is 1 <sup>[145, 146]</sup>. For the PL measurement, a supercontinuum fiber laser was used as excitation source as described in section 3.3.1.

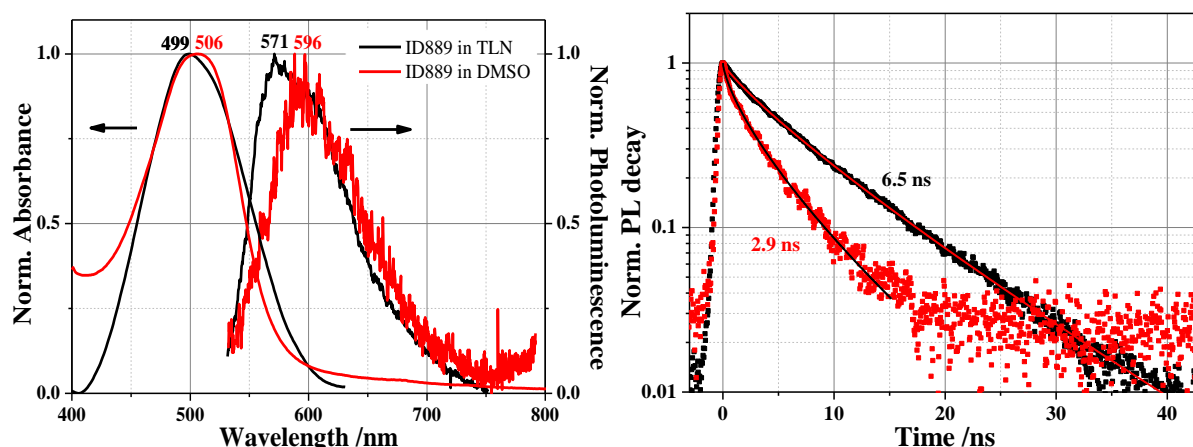


Figure 5-6. (a) Normalized absorption and emission spectra of 0.1 mM ID889 solutions in toluene (TLN, black) and dimethylsulfoxide (DMSO, red) solvent; (b) Decay of the PL in dye solutions of TLN (black) and DMSO (red) obtained from Streak Camera measurements and decay with lifetimes of 6.5 and 2.9 ns for TLN and DMSO, respectively. The solid lines correspond to stretched exponential fits.

Table 5-2. Summarized fitting parameters of stretched exponential decay ( $I(t) = A \cdot \exp\left(-\left(\frac{t}{\tau}\right)^\beta + y_0\right)$ ) in the two different dye solutions.

	A	$y_0$	$\beta$	$\tau$
ID889 in TLN	1	0	0.84	6.51
ID889 in DMSO	1	0	0.71	2.85

Upon illumination, rearrangement of the solvent shell surrounding the dye molecules is not as fast as the dye molecules' electronic transition. The solvent shell will be arranged around the dye's excited state after the electronic transition and then will create an additional field on the dye molecules. Different magnitudes of electric field, depending on the kind of solvent, will shift the energy levels of the dye molecules, leading to changes in absorption spectra, i.e. red-shifted absorption spectra in polar solvents.

ID889 shows positive solvatochromism of the absorption and emission in more polar solvents due to a larger dipole moment in the excited state that is favorable for electron injection: a smaller Stokes shift from 499 nm to 571 nm in TLN, but a slightly larger shift from 506 nm to 596 nm in DMSO as shown in Figure 5-6 (a). A larger Stokes shift in the more polar solvent DMSO can be assigned to a significant change of the dipole moment of the dye between the excited state and the ground state. The lower photoluminescence quantum efficiency in DMSO also supports the idea that ID889 exhibits strong changes in dipole moment.

Turning to the decay of the PL shown in Figure 5-6 (b), stretched exponential fitting reveals lifetimes of 6.5 and 2.9 ns for TLN (black) and DMSO (red) solvent, respectively. The shorter PL lifetime of ID889 in the polar DMSO solvent can originate from enhanced non-radiative decay or a stronger intramolecular CT state character caused by changes in the dipole moment due to the more polar solvent shell. From the measurement in the polar solvent, we can analogize changes in the dye's excited state when Li cations are used on films, since an addition of Li and the use of a polar solvent cause effects by creating a local electric field. Detailed data fitting parameters are shown in Table 5-2.

This result is consistent with a calculation of dipole moments by TD-DFT as shown in Table 5-3. A highly increased dipole moment in the excited state compared to the ground state can lead to favorable injection into the conduction band of titania.

Table 5-3. Dipole moments of ID889's ground and first excited state.

Dipole moments	$\mu_g$	$\mu_e$
ID889	9.3 D	48.2 D

### 5.4.2. Transient Absorption (TA) measurements

Analysis of transient absorption (TA) data of the dye in solution is complicated due to the number of photophysical processes which occur. This includes stimulated emission, (photo-) induced absorption, and CT state generation. These processes, in solution, are strongly influenced by the solvent polarity; therefore, PL spectra of dye solutions of different polarity solvents can be used to distinguish these absorption features.

The early time (ps-ns) pump-probe spectra of two 0.1 mM dye solutions in TLN and DMSO can be seen in Figure 5-7. In the less polar TLN solvent shown in Figure 5-7 (a), the exciton-induced absorption is observed at early times (ps) and then the intramolecular CT states-induced absorption is observed afterwards. The relaxation processes generally take place on a femto- to sub-one hundred picosecond timescale and this is clearly observed from the less polar solvent due to the lower dielectric constant of TLN. For the more polar DMSO solvent, the CT-induced absorption is mainly observed and the exciton seems to decay on an ultrafast timescale. The faster decay at the CT-state is seen over the whole wavelength range, which is consistent with the decay in the PL measurements.

Figure 5-8 shows the dynamics of excited states from the spectral region where they are free from PL influence: 780-820 nm for an ID889 TLN solution and 800-840 nm for an ID889 DMSO solution. ID889 in DMSO shows a signal rise up to 3 ps and fast decay afterwards, whereas ID889 in TLN rises up to 200 ps followed by a moderately slow decay. This is attributed to different relaxation processes leading to different formation rates of intramolecular CT states, in line with the polarity of the solvent. Hence, the solvents having different dipole moments affect significantly the decay dynamics.

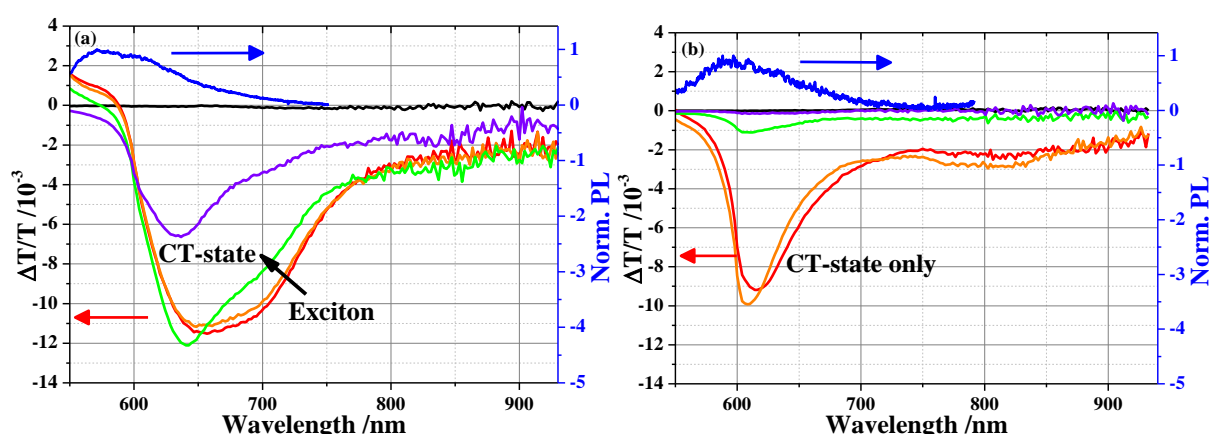


Figure 5-7. Short delay (ps-ns) broadband transient absorption spectra of ID889 solution (a) in TLN and (b) in DMSO in the visible spectral region at delay times of 1 ps (red), 3ps (orange), 30 ps (green), and 3000 ps (purple). The pump fluence is  $37.56 \mu\text{J cm}^{-2}$  at 510 nm for both measurements. Two blue lines represent the PL spectra of each sample.

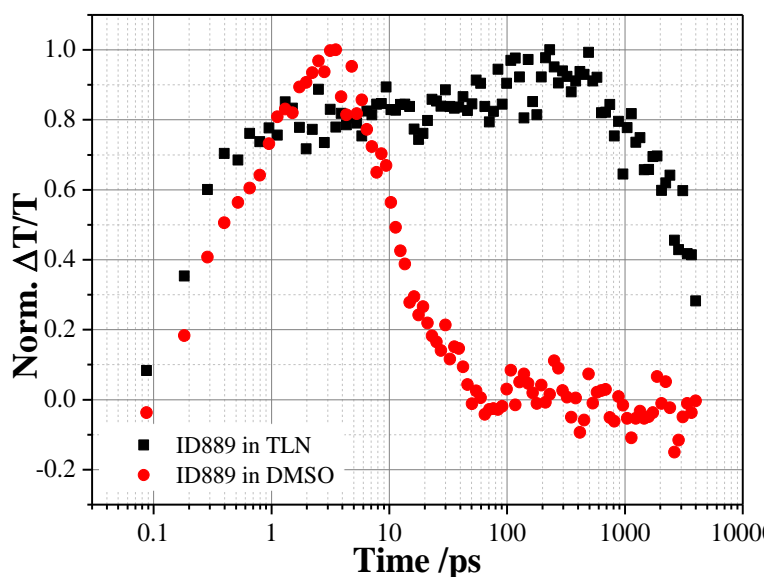


Figure 5-8. Early time dynamics of the exciton-induced absorption at different wavelength regions: 780-820 nm for ID889 TLN solution (black) and 800-840 nm for ID889 DMSO solution (red).

ID889 in solution shows an excited state PL lifetime of 2.8-6.5 ns, whereas it exhibits picosecond dynamics in TA measurements. The difference between the two measurements is that the TA spectroscopy measures the absorption of all species while Streak camera measurements detect the emissive states even if they show very low photoluminescence quantum yield. To conclude, faster decay dynamics in more polar solvents seen in the TA measurements reflect the different environment around the dye molecules implying different formation rates of CT states that can affect the injection process, similar to the addition of Li-TFSI cations on films.

### 5.5. Time-resolved photoluminescence (PL) of dye-sensitized films

From the solvent polarity dependent changes of the dipole moment and of the CT state's kinetics shown in the previous section, it can be inferred that changes in the local electric field in the surrounding of dye molecules occur upon addition of Li. In this section, the PL lifetimes were measured using a Streak Camera System, when the dye is adsorbed on alumina and titania surfaces.

Alumina is an insulator with a large bandgap of 8.5-9.9 eV<sup>[147]</sup>. It cannot accept electrons from the LUMO level of organic dye molecules because of its high conduction band level of 0.2 eV. For PL decay dynamics on an alumina sample, the same experimental setup as described above was used due to the relatively long lifetime of the dye's excited state. With an alumina sample, one can study the excited state lifetime of a dye adsorbed on a metal oxide film through the PL dynamics.

Figure 5-9 (a) shows normalized PL decays of dyes adsorbed on alumina with (**Sample 1**, black) and without (**Sample 2**, red) application of Li cations. The lifetime of **Sample 1** is determined to be 3.2 ns



when the excited-state dynamics are fitted with a stretched exponential function (amplitude and offset are set to 1 and 0, respectively). The decay mainly originates from singlet exciton quenching and/or inter-/intra-molecular CT state formation. An intramolecular CT state can be formed by redistribution of charge in ID889 upon excitation, whereas an intermolecular CT state may be created through a charge hopping process when two dye molecules have the same energy and are close to each other. Compared to the solution measurement, the lifetime of **Sample 1** is shorter than that of ID889 in TLN solution (6.5 ns), but it is still long enough for dye molecules to inject electrons.

With application of Li salts on the alumina surface (**Sample 2**, red), **Sample 2** does not show the same properties any longer. The Li cation is small enough to enter the mesoporous metal oxide nanoparticles or to stay at the interface between the metal oxide layer and the dye molecules. Due to the interaction of Li salts with dye molecules, the PL is further quenched and the lifetime is decreased to 1.4 ns (the lifetime is 2.9 ns in ID889 solution in DMSO) when the fitting is done by a stretched exponential decay. Faster PL decay of **Sample 2** indicates an increased radiationless decay process and/or due to an interaction of dye molecules with Li ions (changes in inter-/intra-molecular CT state). The solid lines in Figure 5-9 (a) correspond to stretched exponential fits.

Titania is a metal oxide semiconductor with a bandgap of about 3.2 eV<sup>[132]</sup> and dye molecules are able to inject electrons due to the low-lying conduction band of TiO<sub>2</sub>. When ID889 is adsorbed onto the TiO<sub>2</sub> surface (**Sample 4**, black), the PL decay shown in Figure 5-9 (b) becomes significantly faster than in solution or on an alumina surface. The decreased lifetime of the dye's excited state can be an indication of injection. However, absolute comparison of the lifetimes between alumina and titania may be somewhat difficult, since binding modes on the two nanoparticles can be different, as can be the formation of a charge transfer state. The PL lifetime of **Sample 4** was determined to be 54.8 ps by time-resolved PL measurements. For detailed information see Chapter 3.3.

By the application of Li cations (**Sample 5**), the PL decay is not significantly changed from that of **Sample 4**. The lifetime of **Sample 5** was determined to be 52.2 ps with a stretched exponential function. Here, we need to note that the PL measurement is not directly related to charge generation (even after injection takes place in the sample) as only emissive species of the dye molecules' excited state can be probed in PL measurements. Hence, the decay dynamics simply explain the status of dye molecules in the excited state when they are exposed to Li cations. We can only tell that the lifetime of 52.2 ps appears to be long enough to inject electrons, if this is the lifetime of the dye's excited state interacting with Li cations, considering that the injection process takes place on an ultrafast time scale<sup>[25-28, 148]</sup>. Lifetimes of **Sample 4** and **5** were obtained by stretched exponential decays with amplitude of 1 and an offset of 0.

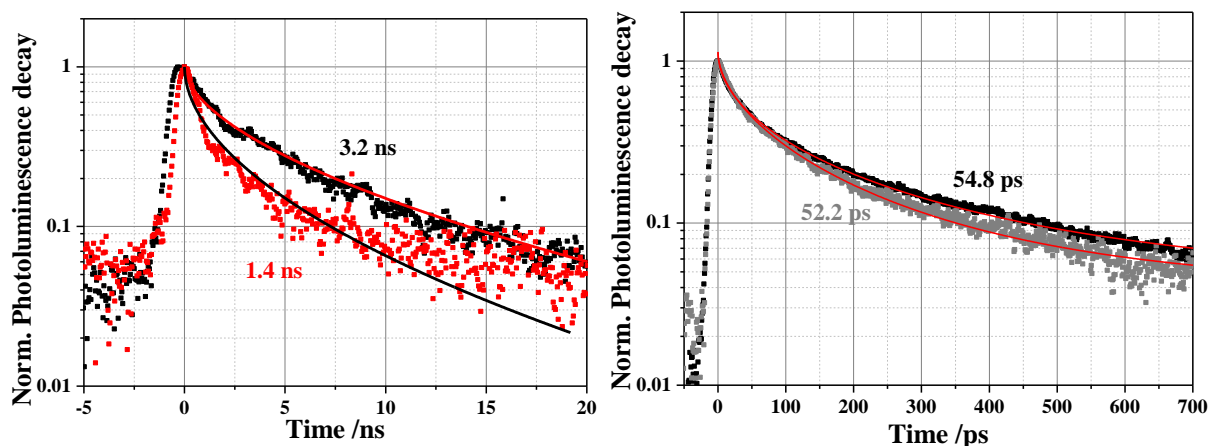


Figure 5-9. (a) Normalized photoluminescence (PL) decay of ID889 on alumina without application of Li cations (**Sample 1**, black scatter) and fitting (red solid line) with a lifetime of 3.2 ns. PL decay of ID889 on alumina with Li cations (**Sample 2**, red squares) and fitting (black solid line) with a lifetime of 1.4 ns. Lifetimes are obtained from a stretched exponential function. (b) Time-resolved photoluminescence measurement of ID889 adsorbed on TiO<sub>2</sub> layer (**Sample 4**, black) and with Li cations (**Sample 5**, gray). The lifetimes were determined to be 54 and 52 ps for **Sample 4 and 5**, respectively.

Given these circumstances, it seems that the PL decay of **Sample 4** originates from dye molecules in a state unsuitable for electron injection since most excited states will go through an ultrafast injection process (we observed the injection in the PIA measurement). Here, we can consider that there are two pools of ID889 dye molecules, one pool that is highly affected by Li cations and the other pool that is less affected by Li cations. On application of Li salts, a Li cation-inactive pool in the dye's excited state may show PL quenching, whereas a Li cation-active pool in the excited state may simply contribute to injection, rather than showing PL. Further description will be introduced in chapter 5.6.3.

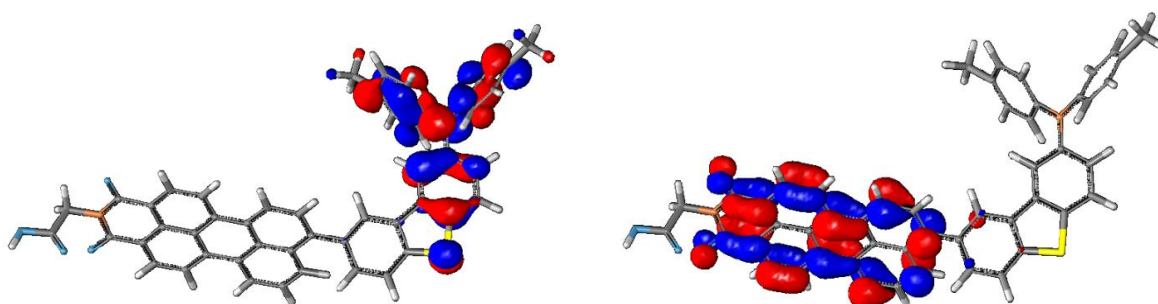


Figure 5-10. The charge distribution of the HOMO (left) and of the LUMO (right) calculated from TD-DFT.

This hypothesis is supported by the observation of induced absorption of charges in the PIA measurement shown in Figure 5-5. In PIA, the slightly increased signal strength of dye cation absorption in **Sample 5**, compared to the absorption of dye cations without Li cation salts in **Sample 4**, indicates that some Li cation-active pools become activated for injection and show increased charge generation.

This can be additionally confirmed from the fairly localized electronic charge distribution of the HOMO/LUMO levels in DFT calculations shown in Figure 5-10. Upon excitation, most electron density is distributed in the proximity of the anchor group that is suitable for injection even without application of Li salts. By addition of Li cations, some Li cation-inactive pools in an excited state will become active, contributing to charge separation, and a Li cation-inactive pool exists, not participating in injection but going through recombination or relaxation. This is why we observe an enhanced signal strength of long-lived species in the PIA measurement in **Sample 5**, and a similar dye excited state lifetime in Figure 5-9 (b).

## 5.6. Transient absorption spectroscopy on films

### 5.6.1. Main species observed

Transient absorption spectroscopy (TAS) allows detection of the excited state dynamics of different transient species going through a relaxation, transition, or recombination process. In this section, the charge generation and recombination process will be described by TA spectra and kinetics of each species such as primary photoexcitation, dye cation, and hole-conductor (Spiro-OMeTAD) cation.

Primary photoexcitations are short-lived excitons, showing exciton-induced absorption and inter-/intra-molecular charge-transfer (CT) states. The absorption of the latter (CT states) can be clearly observed by TA measurements carried out on an alumina sample or a solution of the dye because there the dye does not undergo a charge separation process. In the case of an efficient dye adsorbed on a TiO<sub>2</sub> surface (i.e. the dye injects electrons, sometimes without the aid of additives), it may be difficult to observe the exciton-induced absorption from primary photoexcitations in our setup since the dye injects electrons on an ultrafast timescale (fs-ps). In a sample treated with Li-TFSI salts, absorption of primary excitations can be observed on a very early timescale, compared to a sample not treated with Li cations, and TA spectra of primary excitations overlapped with absorption spectra of other species on later timescales.

The observation of oxidized dye molecules is evidence of an electron-injection process from the dye's excited state. Absorption spectra of oxidized dyes generally span across a broad wavelength range from the visible to the near-infrared region and often overlap with absorption spectra of other species such as excitons or oxidized hole-conductor molecules. This absorption feature, namely the dye cation

induced absorption, can be observed from dyes adsorbed on TiO<sub>2</sub> treated with Li cations (i.e. **Sample 5** and **6**) due to enhanced electron injection, leading to a facilitated charge separation process.

The TA signal of oxidized hole-conductor molecules, namely spiro-OMeTAD cations, is a result of a hole transfer process from the oxidized dye molecule to the hole-conductor. Once a dye cation is generated, it can either recombine with electrons injected in the titania layer or transfer a hole to a hole-conductor such as the spiro-OMeTAD. Hence, the charge-induced absorption of an oxidized hole-conductor molecule indicates the regeneration of the dye's ground state or the formation of a dye anion, if reductive quenching occurs<sup>[125]</sup>.

### 5.6.2. Charge Transfer (CT) states on alumina

In this section, the generation of primary photoexcitations and charge transfer (CT) states is presented from short-time (fs-ns) TA spectra of **Sample 1** and **2**. The CT state can be observed on alumina surfaces after an addition of Li-TFSI that redistributes the charge densities across the dye molecules and induces local electric fields at the interface. However, the CT state can be differentiated from the dye cation (free charges) absorption by fluence series measurements, although the spectral range of the two species often overlaps. For the short-delay TA measurement of ID889, an excitation at 510 nm is used for all samples, since ID889 shows the strongest absorbance signal around 500 nm as shown in Figure 5-2 (a) and all TA data are plotted at the lowest excitation fluence.

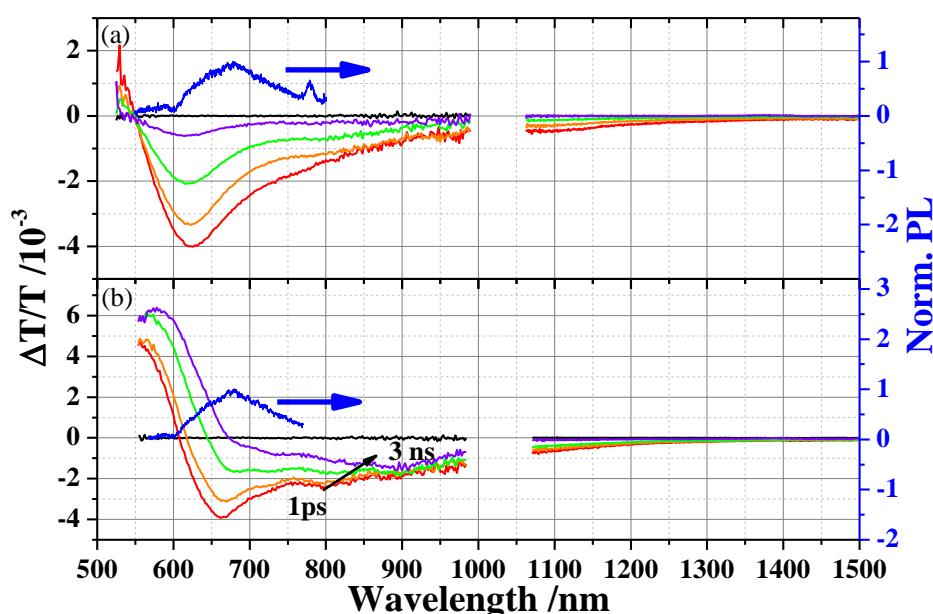


Figure 5-11. Short delay (ps-ns) broadband TA spectra of **Sample 1** (a) and of **Sample 2** (b) at delay times of 1 ps (red), 3 ps (orange), 30 ps (green), and 3000 ps (purple). The pump fluence at 510 nm is 6.4  $\mu\text{J cm}^{-2}$  for the visible and 25.8  $\mu\text{J cm}^{-2}$  for the near infrared measurements in **Sample 1**. For **Sample 2** fluence is 5.9  $\mu\text{J cm}^{-2}$  for the visible and 24.2  $\mu\text{J cm}^{-2}$  for the near infrared measurements. Two blue lines represent the PL spectra of each sample.

Figure 5-11 (a) shows the short-delay spectra and time-resolved PL spectrum of ID889 adsorbed on alumina (**Sample 1**). The short-delay spectra of **Sample 1** show three pronounced features: a positive TA signal up to 550 nm, an isosbestic point, and a broad negative TA signal extending to the near infrared wavelength range. The positive and negative signals are assigned to ground state bleaching (GSB) and photoinduced absorption (PIA) of primary excitations. A clear isosbestic point is observed at 550 nm where GSB and PIA signals show the same molar absorptivity. The broad photoinduced signals of the primary excitation seen due to the inability to inject electrons range from 550 to over 1500 nm as shown in Figure 5-11 (a). Comparing the PL spectrum (lifetime of 3.2 ns) with the PIA of the primary excitation (measurement up to 4 ns), shows a significant overlap.

In the TA spectrum of ID889 adsorbed on  $\text{Al}_2\text{O}_3$  treated with Li-TFSI (**Sample 2**) shown in Figure 5-11 (b), an isosbestic point is no longer observed and instead significant spectral shifts are observed as delay times increase. As stated above in the time-resolved PL measurements, **Sample 2** shows a different absorption of the dye's primary excitation due to an addition of Li-TFSI. Therefore, Li-TFSI results in changes of the dye ground state absorption (no isosbestic point) and causes stimulated emissions between 600 – 670 nm. The strong absorption at 900 nm can be assigned to an intramolecular CT state due to the localized HOMO and LUMO levels or an interfacial CT state between dye molecules and the alumina surface induced by the addition of Li cations.

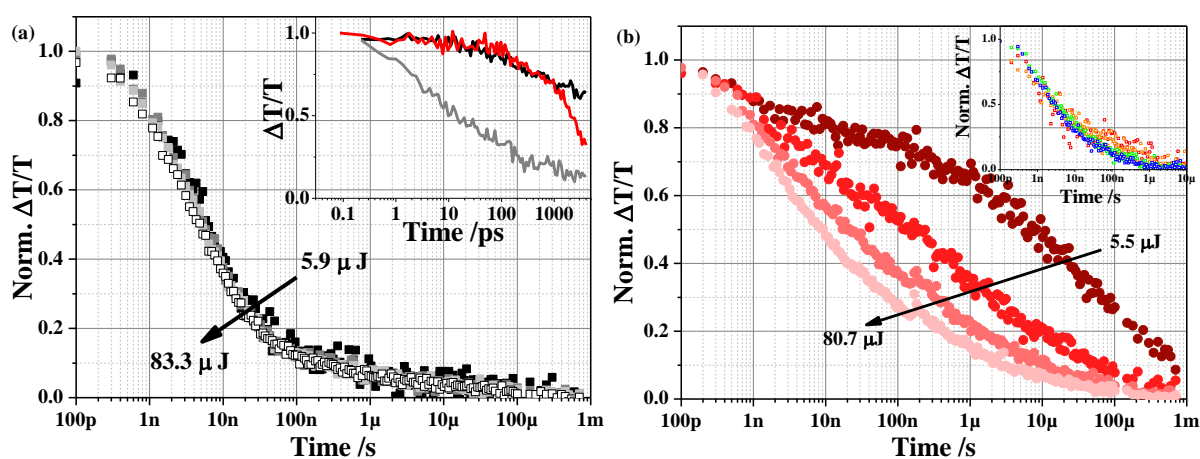


Figure 5-12. (a) Normalized decay dynamics (long-delay measurement) of CT state absorption signal between 875 nm and 925 nm in **Sample 2** with different pump fluences:  $5.9 \mu\text{J cm}^{-2}$  (black),  $12.3 \mu\text{J cm}^{-2}$  (gray),  $66.7 \mu\text{J cm}^{-2}$  (light gray), and  $83.3 \mu\text{J cm}^{-2}$  (white). Inset: The dynamics of the PIA signal from **Sample 1** (gray), **2** (black), and **5** (red) probed at a wavelength between 875 and 925 nm. (b) Normalized decay dynamics (long-delay measurement) of the dye cation's absorption between 830 nm and 850 nm in **Sample 5** with different pump fluences:  $5.5 \mu\text{J cm}^{-2}$  (dark red),  $30.1 \mu\text{J cm}^{-2}$  (red),  $50.5 \mu\text{J cm}^{-2}$  (pale red) and  $80.7 \mu\text{J cm}^{-2}$  (pink). Inset: The dynamics of the PIA signal from **Sample 4** in long-delay measurements, showing weaker fluence dependence.

The inset of Figure 5-12 (a) compares the dynamics of the PIA signal from **Sample 1**, **2**, and **5** probed at a wavelength between 875 and 925 nm. The decay of **Sample 1** (gray) is significantly faster than that of **Sample 2** (black) due to the decay of primary excitations, namely excitons, whereas the PIA decay dynamics of ID889 on titania with Li cation additive (**Sample 5**, red) looks fairly similar to that of **Sample 2**. This means that **Sample 1** shows mainly exciton decay, while the absorption of the CT state at 900 nm from **Sample 2** looks similar to the absorption features of the dye cation from **Sample 5**. However, we need to note that these two absorption features are basically generated through different routes.

This fact is supported by long-delay TA measurements (ns- $\mu$ s) that allow detection of the presence of free charge carriers. Figure 5-12 (a) presents fluence dependent measurements of **Sample 2** showing decay dynamics of CT states at pump energies between 5.9  $\mu\text{J cm}^{-2}$  and 83.3  $\mu\text{J cm}^{-2}$ , whereas **Sample 5** shows a strong fluence dependence as shown in Figure 5-12 (b). The kinetics of **Sample 2** are not fluence dependent in the wavelength range between 875 nm and 925 nm, where a strong absorption of the CT state has been observed. This indicates that there is no free charge carrier generated in **Sample 2** and the strong absorption feature is presumably attributed to an interfacial CT state, looking similar to dye cation's decay dynamics.

Figure 5-12 (b) shows the decay dynamics of the oxidized dye ranging from 830 to 850 nm with different fluence from 5.5 to 80.7  $\mu\text{J/cm}^2$  for **Sample 5**. Clearly, the higher the fluence, the faster the decay observed. In comparison, the inset of Figure 5-12 (b) presents the fluence dependence of **Sample 4** in long-delay measurements, indicating weaker fluence dependence than in **Sample 5** due to a small amount of charge generation and mainly fast recombination. Detailed information is given in the next section.

### 5.6.3. Generation of free charge carriers after addition of Li-TFSI on titania surface

As shown in the previous section, ID889 does not create free charge carriers on alumina, but evidence of a local electric field (based on red-shifted PIA signals) and charge transfer states (based on the strong absorption feature at 900 nm) are observed after addition of Li cations. In this section, the generation of free charge carriers on titania is investigated by TA measurements.

ID889 injects electrons into  $\text{TiO}_2$  on an ultrafast timescale owing to its higher LUMO energy level than the conduction band when it is adsorbed on the metal oxide semiconductor surface. Charge generation via injection has already been proved by the observation of absorption of long-lived species in PIA measurements, where signals indicate the presence of charges. Changes in PIA spectra in time can be observed in the following TA measurements.

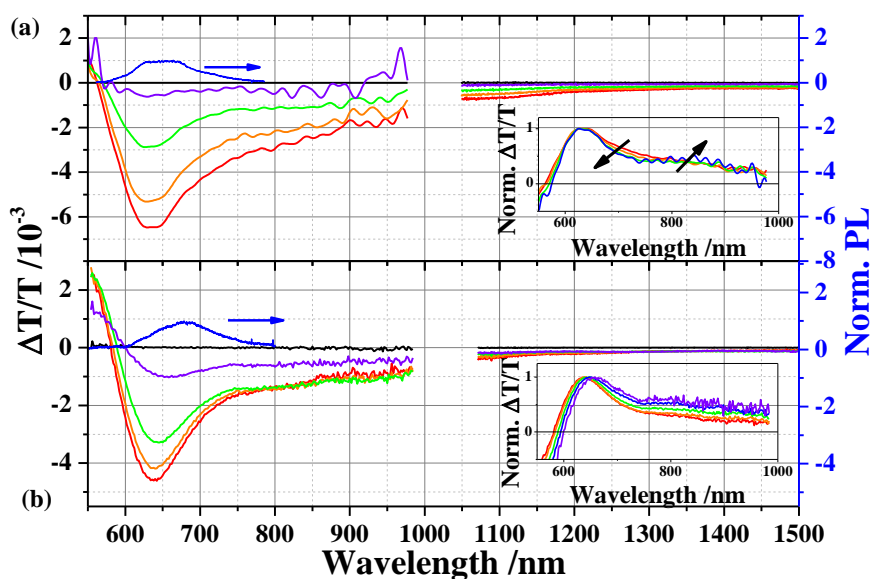


Figure 5-13. TA spectra on the femto- to nano-second timescale and PL spectra of **Sample 4** (a) and of **Sample 5** (b) at delay times of 1 ps (red), 3 ps (orange), 30 ps (green), and 3000 ps (purple). The pump fluence at 510 nm is  $18.5 \mu\text{J cm}^{-2}$  in the visible and  $36.0 \mu\text{J cm}^{-2}$  in the NIR for **Sample 4** and  $18.5 \mu\text{J cm}^{-2}$  in the visible and  $25.0 \mu\text{J cm}^{-2}$  in the NIR for **Sample 5**. Two blue lines represent the PL spectra of each sample. Insets: TA spectra of **Sample 4** and **Sample 5** in the visible normalized to the minimum value of each spectrum.

Figure 5-13 (a) displays broadband visible and NIR pump-probe spectra of ID889-sensitized  $\text{TiO}_2$  (**Sample 4**). The broad PIA signals appear to be mainly originating from primary excitations, since the PIA signal across a broad wavelength range from the visible to the near-infrared region looks similar to that in ID889 on  $\text{Al}_2\text{O}_3$  (**Sample 1**) which peaks at 620 nm, showing a red-shift due to presumably different adsorption mode. However, the inset of Figure 5-13 (a), which shows the spectra in the visible normalized to the PIA peak, provides evidence of injection. The PIA signals between 800 - 900 nm show almost no or a minor increase due to generation of oxidized dye molecules (as a consequence of the injection process), whereas the PIA signals between 650 - 800 nm diminish due to a decrease in absorption of the exciton. Thus, it can be stated that the dye cation is generated from the exciton (injection from exciton); however, the dye cation signals seem to be very weak. Generation of the dye cation is also supported by the spectrum at later time of **Sample 4**, which looks similar to that of the earlier timescale of ID889 on  $\text{TiO}_2$  with Li cations, namely **Sample 5**, in turn indicating slower injection in **Sample 4** than in **Sample 5**. The PIA signals of **Sample 4** between 620 - 640 nm are likely influenced by PL, since the rather flat shape of the PIA signal looks like that of the PL spectrum which has a lifetime of 54 ps as shown in Figure 5-9 (b).

After the application of Li-TFSI salts, the PIA signals red-shift about 20 nm as shown in Figure 5-13 (b), likely due to the ground state absorption being influenced by generation of a local electric field (Stark Effect). **Sample 5** shows a shoulder rising between 750 - 980 nm as the delay time increases as

shown in the inset of Figure 5-13 (b) where all spectra in the visible are normalized to the minimum value of each spectrum. This increasing feature is attributed to the PIA signal of the oxidized dye molecules by addition of Li-TFSI salts. Interestingly, most signals in the visible and NIR spectral region are not fully decayed and still remain after 4 ns, indicating long-lived species, in contrast to the measurement presented for **Sample 4**. The long-lived species in **Sample 5** seems to be mainly due to reduced recombination with the help of Li cations as shown in Figure 5-14.

To get insight into the role of Li cations in recombination processes, the early time dynamics of dye cations of **Sample 4** and **5** were monitored at 830 – 850 nm, as shown in Figure 5-14. Absorption of dye cations in this wavelength range was also observed from steady-state absorption measurements as shown in Figure 5-2, quasi-steady-state PIA measurements as shown in Figure 5-5, and in the inset of Figure 5-13 (b). After the application of Li, **Sample 5** shows a constant signal up to 10 ps, whereas **Sample 4** shows constantly decreasing dye cation signals, likely due to back electron transfer or exciton decay.

The lifetime of oxidized dye molecules in **Sample 4** is determined to 3.7 ps whilst that in **Sample 5** is 2815 ps using stretched-exponential fits. Amplitude and offsets are set to 1 and 0, respectively. The lifetime of **Sample 4** is rather short compared to the typical lifetime of dye cations (generally, a few tens of picoseconds); hence, it can be a convolution of fast recombination of dye cations and exciton decay. The much longer dye cation lifetime observed in **Sample 5** is assigned to reduced recombination. Consequently, addition of Li-TFSI appears not only to facilitate injection, but also to reduce recombination.

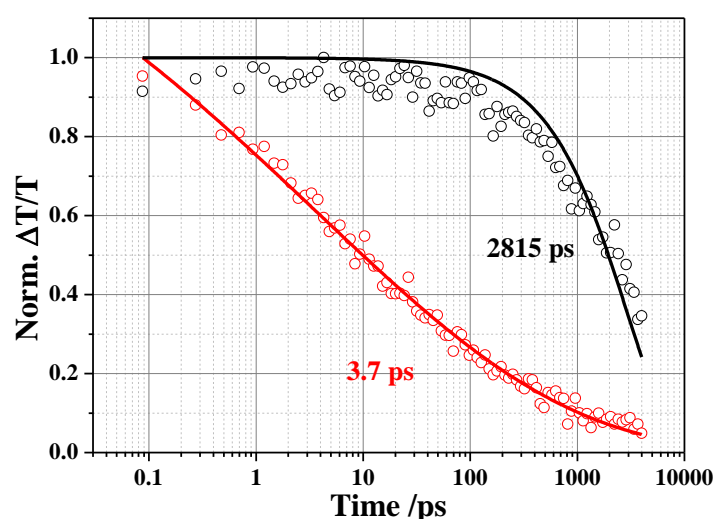


Figure 5-14. Normalized decay dynamics (ps-ns) of the dye cation absorption observed between 830 and 850 nm in ID889 on titania (**Sample 4**, red) and in ID889 on titania plus Li cations (**Sample 5**, black). The solid lines correspond to stretched exponential fits for **Sample 4** and **5**.



Enhanced charge generation of free charge carriers in **Sample 5** is supported by long delay (1 ns – 0.1ms) TA measurements where detection of long-lived species such as charges is possible. A broad negative PIA signal in the visible and NIR entirely originates from absorption of dye cations as shown in Figure 5-15. Figure 5-15 (a) shows the result of long delay TA experiments on **Sample 4** indicating two absorption features as observed in the short delay TA measurements shown in Figure 5-13 (a): one absorption feature around 620-640 nm and the other around 800-900 nm. The PIA signal peaking around 620-640 nm is assigned to excitons and the distinct feature observed around 800-900 nm is due to the PIA signal of dye cations.

On application of Li cations (**Sample 5**), the primary excitation is no longer observed due to fast injection and instead a strong absorption of dye cation molecules is seen in the visible (600 – 900 nm) and the near-infrared (1250 – 1400 nm) range as shown in Figure 5-15 (b). Also, the signal amplitude is increased by 2-6 times, even though the excitation energies are the same, when compared to **Sample 4**, meaning that more long-lived species such as charges (via injection) are generated or that the cross-sections of the dye cation become larger. In **Sample 5**, the GSB and isosbestic point red-shift by approximately 30 nm, compared to **Sample 4**, due to a local electric field induced by Li ions. Here, it confirms again that the strongest PIA signal of the dye cation is observed around 840 nm as described in Figure 5-13 (b).

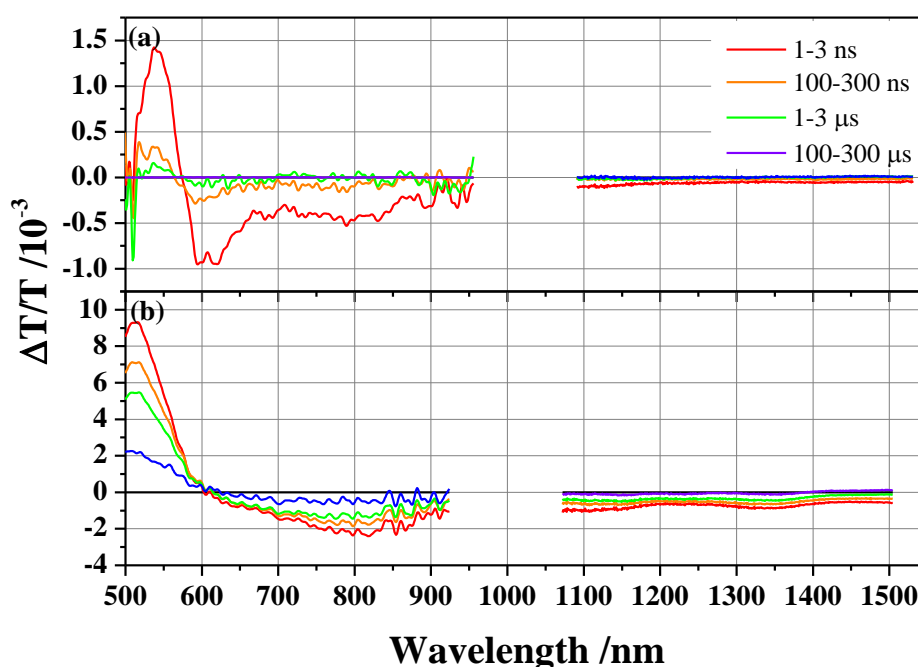


Figure 5-15. Long delay (ns - sub-ms) broadband TA spectra of **Sample 4** (a) and of **Sample 5** (b) with delay times of 1 ns (red), 100 ns (orange), 1 μs (green), and 100 μs (purple). Excitation at 532 nm and energy density of 4.9 μJ cm<sup>-2</sup> in the visible and 6.2 μJ cm<sup>-2</sup> in the NIR for **Sample 4** and of 4.9 μJ cm<sup>-2</sup> in the visible and 7.5 μJ cm<sup>-2</sup> in the NIR for **Sample 5**.

To conclude, the injection process of ID889 becomes faster after addition of Li cations, which stabilizes the dye's CT states and suppresses back-electron transfer. Faster injection can be probed by the oxidized dye molecule's absorption feature between 830 - 850 nm, while the suppressed recombination is seen as an increase in lifetime to 2815 ps in **Sample 5** from 3.7 ps in **Sample 4**.

#### 5.6.4. Regeneration using Spiro-OMeTAD and the critical role of Li-TFSI

For photovoltaic performance, the oxidized dye molecules need to be reduced by a redox couple from a liquid-state redox mediator or by hole transfer from a solid-state hole conductor. For a solid-state DSC using ID889, an organic hole conductor, namely spiro-OMeTAD, is used to regenerate the dye cation and to transport holes to the electrode. In this section, a sample having a device-like structure (**Sample 6**) gives insight into the recombination and charge generation processes as in an actual device. The sample preparation is described in Chapter 3.1.1.

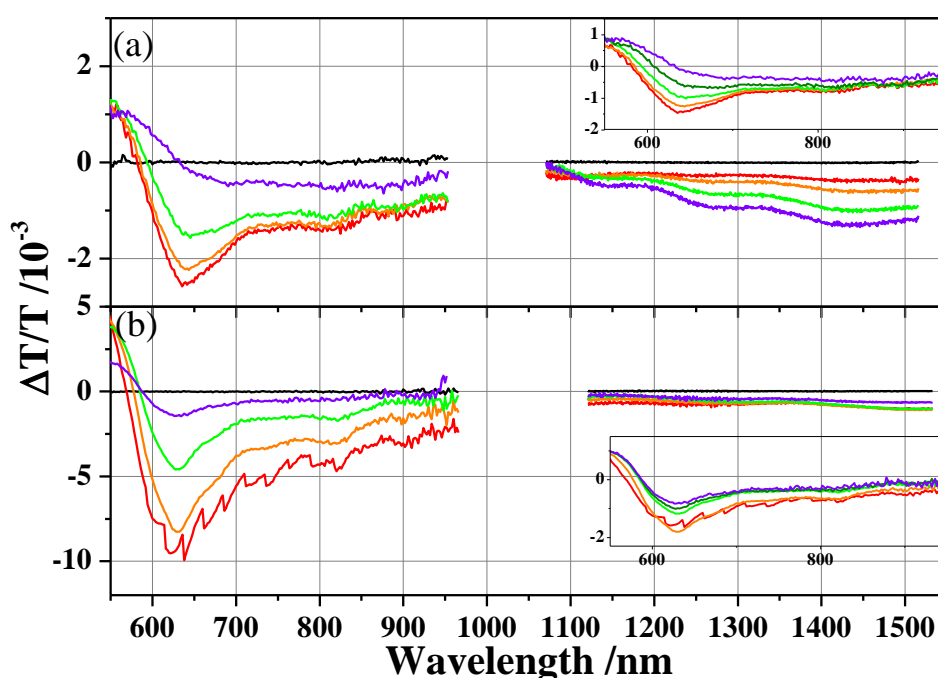


Figure 5-16. Broadband TA spectra of (a) ID889 on  $\text{TiO}_2$  with Li-TFSI/*t*BP/spiro-OMeTAD (complete device structure, **Sample 6**) and (b) ID889 on  $\text{TiO}_2$  with *t*BP/spiro-OMeTAD (**Sample 7**) on short-delay time scale (ps - ns) at delay times of 1 ps (red), 3 ps (orange), 30 ps (green), and 3000 ps (purple). The insets: The spectra in the visible normalized to the maximum value of each spectrum. The pump fluence at 510 nm is  $5.75 \mu\text{J cm}^{-2}$  for the visible and  $23.3 \mu\text{J cm}^{-2}$  for the infrared measurements in **Sample 6** and  $14.8 \mu\text{J cm}^{-2}$  for the visible and  $11.3 \mu\text{J cm}^{-2}$  for the infrared measurements in **Sample 7**.

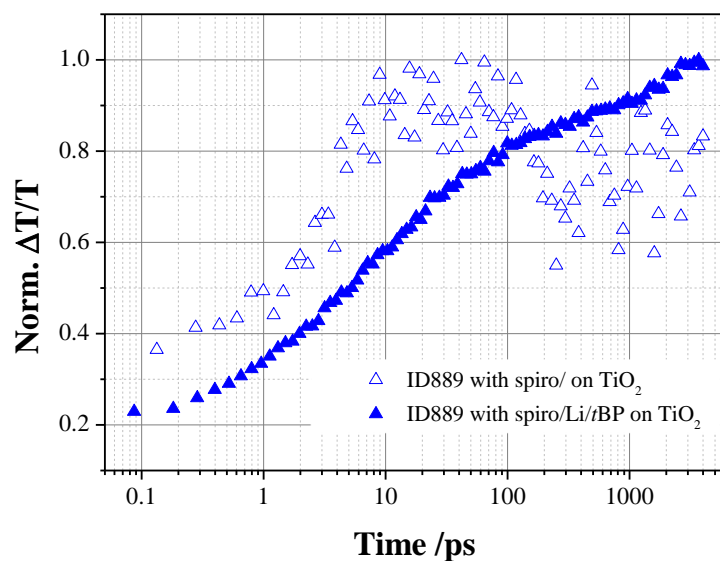


Figure 5-17. Normalized decay dynamics (short-delay measurement) of the oxidized spiro-OMeTAD's absorption between 1400 - 1430 nm in **Sample 6** (closed) and **7** (open) with pump fluences  $23.3 \mu\text{J cm}^{-2}$  for **Sample 6** and  $11.3 \mu\text{J cm}^{-2}$  **Sample 7**.

Figure 5-16 (a) shows pump-probe spectra of a complete device-like sample (with a structure of titania/dye/spiro-OMeTAD, Li-TFSI, and *t*BP, **Sample 6**). The most remarkable change, compared to **Sample 4** and **5**, is a rise of a PIA signal in the NIR up to 4 ns, indicating generation of states that have not been observed before. They may originate from the dye cation that is also observed in the NIR; however, this increasing feature is attributed to the absorption of oxidized spiro-OMeTAD molecules, since the spiro-OMeTAD cation absorption spectrum ranges from 1100 nm to 2100 nm, peaking at 1600 – 1700 nm as shown in Chapter 4.4.<sup>[149]</sup> As another proof, the NIR at the early time range of 1-1.5 ps shown in Figure 5-16 (a) looks very similar to the absorption spectrum of the dye cation in the NIR on the later time range shown in Figure 5-13 (b). Therefore, the rise of the PIA signals in the NIR region is attributed to spiro-OMeTAD taking holes from the oxidized dye molecules thereby creating absorption of hole-conductor cations. An isosbestic point indicates a transition between two species, namely dye cation and oxidized spiro-OMeTAD, with the same molar absorptivity at 1110 nm.

Owing to the regeneration process, the oxidized dye molecule's absorption becomes less significant not only in the NIR but also in the visible region between 800 - 850 nm, where the absorption of the oxidized dye is observed. In Figure 5-16 (a), the rather strong absorption that is observed at the early timescale between 800 – 850 nm disappears as the delay time increases as confirmed by the inset showing spectra normalized to the maximum value in the visible range. However, remaining signals may indicate that there are Li-inactive sites.

Figure 5-16 (b) shows the short-delay spectra of a device-like sample without Li-TFSI (with this structure: titania/dye/spiro-OMeTAD/*t*BP, **Sample 7**). Interestingly, the primary excitation between 620 - 640 nm is still observed on the later timescale, implying an inefficient injection process. Based on the observation of remaining primary excitations, it appears that only a small amount of dye cation is generated and also regeneration of dye cations is not efficient. This is confirmed by both the visible and NIR range. In the visible, the dye cation molecules' long-lived absorption is observed between 800 – 850 nm which should be reduced by the hole transfer process to the hole conductor, thereby indicating an inefficient regeneration process if Li cations are not used in the device. This can be clearly observed from the inset of Figure 5-16 (b). In the NIR, the signal strengths are very weak compared to **Sample 4** and **6**, and this reflects inefficient regeneration by the hole conductor molecule.

The inefficient regeneration in **Sample 7** is also supported from the decay dynamics of the oxidized hole conductor signal taken between 1400 - 1430 nm when compared to that in **Sample 6** as shown in Figure 5-17. The PIA signal of **Sample 7** increases up to 10 ps and afterwards starts decaying continuously, whereas the generation of the oxidized spiro-OMeTAD molecule in **Sample 6** continues until 4 ns as reflected by the increasing signal. Thus, in **Sample 7**, we cannot exclude a possibility of reductive quenching that also contributes to charge generation from an anionic dye molecule due to preceding hole transfer to a hole conductor, since the absorption of primary excitation is still observed and dye cation charge generation is not efficient. Therefore, the decay in **Sample 7** after 10 ps shows that the regeneration process is not as efficient as in **Sample 6**.

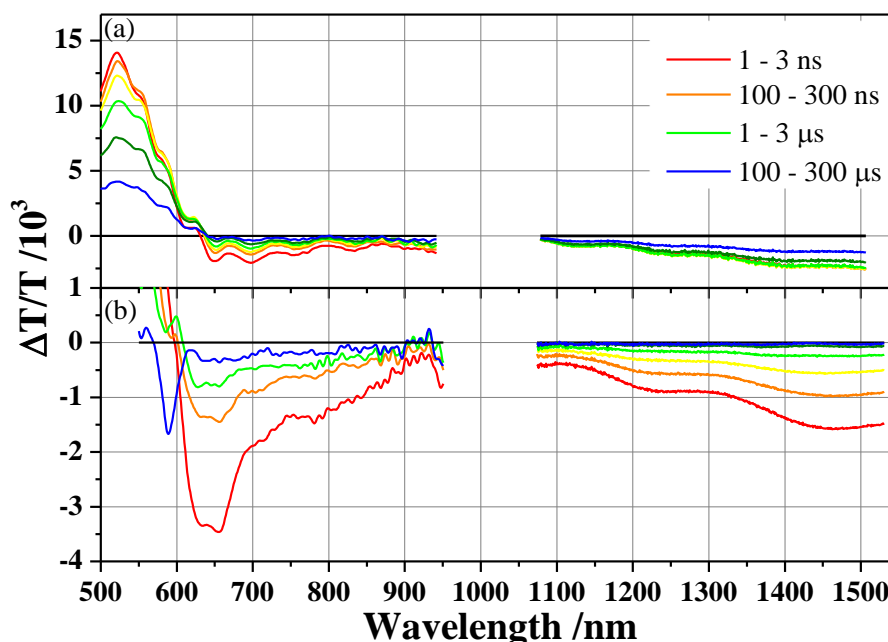


Figure 5-18. (a) Long delay (ns-sub-ms) broadband TA spectra of **Sample 6** (a) and of **Sample 7** (b) with delay times of 1 ns (red), 100 ns (orange), 1  $\mu$ s (green), and 100  $\mu$ s (blue). Excitation at 532 nm and energy density of 45.2  $\mu$ J  $\text{cm}^{-2}$  in the visible and 51.7  $\mu$ J  $\text{cm}^{-2}$  in the NIR for **Sample 6** and of 52.7  $\mu$ J  $\text{cm}^{-2}$  in the visible and 70.0  $\mu$ J  $\text{cm}^{-2}$  in the NIR for **Sample 7**.

Long-time delay (ns –  $\mu$ s) TA spectra of **Sample 6** and **7** are shown in Figure 5-18. From **Sample 6** (Figure 5-18 (a)), the distinct absorption signals of the dye cation that were observed around 840 nm in Figure 5-15 (a) are no longer seen due to the efficient regeneration process. The continuously increasing signals in the short-time delay measurements shown in Figure 5-16 (a) finally start to decrease after a rise of the signal up to 200 ns in the long-time delay measurements shown in Figure 5-18 (a), indicating the end of charge transfer and beginning of recombination between the injected electrons and the oxidized spiro-OMeTAD molecules.

This decay dynamics of **Sample 6** is depicted as a black curve in Figure 5-19 (a), taken from the same wavelength region between 1400 -1430 nm in Figure 5-16. The regeneration time in **Sample 6** was determined to be 335.6  $\mu$ s at the weakest excitation fluence when a stretched exponential function is used with an amplitude of 1 and an offset of 0. The kinetics are fluence dependent in this wavelength range due to the presence of free charge carriers, leading to a non-geminate recombination process.

Turning to **Sample 7**, the absorption features of both the primary excitation and dye cation still exist in the visible region as shown in Figure 5-18 (b), maybe showing evidence of reductive quenching, and the absorption of the oxidized spiro-OMeTAD in the NIR decreases constantly, indicating a small amount of charge generation. This is confirmed from the fluence dependence in **Sample 7** as shown in Figure 5-19 (b) showing similar decay dynamics.

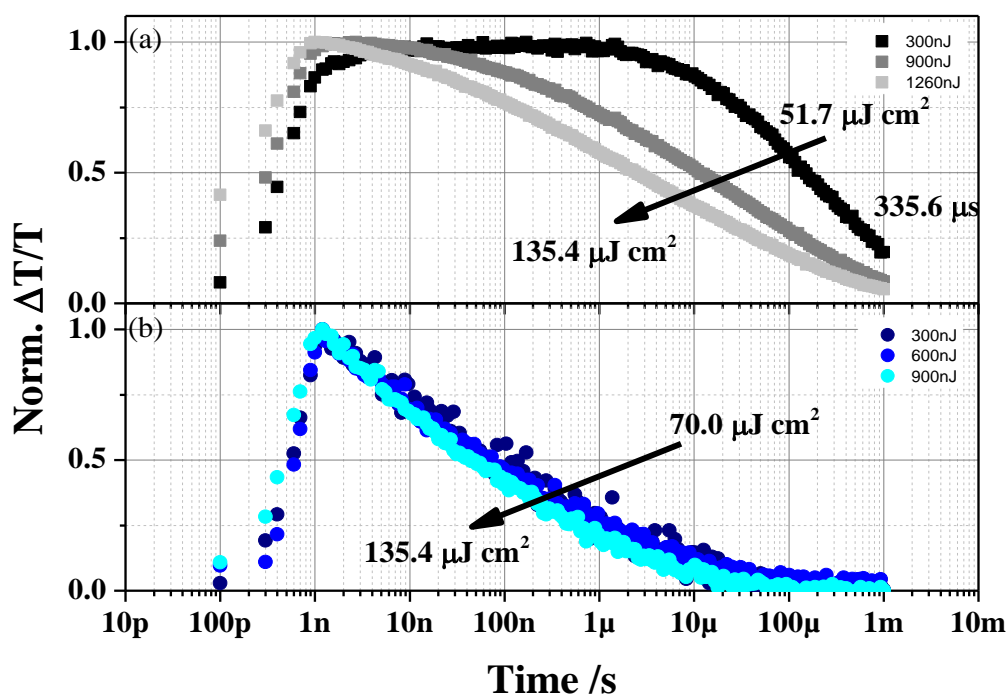


Figure 5-19. Normalized decay dynamics (long-delay measurement) of the oxidized hole conductor's absorption between 1400 – 1430 nm in **Sample 6** (a) and **Sample 7** (b) at different pump fluence.

To summarize, the free charge carriers created by addition of Li-TFSI in the device-like structure, i.e. **Sample 6**, show non-geminate recombination. Although we observed that ID889 injects electrons without any additives, the role of Li-TFSI still appears to be critical in the device. Thus, the device-like structure without Li cation additives in **Sample 7** shows a weak fluence dependence due to its inability to generate free charges or fast recombination. Furthermore, even if charges are generated, most charges recombine on the early time scale. Therefore, the addition of Li cations helps generation of free charge carriers and reduces recombination, and thus is very important to improve the photocurrents in solid-state DSCs using ID889.

### 5.7. Reductive quenching

Reductive quenching, or preceding hole transfer, is another possible charge generation channel that is observed only in solid-state DSCs. In this process, electrons are injected from an anionic dye molecule created by a preceding hole transfer from the dye's exciton to the hole conductor material. This process is considered less efficient than the ordinary generation channel <sup>[125]</sup>.

In Figure 5-16 (a), the spectra show a shoulder between 800 – 850 nm where both dye anion and cation molecules strongly absorb photons, as shown in Figure 5-2. Thus, there is a need to find out if this is an indication of reductive quenching occurring in **Sample 6**. To explore if the pronounced absorption feature between 800 – 850 nm originates from the dye cation or anion molecule, a blended solution consisting of dye, spiro-OMeTAD, and chlorobenzene at a ratio of 1:40:400 wt% <sup>[133]</sup> was spin-cast on a quartz glass. This sample (**Sample 8**) enables the observation of a hole-transfer process from the dye to the hole conductor in the absence of the titania layer.

Figure 5-20 (a) shows broadband TA spectra of **Sample 8** on the fs - ns timescale and the inset the normalized spectra of **Sample 8** and **3** (black and red lines, respectively). The spectra of **Sample 8** show a shoulder of an absorption peak around 800 nm where the dye anion molecule strongly absorbs photons, as shown in Figure 5-2. In fact, there are three reasons to believe that this sample creates dye anion molecules.

First, a rise of the signals observed beyond 1190 nm up to 15 ps (green in Figure 5-20 (a)) is attributed to a hole transfer process from the dye to the hole conductor material, since the shape of the spectra is fairly similar to that of the oxidized hole conductor's absorption spectra (compare Figure 5-16 (a)). This implies that the dye has the possibility of reductive quenching due to the energy levels of the HOMOs of ID889 and spiro-OMeTAD (changes in concentration gradient of free charge holes).

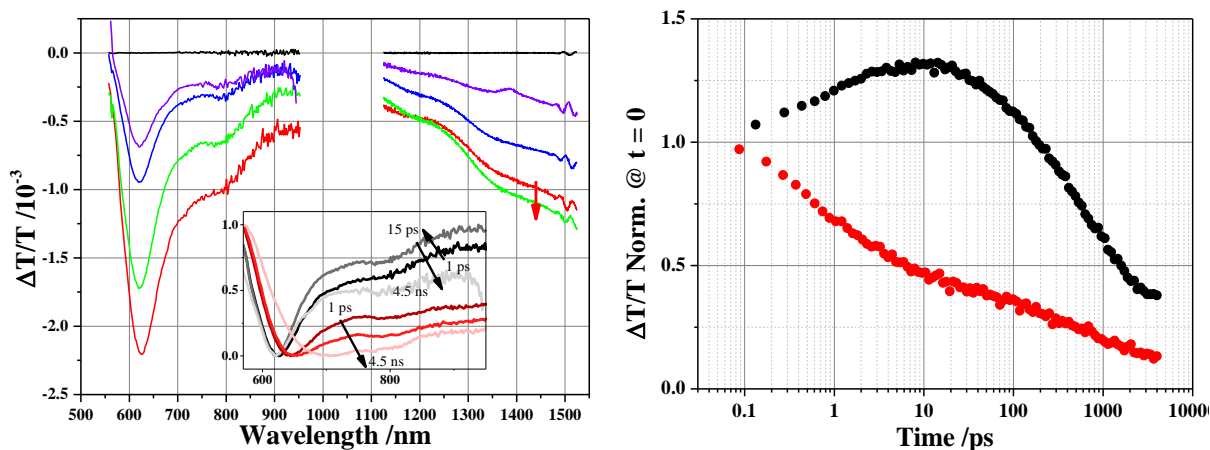


Figure 5-20. (a) Short delay (ps-ns) broadband transient absorption spectra of an ID889:Spiro-OMeTAD blend sample (**Sample 8**) at delay times of 1 ps (red), 15ps (green), 300 ps (blue), and 3000 ps (purple). The pump fluence at 510 nm is  $33.8 \mu\text{J cm}^{-2}$  in the visible and  $45.4 \mu\text{J cm}^{-2}$  in the NIR. Inset: Normalized TA spectra of **Sample 8** (black lines) and of **Sample 3** (red lines) at delay times of 1 ps, 15 ps, and 4.5 ns as color becomes pale. (b) Decay dynamics between 1400 – 1430 nm of **Sample 3** (red) and **8** (black) normalized at the delay time of 0.

Second, the absorption of **Sample 8** beyond 650 nm (black lines) decreases in 15 ps and then increases up to 4 ns as shown in the inset of Figure 5-20 (a) when the spectra are normalized. This is because the exciton decay leads to a rise of signals attributed to the generation of the dye anion up to 15 ps, since **Sample 8** cannot create the dye cation, but can create the dye anion via a hole transfer process. On the contrary, a device-like sample built on  $\text{Al}_2\text{O}_3$  (red lines, **Sample 3**) shows a rise of signals due to the generation of CT states from primary excitations (showing the absorption characteristics similar to the dye cation) formed by the use of Li-TFSI and spiro-OMeTAD as the delay time increases as shown in the inset of Figure 5-20 (a). Theoretically, **Sample 3** should show the absorption due to reductive quenching; however, ID889 instead shows dye cation-like absorption characteristics due to the use of Li-TFSI salts and spiro-OMeTAD, indicating that injection is more favorable than in **Sample 8**. This is supported again by the spectral red-shift and weak signal of the primary excitation observed from **Sample 3** (red lines) shown in the inset of Figure 5-20 (a), whereas **Sample 8** (black lines) shows remaining primary excitations as the delay time increases. Furthermore, the difference in the decay dynamics of **Sample 3** and **8** shown in Figure 5-20 (b) helps to determine whether or not the charges are generated by the hole conductor.

In order to determine the decay dynamics of the exciton and charge transfer (CT) state in **Sample 8**, the TA data matrix was deconvoluted by multivariate curve resolution (MCR). MCR analysis determines spectra and concentration profiles of each species based on physical constraints. **Sample 1** exclusively shows exciton kinetics. Therefore, the TA spectrum of **Sample 1** is used in the

deconvolution of **Sample 8** to determine the concentration profiles of exciton and CT state in **Sample 8**. The parameters from a global fit of the concentration profiles are summarized in Table 5-4.

Table 5-4. Parameters extracted from the global fit of the exciton and CT state dynamics in **Sample 8** when a two-exponential decay fit is used.

$y = A_1 \cdot \exp\left(\frac{-x}{t_1}\right) + A_2 \cdot \exp\left(\frac{-x}{t_2}\right) + y_0$	Exciton	CT state
$A_1$	$0.22 \pm 0.03$	$-0.29 \pm 0.05$
$t_1$	1.34 (set)	$1.34 \pm 0.24$
$A_2$	$0.10 \pm 0.01$	$0.63 \pm 0.01$
$t_2$	$39.95 \pm 7.79$	$508.51 \pm 15.30$
$y_0$	$0.01 \pm 0.003$	$0.35 \pm 0.01$

The excited dye molecules enter the CT state (reductive quenching) very fast, showing an inverse rate of 1.3 ps, and the CT states decay to the ground state with a rather slow inverse rate of 508 ps, which is two orders of magnitude longer than the exciton lifetime. In addition, the largest amount of CT states is generated on a subpicosecond timescale correlated to the initial fast drop in the exciton population. However, this initial fast rise was not fitted since it is affected by the system response of our TA setup. The exciton decay was then modeled with a biexponential function, in which one rate was fixed to the 1.3 ps obtained from the CT rise. The second rate constant describes the exciton decay to the ground state, yielding 39.95 ps.

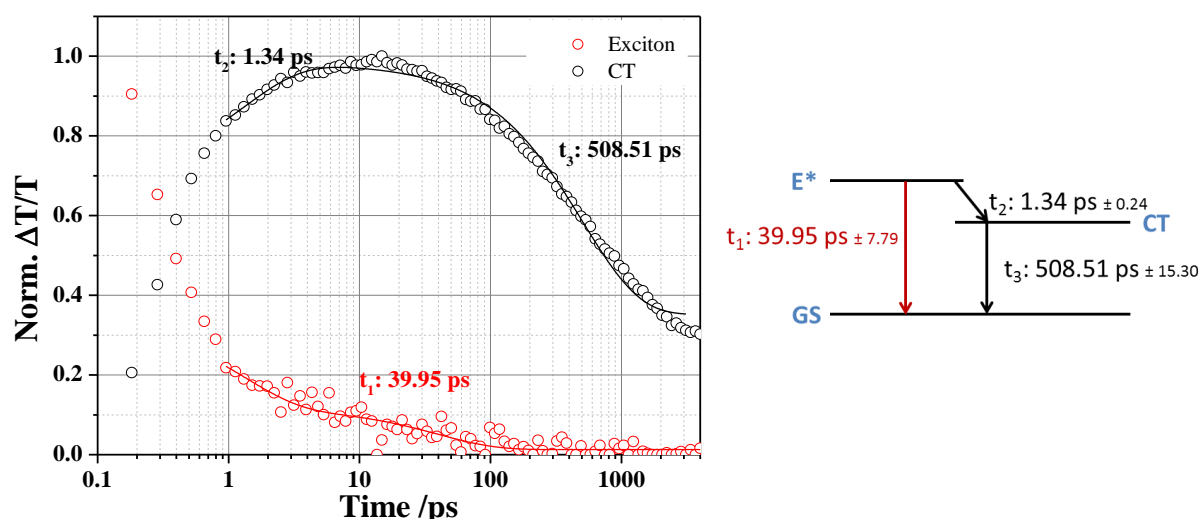


Figure 5-21. (a) Decay kinetics of exciton and charge transfer state (CT formed by preceding hole transfer process) from **Sample 8** using bi-exponential fits represented as solid lines. (b) A schematic diagram of the excited state and transfer processes in **Sample 8**.



The rise of the signal up to 15 ps in **Sample 8** shown in Figure 5-20 (b) implies a hole transfer process from the neutral dye (exciton) to the hole conductor spiro-OMeTAD. However, we note that these fitting parameters should be only considered as a parameterization to quantify the processes. Figure 5-21 shows the decay kinetics of the exciton and CT state with two exponential fits and a schematic energy level diagram of **Sample 8**.

Thirdly, we can determine the origin of the absorption spectrum based on the shape/amplitude of the spectrum. Figure 5-22 shows the steady-state absorption spectra of dye anion (dotted black) and cation (dotted red) compared to the TA spectra of **Sample 8** (solid black), **Sample 3** (solid blue), and **Sample 6** (solid greens). The dotted lines show the intrinsic absorption of each ionic dye molecule obtained from subtraction of the absorption spectra from the dye's ground state absorption spectrum. For the creation of dye cation and anion in the steady-state UV-vis absorption measurements, iron(III)chloride and Lupasol are used, respectively. The detailed experimental preparation is explained in Chapter 3.2.3. The solid black (450 ps), red (30 ps), blue (10 ps), and greens (1 ps, 4 ns) lines represent the TA spectra of **Sample 8**, **5**, **3** and **6**, respectively. Each graph shows the absorption features of the CT state and the dye cation. **Sample 8** seems to form the dye anion via a hole transfer as the TA spectrum of **Sample 8** is very alike the absorption spectrum obtained from the dye anion molecule, whereas the other spectra look like the absorption spectra of the dye cation as shown in Figure 5-22. The absorption spectrum of the dye anion (dotted black) from the steady-state absorption measurements shows a small blue-shift, compared to the TA spectrum of **Sample 8**, and it is due to the presence of iron(III)chloride.

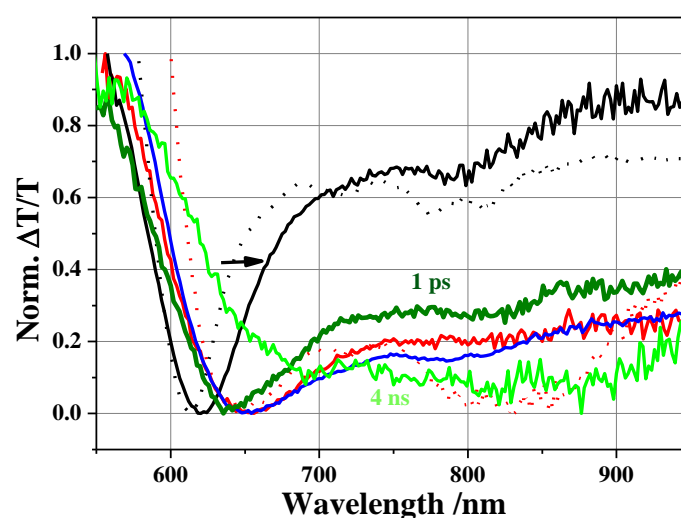


Figure 5-22. Normalized steady-state absorption of cationic (dotted red)/anionic (dotted black) dye molecules and normalized TA spectra of **Sample 8** (solid black), **5** (solid red), and **3** (solid blue).

Given the evidence above, the reductive quenching process seems plausible when the ID889 dye is used with spiro-OMeTAD. Therefore, MCR analysis was carried out again in order to study if there is a reductive quenching process in the ID889 device.

The TA data of **Sample 4**, **5**, and **6**, obtained from the short-time measurements in the NIR, are used in the analysis to extract the kinetics of excitons. Figure 5-23 (a) presents the spectra of excitons as solid lines and charges as dotted lines. This analysis is carried out under the assumption of non-negativity of spectra and kinetics.

In **Sample 4**, the absorption of the dye cation (dotted blue in Figure 5-23 (a)) slightly increases with the wavelengths, whereas that of the exciton (solid blue) decreases. This increasing absorption of the dye cation is previously observed due to a small amount of dye cation generated as observed from the inset of Figure 5-13 (a). Likewise, the spectra of the exciton (solid red) and charges (dotted red) in **Sample 5** can be separated due to their different absorption characteristics. The exciton decays very quickly after the addition of Li cations. For **Sample 6**, only two species can be found from the initial guess. One species is assumed to be the oxidized spiro-OMeTAD molecule (dotted black) due to its increasing absorption strength, and the other species could be the dye cation or the exciton. However, it appears to be the exciton (solid black) as the second species completely vanishes in 60-200 ps as shown in Figure 5-23 (b), represented in black. The lifetime of the dye cation should be longer than this, as observed from Figure 5-12 (b) and 5-14.

Figure 5-23 (b) shows the decay dynamics of the exciton obtained by MCR analysis. The excitons in all samples completely decay in 200-300 ps with similar decay rates, implying that there is no reductive quenching in a complete device structure (**Sample 6**) that shows the same exciton characteristics as **Sample 4**.

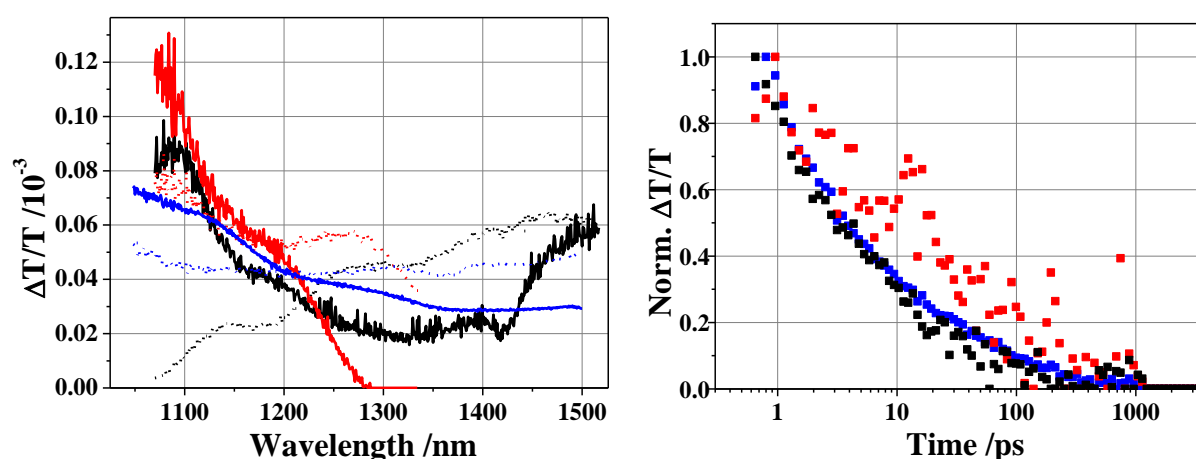


Figure 5-23. (a) Spectra of the exciton (solid) and the charges (dotted) in **Sample 4** (blue), **5** (red), and **6** (black) obtained from MCR analysis using the TA data and (b) kinetics of exciton from **Sample 4** (blue), **5** (red), and **6** (black).

This is consistent with the result of time-resolved PL measurements shown in Figure 5-9 (b), where the lifetimes of the dye's excited states in **Sample 4** and **5** are 54 and 52 ps, respectively, implying similar exciton dynamics in **Sample 4** and **5**. In addition, absence of reductive quenching in ID889 is strongly supported by the measurements on **Sample 3** that did not show any evidence of hole transfer when spiro-OMeTAD and Li cations are used, although it could show reductive quenching due to the energy levels. Upon application of spiro-OMeTAD and Li cations, large changes in the dipole moment of ID889 between the excited state and the ground state encourage an injection process on the ultrafast time scale rather than reductive quenching. Furthermore, in Figure 5-22, the TA spectrum of the device-like sample, **Sample 6**, follows the cationic dye molecules' absorption spectrum over the whole range of short-delay times (light green: 1ps, dark green: 4 ns). This strongly implies that **Sample 6** injects electrons from presumably neutral dye molecules rather than from the anionic dye molecules.

To conclude, although **Sample 8** shows anion formation via hole transfer to a hole conductor, MCR analysis shows that a device-like structure, **Sample 6**, seems to go through injection from the neutral excited state based on the observation of the same decay kinetics of excitons in all samples, likely owing to facilitated injection by the addition of Li cations.

## 5.8. ID889: Conclusions

The highly efficient push-pull type dye ID889 consists of a carboxylic acid anchoring group, a perylene monoimide as an acceptor, and a fused dibenzothiophene with triarylamine as a  $\pi$ -conjugated bridge and donor moiety. ID889 shows a high molar extinction coefficient of  $28,382 \text{ M}^{-1}\text{cm}^{-1}$  at 512 nm in dichloromethane and ID889-sensitized films also show high absorbance corresponding to an optical density of about 1.5 - 2 around 500 nm.

To investigate the injection properties of ID889, sensitized alumina and titania films were used for optical spectroscopy measurements. From the short-time (fs - ps) TA measurements of ID889 adsorbed on alumina (**Sample 1**), only two features, the ground state bleaching (GSB) and photoinduced absorption were observed, separated by a clear isosbestic point at 550 nm. The lifetime of the dye's excited state significantly changed from 3.2 ns to 1.4 ns when Li-TFSI was used on the alumina film (**Sample 2**), since ID889 interacts strongly with the Li cation rather than showing electronically inactive properties as in **Sample 1**. Therefore, we are able to observe the absorption of an intramolecular/interfacial charge transfer state. Highly localized charge distribution and a larger Stokes shift in polar solvents and Li-treated films originate from a larger dipole moment in the excited state than in the ground state.

The short-delay TA measurements of ID889 adsorbed on titania (**Sample 4**) mainly show two distinct features, i.e. GSB and photoinduced absorption (PIA) of the primary photoexcitation. The absorption of the dye cation in **Sample 4** was not clear from the short-delay measurement, but it emerges in the long-delay TA measurements (ns –  $\mu$ s) and the quasi-steady-state PIA measurements (ns –  $\mu$ s) that allowed monitoring of long-lived charges. For ID889 adsorbed on titania treated with Li cations (**Sample 5**), the absorption feature of the dye cation molecule became prominent even on pico-second timescales in short-delay TA measurements and the presence of the dye cation was supported by the observation of non-geminate recombination of free charge carriers from fluence dependent long-delay measurements. Hence, Li-TFSI salts not only facilitate electron injection, but also suppress a recombination channel. This can be seen from the decay dynamics of the dye cation in **Sample 4** and **5** showing lifetimes of 3 and 2800 ps, respectively.

The role of Li-TFSI in a device-like sample is critical. In a device-like sample (**Sample 6**), the absorption of the primary excitation was no longer observed in the short-delay measurements owing to ultrafast charge injection and the dye cation absorption disappeared in the long-delay measurements owing to efficient regeneration by spiro-OMeTAD. A device-like sample without Li cation additive (**Sample 7**) showed a rise of the oxidized hole conductor signal only up to 10 ps, whereas the signal increased up to 200 ns in **Sample 6**. This is in line with the observation of the exciton and dye cation signal from **Sample 7** in the long-delay measurements due to inefficient injection. This implied that only a small amount of free charge carriers was generated in **Sample 7** and they were short-lived or recombination outperformed regeneration.

For an ID889 blend with spiro-OMeTAD (**Sample 8**), a rise of a signal originating from a hole transfer in the NIR TA measurements was observed. However, when Li-TFSI salt was used in ID889-sensitized films, ID889 showed strong CT states on an alumina layer i.e. a device-like structure on alumina (**Sample 3**) or promoted injection into a titania layer in **Sample 5** and **6**. The similar decay dynamics of the exciton in **Samples 4, 5, and 6**, with lifetimes of 200-300 ps, indicated that ID889 injected electrons from the dye's excited state rather than by formation of dye anions after a preceding hole transfer process to spiro-OMeTAD.

With the advantageous properties of ID889 described above, the best solid-state ID889 DSCs exhibited an efficiency of 4.5 %, exceeding the best efficiency of 3.2 % in solid-state DSCs using perylene derivatives, reported to date. Owing to the excellent injection properties of ID889, the device showed a short circuit current of 7.5 mA·cm<sup>-2</sup> and the external quantum efficiency reached 75 % around 500 nm. However, the absorption range is limited, unfortunately harvesting a relatively small amount of solar photons.

In summary, for efficient photovoltaic devices, addition of Li-TFSI is crucial and important to generate and stabilize free charge carriers, as well as to regenerate oxidized dye molecules, although

the dye can inject without the aid of Li cations. In addition, direct injection from the dye's excited states rather than by a preceding hole transfer appears to make the ID889 devices efficient.

## 6. CYCLOPENTADITHIOPHENE (CPDT) BUILDING BLOCK DYES

D- $\pi$ -A type organic dyes using cyclopentadithiophene (CPDT) moieties as bridging units have shown excellent efficiencies, up to 10 %, when they are used with a cobalt (II/III) electrolyte as a redox mediator and efficiencies of 3 % in solid-state DSCs using spiro-OMeTAD, respectively <sup>[101-103]</sup>.

Here, the photophysical properties of novel D- $\pi$ -A type organic dye molecules that consist of a CPDT bridging unit with four different donor moieties are investigated. Changes in lifetimes of excited states and injection efficiencies in the presence and absence of Li cations are studied to get insight into the charge injection properties and results from quasi-steady-state photoinduced absorption and transient absorption experiments are correlated to changes in the power conversion efficiency.

### 6.1. Materials and samples

Four novel CPDT dye molecules are investigated, namely FPH224, 231, 233, and 303. FPH224, 231, and 233 consist of cyanoacrylic acid as an acceptor (anchor) unit, a cyclopentadithiophene (CPDT) moiety as a bridging unit, and triphenylamine-based moieties as a donor unit. FPH303 has the same molecular structure as FPH224 but with a different anchor group, namely rhodanine-3-acetic acid. The cyanoacrylic acid is used to withdraw electrons from the donor building block and triphenylamine is used as donor as it is electron-rich. The  $\pi$ -conjugated CPDT bridging-unit not only plays a role in the charge transfer from the donor to the acceptor, but also contributes to photon harvesting. The molecular structures of the four CPDT dye molecules are shown in Figure 6-1 (a).

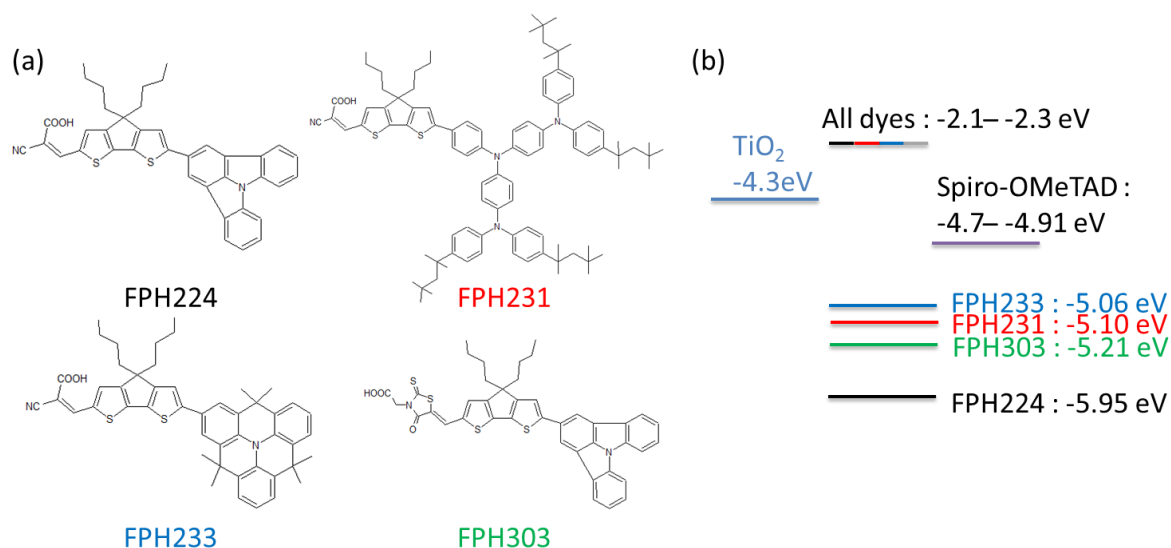
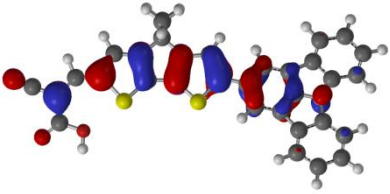
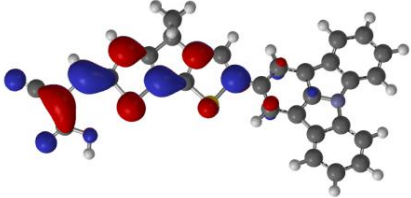
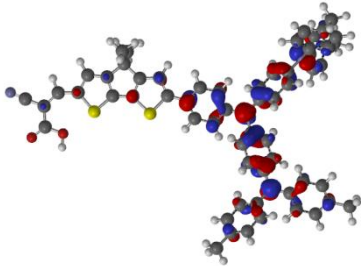
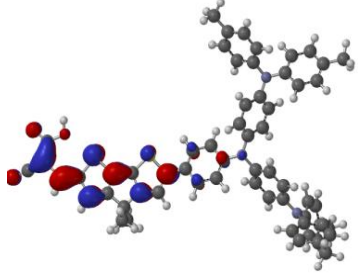
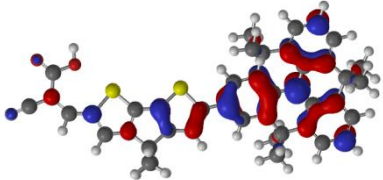
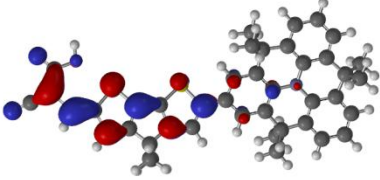
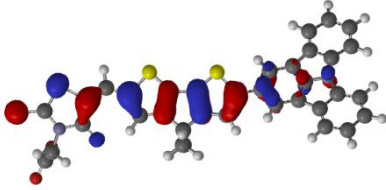



Figure 6-1. Molecular structures of FPH 224, 231, 233, and 303 (a), and the HOMO levels measured by cyclic voltammetry (b).

Table 6-1. Calculated orbital surfaces and HOMO/LUMO energies of the FPH series of dye molecules.

	HOMO	LUMO
FPH224	 - 5.35 eV	 -2.63 eV
FPH231	 -4.62 eV	 -2.55 eV
FPH233	 -4.95 eV	 -2.63 eV
FPH303	 -5.18 eV	 -2.69 eV

In Figure 6-1 (b), the highest occupied molecular orbital (HOMO) levels of the 4 dye molecules are also presented, which were obtained by cyclic voltammetry (CV) on dye solutions in which platinum electrodes were used and the field was scanned at a rate of 100 mV/s. The HOMO levels of the FPH dye series appear to be lower than the HOMO level of spiro-OMeTAD, allowing regeneration. However, these energy levels may not be suitable for a redox process in a liquid-state dye-sensitized solar cell using a cobalt electrolyte which has a potential energy of 5.2-5.4 eV. Unfortunately, pronounced peaks (representing LUMO levels) in the reduction wave of the CV measurements were not observed, but we could approximate the LUMO levels from the onset of absorption in solution and films. The LUMO levels of the dye molecules are much higher than the conduction band of titanium

dioxide, ranging from 2.1 to 2.3 eV. The energy levels of the transparent conductive oxide (TCO), TiO<sub>2</sub>, spiro-OMeTAD, and the silver electrode are found elsewhere<sup>[137-142]</sup>.

Orbital surfaces and energy levels of the HOMO/LUMO are calculated by density functional theory (B3LYP 6-31G) and are shown in Table 6-1. FPH224 shows the lowest lying HOMO level, however shifted by 0.6 eV compared to the experimental data, whereas FPH303 and 233 exhibit fairly similar HOMO levels compared to the CV measurements. The HOMO level of FPH231 is 0.4 eV lower than that of the CV measurement. We note that FPH231 and 233 show fairly localized charge distributions in the donor moiety (HOMO) and in the acceptor moiety (LUMO), thus good injection properties can be expected. In addition, it is observed that wavefunctions in the LUMO level of FPH224 are localized at the cyanoacrylic acid acceptor, but those in the LUMO level of FPH303 are localized at rhodanine-3-acetic acid. Hence, injection from FPH303 is expected to be less favorable than that from FPH224.

The samples for device fabrication and for optical spectroscopy were prepared as described in the experimental section 3.1. For solution measurements, a 0.1 mM dye solution was prepared. The sensitization of metal oxide films was carried out at 40°C for 15 hours in tetrahydrofuran (THF). For device fabrication, the small molecule hole transporter spiro-OMeTAD is used to regenerate the oxidized dye molecules and Li-TFSI and *t*BP are used to optimize the photocurrent and the photovoltage in the device, respectively.

## 6.2. Dyes in solution

### 6.2.1. Absorption and emission spectra

The FPH series of dye molecules shows high molar extinction coefficients in tetrahydrofuran (THF) of 50000 M<sup>-1</sup>cm<sup>-1</sup> at 463 nm for FPH224, 45000 M<sup>-1</sup>cm<sup>-1</sup> at 500 nm for FPH231, 55000 M<sup>-1</sup>cm<sup>-1</sup> at 473 nm for FPH233, and 43000 M<sup>-1</sup>cm<sup>-1</sup> at 522 nm for FPH303, which are at least three times higher than those of the Ru(II) complex dye Z907 (13000 M<sup>-1</sup>cm<sup>-1</sup> at 520 nm) that is used as a reference dye for solid-state DSCs.

In this section, the steady-state absorption and time-resolved photoluminescence emission spectra of 4 dyes in solvents of different polarity are investigated, giving insight into changes in dipole moments between ground state and excited state as described in Chapter 4.4.

Figure 6-2 shows normalized absorption and emission spectra of 0.1 mM dye solutions using toluene (TLN) and tetrahydrofuran (THF). TLN and THF are deliberately selected for their difference in polarity. When the polarity of water is set to 1, the polarities of TLN and THF are 0.099 and 0.207, respectively. Generally, the absorption spectra of the four dyes in THF are similar, but those in TLN



significantly differ depending on the dyes. In each panel, the darker and paler lines represent the less polar solvent TLN and the more polar solvent THF, respectively.

When dye molecules are dissolved in solvents, the dipoles of dye and solvent molecules interact with each other: the dipoles of the solvent molecules orient around the photoexcited state of dye molecules. The internal relaxation of energetically high vibrational states generated upon excitation of the dye molecules occurs on a fs timescale. Therefore, the Stokes shift in a non-polar solvent is determined by the energy difference of the vibrational states involved in absorption and emission. In a more polar solvent, a larger Stokes shift is observed due to the larger orientation polarizability of the solvent that consists of both solvent reorientation and electronic redistribution (electronic transition) of the solvent molecules. Electronic transitions are much faster than the solvent reorientation around excited dye molecules, which leads to shifts of emission spectra in more polar solvents.

The absorption/emission spectra of FPH224 and FPH233 exhibit similar changes as shown in panel (a) and (c). FPH224 in TLN peaks at 422 nm in the absorption spectrum and at 537 nm in the emission spectrum, showing a Stokes shift of 115 nm, while FPH233 peaks at 406 nm in the absorption and at 547 nm in the emission spectrum, exhibiting a Stokes shift of 146 nm. The Stokes shift becomes slightly larger in the more polar solvent, i.e. 130 nm for FPH224 in THF and 157 nm for FPH233 in THF.

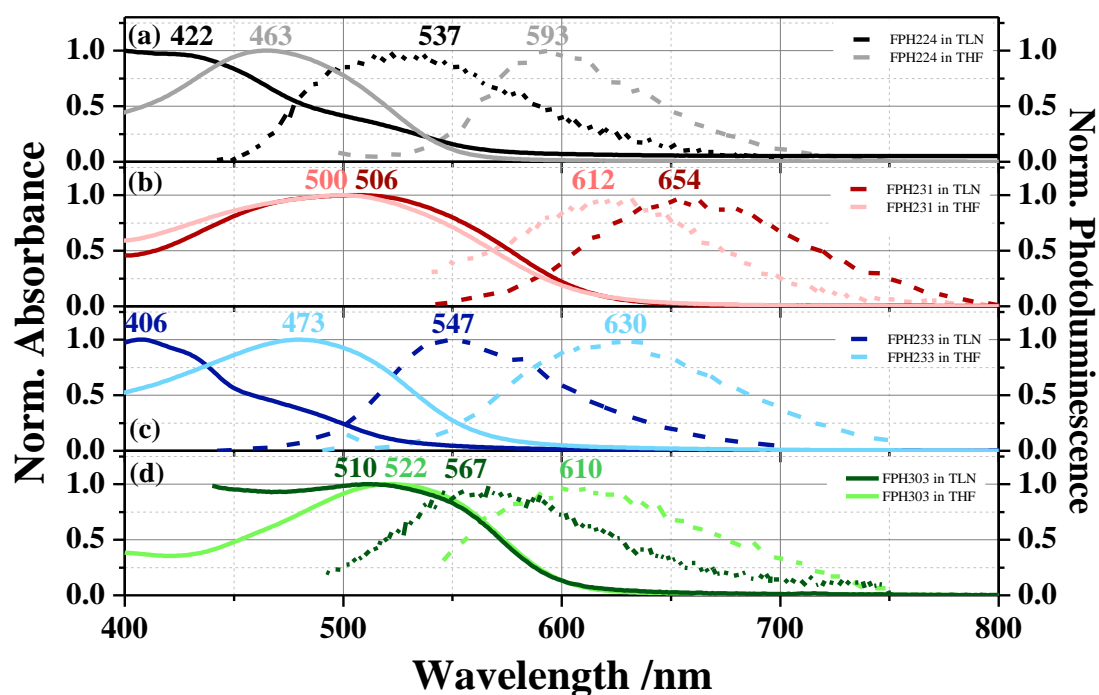


Figure 6-2. Normalized absorption and emission spectra of 0.1 mM FPH224 (panel a, black), 231 (panel b, red), 233 (panel c, blue), and 303 (panel d, green) in the less polar solvent TLN (dark) and in more polar solvent THF (pale).

Interestingly, the FPH231 dye in solution shown in panel (b) blue-shifts as the solvent polarity increases indicating a negative solvatochromism, since the absorption peak changes from 506 nm (less polar TLN) to 500 nm (more polar THF) and the emission from 654 nm (TLN) to 612 nm (THF). It implies that the dipole moment of FPH231 may be more stabilized in the ground state than in the excited state, presumably leading to unfavourable injection properties in DSCs. This is further analyzed in Chapter 6.4 by means of PIA spectroscopy.

FPH303 shown in panel (d) exhibits a positive solvatochromic shift as the solvent polarity increases, and the Stokes shift in the more polar solvent is much larger (from 522 nm to 610 nm) than that in the less polar solvent (from 510 nm to 567 nm). Given the increased Stokes shift in more polar solvents, FPH303 is, therefore, expected to have larger dipole moment in the excited state than in the ground state. In addition, as expected, the absorption spectra of FPH303 red-shift further compared to FPH224 due to the introduction of the rhodanine 3-acetic-acid acceptor group.

The LUMO levels can be derived from onsets of the absorption and emission spectra, revealing 2.28 eV for FPH224, 2.17 eV for FPH231, 2.24 eV for FPH233, and 2.20 eV for FPH303 when the emission spectra of the four dye solutions in THF are used. The LUMO levels of the four dyes seem to be located high enough to be able to inject electrons into the conduction band of titania as schematically shown in 6-1 (b).

### 6.2.2. Decay dynamics

Figure 6-3 shows decay transients of the four dyes in solvents of different polarity. For detection of PL dynamics, time-resolved photoluminescence (PL) Streak Camera measurements were carried out. In the less polar solvent TLN, FPH224 shows the longest PL lifetime of 2.6 ns, whilst FPH231 and 303 show the shortest lifetimes of 1.3 ns. The PL lifetime of FPH233 is determined to be 2.0 ns. Originally, FPH303 is designed to spatially localize charge density on the donor and acceptor moieties by employing electron-withdrawing atoms, but it appears that the additional rhodanine-3-acetic acid ring significantly decreases the PL lifetime from 2.6 ns to 1.3 ns in FPH224.

For the fitting of the dynamics, a stretched-exponential decay is used and amplitude and offsets are set to 1 and 0, respectively. The fitting parameters are summarized in Table 6-2.

Table 6-2. Parameters of stretched-exponential decay fitting in 4 CPDT dye solutions in TLN.

	A	$y_0$	$\beta$	$\tau$ /ns
FPH224	1	0	0.77927	2.60
FPH231	1	0	0.81783	1.29
FPH233	1	0	0.93401	2.02
FPH303	1	0	0.80042	1.31

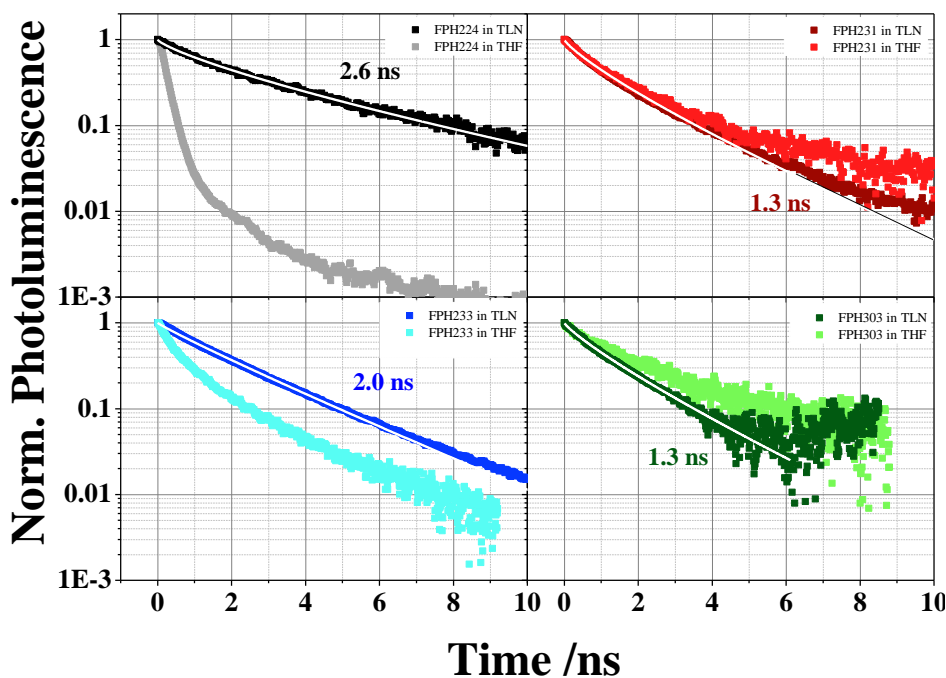


Figure 6-3. Photoluminescence decay transient of 0.1 mM FPH224 (black), 231 (red), 233 (blue), and 303 (green) solutions in a polar solvent (darker lines, THF) and in a less polar solvent (lighter lines TLN). The solid lines correspond to stretched-exponential fits.

In the more polar solvent THF, FPH224 and 233 explicitly show a faster decay than in TLN solutions, whereas FPH231 and 303 show slower or similar decay transients than in TLN. The faster decay of FPH224 and 233 in THF presumably originates from enhanced non-radiative decay channels since a decreased photoluminescence quantum efficiency (PLQE) is also observed for the two dye molecules. The measurements in solvents of different polarity enable us to predict the influence of Li-TFSI on films that significantly affect the injection properties. More polar solvents may create similar environments as in Li-treated samples. Hence, FPH224 and 233 are expected to have significantly decreased lifetimes on Li-treated alumina surfaces compared to samples without Li cations, whereas FPH231 and 303 are expected to show similar or slightly decreased lifetimes on Li-treated alumina surfaces.

### 6.3. Films

#### 6.3.1. Absorption and Emission spectra

The FPH series of dye molecules are expected to show high photocurrents in devices due to high absorbance. Most dye molecules in solution seemed to show sufficient lifetimes of the excited states to inject electrons into the conduction band of titania as shown in the previous section. However, the lifetime can be reduced by impediments such as adsorption mode/direction of the dye molecules or

interactions between dye molecules. Therefore, transient decay rates from films and the influence of the addition of a Li cation additive, which is critical for electron injection, need to be considered to correlate device performance to photophysical properties.

As explained in Chapter 4 and 5, a Li-TFSI additive is often used in DSCs to facilitate electron injection by lowering the conduction band of TiO<sub>2</sub>. Li cations that reside inside the TiO<sub>2</sub> nanoparticles or at the surface of TiO<sub>2</sub> create a polar environment around the dye molecules, so that negative charges in the acceptor moiety of the dye molecule become favorable for electron injection.

Figure 6-4 shows normalized absorption and emission spectra of 4 dye molecules adsorbed on a TiO<sub>2</sub> surface in the absence (black, red, blue, and green lines) and absence (gray, pink, sky blue, yellow-green lines) of Li cations. When the Li-TFSI salt is employed in films, FPH224, 233, and 303 show a larger Stokes shift as shown in panel (a), (b), and (d), respectively. This indicates that these dye molecules have a larger dipole moment in the excited state than in the ground state, leading to a more favorable injection process. FPH224 and 303 show similar Stokes shifts, but the absorption and emission spectra of FPH303 red-shift further compared to FPH224 due to the rhodanine-3-acetic acid anchoring group. Red-shifted absorption and emission spectra after application of Li cations are related to the Stark effect that causes shifts of the energy levels of the dye. As explained in Chapter 4 and 5, injected electrons can induce local electric fields, and the orientation of the induced electric field and the dipole moment of the dye molecules determine the shift of absorption/emission spectra depending on their directions. Therefore, shifted absorption and emission spectra provide information about the dipole moment.

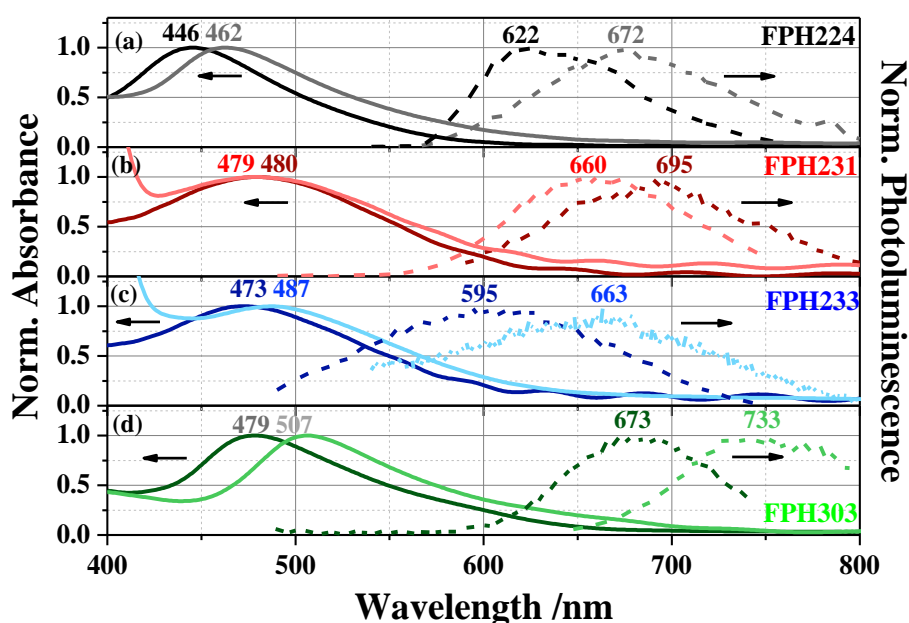


Figure 6-4. Normalized absorption and emission spectra of FPH224 (panel a), 231 (panel b), 233 (panel c), and 303 (panel d) adsorbed on titania in the presence (black, red, blue, and green lines) and absence (gray, pink, sky blue, yellow-green lines) of Li cations.

As expected from the solution measurements, the absorption and emission spectra of FPH231 blue-shift with the addition of Li cations due to a more stabilized dipole moment in the ground state than in the excited state: from 480 nm to 479 nm in absorption spectra and from 695 nm to 660 nm in emission spectra. This is because Li cations create similar conditions to the excited state by creating a polar environment around the dye molecules.

From the maximum of the 0-0 transitions of the film measurement, the LUMO levels of dye molecules are determined to be around -3.0 – -3.9 eV which is still high enough to inject electrons into the conduction band of titania.

### 6.3.2. PL dynamics

In this section, the PL lifetimes of the dyes on films are discussed. The mean-lifetime is recorded with a Streak camera system and for all samples in the experiment, the same excitation fluence of 0.5 mW and measurement parameters are used to compare the PL intensities. The dye molecules are adsorbed on alumina and titania surfaces to distinguish the intrinsic lifetime on metal oxide particles from alternations caused by electron injection into titania.

Figure 6-5 (a) shows the normalized photoluminescence decays of the dye molecules adsorbed onto an alumina surface in the absence (full squares) and presence (hollow squares) of Li-TFSI. The dye molecules show lifetimes, which decreased from nanoseconds in solution to picoseconds, when they are adsorbed on metal oxide nanoparticle films.

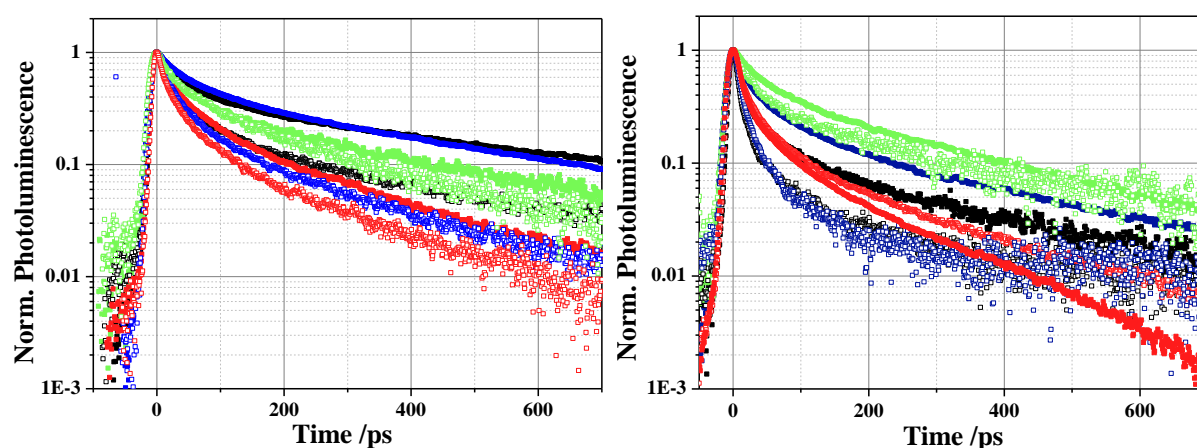


Figure 6-5. Normalized photoluminescence decay of (a) FPH224 (black), 231 (red), 233 (blue), and 303 (green) on alumina in the absence (full) and presence (hollow) of Li-TFSI, and (b) FPH224, 231, 233, and 303 on titania in the absence (full) and presence (hollow) of Li-TFSI.

Table 6-3. Stretched-exponential PL fitting parameters of the FPH series of dye molecules on Al<sub>2</sub>O<sub>3</sub>.

Dye	Condition	A	y <sub>0</sub>	β	τ /ps
FPH224	Without Li	1	0	0.46546	118.88
	<b>With Li</b>	<b>1</b>	<b>0</b>	<b>0.4814</b>	<b>43.30</b>
FPH231	Without Li	1	0	0.58943	50.48
	<b>With Li</b>	<b>1</b>	<b>0</b>	<b>0.5759</b>	<b>31.23</b>
FPH233	Without Li	1	0	0.5635	143.02
	<b>With Li</b>	<b>1</b>	<b>0</b>	<b>0.58338</b>	<b>41.41</b>
FPH303	Without Li	1	0	0.51681	80.47
	<b>With Li</b>	<b>1</b>	<b>0</b>	<b>0.57884</b>	<b>75.06</b>

FPH224 (black) and 233 (blue) on Al<sub>2</sub>O<sub>3</sub> show relatively long lifetimes of the excited states of 143 ps and 118 ps compared to FPH303 (green) and FPH231 (red) on Al<sub>2</sub>O<sub>3</sub>, exhibiting lifetimes of 80 ps and 50 ps, respectively. The lifetimes are significantly reduced compared to solution measurements, but the longer lifetime of FPH224 and 233 are consistent with the PL decays in solution as shown in Figure 6-3. Furthermore, by addition of Li cations, the dye molecules (data shown as hollow squares in Figure 6-5 (a)) show similar transient decays as in solution measurements, when the more polar solvent THF is used.

The four different dye molecules can be divided into two groups: Li-active FPH224 and 233 and Li-inactive FPH231 and 303. This can be due to different intramolecular/interfacial charge transfer (ICT) states, leading to different sensitivity to Li cations. When Li cations are added to alumina, FPH224 and 233 show a much stronger decrease in PL lifetime than FPH231 and 303 likewise the solution measurements. The lifetimes of FPH224 and 233 are changed from 118 ps to 43 ps and from 143 ps to 41 ps, respectively, whereas FPH231 and 303 show mere changes from 50 ps to 31 ps and from 80 ps to 75 ps.

The lifetimes are obtained by using stretched-exponential decay fits with an amplitude of 1 and an offset of 0, and the detailed parameters are summarized in Table 6-3.

The dye molecules can inject electrons into the conduction band of titania when they are adsorbed on titania and photoexcited. Upon addition of Li cations to the TiO<sub>2</sub> surface, the Li cations activate TiO<sub>2</sub> and more dyes can participate in the injection process. Since the injection typically takes place on an ultrafast timescale, the emission presumably originates from non-injecting dye molecules.

The normalized PL decays of the four dyes adsorbed onto titania in the absence (closed squares) and presence (open squares) of Li cations are shown in Figure 6-5 (b). Interestingly, FPH224 (black) and 233 (blue) show relatively significant changes in PL lifetimes when a gamma function is used <sup>[94, 104]</sup>, i.e. for FPH224 from 44 ps to 18 ps and for FPH233 from 86 ps to 19 ps, however, FPH231 and 303 hardly show any change in the decay rates after addition of Li cations, i.e. for FPH231 from 35 ps to 42 ps and for FPH303 from 143 ps to 115 ps. Unlike the stretched-exponential fitting, varying exponents ( $\beta$ ) are considered in a gamma function to derive the PL lifetimes of each dye and to compare the dyes. The lifetimes obtained from the gamma function show a clearer effect of the addition of Li cations than stretched-exponentials fits. The stretched-exponential fitting parameters and PL lifetimes are summarized in Table 6-3.

This implies that a large amount of Li cation-active sites is present in FPH224 and 233, whereas FPH303 exhibits a smaller amount of Li cation-active sites. As another possibility, FPH303 may already inject electrons on an ultrafast timescale in the absence of Li and thus has only few Li cation-active sites. If the dye injects electrons on an ultrafast timescale even without Li cations then, the amplitude should not change; however, small change after the use of Li cations is observed compared to the sample without Li cations as shown in Figure 6-8. Furthermore, transient absorption spectra of FPH303 on TiO<sub>2</sub> without Li cations are rather similar to those of FPH303 on Al<sub>2</sub>O<sub>3</sub> without Li cations (that mainly shows the absorption of the exciton) as shown in Figure 6-18 (a and b), indicating that the injection does not take place in FPH303 on TiO<sub>2</sub>. Further results will be discussed in chapter 6.5.3. It is thus more likely that the injection from FPH303 is not favorable, as FPH303 shows a relatively long lifetime even after Li cation application as shown in Figure 6-5. For FPH231, the lifetime of the excited state slightly increases after the use of Li cations, which is due to a less stabilized dipole in the excited state.

Table 6-4. Stretched-exponential fitting parameters of FPH series dye molecules on TiO<sub>2</sub>.

		A	y <sub>0</sub>	$\beta$	$\tau$	$\tau$ (gamma F)
FPH224	Without Li	1	0	0.47659	22.13	44.83
	<b>With Li</b>	<b>1</b>	<b>0</b>	<b>0.66293</b>	<b>13.91</b>	<b>18.60</b>
FPH231	Without Li	1	0	0.65493	25.92	35.12
	<b>With Li</b>	<b>1</b>	<b>0</b>	<b>0.58075</b>	<b>27.09</b>	<b>42.59</b>
FPH233	Without Li	1	0	0.53597	49.05	86.98
	<b>With Li</b>	<b>1</b>	<b>0</b>	<b>0.79912</b>	<b>17.44</b>	<b>19.77</b>
FPH303	Without Li	1	0	0.61528	98.41	143.40
	<b>With Li</b>	<b>1</b>	<b>0</b>	<b>0.51125</b>	<b>65.92</b>	<b>115.11</b>

### 6.3.3. Injection Efficiency (IE)

The lifetimes obtained above simply represent the inverse decay rates of the fluorescence, but they are not strictly connected to the number of emitted photons. As an example, FPH303 exhibits similar lifetimes before and after employing Li cations on the TiO<sub>2</sub> surface as shown in Figure 6-5 (b), however, there is a significant change in the number of emitted photons. Hence, we need to determine the quantum/injection efficiency by comparing the number of emitted photons of the samples, which is possible, as the intensity of excitation and the parameters of the MCP, the average number of shots, and the exposure time are kept constant to all measurements as described above. As an approximation, we exclude non-radiative decay channels in the dye molecules and assume that the number of the dyes' excited states upon excitation does not change.

Figure 6-6 shows the PL intensities of the samples as a function of the decay time (picoseconds) after excitation at 400 nm at a fluence of 0.5 mW. Panel (a) shows the PL intensity of dyes on a Al<sub>2</sub>O<sub>3</sub> surface (solid lines, no injection) compared to a TiO<sub>2</sub> surface (dotted lines, injection possible), which provides an estimate of how efficiently the dye can inject electrons into TiO<sub>2</sub> by integrating each graph. Interestingly, FPH231 shows the highest injection efficiency (IE) among the dye molecules with 97 % ( $97\% = (1 - 21989/889709)*100$ ) although the lifetime changes little from 50 ps on Al<sub>2</sub>O<sub>3</sub> to 25 ps on TiO<sub>2</sub>. The integration of each dye's PL intensity is summarized in Table 6-5. FPH224, 233, and 303 exhibit an IE of 92% ( $92\% = (1 - 35605/442174)*100$ , lifetime changes from 118 ps on Al<sub>2</sub>O<sub>3</sub> to 22 ps on TiO<sub>2</sub>), 81 % ( $81\% = (1 - 199306/1023354)*100$ , lifetime changes from 143 ps on Al<sub>2</sub>O<sub>3</sub> to 49 ps on TiO<sub>2</sub>), and 63 % ( $63\% = (1 - 40049/106791)*100$ , lifetime changes from 80 ps on Al<sub>2</sub>O<sub>3</sub> to 98 ps on TiO<sub>2</sub>), respectively.

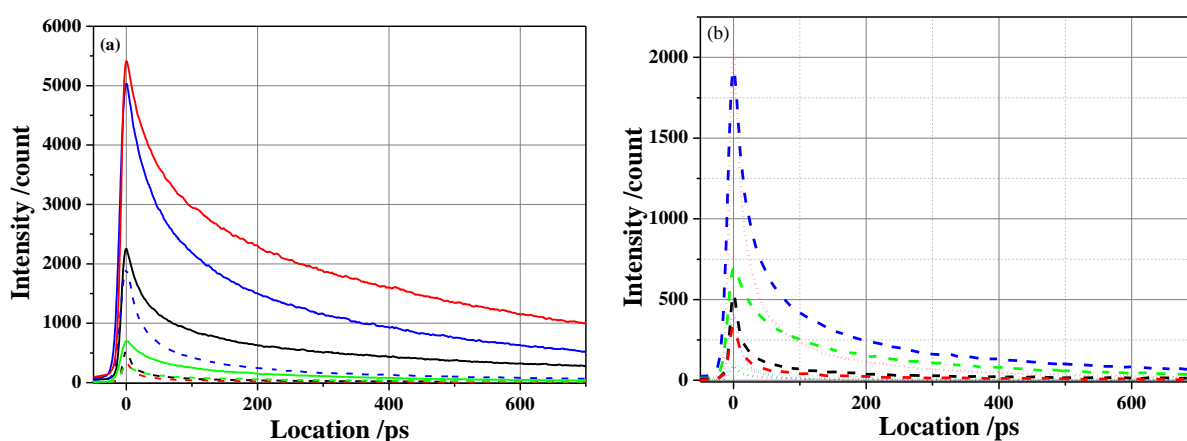


Figure 6-6. Photoluminescence decay curves of (a) FPH224 (black), 233(blue), and 303 (green) on Al<sub>2</sub>O<sub>3</sub> (solid lines) and on TiO<sub>2</sub> (dashed lines), and of (b) dye molecules on TiO<sub>2</sub> in the absence (dashed lines) and presence (dotted lines) of Li cation.



Table 6-5. The integrated number of photons emitted from dyes on film surfaces.

PL Intensity	FPH224	FPH231	FPH233	FPH303
On Al <sub>2</sub> O <sub>3</sub>	442174	889709	1023354	106791
On TiO <sub>2</sub>	35605	21989	199306	40049
Li treated TiO <sub>2</sub>	5934	117371	10688	14075

By application of Li cations as shown in panel (b) in Figure 6-6, the dye molecules reveal some interesting details of the injection process. As pointed out above, we observe PL mainly from the dye molecules that do not take part in the injection process, therefore, the IEs in Figure 6-6 (b) depend on the Li cation-active states of the dye molecules. FPH233 shows the highest IE of 95 % ( $95 \% = (1 - 10688/199306)*100$ ), followed by FPH224 with an IE of 84 % ( $84 \% = (1 - 5934/35605)*100$ ) whereas FPH303 shows a low IE of 65 % ( $65 \% = (1 - 14075/40049)*100$ ). Surprisingly, when the Li cation additive is used, more photons are emitted in case of FPH231 on TiO<sub>2</sub>, leading to a reduced injection efficiency of approximately 11 %. This is due to different Li cation-active states compared to the other dye molecules, causing unfavorable injection. To simply compare the PL from Li-cation-treated-TiO<sub>2</sub> surfaces with those of Al<sub>2</sub>O<sub>3</sub> surfaces, FPH224 and 233 show injection efficiencies close to unity (For 224:  $98.6 \% = (1-5934/442174)*100$ , For 233:  $99 \% = (1-10688/1023354)*100$ ), whilst FPH231 and 303 show an injection efficiency of 87 % (For FPH231:  $87 \% = (1-117371/889709)*100$ , For FPH303:  $87 \% = (1-14075/106791)*100$ ). In this sense, FPH224 and 233 are considered to inject electrons into TiO<sub>2</sub> nanoparticles more efficiently and furthermore to possess more Li cation-active states; however, it seems that some of the states in FPH231 and 303 do not contribute to injection even after the addition of Li cations. Therefore, the devices using FPH224 and 233 are expected to achieve higher photocurrents than the devices using FPH231 and 303.

#### 6.4. Device Characteristics and Photoinduced Absorption (PIA) experiments

In this chapter, the device performance is reported and photocurrents of devices are set into relation to the previously explained changes of the dipole moments and the enhanced injection efficiency (IE) after application of Li cations. Furthermore, the role of long-lived charges observed by photoinduced absorption (PIA) spectroscopy is investigated.

##### 6.4.1. J-V curves and EQE

Solid-state dye-sensitized solar cells (DSCs) were fabricated as described in Chapter 3.1.1. Figure 6-7 (a) shows the J-V curves of solid-state DSCs containing FPH224 (black), 231 (red), 233 (blue), 303 (green), and Z907 (purple) measured under solar illumination of AM 1.5 G. For comparison, devices

were all fabricated in the same batch. A reference device using the ruthenium complex Z907 exhibits the best power conversion efficiency of 1.8 % with a short circuit current of  $3.31 \text{ mA}\cdot\text{cm}^{-2}$ , an open circuit voltage of 860 mV, and a high fill factor of 63 %. Among the CPDT dyes, FPH233 shows the best efficiency of 1.67 % followed by FPH224 with 1.56 %, and FPH233 and 224 exhibit higher short circuit currents than the photocurrent in the reference device, of  $3.93$  and  $3.75 \text{ mA}/\text{cm}^2$ , respectively. Good injection properties of FPH224 and 233 are expected due to enhanced ICT properties, long excited state lifetimes, and higher IE than FPH231 and 303 as reported in the previous chapter. The photophysical properties of FPH231 such as the negative solvatochromism, which is unfavorable for electron injection, appear to play a critical role for the photocurrents of devices. Furthermore, FPH303 showing a large fraction of Li cation-inactive sites in turn shows a reduced short circuit current in devices. The detailed photovoltaic parameters of the devices obtained from their J-V curves are summarized in Table 6-6.

Figure 6-7 (b) shows the external quantum efficiencies of 4 different devices and in the inset the internal quantum efficiencies are shown. Both FPH224 and 233 reach about 30% EQE and IQE, whereas FPH231 and 303 reach only 10 - 13 % EQE and 11 - 17% IQE, respectively. These numbers are comparable to the ratio of the photocurrents measured in the devices and the maximum obtainable photocurrent calculated from the absorption of the sensitized films assuming 100% IQE.

The maximum obtainable short circuit currents are  $12.6 \text{ mA}/\text{cm}^2$  for FPH224,  $12.2 \text{ mA}/\text{cm}^2$  for FPH231,  $13.5 \text{ mA}/\text{cm}^2$  for FPH233, and  $14.8 \text{ mA}/\text{cm}^2$  for FPH303 when the internal quantum efficiency is considered to be unity. However, only 30%, 20%, 29%, and 10% of the expected short circuit currents are measured in devices with FPH224, 231, 233, and 303, respectively. Likely reasons for this reduction are loss channels such as incomplete pore filling and recombination between injected electrons and oxidized dye/hole conductor molecules in the device.

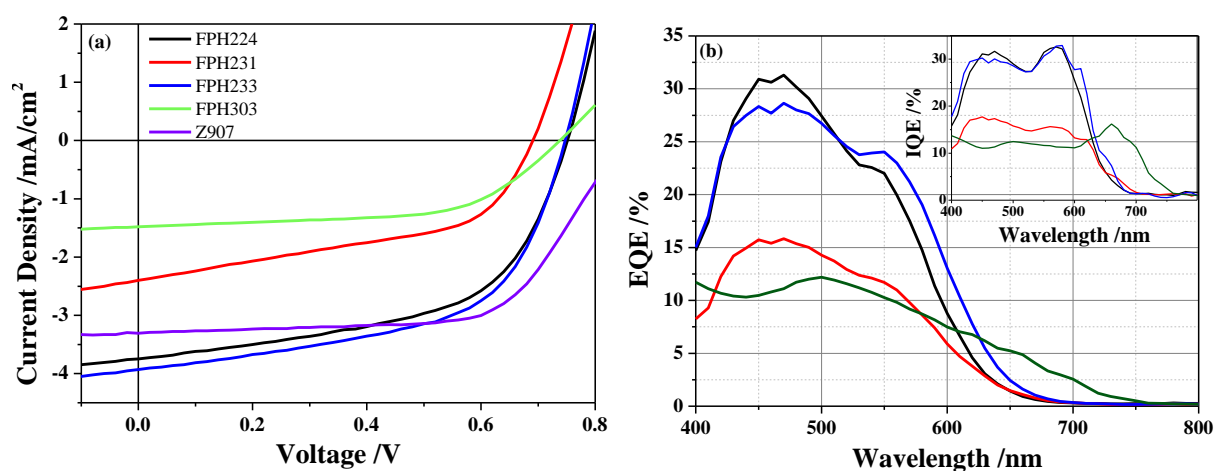


Figure 6-7. (a) J-V curves of solid-state DSC using FPH224 (black), 231 (red), 233 (blue), 303 (green), and Z907 (purple) measured under  $100 \text{ mW}/\text{cm}^2$  AM 1.5 G solar intensity and (b) external quantum efficiency of each device.

Table 6-6. Photovoltaic parameters of the devices obtained from their J-V curves.

	$V_{OC} / V$	$J_{SC} / \text{mA}/\text{cm}^2$	FF	Efficiency /%
Z907	0.86	3.31	0.63	1.80
FPH224	0.76	3.75	0.54	1.56
FPH231	0.70	2.40	0.48	0.82
FPH233	0.74	3.93	0.57	1.67
FPH303	0.74	1.48	0.59	0.65

For FPH303, it is clear from the IQE measurements that photons are collected from redder spectral regions than for FPH224, however with a lower efficiency. In fact, FPH303 exhibits the lowest EQE and IQE values. This will be further studied by transient absorption measurements demonstrated in Chapter 6.5.

#### 6.4.2. Quasi-steady-state Photoinduced Absorption (PIA) experiments

Quasi-steady-state photoinduced absorption measurements were carried out to investigate long-lived species such as charges, which have a direct influence on the performance of each device.

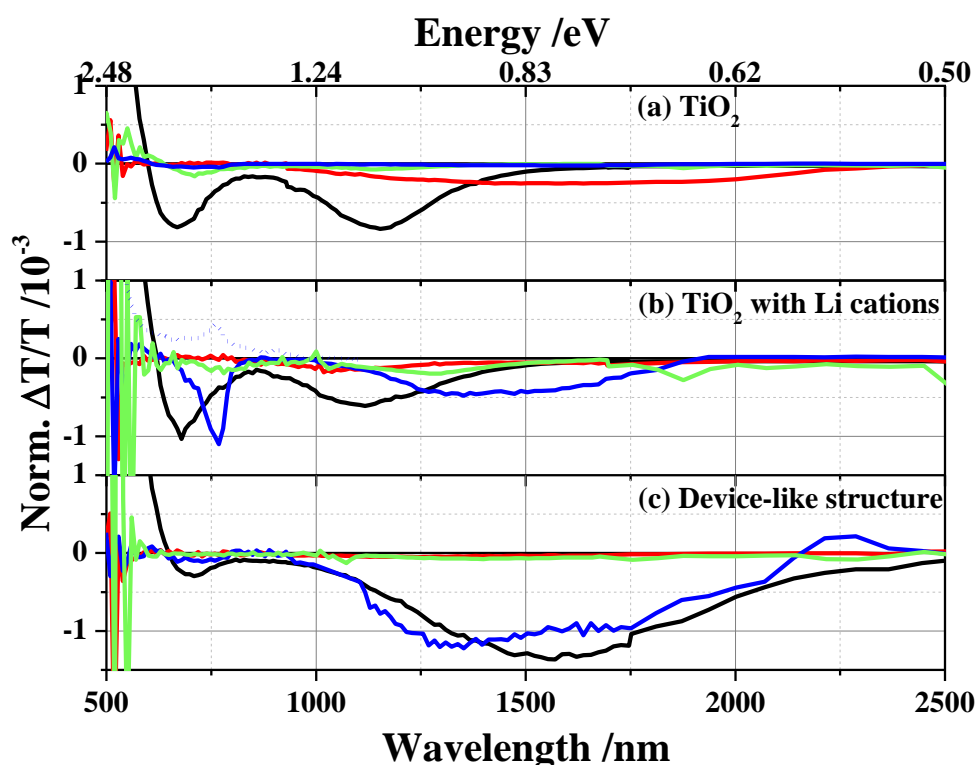


Figure 6-8. Quasi-steady-state photoinduced absorption spectra of FPH224 (black), FPH231 (red), FPH233 (blue), and FPH303 (green) adsorbed on  $\text{TiO}_2$  (a), of the four dye molecules on  $\text{TiO}_2$  after application of Li cations (b), and in device-like structures (c). The samples were excited at 530 nm with high power LED.

Figure 6-8 shows the PIA spectra obtained from the dye molecules on TiO<sub>2</sub> (panel a), the dyes on TiO<sub>2</sub> after application of the Li additive (panel b), and in device-like structures on TiO<sub>2</sub> (TiO<sub>2</sub>/dye/spiro-OMeTAD + Li-TFSI + *t*BP). The samples were excited at 530 nm by a green LED and all data were normalized to the absorbance of each sample at the excitation wavelength. FPH224, 231, and 233 show positive signals up to 530 nm and FPH303 up to 640 -660 nm, which are probably due to a Stark effect, and broad negative signals from oxidized dye and hole conductor up to the infrared region.

In panel (a), FPH224 (black) shows the strongest GSB or Stark effect and photoinduced (PI) signals among the series of dye molecules, indicating that charges are generated very efficiently and that they have a long lifetime even without the Li additive. FPH231 also shows negative signals in the NIR, but almost no PIA signal in the visible range. FPH233 and 303 show the lowest signals, implying only a small amount of electron injection and a short lifetime. Most dye molecules show long-lived charges resulting from injection even without the help of Li cations.

In panel (b), FPH224 and 233 exhibit strong PIA signals, which are assigned to the absorption of dye cations. The addition of Li cations facilitates injection, meaning that more charges are generated. Especially, FPH233 shows a very sharp peak around 770 nm that is due to the absorption of the dye cation. When iron(III) chloride solution is used in a 0.1 mM FPH233 dye solution, the sample starts to show distinct cationic charge absorption features around 770 nm that were not observed from either the dye solution or the sensitized films without any additive. The steady-state absorption spectrum of the FPH233 dye cation that is obtained by the use of a FeCl<sub>3</sub> solution is represented as dotted blue line and hence the sharp PIA peak of FPH233 around 770 nm is regarded as the absorption of the dye cations.

FPH303 seems to generate more charges after addition of Li cations (the amplitude of PIA signals increases by 2 times) but the change is insignificant compared to FPH224 and 233. In FPH231, the amplitude of the signal is about 4 times smaller and the PIA signal is blue-shifted. This is due to a lower dipole moment in the excited state and therefore the dye generates more charges in the less polar environment (without Li cation) that provides a relatively similar ground state rather than the polar environment (with Li cation). This was previously observed in transient PL measurements as shown in Figure 6-5 (b) and 6-6 (b), which demonstrated longer lifetimes and higher PLQE without the addition of Li cations.

Panel (c) shows the photoinduced absorption spectra of complete device-like samples and the broad negative signals seen here are generally created by regeneration. FPH224 and 233 show the strongest absorption signals around 1500 nm where the oxidized hole conductor, spiro-OMeTAD, absorbs strongly. We note that the signals between 650 nm and 790 nm in FPH224 and 233, which are due to oxidized spiro molecules, are largely due to the efficient regeneration process, while FPH231 and 303 show almost no signals in the same wavelength ranges. This is closely related to higher J<sub>SC</sub> and FF of

devices using FPH224 and 233 than devices using FPH231 and 303. Furthermore, in the near infrared region, FPH231 and 303 show almost no absorption signal of the oxidized spiro-OMeTAD in good agreement with the poor efficiency of devices using these dyes. However, we note that the signal heights in PIA experiments cannot be used as an absolute comparison of the amount of charge generation, since PIA signals are always a combination of the number of species and their lifetimes. We therefore also performed transient absorption experiments on the samples.

## 6.5. Transient Absorption Spectroscopy

From the PIA measurements presented above, we could detect long-lived charges on a micro- to millisecond timescale which already provided a qualitative assessment explaining the difference in power conversion efficiency of the four different dye molecules. However, getting information about the injection, charge generation, and recombination processes, taking place on a picosecond to nanosecond timescale, is not possible from PIA measurements. In this section, we present further reasons for the difference in device efficiency by using transient absorption spectroscopy (TAS).

### 6.5.1. FPH224

Figure 6-9 compares the time-resolved absorption spectra of FPH224 with different additives in the time range from 3 ps to 3 ns. In panel (a), the transient pump-probe spectra of FPH224 adsorbed on  $\text{TiO}_2$  show two distinct features: positive TA signals up to 585 nm and negative TA signals extending to the near-infrared wavelength range. The positive and negative signals are assigned to ground state bleach (GSB) and photoinduced absorption (PIA) of excitons and dye cations. The long-lived negative PIA around 900 nm is not influenced by either the Stark effect or the PL spectrum; therefore, this wavelength region is assigned solely to dye cation absorption. Furthermore, these long-lived signals in the visible and NIR are not observed from FPH224 adsorbed on  $\text{Al}_2\text{O}_3$ , where we can observe only excitons including intra, inter, and interfacial charge transfer states. Therefore, the absorption of excitons and dye cations are observed in between 650-700 nm and between 800-1000 nm, respectively, and detection of long-lived dye cations implies that FPH224 is able to inject electrons without the help of Li additives.

In panel (b), the transient absorption spectra of FPH224 after addition of Li cations are shown. They show clear evidence of long-lived charge generation. The amplitude of the charge absorption signal is stronger and most of the signal between 800-1000 and between 1150-1200 nm remains even after 3 ns. This is explained by enhanced absorption resulting from increased charge generation and decreased back electron transfer due to fast injection by the aid of Li cations. However, the spectrum at later times in panel (b) reflects the existence of dye cations as well as the decay of electrons in  $\text{TiO}_2$  nanoparticles because the strong peak between 650 – 750 nm looks still similar to the transient

absorption spectrum in panel (a). These peaks red-shift due to a Stark effect that interferes with the ground state bleach of the dye molecules after insertion of Li cations.

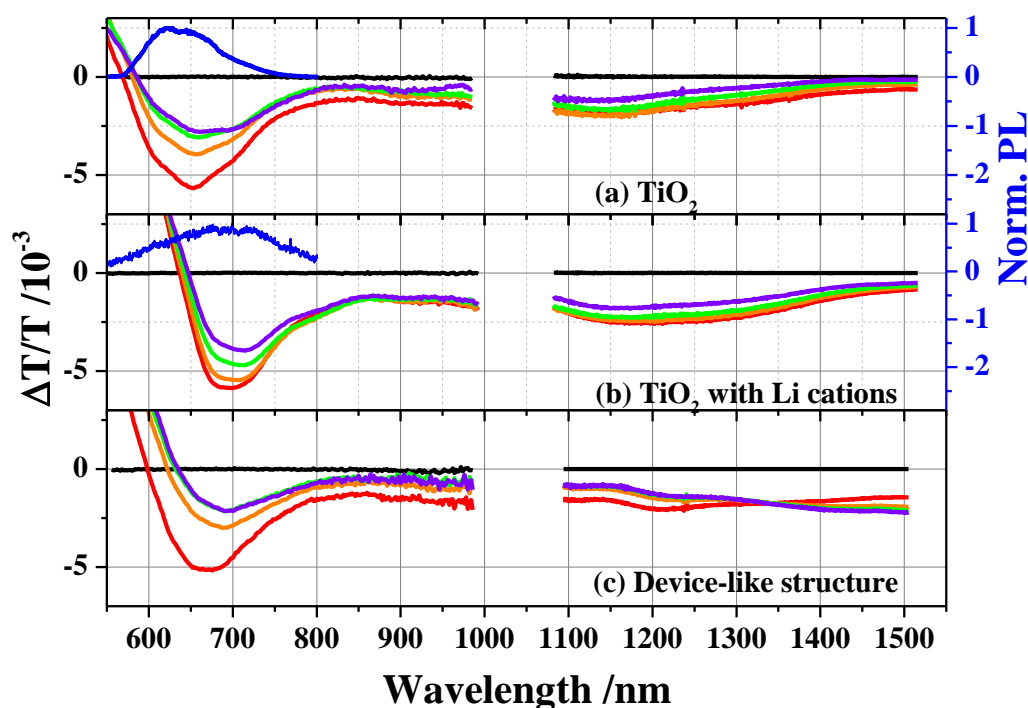


Figure 6-9. Short delay (ps-ns) broadband TA spectra of FPH224 on  $\text{TiO}_2$  (a), of FPH224  $\text{TiO}_2$  after application of Li cations (b), and of FPH224 on  $\text{TiO}_2$  with Li-TFSI/tBP/spiro-OMeTAD (complete device structure) at delay times of 3 ps (red), 30 ps (orange), 300 ps (green), and 3 ns (purple). The pump fluence at 520 nm is  $5.5 \mu\text{J cm}^{-2}$  for the visible and  $7.0 \mu\text{J cm}^{-2}$  for the near infrared measurements. The two blue lines represent the PL spectra of each sample.

The complete device-like structure shown in panel (c) shows four interesting features: blue-shifted PIA spectra in the visible, constantly decreasing signals around 900 nm, a clear isosbestic point at 1350 nm, and increasing signals beyond 1350 nm. First, the blue-shifted PIA in the visible range is caused by an interaction of the local electric field with the dipole moment of the excited state. In panel (b), the direction of the dipole moment in the excited state is the same as the local electric field induced by the Li cations, leading to lower energy levels of the dye. However, a large electric field pointing towards the  $\text{TiO}_2$  surface is created when spiro-OMeTAD is added, resulting in blue-shifted PIA spectra compared to the spectra in panel (b). Secondly, the signal around 900 nm where the absorption of dye cations is expected decays constantly. Hence, efficient regeneration seems to be active due to the hole conductor, namely spiro-OMeTAD, reducing the dye cations absorption. Thirdly, an isosbestic point at 1350 nm provides clear evidence of hole transfer from the cationic dye molecules to spiro-OMeTAD. Last, the increasing signal beyond 1350 nm is mainly caused by the dye regeneration that continues even after 3 ns. For comparison of the absorption spectra of the oxidized spiro, see Chapter 4.6. Therefore, the large photocurrent of the FPH224 device appears to be due to an

efficient regeneration process and the creation of long-lived charges. For determining the kinetics, the wavelength regions of the exciton, dye cation, and oxidized spiro signals are selected as 650 – 700 nm, 870 – 920 nm, and 1450 – 1500 nm, respectively.

In the short-delay TA spectra, most signals are long-lived and hardly decay on the first 3 ns. In order to observe the kinetics of charges, long time delay TA measurements were carried out that detect photophysical events from 1 ns – 0.1 ms. Figure 6-10 compares the long delay (ns –  $\mu$ s) broadband transient TA spectra of FPH224 on  $\text{TiO}_2$  (panel a), of FPH224 on  $\text{TiO}_2$  with the Li-TFSI additive (panel b), and of FPH224 device-like structures (panel c). Interestingly, all panels in Figure 6-10 show isosbestic points in the visible range where probably only two TA features, GSB and PIA of the dye cations, are observed with the same molar absorptivity indicating that excitons are only observed in short-time delay TA measurements.

In panel (a), the TA spectrum after 1 ns looks similar to that at the later time in the short-delay TA measurement shown in Figure 6-9 (a). Most of the observed broad, negative PIA signals in the visible and NIR decay in 1 – 2  $\mu$ s, indicating that the charges recombine with a moderate rate due to presumably back electron transfer from  $\text{TiO}_2$  to dye cations.

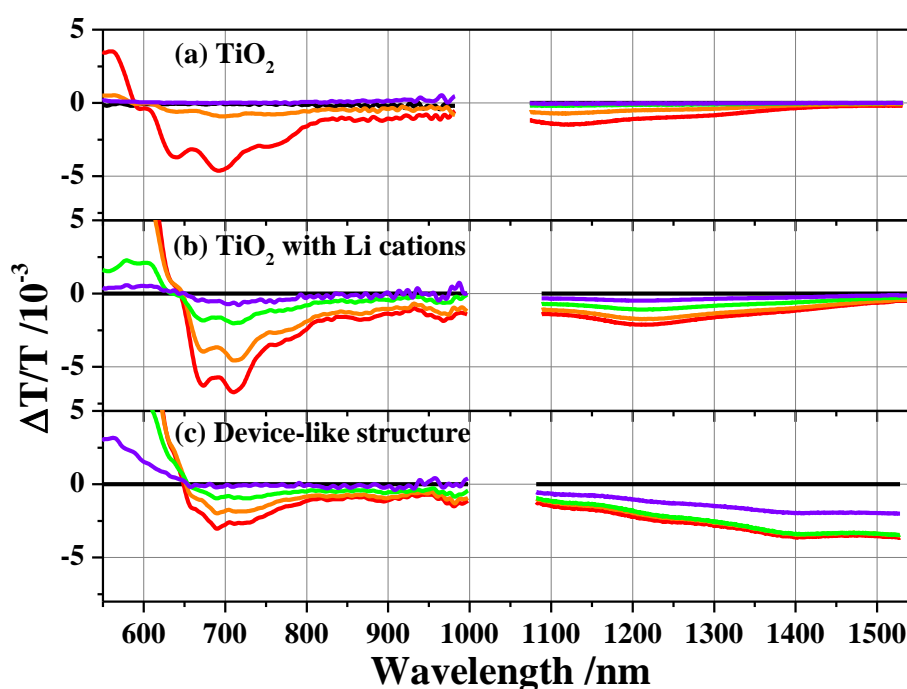


Figure 6-10. Long delay (ns –  $\mu$ s) broadband transient absorption spectra of (a) FPH224 on  $\text{TiO}_2$ , and (b) FPH224 on  $\text{TiO}_2$  after addition of Li-TFSI, and (c) FPH224 device-like structure in the visible and the NIR spectral region at delay times of 1 ns (red), 100 ns (orange), 10  $\mu$ s (green), and 100  $\mu$ s (purple). The samples were excited at 532 nm with a pump fluence of 7.2  $\mu\text{J cm}^{-2}$  for the visible and 8.0  $\mu\text{J cm}^{-2}$  for the NIR measurements.

Upon addition of Li cations (panel (b)), the sample shows long-lived absorption features that are in line with an efficient performance of the device with a high photocurrent. It is worth to note that the amplitude of the signals in panel (b) is increased compared to that in panel (a), indicating that more charges are created. This increased signal height is mainly due to the generation of dye cations (between 850 – 900 nm) which show fluence dependent recombination dynamics as shown in Figure 6-11 (a). This stronger dependence on fluence is likely due to more efficient charge generation after the addition of Li cations, whereas FPH224 on TiO<sub>2</sub> shows weaker fluence dependence due to less charge generation as shown in the inset of Figure 6-11. Higher fluence causes faster recombination in the sample with Li additive, indicating a non-geminate recombination process. Therefore, the use of Li cations in FPH224 device seems to be necessary for better charge generation.

A complete device-like structure using FPH224 shown in panel (c) of Figure 6-10 shows fingerprints of the absorption of the dye cations in the visible range and the absorption of spiro cations in the NIR. The amplitude of the signals in the visible decreases compared to that in panel (b), indicating that a smaller amount of dye cations is observed due to the regeneration process. Constantly increasing signals between 1350 – 1550 nm in short-delay TA signals in Figure 6-9 (c) increase up to 1  $\mu$ s (see Figure 6-22) corresponding to the regeneration process by the hole conductor, namely spiro-OMeTAD, and finally start to decrease afterwards.

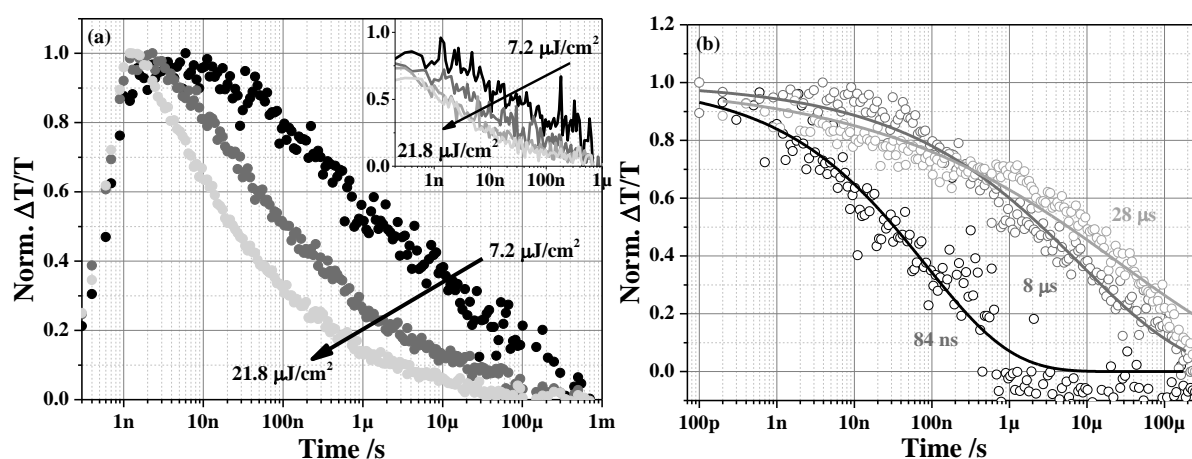


Figure 6-11. (a) Fluence dependence of the kinetics between 850 - 900 nm in FPH224 on TiO<sub>2</sub> with the Li-TFSI additive. The inset: Fluence dependence on FPH224 adsorbed on TiO<sub>2</sub> at the same wavelength region. (b) Long delay recombination dynamics of the photoinduced absorption probed at the wavelength regions between 850 – 900 nm in FPH224 on TiO<sub>2</sub> (black), in FPH224 on TiO<sub>2</sub> with Li-TFSI salts (dark grey), and in FPH224 device-like structure (light grey).

Figure 6-11 (b) shows the lifetime of dye cations in three samples parameterized by a stretched-exponential with an amplitude of 1 and an offset of 0. The wavelength region between 850 - 900 nm is



selected to track the kinetics of dye cations in order to exclude the possibility of interference caused by the Stark effect. FPH224 on TiO<sub>2</sub> shows a carrier lifetime of 84 ns, whereas the addition of Li-TFSI increases the lifetime up to 8 μs. Therefore, the use of Li cations helps to facilitate injection as well as to suppress a recombination channel. Interestingly, the dynamics of dye cations in the complete device-like sample shows a faster decrease of 200 ns than that in Li treated samples. This is due to an efficient regeneration process, but the dye cations still seem to remain until later times, showing a lifetime of 28 μs.

### 6.5.2. FPH233

As shown in previous sections, FPH233 achieved the highest power conversion efficiency in devices using the FPH series of dye molecules owing to presumably a significant change in the dipole moment, high injection efficiency, and long-lived charges.

Figure 6-12 compares the visible and NIR pump-probe spectra between 3 ps and 3 ns of FPH233 adsorbed on TiO<sub>2</sub> with different additives, and shows the PL spectra. Panel (a) shows the TA spectra of FPH233 adsorbed on TiO<sub>2</sub> without any additive. The GSB signal extends to 600 nm and the broad negative PIA signals extend to the NIR. Most signals decay within 3 ns in the visible and NIR spectral range and there is no clear evidence that injection takes place in this sample. The reason can be found from the spectral shape and the fluence dependent measurements. When the spectral shape of panel (a) is compared to that of FPH233 on Al<sub>2</sub>O<sub>3</sub> (panel b) and FPH233 on TiO<sub>2</sub> with Li cations (panel c), it appears more like the spectral shape of FPH233 on Al<sub>2</sub>O<sub>3</sub> showing mainly exciton absorption. Hence, FPH233 on TiO<sub>2</sub> seems to show the absorption of excitons, rather than the absorption of dye cations. The fluence measurements that can detect the existence of long-lived species show no fluence dependence. This will be further revealed in the inset of Figure 6-14.

Upon addition of Li cations as shown in panel (c), the TA spectra of FPH233 show two pronounced absorption features: a strong absorption around 780 nm and an increasing absorption peak in the NIR. These two features are assigned to the generation of dye cations by electron injection with the aid of Li cations. This was confirmed by quasi-steady-state PIA measurements on the same sample that showed a similar PIA spectrum as the TAS at 3 ps. Therefore, the injection seems to take place on an ultrafast timescale. Hence, exciton-induced absorption is likely absent due to fast injection in that the spectral shape of panel (c) looks quite different from the spectra in panel (a) and (b). Interestingly, the signals are fairly long-lived even beyond 3 - 4 ns, which supports a favorable injection process in FPH233 with the use of Li cations as is expected from the transient PL measurements, showing a big change in lifetimes upon the addition of Li cations. In order to compare the kinetics of dye cations in different samples the signals in the wavelength region between 850 - 900 nm are chosen where the signals are not affected by the Stark effect in the visible range. The spectral range of the dye cation in the NIR is deliberately not selected because it is very similar to the absorption spectra of spiro-cations.

The early time absorption feature of the dye cations peaking at 780 nm in a complete device-like sample is very similar to that in panel (c), but disappears as the delay time increases due to efficient regeneration by the hole conductor, as shown in panel (d). Strong absorption signals constantly increasing up to 3 - 4 ns in the NIR are considered to be due to the oxidized hole conductor, created by hole transfer, rather than the absorption of the dye cation. Unlike FPH224, a clear isosbestic point is not observed because the NIR absorption of dye cations is fairly similar to that of spiro cations in the NIR. However, the amplitude of the late signal (purple, 3 ns) from the visible (dye cation) and NIR (hole conductor) supports the effective hole transfer in the device using FPH233.

It is worth to note the changes in amplitude of the absorption spectra of the dye cations in Figure 6-12. The amplitude of the absorption spectra of the dye cations increases to 2.26 at 775 nm in panel (c) from 1.18 at 720 nm in panel (a) and decreases to 1.79 at 775 nm due to the regeneration of dye cations in panel (d). Changes in the amplitude can point to charge generation by Li-TFSI and to regeneration by a hole conductor. The constantly increasing signal of FPH233 in the NIR in the short-time delay TA measurement will be further investigated in the long-time delay TA measurement to determine the lifetime of the spiro/dye cations.

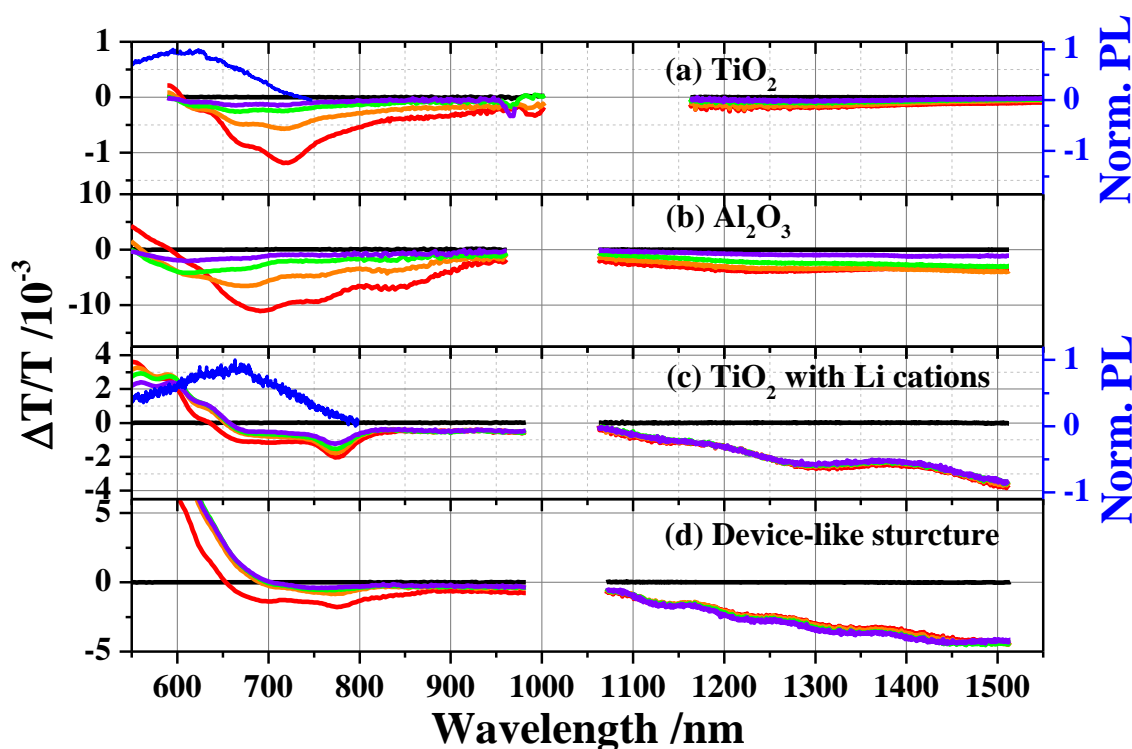


Figure 6-12. TA spectra on the femto- to nano-second timescale and PL spectra of FPH233 on TiO<sub>2</sub> (a), of FPH233 on Al<sub>2</sub>O<sub>3</sub> (b), of FPH233 on TiO<sub>2</sub> after addition of Li cations (c), and of a FPH233 device-like sample (d) at delay time of 3 ps (red), 30 ps (orange), 300 ps (green), and 3000 ps (purple). The pump fluence at 510 nm is 5.5  $\mu\text{J cm}^{-2}$  in the visible and 7.0  $\mu\text{J cm}^{-2}$  in the NIR.

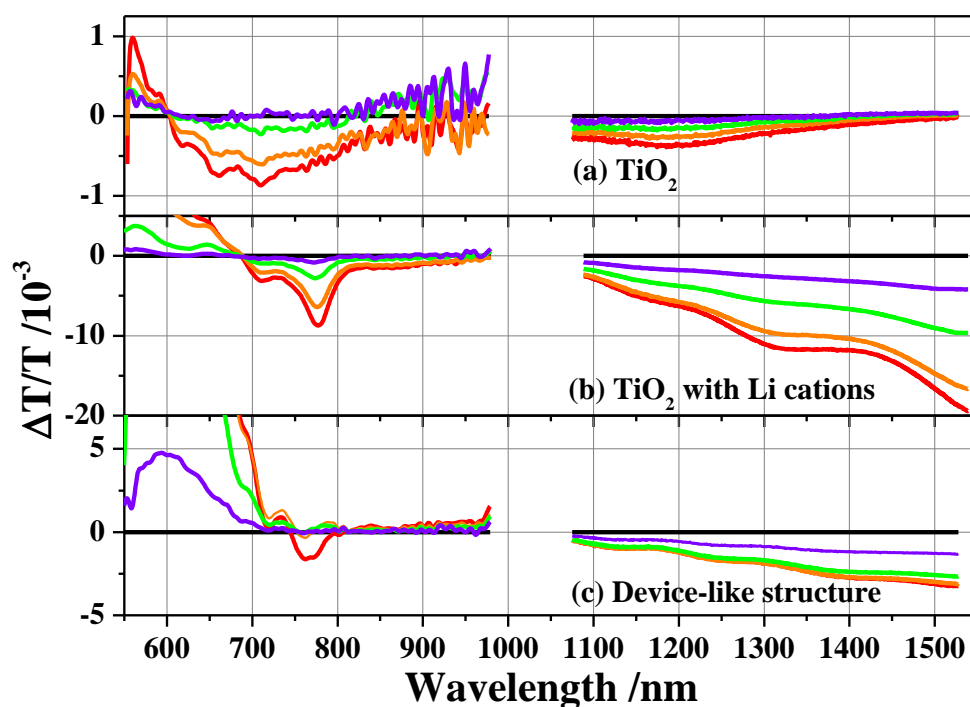


Figure 6-13. Long delay (ns –  $\mu$ s) broadband transient absorption spectra of (a) FPH233 on  $\text{TiO}_2$ , and (b) FPH233 on  $\text{TiO}_2$  after addition of Li-TFSI, and (c) FPH233 device-like structure in the visible and the NIR spectral region at delay times of 1 ns (red), 100 ns (orange), 10  $\mu$ s (green), and 100  $\mu$ s (purple). The samples were excited at 532 nm with a pump fluence of  $7.2 \mu\text{J cm}^{-2}$  for the visible and  $8.0 \mu\text{J cm}^{-2}$  for the NIR measurements.

Figure 6-13 shows long time delay TA measurements of the same samples that enable us to detect long-lived species like dye cations and spiro-cations. All three spectra show clear isosbestic points in the visible due to existence of only two species, namely the GSB and PIA of the charges.

FPH233 on  $\text{TiO}_2$  shown in panel (a) demonstrates very weak transient absorption spectra that are assigned to mostly PIA signals of excitons. As stated above, FPH233 appears not to inject electrons into the conduction band of  $\text{TiO}_2$  without any additive which is supported by fluence dependent measurements. As shown in the inset of Figure 6-14 (a), the dynamics of dye cations are tracked between 850 – 900 nm, where the absorption of dye cations is mainly observed. The dynamics are independent of pump fluence implying that no free charges are generated.

By the addition of Li cations as shown in Figure 6-13 (b), the amplitude of the PIA signal increases especially in the NIR due to the large amount of free charge carriers that are generated after the addition of Li cations. The generation of dye cations is supported by fluence dependent measurements as shown in Figure 6-14 (a) showing a non-geminate recombination process. Strong, sharp peaks between 750 – 800 nm that represent the absorption spectra of the dye cations remain up to 0.1 - 0.2 ms, and most signals are fairly long-lived. The kinetics of the dye cations in the NIR start to decrease from 10 ps onwards in the short-time delay measurement and constantly decrease with big changes in

long-time delay measurement. Hence, the strong amplitude and the long-lived signals indicate that the use of Li cations in this dye molecule not only helps injection, but also reduces recombination compared to the sample without Li salts shown in panel (a). For FPH233, the use of Li-TFSI, therefore, is necessary to create charges.

In a complete device-like sample using FPH233 as shown in panel (c) of Figure 6-13, most TA signals in the visible disappear between 200 ns - 1  $\mu$ s due to a very efficient hole transfer process from the oxidized dye to the hole conductor molecules. This is confirmed from Figure 6-14 (b) that compares the kinetics of dye cations in two different samples. The dye cations created in FPH224 on  $\text{TiO}_2$  with Li salt exhibit a lifetime of 8.5  $\mu$ s (which is similar to FPH224 on  $\text{TiO}_2$  with Li salt), but those created in the complete device-like sample show a lifetime of 12.8 ns. This fast decay represents depopulation of dye cations by efficient hole transfer to spiro-OMeTAD. The constantly increasing signals in the NIR in short-time delay TA measurements finally begin to decrease after 100 ns (see Figure 6-22 (b)), indicating the recombination of oxidized hole conductor with injected electrons. This will be further discussed in the next chapter.

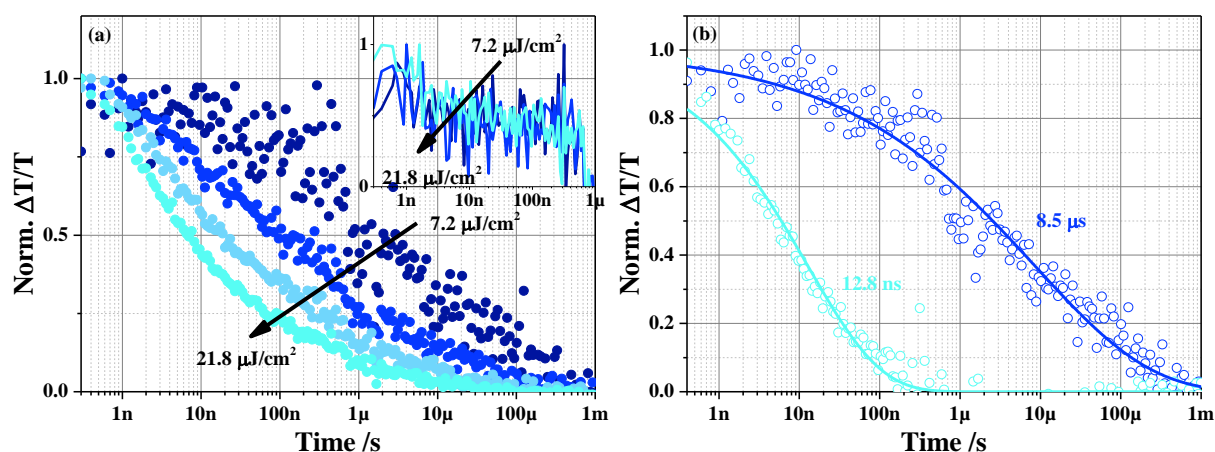


Figure 6-14. (a) Fluence dependence of the kinetics between 850 - 900 nm in FPH233 on  $\text{TiO}_2$  with Li-TFSI additive. The inset: Fluence dependence on FPH233 adsorbed on  $\text{TiO}_2$ . (b) Long delay recombination dynamics of the photoinduced absorption of dye cations probed at the wavelength regions between 850 – 900 nm in FPH224 on  $\text{TiO}_2$  with Li-TFSI salts (blue) and in FPH224 device-like structure (light blue).

### 6.5.3. FPH231

FPH231 shows negative solvatochromism; therefore, the dye exhibits unfavorable injection properties as shown by the PL decay measurements and by the calculation of the injection efficiency after the addition of Li cations that causes a more polar environment around the dye molecules.

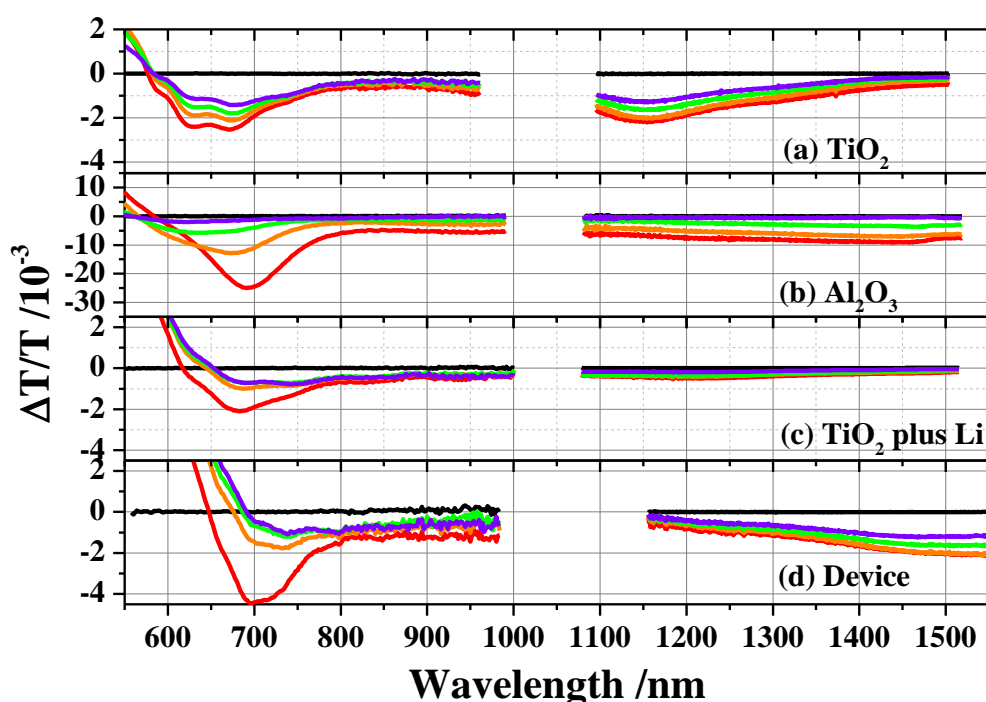


Figure 6-15. TA spectra on the femto- to nano-second timescale of FPH231 on  $\text{TiO}_2$  (a), of FPH231 on  $\text{Al}_2\text{O}_3$  (b), of FPH231 on  $\text{TiO}_2$  with Li cations (c), and of the FPH231 device-like structure sample (d) at delay times of 3 ps (red), 30 ps (orange), 300 ps (green), and 3000 ps (purple). The pump fluence at 510 nm is  $5.5 \mu\text{J cm}^{-2}$  in the visible and  $7.0 \mu\text{J cm}^{-2}$  in the NIR.

Figure 6-15 (a) shows the transient absorption spectra of FPH231 adsorbed on  $\text{TiO}_2$  excited at 510 nm with a fluence of  $5.6 \mu\text{J/cm}^2$ . The positive GSB signals end at around 580 nm and the negative PIA signals start to show up extending up to 1500 nm. The broad negative PIA signals are assigned to the dye cations formed due to electron injection even without the help of Li cations, since the spectral shape, especially in the NIR, is fairly similar to that in FPH231 on  $\text{TiO}_2$  with Li cations in panel (c) rather than that in FPH231 on  $\text{Al}_2\text{O}_3$  in panel (b). Panel (b) shows the short-time delay TA spectra of FPH231 on  $\text{Al}_2\text{O}_3$ , where we can mainly observe the absorption of the exciton and intramolecular charge transfer state when the dye molecule is adsorbed on the film. In panel (b), strong absorption peaks are observed between 650 – 700 nm and most signals decay in 300 - 1200 ps over the whole spectral range, whereas 30 % of the signal remains in panel (a) due to long-lived species. The assignment of the long-lived signals to charges in FPH231 on  $\text{TiO}_2$  is confirmed by the fluence

dependence of long-time delay measurements shown in the inset of Figure 6-17 (a). On a  $\text{TiO}_2$  surface, FPH224 showed a very weak intensity dependence as shown in the inset of Figure 6-11, whereas FPH233 exhibited no charge generation as shown in the inset of Figure 6-14. However, FPH231 adsorbed onto  $\text{TiO}_2$  nanoparticles displays a strong intensity dependence pointing to charge generation.

In panel (c), the transient absorption spectra of FPH231 after addition of Li salt are shown. Unlike FPH224 and 233, the amplitude of the TA spectra decreases upon the use of Li cations, indicating less charge generation in line with the injection efficiency found in FPH231 on  $\text{TiO}_2$  without Li cations. It is difficult to determine if there is charge generation in the short-delay spectra of this sample; however, the decay kinetics in the short delay measurements shown in Figure 6-16 (b) and in the long-delay measurements shown in Figure 6-17 (a) provide evidence for generation of charges in FPH231 on  $\text{TiO}_2$  after application of Li cations.

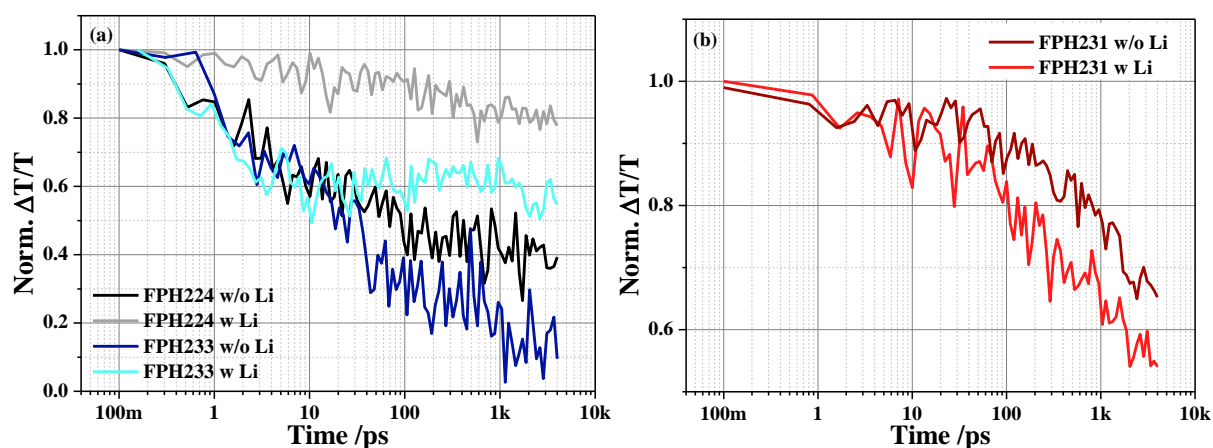


Figure 6-16. (a) Kinetics of the dye cations in FPH224 and 233 with (darker)/ without (paler) Li cations in the short-time delay TA measurements. The kinetics are averaged for FPH224 (black) and 233 (blue) between 850 – 900 nm and between 850 – 900 nm, and those for FPH224 (grey) and 233 (sky blue) with Li cations are taken from 900 – 950 nm and 900 – 950 nm, respectively. (b) Kinetics of the dye cations in FPH231 on  $\text{TiO}_2$  (red, 1150 – 1170 nm) and in FPH231 on  $\text{TiO}_2$  with Li (dark red, 1120 – 1150 nm).

Figure 6-16 compares the kinetics of the dye cations in three different samples with and without Li cations. In panel (a), FPH224 shows 80% of the signal remaining and slowly decaying when Li cations are used on  $\text{TiO}_2$  (gray), compared to the sample without Li salt (black). This is the same for FPH233 showing the same amplitude of the signal after 10 ps (light blue) due to long-lived charges generated with the help of Li cations, whereas the signal of the sample without Li cations constantly decreases due to back electron transfer. Panel (b) shows the changes in the kinetics of FPH231 with (darker red) and without (lighter red) Li cations. The two samples exhibit rather similar decay kinetics indicating that Li cations do not significantly facilitate the charge generation like in FPH224 and 233.

Interestingly, 60 % of the signal remains in the two samples, causing non-geminate recombination as observed in the long-delay measurements shown in the inset of Figure 6-17 (a).

The wavelength region for the detection of dye cations was chosen as NIR, since the strongest absorption peaks are observed between 1100 – 1200 nm as shown in panel (a) of Figure 6-15, which are not observed for excitons as shown in panel (b). The wavelength regions chosen for the detection of the dye cations in FPH224, 233, and 231 in Figure 6-16 are 850 – 900 nm, 850 – 900 nm, 1150 – 1170 nm and those for FPH224, 233, and 231 with Li cations are 900 – 950 nm, 900 – 950 nm, and 1120 – 1150 nm, respectively. The different wavelength regions for these samples are a consequence of their red- and blue-shifted absorption caused by the Stark effect and negative solvatochromism.

A complete-device like sample shown in panel (d) exhibits visible TA spectra similar to the spectra shown in panel (c), which is due to an inefficient injection process. In addition, we note that the amplitude of the late time signal in the NIR is not significantly enhanced compared to the amplitude of the late time signal in the visible. This indicates that regeneration in FPH231 is not as efficient as in FPH224 and 233. The inefficient regeneration is confirmed by the decay kinetics of spiro-cations between 1480 – 1500 nm in short-delay and long-delay measurements shown in Figure 6-17 (b). The signal of the spiro-cations (red) in the short-delay measurement increases up to 10 ps due to hole transfer to the hole conductor material but afterwards, the signal constantly decreases up to 1 ms. Therefore, FPH231 seems to suffer from inefficient hole transfer and recombination between injected electrons and oxidized spiro molecule, in contrast to FPH224 and 233 that show continuously increasing signals in the short-delay measurements. This is the main reason for the smaller photocurrents in the FPH231 devices compared to the FPH224 and 233 devices.

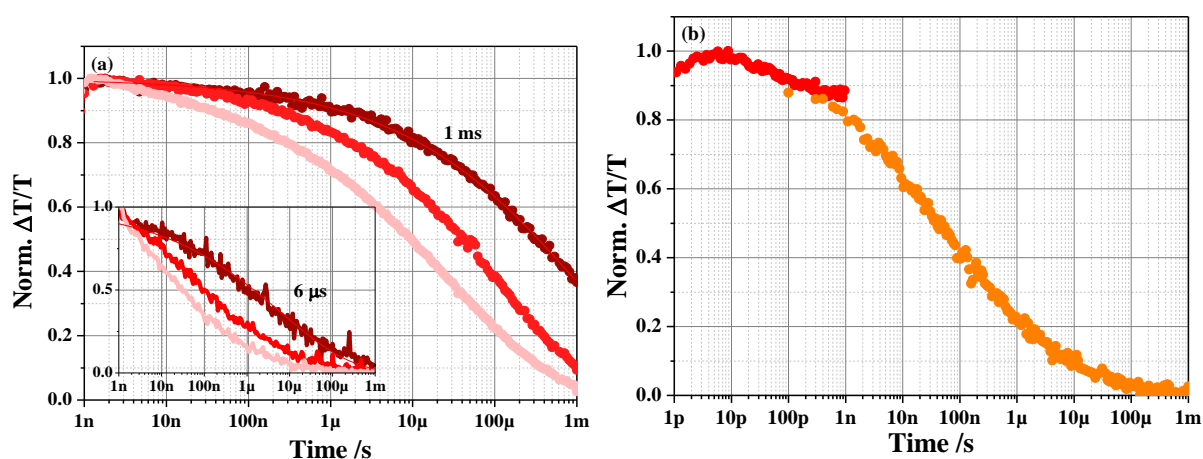


Figure 6-17. (a) Transient absorption kinetics of dye cations monitored between 1150 – 1170 nm in FPH231 on  $\text{TiO}_2$ . Inset: the kinetics of dye cations between 1120 – 1150 nm in FPH231 on  $\text{TiO}_2$  with Li cations. (b) Transient absorption kinetics of a solar cell probed between 1480 – 1500 nm where the spiro cations dominate the photoinduced absorption.



#### 6.5.4. FPH303

FPH303 is expected to have a large change in the dipole moment between the ground and excited state, but it exhibits rather low injection efficiency presumably due to having a small amount of Li cation-active sites. In this section, the charge generation and recombination processes of FPH303 are demonstrated by TA measurements.

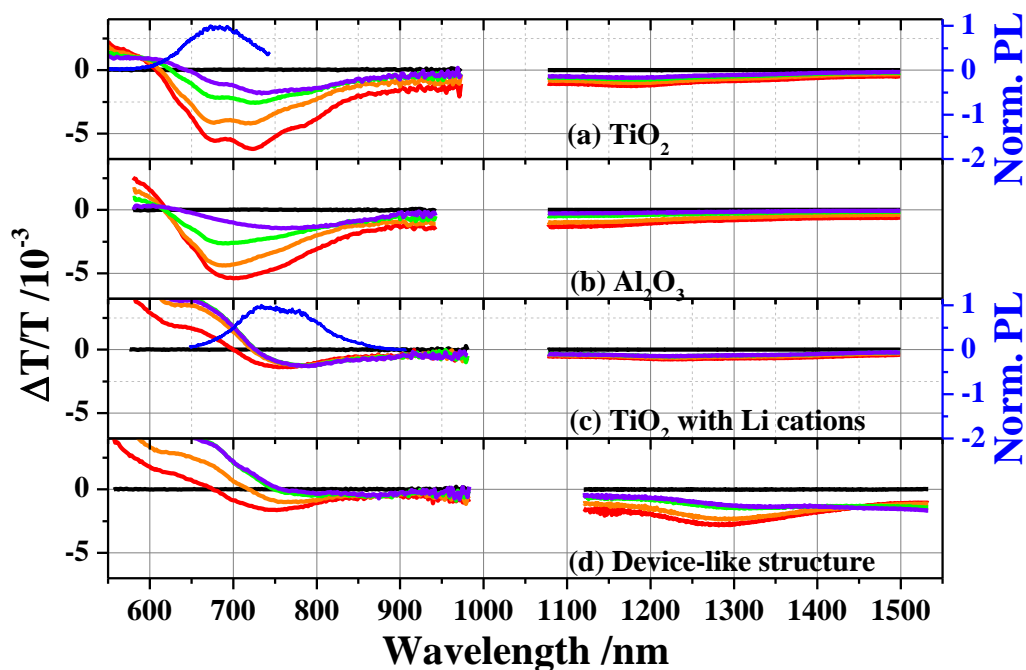


Figure 6-18. TA spectra on the femto- to nano-second timescale and PL spectra of FPH303 on  $\text{TiO}_2$  (a), of FPH303 on  $\text{Al}_2\text{O}_3$  (b), of FPH303 on  $\text{TiO}_2$  with Li-TFSI (c), and of a FPH303 solar cell (d) at delay times of 1 ps (red), 3 ps (orange), 30 ps (green), and 3000 ps (purple). The pump fluence at 510 nm is  $5.7 \mu\text{J cm}^{-2}$  in the visible and  $7.2 \mu\text{J cm}^{-2}$  in the NIR. Two blue lines in panel (a) and (c) represent the PL spectra of each sample.

Figure 6-18 compares the time-resolved absorption spectra of FPH303 on  $\text{TiO}_2$  (a), of FPH303 on  $\text{Al}_2\text{O}_3$  (b), of FPH303 on  $\text{TiO}_2$  with Li (c), and of a FPH303 solar cell sample (d) in the time range between 3 ps – 3 ns.

In panel (a), the TA spectra of FPH303 on  $\text{TiO}_2$  show a positive signal corresponding to the GSB in the shorter wavelength region and a broad negative PIA signal extending to the NIR. The TA spectra of FPH303 on  $\text{TiO}_2$  shown in panel (a) look more alike those of the FPH303 dye solution and of FPH303 on an  $\text{Al}_2\text{O}_3$  surface shown in panel (b) than alike those of FPH303 with Li cations shown in panel (c). However, we cannot rule out injection in this sample. This is confirmed by Figure 6-19 that shows the kinetics between 1150 – 1200 nm where the absorption of the dye cations is expected. The wavelength region in the visible is deliberately not chosen due to the Stark effect. FPH303 on  $\text{Al}_2\text{O}_3$  (solid green) shown in Figure 6-19 exhibits exciton decay dynamics, since the dye molecule cannot



undergo a charge injection process. When FPH303 is adsorbed on  $\text{TiO}_2$  (olive scatter), the sample shows similar decay kinetics as the exciton decay observed in FPH303 on  $\text{Al}_2\text{O}_3$  up to about 10 ps but deviates afterwards. This is due to electron injection leading to the generation of dye cations. A weak injection in FPH303 on  $\text{TiO}_2$  that shows the absorption of two species, exciton and small amount of charge generation, becomes clear in the inset of Figure 6-20 that shows a fluence series of dynamics of dye cations on  $\text{TiO}_2$ . As shown in the inset, the sample exhibits weak non-geminate recombination seen in long-time delay TA measurements due to a small amount of charge generation.

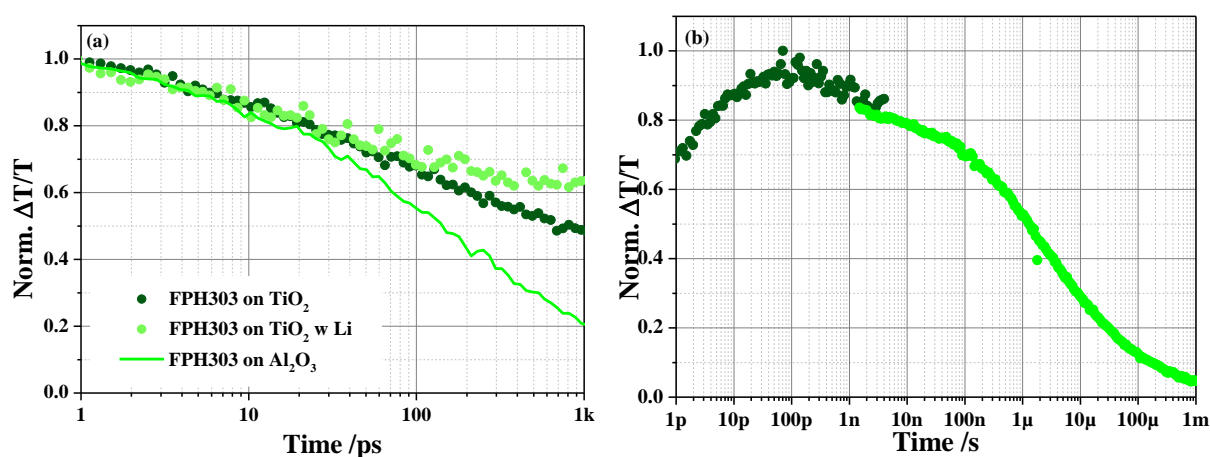


Figure 6-19. Transient absorption kinetics of (a) FPH303 on  $\text{Al}_2\text{O}_3$  (solid green), of FPH303 on  $\text{TiO}_2$  (olive scatter), and of FPH303 on  $\text{TiO}_2$  with the application of Li-TFSI monitored between 1150 – 1200 nm where the dye cations absorb strongly, and of (b) the FPH303 device-like sample monitored between 1450 – 1500 nm.

With the application of Li-TFSI as shown in panel (c) of Figure 6-18, the TA spectra red-shift clearly and show different spectral shapes compared to those in panel (a). The red-shifted absorption is due to field-assisted changes in ground state absorption of the dye molecules and the different spectral shape is due to creation of dye cations or due to an influence of the PL spectrum that has a lifetime of 120 ps. However, we note that the amplitude of these signals is very small compared to panel (a), whereas FPH224 with a different anchoring group shows stronger amplitude signals by addition of Li cations due to facilitated injection. This indicates that injection may take place in FPH303 by the help of Li cations leading to the generation of free charge carriers; however, the amount of generated charges appears to be relatively small. This can be due to the charge distribution being localized on the rhodanine-3-acetic acid moiety rather than localized on the cyanoacrylic acid. The creation of dye cations is observed from the decay kinetics as shown in Figure 6-19 (a). The dye cations in the sample of FPH303 with Li-TFSI (green scatter) show a similar decay up to 100 ps compared to the sample of FPH303 on  $\text{TiO}_2$  without Li additive, but exhibit a suppressed recombination afterwards. This is presumably due to slightly more charge generation by the help of Li cations. The divergence of two

scattered lines becomes obvious in the long-time delay TA measurements because Li cations promote the electron injection from FPH303. Figure 6-20 shows the fluence dependence of the dye cation dynamics in the sample of FPH303 with Li cations, which has a stronger dependence on fluence than in the sample of FPH303 on  $\text{TiO}_2$  as shown in the inset due to more charge generation. To conclude, FPH303 injects electrons like FPH224 without the help of Li cations, although localized charges on rhodanine-3-acetic acid are unfavorable for the electron injection. By the application of Li cations, the dye generates dye cations; however, injection is not significantly enhanced.

The device-like sample shown in panel (d) exhibits a similar spectrum compared to panel (c). The photoinduced absorption features in the NIR range between 1250-1350 nm are due to cationic dye molecules as the strong absorption signals are also observed in panel (c). However, the signals left at later times in this wavelength range still show the absorption of dye cations and are likely due to inefficient regeneration. In the NIR, a fast decreasing absorption signal of the dye cations, an isosbestic point at 1450 nm, and an increasing signal between 1450 – 1550 nm are observed due to hole-transfer from the oxidized dye molecules to the hole conductor. Especially the signal beyond the isosbestic point shows an increase up to 100 ps as shown in Figure 6-19 (b). In the long-delay measurements, the FPH303 device-like sample shows a continuously decreasing signal caused by recombination of the injected electrons with oxidized dye or with oxidized spiro-OMeTAD. Therefore, the regeneration in this dye molecule is less inefficient than FPH224 and 233, based on the fact that dye cation signals remain in the NIR and the regeneration process requires around 100 ps.

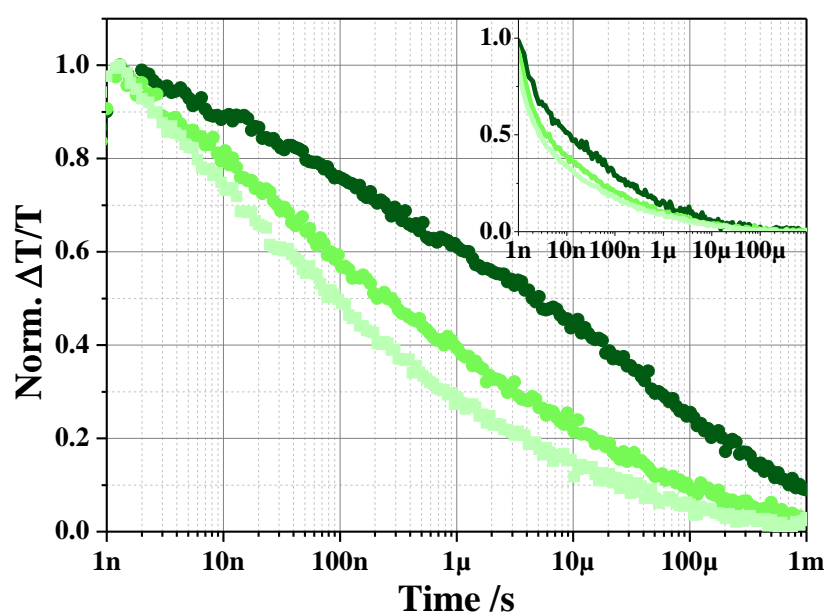


Figure 6-20. Intensity dependence measurement of FPH303 on  $\text{TiO}_2$  with Li cations for the wavelength between 1150 – 1200 nm. The inset: Intensity dependence measurement of FPH303 on  $\text{TiO}_2$  for the same wavelength.

## 6.6. Comparison of charge generation and regeneration of all four dyes

In this section, the kinetics of the dye cations and spiro cations of the four dye molecules will be compared to understand the reason for the different performance of the devices. Figure 6-21 (a) shows the transient absorption kinetics of dye cations from the samples with Li cations. The wavelengths selection is same as above, between 850 – 900 nm for FPH224, 1180 – 1200 nm for FPH231, 850 – 900 nm for FPH233, and 1150 – 1200 nm for FPH303. Interestingly, FPH231 and 303 show fast decay rates of the dye cations while FPH224 and 233 exhibit rising signals up to 100 ps – 1 ns by slower generation of dye cations. Generally, fast injection from the dye molecules results in an efficient performance of the device. This small amount of injection appears to be attributed to the negative solvatochromic property of FPH231 and low injection efficiency of FPH303. For FPH224 and 233, the decay dynamics show a moderate rate resulting from slow charge generation and/or slow recombination between the injected electrons and the oxidized dye molecules.

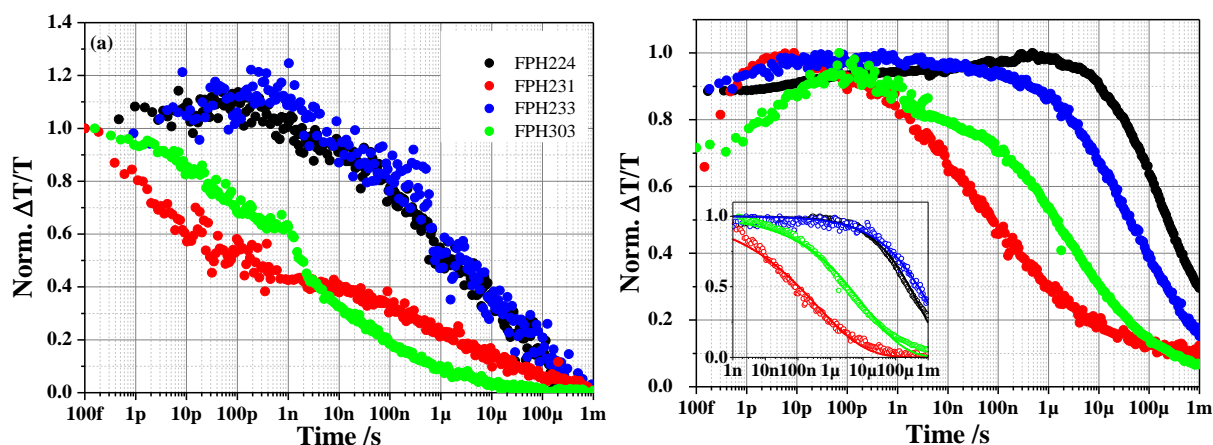


Figure 6-21. Transient absorption kinetics of (a) dye cations measured with samples of the dye adsorbed on  $\text{TiO}_2$  after addition of Li cations and of (b) spiro cations in the solar cell-like samples. FPH224, 231, 233, and 303 are represented in black, red, blue, green lines, respectively. The inset shows the dynamics of spiro cations in long-time delay measurements.

Panel (b) shows the ps – ms dynamics of oxidized spiro-OMeTAD molecules of the four samples monitored between 1400-1450 nm for FPH224, 231, and 233, and between 1450 – 1500 nm for FPH303. The absorption of the oxidized hole conductor material in this wavelength range is assigned by steady-state absorption measurements as shown in Figure 4-12 and quasi-steady-state PIA measurements as shown in Figure 6-8. In the solar cell-like samples, FPH224 and 233 exhibit a slightly increasing or constant signal up to 1 ns – 1  $\mu$ s, whereas FPH231 and 303 show rising signals only up to 10 – 100 ps. For FPH231 and 303 fast increasing signals are considered to be due to reductive quenching, since both dyes showed remaining exciton signals (as shown in Figure 6-15 (d) and -18 (d)) and the small PIA signals of the dye cations even after Li cations were used. This indicates

that the dye cation is generated by reductive quenching rather than by electron injection from the exciton.

Table 6-7. Parameters of the spiro cations in the 4 dyes in a solar cell when stretched-exponential fits are used.

	A	$y_0$	$\beta$	$\tau$ /s	$\tau$ (gamma F, /s)
FPH224	1	0	0.53	$5.2 \cdot 10^{-4}$	$9.4 \cdot 10^{-4}$
FPH231	1	0	0.29	$3.7 \cdot 10^{-7}$	$2.0 \cdot 10^{-6}$
FPH233	1	0	0.46	$1.1 \cdot 10^{-3}$	$2.6 \cdot 10^{-3}$
FPH303	1	0	0.35	$1.1 \cdot 10^{-5}$	$5.5 \cdot 10^{-5}$

The solid lines in the inset of panel (b) correspond to stretched exponential fits of the spiro cation signal in the four solar cells, and the parameters for the fitting are summarized in Table 6-7. The longest lifetime of oxidized spiro-OMeTAD is observed in FPH233 devices with 2.6 ms, followed by FPH224 exhibiting a lifetime of 0.9 ms, when a gamma function is used due to different  $\beta$  in the stretched exponential fitting. FPH231 and 303 show a faster decay of 2.0  $\mu$ s and 0.5  $\mu$ s, respectively. This presents critical evidence for the different power conversion efficiency in the devices.

#### 6.7 CPDT building block sensitizers: Conclusions

Four novel CPDT dye molecules were investigated named FPH224, 231, 233 and 303. FPH224, 231, and 233 consist of cyanoacrylic acid as an acceptor (anchoring) unit, a cyclopentadithiophene (CPDT) moiety as a bridging unit, and triphenylamine-based moieties as a donor unit. FPH303 has the same molecular structure as FPH224, but has a different anchor group, namely rhodanine-3-acetic acid.

The LUMO levels of the four dye molecules as obtained from density functional theory (DFT) calculations and the maximum of the 0-0 transitions in absorption/emission spectra are located high enough to ensure electron injection, whereas the HOMO levels are fairly close to the HOMO level of spiro-OMeTAD. Therefore, it is expected that injection rates may be similar and high, but the regeneration is expected to be depending on the dye molecule.

FPH224 and 233 have similar changes in dipole moment between the ground and excited state based on the DFT calculation, which is experimentally confirmed by absorption/emission spectra in solvents with different polarity as well as from titania nanoparticles films with/without Li-TFSI, which increases the polarity in the films. FPH303 has a larger dipole moment in the excited state, but it does not seem to lead to a high injection yield probably due to a large amount of Li cation-inactive sites. FPH231 shows negative solvatochromism in the absorption/emission spectra of solution and film

samples, and this is considered to create an unfavorable environment for the electron injection in the presence of Li salts when a normal device structure is used.

Time-resolved Streak camera measurements allow investigating injection properties of dye molecules by measuring the PL intensity. The injection efficiency is calculated from the titania films with/without Li cations and FPH231 and 303 are found to exhibit a low injection efficiency of 87 %, while FPH224 and 233 show an injection efficiency of 99% under the assumption that non-radiative deactivation is excluded. This fairly well correlates with the photocurrents and the J-V characteristics of the devices, where FPH224 and 233 show higher photocurrents than FPH231 and 303.

The higher photocurrents of FPH224 and 233 devices are also confirmed by quasi-steady-state photoinduced absorption (PIA) measurements that detect long-lived species such as dye cations or spiro cations as a result of injection and hole transfer. In general, FPH224 and 233 exhibit strong PIA signals of dye cations and spiro cations after the addition of Li-TFSI and spiro-OMeTAD, indicating efficient charge generation and regeneration. FPH231 and 303 show absorption of dye cations in the sample without any additive; however, the amplitude of the dye cation signal in FPH231 becomes weaker after the addition of Li salt and the PIA signals of the spiro cations in the FPH231 and 303 device-like structure are significantly weaker compared to the FPH224 and 233 devices.

Transient absorption (TA) measurements on FPH224 provide evidence of charge generation on TiO<sub>2</sub> even without Li-TFSI and of increased lifetime of dye cations by the use of Li additives due to reduced back electron transfer. FPH303 has the same donor but different acceptor moiety as compared to FPH224 and also injects electrons without the Li additive, but the kinetics in short delay measurements reveal that FPH303 has only a small Li cation-active pool, causing inefficient charge generation. By the addition of Li cations, FPH233 shows very strong and sharp signals at 780 nm where the oxidized dye molecule strongly absorbs photons, and prolonged decay transients of the dye cations. However, it does not show any proof of injection on TiO<sub>2</sub> surfaces without Li-TFSI as observed from the PIA measurements. The decay kinetics of FPH231 on titania (1 ms) is much slower than that of FPH231 on titania with Li cations (6 μs), which is consistent with the long-lived signals in short-delay TA spectra of FPH231 on TiO<sub>2</sub> in the NIR.

An efficient regeneration process of the dye cations is observed for FPH224 and 233 solar cells that show continuously increasing, long-lived signals in the short-time TA delay measurements, whereas the FPH231 device shows decaying signals after 10 ps, and the hole transfer in the FPH303 device seems to be finished after around 100 ps. These increasing signals appear to originate from reductive quenching, since both dyes showed residual exciton signals and small PIA signals of the cations even after Li cations were used. Furthermore, the difference in the decay of the four dye's spiro cations strongly determines the photocurrents in the devices.

In conclusion the combination of dipole moments, reactivity of the molecules toward Li cation, and the generation of long-lived dye/spiro cations are closely correlated to the power conversion efficiency of the devices.

## 7. DISCUSSION

The photophysical properties of solid-state dye-sensitized solar cells using a series of rylene dye molecules, perylene monoimide derivative dyes, and cyclopentadithiophene dyes as sensitizers were investigated in this thesis. In this section, four factors affecting the power conversion efficiency of solar cell devices are further discussed separately: energy levels, anchoring groups, dipole moments, and dynamics of long-lived charges.

### 7.1 The importance of energy levels

The HOMO and LUMO energy levels of dye molecules are critical factors determining the device performance. The LUMO level of a dye molecule should be higher than the conduction band of titania to ensure an efficient injection process and the HOMO level should be lower than the HOMO level of the hole transporter (such as spiro-OMeTAD) for fast and quantitative regeneration of oxidized dye molecules.

In the series of rylene dye molecules, the di-carboxylic acids of the perylene molecules, PMIMA, has a HOMO level of -5.33 eV and a LUMO level of -2.80 eV. When additional naphthalene units are added, the energy bandgaps of the di-carboxylic acids of the terylene molecules (TMIMA) and the di-carboxylic acids of the quaterylene molecules (QMIMA) are decreased and the HOMO/LUMO levels shift to -5.17/-3.09 and -4.88/-3.19, respectively. These energy levels appear to be suitable for efficient devices, as the conduction band of titania and the HOMO level of the hole conductor are between -4.0 – -4.3 eV and -4.7 – -4.9 eV (vs vacuum level), respectively. Hence, in quasi-steady-state photoinduced absorption (PIA) spectroscopy, TMIMA and QMIMA showed lower injection and regeneration than PMIMA. This led to reduced external quantum efficiencies (EQE) and poor power conversion efficiencies in devices.

The perylene monoimide derivative dye, namely ID889, provides adequate energy levels, a HOMO of -3.5 eV and a LUMO of -5.15 eV, which are suitable for efficient injection and regeneration. In addition, fairly localized electronic charge distribution in the molecule indicated that the LUMO and HOMO levels were mainly determined by the acceptor moiety and the donor moiety, a  $\pi$ -conjugated bridge fused dibenzothiophene with triarylamine, respectively. The energy levels allowed a high efficiency of 4.5% to be obtained with the EQE reaching 75% in a solid-state dye-sensitized solar cell.

Most of the FPH series of dye molecules showed similar LUMO levels due to the same cyanoacrylic acid moieties that act as electron acceptors in the push-pull type dye. However, the HOMO levels varied due to different triarylamine-based donor moieties, confirmed by DFT calculated orbital surfaces. FPH224 and 233 showed better power conversion efficiencies in devices with HOMO levels

of -5.35 – 5.95 eV and -4.95 – -5.06 eV, respectively, which were suitable for regeneration of oxidized dye molecules. The HOMO level of FPH231 (-4.62 – -5.10 eV) was similar to or higher than the HOMO level of spiro-OMeTAD; it was, therefore, expected to suffer from poor regeneration, which was confirmed by PIA measurements. FPH303 exhibited good energy levels with a HOMO of -5.18 – -5.21 eV and a LUMO of -2.69 – -2.15 eV, however, injection and regeneration signals were significantly weaker compared to FPH224 and 233 in PIA measurements.

The FPH dyes did not show good power conversion efficiencies in liquid-state dye-sensitized solar cells, since the redox potential of redox mediators such as cobalt complexes (-5.06 eV) or iodide redox (-4.8 eV) shuttles are located much lower than the HOMO levels of the FPH series dye molecules. Therefore, these dye molecules are more suitable for solid-state DSCs.

## 7.2 The effect of anchoring groups

Anchor groups aid adsorption onto mesoporous metal oxide nanoparticles as well as acting as channels for electron injection. In this report, four types of anchoring groups (carboxylic, cyanoacrylic, rhodanine-3-acetic, and anhydride acid) were used and they were found to exhibit different photophysical characteristics.

Generally, carboxylic acid anchoring groups are widely used due to easy synthesis, stability, and because they offer more adsorption sites. Carboxylic acid groups can be combined with strong electron withdrawing acceptor moieties such as cyanoacrylic acid or rhodanine-3-acetic acid in order to obtain enhanced efficiency of electron injection<sup>[150]</sup>. Carboxylic and cyanoacrylic acid anchor groups were found to inject electrons well into titania as shown in chapter 5 and 6, whereas anhydride and rhodanine-3-acetic acid anchoring groups showed unfavorable electron injection as demonstrated in chapter 4 and 6.

The reason could be that carboxylic and cyanoacrylic acids showed fairly localized electron densities in the acceptor blocks in the LUMO levels: ID889 with carboxylic acid, and FPH224 and FPH233 with cyanoacrylic acid, exhibited strong charge distribution in the anchor groups, which could be significantly influenced by the use of Li cations.

Dye molecules with an anhydride acid anchor group (P-, T-, and Q-MIMA) undergo ring opening to adsorb onto the titania surface. This changed the direction of the dipole moment, which negatively affects electron injection. This was supported by DFT calculations showing that charge distributions are localized in the  $\pi$ -conjugated bridge building block, far away from the titania surface/acceptor. Furthermore, when potassium salts of the di-carboxylic acids in solution (ring opened form) were used in photoluminescence measurements, reduced excited state lifetimes indicated enhanced non-radiative deactivation.



Dye molecules with rhodanine-3-acetic acid anchor groups (FPH303) also suffer from poor injection due to charges localized on the acceptor group, rather than spreading over the carboxylic acid. This result is consistent with the literature <sup>[110, 151-154]</sup>. However, we cannot simply state that the poor injection properties of a dye molecule with rhodanine-3-acetic acid solely originate from the anchoring group, since intramolecular charge transfer states could also play a crucial role in injection.

We note that improper anchoring groups do not show significantly improved injection efficiency even after the use of Li cations. As stated above, this could be due to either a poor injection property of the anchoring group or a dipole moment that was not large enough to drive the injection.

### 7.3 The role of dipole moments

Push-pull dye molecules have a strong dipole moment in the ground and excited state. In this section, the role of the dipole moment of a dye molecule on the photophysical processes in a device, especially the electron injection process, will be revealed.

First, dipole moments are the origin of the solvatochromism of dye molecules when solvents of different polarity are used. In this thesis, most dye molecules showed positive solvatochromic properties indicating to a stabilization of the excited state; however, FPH231 discussed in chapter 6 exhibited negative solvatochromism, indicating that the excited state was destabilized in polar solvents. Hence, the use of Li cations, which similarly creates a polar environment at the metal oxide nanoparticles/dye interface may lead to unfavorable electron injection.

Secondly, strong dipole moments can enhance electron injection yields when a dye molecule shows a larger dipole moment in the excited state and/or when a dye molecule is inactivated by Li-cations. In chapter 5, ID889 exhibited an excited state dipole moment of 48.2 Debye that is five times higher than its dipole moment in the ground state of 9.3 Debye. The larger dipole moment in the excited state is in line with red-shifted emission spectra in polar solvents and the formation of charge transfer states on an alumina surface when Li additives are used. ID889 showed the highest photocurrents among all organic dye molecules investigated in this dissertation and this is to a large extent due to the larger dipole moment in the excited state leading to facilitated injection. In the cyclopentadithiophene series of dye molecules, FPH224 and 233 were found to have similar dipole moments, based on their similar absorption/emission spectra and Stokes shifts in solvents of different polarity, and these two molecules exhibited similar efficiencies with similar photocurrents in devices, indicating injection properties are not very different.

Thirdly, the direction of the dipole moment can indicate if an injection process from a dye molecule is favorable or not. The orientation of dipole moments points from negative charges to positive charges and then a dipole moment pointing away from the titania surface indicates favourable injection. As

shown in chapter 4, when anhydride anchoring groups (P-, T-, and Q-MIMA) undergo ring opening during adsorption, the dipole moment direction changes pointing towards the interface, leading to poor injection. Although these molecules showed slightly enhanced charge generation after the use of Li-TFSI as shown by photoinduced absorption measurements, the dipole moment pointing towards the titania surface overruled the effect on device performance compared to the use of Li cations.

Last, a strong dipole moment causes a significant Stark effect by interacting with the local electric field at the interface, thus, all dynamics of dye cations were taken at wavelength regions above 800 nm in order to avoid interference by the Stark effect.

However, there was one exception among the dye molecules studied here: FPH303 has a larger dipole moment in the excited state; however, this did not cause efficient injection as shown by transient absorption measurements. The reason why FPH303 did not show efficient injection despite having a larger dipole moment in the excited state is its sensitivity to Li cations. For instance, in photoluminescence decay measurements on the CPDT series of dyes in solutions or on films, FPH224 and 233 showed a significant decrease in lifetime in polar solvents or after addition of Li cations, whereas FPH303 showed a rather similar or only slightly decreased lifetime regardless of Li cation use. Furthermore, FPH303 exhibited the lowest injection rate of 87% , as did FPH231, whereas FPH224 and 233 showed an injection-efficiency close to unity (99%), when the PL intensities of Li-treated titania samples were compared to those from alumina surfaces.

Dipole moment and sensitivity to Li cations appear to be closely related to efficient injection, since Li-TFSI draws more electron density towards the interface. For instance, ID889, which injected electrons even without the help of Li cations, showed improved electron injection after the use of Li cations, because the existence of Li-active sites in ID889 samples increased the injection-efficiency although the electron densities were mostly localized at the acceptor moiety rather than at the anchoring group. For rylene dyes, as pointed out above, it seemed that they had Li-active sites, since we could observe larger signals by quasi-steady-state photoinduced absorption spectroscopy, but the dipole moment pointing towards the titania surface overcompensated the effect of Li-active sites. FPH224 and 233 clearly exhibited a larger amount of charge generation after the use of Li cations in long-delay measurements as they have favorable dipole moments. However, as stated above, FPH303 seems to have a larger dipole moment in the excited state, but is not activated by Li-cations, thus only leading to short-lived charges.

## 7.4 Recombination of charges

In solid-state dye-sensitized solar cells, two types of charged molecules can be detected: dye cations and spiro cations. The yield and dynamics of these cations on  $\mu\text{s}$  –  $\text{ms}$  timescale is directly related to the power conversion efficiency of a device.

As shown in chapter 4, rylene dyes exhibited poor efficiencies ranging from 0.02% to 0.29%. Among the series of rylene dye molecules, PMIMA showed the strongest signals of dye cations and spiro cations in PIA measurements, but still suffered from low photovoltages and photocurrents compared to a ruthenium complex dye-sensitized solar cell. TMIMA and QMIMA exhibited almost no meaningful signals from spiro cations, leading to not only low photocurrents but also to poor photovoltages and fill factors due to recombination.

ID889 shown in chapter 5 exhibited the best performance of 4.5% among the organic dye molecules investigated in this dissertation and this seemed to originate from very efficient charge generation and regeneration. Furthermore, by using soft-modelling multivariate curve resolution (MCR), we found that ID889 showed no reductive quenching, a process that is known to be a less efficient charge generation mechanism than the ordinary charge generation path, due to a preceding hole transfer from oxidized dye molecules to the hole transporter. In MCR analysis, exciton dynamics from a device-like sample were very similar to the exciton decay from a dye adsorbed on titania or adsorbed on Li-treated titania. Therefore, long-lived charge generation in ID889 is mainly from the dye's excited state rather than from anionic dye molecules, in turn leading to efficient charge generation.

In the CPDT series of dye molecules shown in chapter 6, FPH224 and 233 showed better efficiencies of 1.56 – 1.67 % when compared with FPH231 and 303, which showed a PCE of 0.65 – 0.82 %. The difference between the efficiencies mainly originated from enhanced photocurrents in the devices. In PIA measurements, FPH233 and 224 showed strong charge generation and regeneration signals after the use of Li cations and spiro-OMeTAD as hole conductor, respectively. FPH233 exhibited no remaining dye cation signals, leading to the best performance.

## 7.5 Conclusion

In order to achieve high power conversion efficiency in solid-state dye-sensitized solar cell, several factors need to be considered. First of all, the HOMO level of the dye molecule needs to be lower than the HOMO of the hole transporter for efficient regeneration and the LUMO level of the dye molecule needs to be higher than the conduction band of the metal oxide nanoparticles for electron injection. Secondly, the anchoring group should not interfere or affect electron injection after adsorption onto nanoparticles and electron density localized near anchoring and acceptor moieties is desirable for an efficient injection process. Thirdly, the dipole moment and sensitivity to Li-cation of a dye molecule

are important for high photocurrents in a device. For efficient injection, the dipole moment needs to point away from the metal oxide surface, and injection is facilitated when the magnitude of the dipole moment in the excited state is larger than in the ground state. If the metal oxide-dye interface has a significant amount of Li-active sites then the injection efficiency and charge generation can be improved by addition of Li-TFSI. Last, observation of long-lived charges after addition of Li-TFSI or a hole conductor such as spiro-OMeTAD is directly related to a high power conversion efficiency.

Figure 7-1 shows a summary consisting of factors that significantly affect the device efficiency, and the dye molecules investigated in this dissertation. ID889, FPH224 and 233 have Li cation-active sites, favourable dipole moments, and create long-lived charges, ultimately resulting in high performing devices.

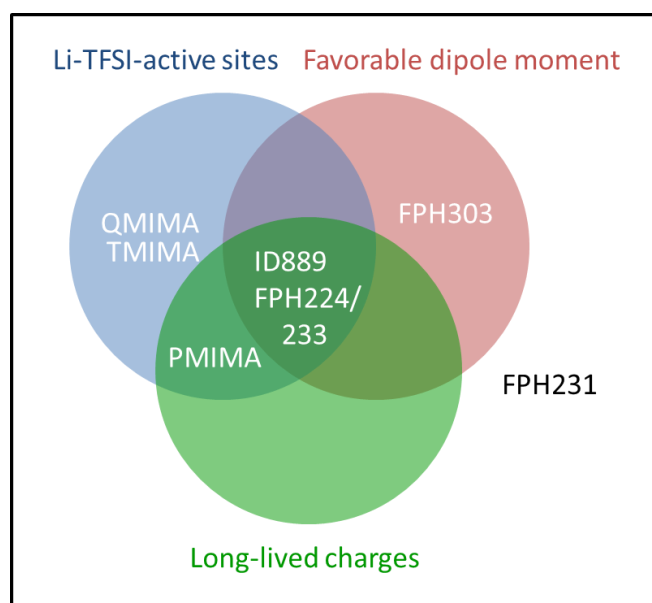


Figure 7-1. Schematic diagram representing factors that affect the power conversion efficiency.

## 8. REFERENCES

1. Administration, U.S.E.I. *International energy outlook 2013*. 2013; Available from: <http://www.eia.gov/forecasts/ieo/index.cfm>.
2. Lee, M.M., et al., *Efficient Hybrid Solar Cells Based on Meso-Superstructured Organometal Halide Perovskites*. *Science*, 2012. **338**(6107): p. 643-647.
3. Burschka, J., et al., *Sequential deposition as a route to high-performance perovskite-sensitized solar cells*. *Nature*, 2013. **499**(7458): p. 316-+.
4. Liu, M., M.B. Johnston, and H.J. Snaith, *Efficient planar heterojunction perovskite solar cells by vapour deposition*. *Nature*, 2013. **501**(7467): p. 395-+.
5. Yu, G., et al., *POLYMER PHOTOVOLTAIC CELLS - ENHANCED EFFICIENCIES VIA A NETWORK OF INTERNAL DONOR-ACCEPTOR HETEROJUNCTIONS*. *Science*, 1995. **270**(5243): p. 1789-1791.
6. Tang, C.W., *2-LAYER ORGANIC PHOTOVOLTAIC CELL*. *Applied Physics Letters*, 1986. **48**(2): p. 183-185.
7. Koster, L.J.A., S.E. Shaheen, and J.C. Hummelen, *Pathways to a New Efficiency Regime for Organic Solar Cells*. *Advanced Energy Materials*, 2012. **2**(10): p. 1246-1253.
8. Gruber, M., et al., *Thermodynamic Efficiency Limit of Molecular Donor-Acceptor Solar Cells and its Application to Diindenoperylene/C60-Based Planar Heterojunction Devices*. *Advanced Energy Materials*, 2012. **2**(9): p. 1100-1108.
9. Giebink, N.C., et al., *Thermodynamic efficiency limit of excitonic solar cells*. *Physical Review B*, 2011. **83**(19).
10. Kirchartz, T., K. Taretto, and U. Rau, *Efficiency Limits of Organic Bulk Heterojunction Solar Cells*. *Journal of Physical Chemistry C*, 2009. **113**(41): p. 17958-17966.
11. Lunt, R.R., et al., *Practical Roadmap and Limits to Nanostructured Photovoltaics*. *Adv Mater*, 2011. **23**(48): p. 5712-5727.
12. Shockley, W. and H.J. Queisser, *DETAILED BALANCE LIMIT OF EFFICIENCY OF P-N JUNCTION SOLAR CELLS*. *Journal of Applied Physics*, 1961. **32**(3): p. 510-&.
13. He, Z., et al., *Enhanced power-conversion efficiency in polymer solar cells using an inverted device structure*. *Nature Photonics*, 2012. **6**(9): p. 591-595.
14. Vogel, R., K. Pohl, and H. Weller, *SENSITIZATION OF HIGHLY POROUS, POLYCRYSTALLINE TiO<sub>2</sub> ELECTRODES BY QUANTUM SIZED CDS*. *Chemical Physics Letters*, 1990. **174**(3-4): p. 241-246.
15. Vogel, R., P. Hoyer, and H. Weller, *QUANTUM-SIZED PBS, CDS, Ag<sub>2</sub>S, Sb<sub>2</sub>S<sub>3</sub>, AND Bi<sub>2</sub>S<sub>3</sub> PARTICLES AS SENSITIZERS FOR VARIOUS NANOPOROUS WIDE-BANDGAP SEMICONDUCTORS*. *Journal of Physical Chemistry*, 1994. **98**(12): p. 3183-3188.
16. Plass, R., et al., *Quantum dot sensitization of organic-inorganic hybrid solar cells*. *Journal of Physical Chemistry B*, 2002. **106**(31): p. 7578-7580.
17. Santra, P.K. and P.V. Kamat, *Mn-Doped Quantum Dot Sensitized Solar Cells: A Strategy to Boost Efficiency over 5%*. *J Am Chem Soc*, 2012. **134**(5): p. 2508-2511.
18. Service, R.F., *ENERGY TECHNOLOGY Perovskite Solar Cells Keep On Surging*. *Science*, 2014. **344**(6183): p. 458-458.
19. Kojima, A., et al., *Organometal Halide Perovskites as Visible-Light Sensitizers for Photovoltaic Cells*. *J Am Chem Soc*, 2009. **131**(17): p. 6050-+.
20. Xing, G., et al., *Long-Range Balanced Electron- and Hole-Transport Lengths in Organic-Inorganic CH<sub>3</sub>NH<sub>3</sub>PbI<sub>3</sub>*. *Science*, 2013. **342**(6156): p. 344-347.
21. Stranks, S.D., et al., *Electron-Hole Diffusion Lengths Exceeding 1 Micrometer in an Organometal Trihalide Perovskite Absorber*. *Science*, 2013. **342**(6156): p. 341-344.

22. Oregan, B. and M. Gratzel, *A LOW-COST, HIGH-EFFICIENCY SOLAR-CELL BASED ON DYE-SENSITIZED COLLOIDAL TiO<sub>2</sub> FILMS*. *Nature*, 1991. **353**(6346): p. 737-740.
23. Yella, A., et al., *Porphyrim-Sensitized Solar Cells with Cobalt (II/III)-Based Redox Electrolyte Exceed 12 Percent Efficiency*. *Science*, 2011. **334**(6056): p. 629-634.
24. Dualeh, A., et al., *Influence of Donor Groups of Organic D- $\pi$ -A Dyes on Open-Circuit Voltage in Solid-State Dye-Sensitized Solar Cells*. *Journal of Physical Chemistry C*, 2012. **116**(1): p. 1572-1578.
25. Asbury, J.B., et al., *Femtosecond IR study of excited-state relaxation and electron-injection dynamics of Ru(dcbpy)<sub>2</sub>(NCS)<sub>2</sub> in solution and on nanocrystalline TiO<sub>2</sub> and Al<sub>2</sub>O<sub>3</sub> thin films*. *Journal of Physical Chemistry B*, 1999. **103**(16): p. 3110-3119.
26. Ramakrishna, G., et al., *Strongly coupled ruthenium-polypyridyl complexes for efficient electron injection in dye-sensitized semiconductor nanoparticles*. *Journal of Physical Chemistry B*, 2005. **109**(32): p. 15445-15453.
27. Kuang, D.B., et al., *High molar extinction coefficient heteroleptic ruthenium complexes for thin film dye-sensitized solar cells*. *J Am Chem Soc*, 2006. **128**(12): p. 4146-4154.
28. Benko, G., et al., *Photoinduced ultrafast dye-to-semiconductor electron injection from nonthermalized and thermalized donor states*. *J Am Chem Soc*, 2002. **124**(3): p. 489-493.
29. Wenger, B., M. Gratzel, and J.E. Moser, *Rationale for kinetic heterogeneity of ultrafast light-induced electron transfer from Ru(II) complex sensitizers to nanocrystalline TiO<sub>2</sub>*. *J Am Chem Soc*, 2005. **127**(35): p. 12150-12151.
30. van de Lagemaat, J., N.G. Park, and A.J. Frank, *Influence of electrical potential distribution, charge transport, and recombination on the photopotential and photocurrent conversion efficiency of dye-sensitized nanocrystalline TiO<sub>2</sub> solar cells: A study by electrical impedance and optical modulation techniques*. *Journal of Physical Chemistry B*, 2000. **104**(9): p. 2044-2052.
31. O'Regan, B.C., et al., *Measuring charge transport from transient photovoltage rise times. A new tool to investigate electron transport in nanoparticle films*. *Journal of Physical Chemistry B*, 2006. **110**(34): p. 17155-17160.
32. Fabregat-Santiago, F., et al., *Electron Transport and Recombination in Solid-State Dye Solar Cell with Spiro-OMeTAD as Hole Conductor*. *J Am Chem Soc*, 2009. **131**(2): p. 558-562.
33. Jennings, J.R. and L.M. Peter, *A reappraisal of the electron diffusion length in solid-state dye-sensitized solar cells*. *Journal of Physical Chemistry C*, 2007. **111**(44): p. 16100-16104.
34. Kruger, J., et al., *Charge transport and back reaction in solid-state dye-sensitized solar cells: A study using intensity-modulated photovoltage and photocurrent spectroscopy*. *Journal of Physical Chemistry B*, 2003. **107**(31): p. 7536-7539.
35. Jonathan Clayden, N.G., Stuart Warren, *Organic Chemistry*. 2, illustrated ed. 2012, Mar 15, 2012: OUP Oxford. 1264.
36. Evans, R.C., Douglas, Peter, Burrow, Hugh D. , *Applied Photochemistry*. 2013, Springer.
37. Ceroni, P., *The Exploration of Supramolecular Systems and Nanostructures by Photochemical Techniques*. Vol. 78. 2012: Springer. 123.
38. Boxer, S.G., *Stark Realities*. *Journal of Physical Chemistry B*, 2009. **113**(10): p. 2972-2983.
39. Johannes G. Vos, R.J.F., Tia E. Keyes, *Interfacial Supramolecular Assemblies*. 2003: Wiley.
40. Keller, U., *Recent developments in compact ultrafast lasers*. *Nature*, 2003. **424**(6950): p. 831-838.
41. Menzel, R., *Photonics (Linear and Nonlinear Interactions of Laser Light and Matter)*. 2007: Springer.
42. Markus Schwoerer, H.C.W., *Organic Molecular Solids*. 2007: Wiley-VCH Verlag GmbH & Co. KGaA.

43. Wannier, G.H., *The structure of electronic excitation levels in insulating crystals*. Physical Review, 1937. **52**(3): p. 0191-0197.
44. Hagfeldt, A. and M. Gratzel, *Molecular photovoltaics*. Accounts of Chemical Research, 2000. **33**(5): p. 269-277.
45. Howard, I.A., et al., *Two Channels of Charge Generation in Perylene Monoimide Solid-State Dye-Sensitized Solar Cells*. Advanced Energy Materials, 2014. **4**(2).
46. Kallioinen, J., et al., *Electron transfer from the singlet and triplet excited states of Ru(dcbpy)(2)(NCS)(2) into nanocrystalline TiO2 thin films*. Journal of Physical Chemistry B, 2002. **106**(17): p. 4396-4404.
47. Bach, U., et al., *Charge separation in solid-state dye-sensitized heterojunction solar cells*. Journal of the American Chemical Society, 1999. **121**(32): p. 7445-7446.
48. Clifford, J.N., et al., *Dye dependent regeneration dynamics in dye sensitized nanocrystalline solar cells: Evidence for the formation of a ruthenium bipyridyl cation/iodide intermediate*. Journal of Physical Chemistry C, 2007. **111**(17): p. 6561-6567.
49. Kelly, C.A., et al., *Cation-controlled interfacial charge injection in sensitized nanocrystalline TiO2*. Langmuir, 1999. **15**(20): p. 7047-7054.
50. Haque, S.A., et al., *Charge recombination kinetics in dye-sensitized nanocrystalline titanium dioxide films under externally applied bias*. Journal of Physical Chemistry B, 1998. **102**(10): p. 1745-1749.
51. Hasselmann, G.M. and G.J. Meyer, *Diffusion-limited interfacial electron transfer with large apparent driving forces*. Journal of Physical Chemistry B, 1999. **103**(36): p. 7671-7675.
52. Trachibana, Y., et al., *Electron injection and recombination in dye sensitized nanocrystalline titanium dioxide films: A comparison of ruthenium bipyridyl and porphyrin sensitizer dyes*. Journal of Physical Chemistry B, 2000. **104**(6): p. 1198-1205.
53. Kuciauskas, D., et al., *Electron transfer dynamics in nanocrystalline titanium dioxide solar cells sensitized with ruthenium or osmium polypyridyl complexes*. Journal of Physical Chemistry B, 2001. **105**(2): p. 392-403.
54. Clifford, J.N., et al., *Molecular control of recombination dynamics in dye-sensitized nanocrystalline TiO2 films: Free energy vs distance dependence*. Journal of the American Chemical Society, 2004. **126**(16): p. 5225-5233.
55. Haque, S.A., et al., *Parameters influencing charge recombination kinetics in dye-sensitized nanocrystalline titanium dioxide films*. Journal of Physical Chemistry B, 2000. **104**(3): p. 538-547.
56. Tachibana, Y., et al., *Subpicosecond interfacial charge separation in dye-sensitized nanocrystalline titanium dioxide films*. Journal of Physical Chemistry, 1996. **100**(51): p. 20056-20062.
57. Nazeeruddin, M.K., et al., *CONVERSION OF LIGHT TO ELECTRICITY BY CIS-X2BIS(2,2'-BIPYRIDYL-4,4'-DICARBOXYLATE)RUTHENIUM(II) CHARGE-TRANSFER SENSITIZERS (X = CL-, BR-, I-, CN-, AND SCN-) ON NANOCRYSTALLINE TIO2 ELECTRODES*. J Am Chem Soc, 1993. **115**(14): p. 6382-6390.
58. Haque, S.A., et al., *Charge separation versus recombination in dye-sensitized nanocrystalline solar cells: the minimization of kinetic redundancy*. Journal of the American Chemical Society, 2005. **127**(10): p. 3456-3462.
59. Chen, C.-Y., et al., *Highly Efficient Light-Harvesting Ruthenium Sensitizer for Thin-Film Dye-Sensitized Solar Cells*. ACS Nano, 2009. **3**(10): p. 3103-3109.
60. Zakeeruddin, S.M., et al., *Design, synthesis, and application of amphiphilic ruthenium polypyridyl photosensitizers in solar cells based on nanocrystalline TiO2 films*. Langmuir, 2002. **18**(3): p. 952-954.

61. Wang, P., et al., *A stable quasi-solid-state dye-sensitized solar cell with an amphiphilic ruthenium sensitizer and polymer gel electrolyte*. *Nat Mater*, 2003. **2**(6): p. 402-407.
62. Wang, P., et al., *Stable new sensitizer with improved light harvesting for nanocrystalline dye-sensitized solar cells*. *Adv Mater*, 2004. **16**(20): p. 1806-+.
63. Nazeeruddin, M.K., et al., *Acid-base equilibria of (2,2'-bipyridyl-4,4'-dicarboxylic acid)ruthenium(II) complexes and the effect of protonation on charge-transfer sensitization of nanocrystalline titania*. *Inorganic Chemistry*, 1999. **38**(26): p. 6298-6305.
64. Wang, P., et al., *High efficiency dye-sensitized nanocrystalline solar cells based on ionic liquid polymer gel electrolyte*. *Chem Commun (Camb)*, 2002(24): p. 2972-2973.
65. Wang, P., et al., *Molecular-scale interface engineering of TiO<sub>2</sub> nanocrystals: Improving the efficiency and stability of dye-sensitized solar cells*. *Adv Mater*, 2003. **15**(24): p. 2101-+.
66. Schmidt-Mende, L., S.M. Zakeeruddin, and M. Gratzel, *Efficiency improvement in solid-state-dye-sensitized photovoltaics with an amphiphilic Ruthenium-dye*. *Applied Physics Letters*, 2005. **86**(1).
67. Snaith, H.J., et al., *High extinction coefficient "Antenna" dye in solid-state dye-sensitized solar cells: A photophysical and electronic study*. *Journal of Physical Chemistry C*, 2008. **112**(20): p. 7562-7566.
68. Karthikeyan, C.S., et al., *Highly efficient solid-state dye-sensitized TiO<sub>2</sub> solar cells via control of retardation of recombination using novel donor-antenna dyes*. *Solar Energy Materials and Solar Cells*, 2007. **91**(5): p. 432-439.
69. Nazeeruddin, M.K., P. Pechy, and M. Gratzel, *Efficient panchromatic sensitization of nanocrystalline TiO<sub>2</sub> films by a black dye based on a trithiocyanato-ruthenium complex*. *Chem Commun (Camb)*, 1997(18): p. 1705-1706.
70. Maeda, T., et al., *Near-infrared Absorbing Squarylium Dyes with Linearly Extended pi-Conjugated Structure for Dye-sensitized Solar Cell Applications*. *Organic Letters*, 2011. **13**(22): p. 5994-5997.
71. Macor, L., et al., *Near-IR sensitization of wide band gap oxide semiconductor by axially anchored Si-naphthalocyanines*. *Energy & Environmental Science*, 2009. **2**(5): p. 529-534.
72. Ono, T., T. Yamaguchi, and H. Arakawa, *Study on dye-sensitized solar cell using novel infrared dye*. *Solar Energy Materials and Solar Cells*, 2009. **93**(6-7): p. 831-835.
73. Hara, K., et al., *Oligothiophene-containing coumarin dyes for efficient dye-sensitized solar cells*. *Journal of Physical Chemistry B*, 2005. **109**(32): p. 15476-15482.
74. Horiuchi, T., et al., *High efficiency of dye-sensitized solar cells based on metal-free indoline dyes*. *J Am Chem Soc*, 2004. **126**(39): p. 12218-12219.
75. Ito, S., et al., *High-conversion-efficiency organic dye-sensitized solar cells with a novel indoline dye*. *Chem Commun (Camb)*, 2008(41): p. 5194-5196.
76. Ito, S., et al., *High-efficiency organic-dye-sensitized solar cells controlled by nanocrystalline-TiO<sub>2</sub> electrode thickness*. *Adv Mater*, 2006. **18**(9): p. 1202-+.
77. Koumura, N., et al., *Alkyl-functionalized organic dyes for efficient molecular photovoltaics*. *Journal of the American Chemical Society*, 2006. **128**(44): p. 14256-14257.
78. Wang, Z.-S., et al., *Hexylthiophene-functionalized carbazole dyes for efficient molecular photovoltaics: Tuning of solar-cell performance by structural modification*. *Chemistry of Materials*, 2008. **20**(12): p. 3993-4003.
79. Ooyama, Y., et al., *Photovoltaic performance of dye-sensitized solar cells based on a series of new-type donor-acceptor-pi-conjugated sensitizer, benzofuro 2,3-c oxazolo 4,5-a carbazole fluorescent dyes*. *Journal of Photochemistry and Photobiology a-Chemistry*, 2009. **203**(2-3): p. 177-185.



80. Yang, C.-H., et al., *Characteristics of triphenylamine-based dyes with multiple acceptors in application of dye-sensitized solar cells*. Journal of Power Sources, 2009. **188**(2): p. 627-634.
81. Zhang, G., et al., *High efficiency and stable dye-sensitized solar cells with an organic chromophore featuring a binary pi-conjugated spacer*. Chemical Communications, 2009(16): p. 2198-2200.
82. Marinado, T., et al., *Rhodanine dyes for dye-sensitized solar cells: spectroscopy, energy levels and photovoltaic performance*. Physical Chemistry Chemical Physics, 2009. **11**(1): p. 133-141.
83. Zhang, F., et al., *Triphenylamine-based dyes for dye-sensitized solar cells*. Dyes and Pigments, 2009. **81**(3): p. 224-230.
84. Li, C., et al., *An Improved Perylene Sensitizer for Solar Cell Applications*. Chemsuschem, 2008. **1**(7): p. 615-618.
85. Ferrere, S. and B.A. Gregg, *Large increases in photocurrents and solar conversion efficiencies by UV illumination of dye sensitized solar cells*. Journal of Physical Chemistry B, 2001. **105**(32): p. 7602-7605.
86. Cappel, U.B., et al., *A Broadly Absorbing Perylene Dye for Solid-State Dye-Sensitized Solar Cells*. Journal of Physical Chemistry C, 2009. **113**(33): p. 14595-14597.
87. Shibano, Y., et al., *Electron-donating perylene tetracarboxylic acids for dye-sensitized solar cells*. Organic Letters, 2007. **9**(10): p. 1971-1974.
88. Edvinsson, T., et al., *Intramolecular charge-transfer tuning of perylenes: Spectroscopic features and performance in Dye-sensitized solar cells*. Journal of Physical Chemistry C, 2007. **111**(42): p. 15137-15140.
89. Ferrere, S. and B.A. Gregg, *New perylenes for dye sensitization of TiO<sub>2</sub>*. New Journal of Chemistry, 2002. **26**(9): p. 1155-1160.
90. Bullock, J.E., et al., *Photophysics and Redox Properties of Rylene Imide and Diimide Dyes Alkylated Ortho to the Imide Groups*. Journal of Physical Chemistry B, 2010. **114**(5): p. 1794-1802.
91. Kamm, V., et al., *Polythiophene:Perylene Diimide Solar Cells - the Impact of Alkyl-Substitution on the Photovoltaic Performance*. Advanced Energy Materials, 2011. **1**(2): p. 297-302.
92. Geerts, Y., et al., *Quaterrylenebis(dicarboximide)s: near infrared absorbing and emitting dyes*. Journal of Materials Chemistry, 1998. **8**(11): p. 2357-2369.
93. Edvinsson, T., et al., *Photoinduced electron transfer from a terrylene dye to TiO<sub>2</sub>: Quantification of band edge shift effects*. Chemical Physics, 2009. **357**(1-3): p. 124-131.
94. Xu, M., et al., *Electrical and photophysical analyses on the impacts of arylamine electron donors in cyclopentadithiophene dye-sensitized solar cells*. Energy & Environmental Science, 2011. **4**(11): p. 4735-4742.
95. Cai, N., et al., *Engineering of Push-Pull Thiophene Dyes to Enhance Light Absorption and Modulate Charge Recombination in Mesoscopic Solar Cells*. Advanced Functional Materials, 2013. **23**(14): p. 1846-1854.
96. Liu, J., et al., *Joint Photophysical and Electrical Analyses on the Influence of Conjugation Order in D-pi-A Photosensitizers of Mesoscopic Titania Solar Cells*. Journal of Physical Chemistry C, 2011. **115**(29): p. 14425-14430.
97. Imahori, H., T. Umeyama, and S. Ito, *Large pi-Aromatic Molecules as Potential Sensitizers for Highly Efficient Dye-Sensitized Solar Cells*. Accounts of Chemical Research, 2009. **42**(11): p. 1809-1818.
98. Karthikeyan, C.S., H. Wietasch, and M. Thelakkat, *Highly efficient solid-state dye-sensitized TiO<sub>2</sub> solar cells using donor-antenna dyes capable of multistep charge-transfer cascades*. Advanced Materials, 2007. **19**(8): p. 1091-1095.

99. Handa, S., et al., *Reducing charge recombination losses in solid state dye sensitized solar cells: the use of donor-acceptor sensitizer dyes*. Chemical Communications, 2007(17): p. 1725-1727.
100. Haque, S.A., et al., *Supramolecular control of charge transfer in dye-sensitized nanocrystalline TiO<sub>2</sub> films: Towards a quantitative structure-function relationship*. Angewandte Chemie-International Edition, 2005. **44**(35): p. 5740-5744.
101. Zhang, M., et al., *Design of high-efficiency organic dyes for titania solar cells based on the chromophoric core of cyclopentadithiophene-benzothiadiazole*. Energy & Environmental Science, 2013. **6**(10): p. 2944-2949.
102. Yella, A., et al., *Molecular Engineering of a Fluorene Donor for Dye-Sensitized Solar Cells*. Chemistry of Materials, 2013. **25**(13): p. 2733-2739.
103. Dualeh, A., et al., *Near-infrared sensitization of solid-state dye-sensitized solar cells with a squaraine dye*. Applied Physics Letters, 2012. **100**(17).
104. Anderson, A.Y., et al., *Quantifying Regeneration in Dye-Sensitized Solar Cells*. Journal of Physical Chemistry C, 2011. **115**(5): p. 2439-2447.
105. Cabau, L., et al., *Light soaking effects on charge recombination and device performance in dye sensitized solar cells based on indoline-cyclopentadithiophene chromophores*. Journal of Materials Chemistry A, 2013. **1**(31): p. 8994-9000.
106. Murakoshi, K., et al., *IMPORTANCE OF BINDING STATES BETWEEN PHOTOSENSITIZING MOLECULES AND THE TiO<sub>2</sub> SURFACE FOR EFFICIENCY IN A DYE-SENSITIZED SOLAR-CELL*. Journal of Electroanalytical Chemistry, 1995. **396**(1-2): p. 27-34.
107. Chen, X. and S.S. Mao, *Titanium dioxide nanomaterials: Synthesis, properties, modifications, and applications*. Chemical Reviews, 2007. **107**(7): p. 2891-2959.
108. Johansson, E.M.J., et al., *Comparing Surface Binding of the Maleic Anhydride Anchor Group on Single Crystalline Anatase TiO<sub>2</sub> (101), (100), and (001) Surfaces*. Journal of Physical Chemistry C, 2010. **114**(35): p. 15015-15020.
109. Voelker, B., et al., *Dye Bonding to TiO<sub>2</sub>: In Situ Attenuated Total Reflection Infrared Spectroscopy Study, Simulations, and Correlation with Dye-Sensitized Solar Cell Characteristics*. Langmuir, 2012. **28**(31): p. 11354-11363.
110. Tian, H., et al., *Phenothiazine derivatives for efficient organic dye-sensitized solar cells*. Chemical Communications, 2007(36): p. 3741-3743.
111. Neubauer, A., et al., *Photophysical Study of Perylene/TiO<sub>2</sub> and Perylene/ZnO Varying Interfacial Couplings and the Chemical Environment*. Journal of Physical Chemistry C, 2011. **115**(13): p. 5683-5691.
112. Abrusci, A., et al., *Influence of Ion Induced Local Coulomb Field and Polarity on Charge Generation and Efficiency in Poly(3-Hexylthiophene)-Based Solid-State Dye-Sensitized Solar Cells*. Advanced Functional Materials, 2011. **21**(13): p. 2571-2579.
113. Bartelt, A.F., et al., *Influence of TiO<sub>2</sub>/Perylene Interface Modifications on Electron Injection and Recombination Dynamics*. Journal of Physical Chemistry C, 2009. **113**(50): p. 21233-21241.
114. Kruger, J., et al., *High efficiency solid-state photovoltaic device due to inhibition of interface charge recombination*. Applied Physics Letters, 2001. **79**(13): p. 2085-2087.
115. Koops, S.E., et al., *Parameters Influencing the Efficiency of Electron Injection in Dye-Sensitized Solar Cells*. Journal of the American Chemical Society, 2009. **131**(13): p. 4808-4818.
116. Poplavskyy, D. and J. Nelson, *Nondispersive hole transport in amorphous films of methoxy-spirofluorene-arylamine organic compound*. Journal of Applied Physics, 2003. **93**(1): p. 341-346.

117. Bach, U., et al., *Solid-state dye-sensitized mesoporous TiO<sub>2</sub> solar cells with high photon-to-electron conversion efficiencies*. *Nature*, 1998. **395**(6702): p. 583-585.
118. Garcia-Canadas, J., et al., *Determination of electron and hole energy levels in mesoporous nanocrystalline TiO<sub>2</sub> solid-state dye solar cell*. *Synthetic Metals*, 2006. **156**(14-15): p. 944-948.
119. Schmidt-Mende, L. and M. Gratzel, *TiO<sub>2</sub> pore-filling and its effect on the efficiency of solid-state dye-sensitized solar cells*. *Thin Solid Films*, 2006. **500**(1-2): p. 296-301.
120. Snaith, H.J., et al., *Efficiency enhancements in solid-state hybrid solar cells via reduced charge recombination and increased light capture*. *Nano Letters*, 2007. **7**(11): p. 3372-3376.
121. Snaith, H.J., et al., *Charge Generation and Photovoltaic Operation of Solid-State Dye-Sensitized Solar Cells Incorporating a High Extinction Coefficient Indolene-Based Sensitizer*. *Advanced Functional Materials*, 2009. **19**(11): p. 1810-1818.
122. *Multivariate Curve Resolution*. Available from: [http://www.cid.csic.es/homes/rtaqam/tmp/WEB\\_MCR/welcome.htm](http://www.cid.csic.es/homes/rtaqam/tmp/WEB_MCR/welcome.htm).
123. von Frese, J., S.A. Kovalenko, and N.P. Ernstring, *Interactive curve resolution by using latent projections in polar coordinates*. *Journal of Chemometrics*, 2007. **21**(1-2): p. 2-9.
124. Ito, S., et al., *Fabrication of screen-printing pastes from TiO<sub>2</sub> powders for dye-sensitised solar cells*. *Progress in Photovoltaics*, 2007. **15**(7): p. 603-612.
125. Meister, M., *Charge Generation and Recombination in Hybrid Organic/Inorganic Solar Cells*, in *Chemistry Department*. 2013, Johannes Gutenberg-Universität Mainz.
126. Do, N.T. and M. Baerns, *EFFECT OF SUPPORT MATERIAL ON THE ADSORPTION STRUCTURES OF FURAN AND MALEIC-ANHYDRIDE ON THE SURFACE OF V<sub>2</sub>O<sub>5</sub>/P<sub>2</sub>O<sub>5</sub> CATALYSTS .2. RESULTS OF INSITU INFRARED SPECTROSCOPIC STUDIES*. *Applied Catalysis*, 1988. **45**(1): p. 9-26.
127. Wilson, J.N., et al., *Reactions of maleic anhydride over TiO<sub>2</sub> (001) single crystal surfaces*. *Journal of Vacuum Science & Technology a-Vacuum Surfaces and Films*, 2000. **18**(4): p. 1887-1892.
128. Vittadini, A., et al., *Formic acid adsorption on dry and hydrated TiO<sub>2</sub> anatase (101) surfaces by DFT calculations*. *Journal of Physical Chemistry B*, 2000. **104**(6): p. 1300-1306.
129. Ashima, H., W.-J. Chun, and K. Asakura, *Room-temperature-adsorption behavior of acetic anhydride on a TiO<sub>2</sub>(110) surface*. *Surface Science*, 2007. **601**(8): p. 1822-1830.
130. Chérubin, N.S., *Dye-sensitized solar cells based on perylene derivatives*, in *Faculty of Science*. 2009, University of Kassel.
131. Nolde, F., et al., *Synthesis and modification of terrylenediimides as high-performance fluorescent dyes*. *Chemistry-a European Journal*, 2005. **11**(13): p. 3959-3967.
132. Gratzel, M., *Photoelectrochemical cells*. *Nature*, 2001. **414**(6861): p. 338-344.
133. Cappel, U.B., et al., *Characterization of the Interface Properties and Processes in Solid State Dye-Sensitized Solar Cells Employing a Perylene Sensitizer*. *Journal of Physical Chemistry C*, 2011. **115**(10): p. 4345-4358.
134. Abrusci, A., et al., *Influence of Ion Induced Local Coulomb Field and Polarity on Charge Generation and Efficiency in Poly(3-Hexylthiophene)-Based Solid-State Dye-Sensitized Solar Cells*. *Advanced Functional Materials*, 2011. **21**(13): p. 2571-2579.
135. Liu, Y., et al., *Investigation of influence of redox species on the interfacial energetics of a dye-sensitized nanoporous TiO<sub>2</sub> solar cell*. *Solar Energy Materials and Solar Cells*, 1998. **55**(3): p. 267-281.
136. Olson, C., et al., *Characterization of the Pore Filling of Solid State Dye Sensitized Solar Cells with Photoinduced Absorption Spectroscopy*. *International Journal of Photoenergy*, 2011. **2011**: p. 1-11.

137. Sugiyama, K., et al., *Dependence of indium-tin-oxide work function on surface cleaning method as studied by ultraviolet and x-ray photoemission spectroscopies*. Journal of Applied Physics, 2000. **87**(1): p. 295-298.
138. Peter, K., et al., *Dual-functional materials for interface modifications in solid-state dye-sensitized TiO<sub>2</sub> solar cells*. Applied Physics a-Materials Science & Processing, 2004. **79**(1): p. 65-71.
139. Leijtens, T., et al., *Hole Transport Materials with Low Glass Transition Temperatures and High Solubility for Application in Solid-State Dye-Sensitized Solar Cells*. ACS Nano, 2012. **6**(2): p. 1455-1462.
140. Chen, Q., et al., *Thick benzocyclobutene etching using high density SF<sub>6</sub>/O-2 plasmas*. Journal of Vacuum Science & Technology B, 2011. **29**(1).
141. Snook, J.H., et al., *Ultraviolet photoelectron spectroscopy of nanocrystalline TiO<sub>2</sub> films sensitized with (2,2'-bipyridyl)ruthenium(II) dyes for photovoltaic applications*. Organic Electronics, 2005. **6**(2): p. 55-64.
142. Michaelson, H.B., *WORK FUNCTION OF ELEMENTS AND ITS PERIODICITY*. Journal of Applied Physics, 1977. **48**(11): p. 4729-4733.
143. Cappel, U.B., et al., *The Influence of Local Electric Fields on Photoinduced Absorption in Dye-Sensitized Solar Cells*. Journal of the American Chemical Society, 2010. **132**(26): p. 9096-9101.
144. Cappel, U.B., et al., *Dye Regeneration by Spiro-MeOTAD in Solid State Dye-Sensitized Solar Cells Studied by Photoinduced Absorption Spectroscopy and Spectroelectrochemistry*. Journal of Physical Chemistry C, 2009. **113**(15): p. 6275-6281.
145. Welton, C.R.a.T., *Solvents and Solvent Effects in Organic Chemistry*. 2010: Wiley-VCH Verlag GmbH & Co. KGaA.
146. ; Available from: <http://webbook.nist.gov/chemistry/>.
147. Palomares, E., et al., *Control of charge recombination dynamics in dye sensitized solar cells by the use of conformally deposited metal oxide blocking layers*. Journal of the American Chemical Society, 2003. **125**(2): p. 475-482.
148. Wenger, B., M. Gratzel, and J.E. Moser, *Rationale for kinetic heterogeneity of ultrafast light-induced electron transfer from Ru(II) complex sensitizers to nanocrystalline TiO<sub>2</sub>*. Journal of the American Chemical Society, 2005. **127**(35): p. 12150-12151.
149. Olson, C., et al., *Characterization of the Pore Filling of Solid State Dye Sensitized Solar Cells with Photoinduced Absorption Spectroscopy*. International Journal of Photoenergy, 2011.
150. Mishra, A., M.K.R. Fischer, and P. Baeuerle, *Metal-Free Organic Dyes for Dye-Sensitized Solar Cells: From Structure: Property Relationships to Design Rules*. Angewandte Chemie-International Edition, 2009. **48**(14): p. 2474-2499.
151. Hara, K., et al., *A coumarin-derivative dye sensitized nanocrystalline TiO<sub>2</sub> solar cell having a high solar-energy conversion efficiency up to 5.6%*. Chemical Communications, 2001(6): p. 569-570.
152. Hara, K., et al., *Design of new coumarin dyes having thiophene moieties for highly efficient organic-dye-sensitized solar cells*. New Journal of Chemistry, 2003. **27**(5): p. 783-785.
153. Hara, K., et al., *Molecular design of coumarin dyes for efficient dye-sensitized solar cells*. Journal of Physical Chemistry B, 2003. **107**(2): p. 597-606.
154. Kitamura, T., et al., *Phenyl-conjugated oligoene sensitizers for TiO<sub>2</sub> solar cells*. Chemistry of Materials, 2004. **16**(9): p. 1806-1812.

## 9. LIST OF ACRONYMS

Btu	British thermal units/joule
BHJ	bulk heterojunction
HJ	heterojunction
FTO	fluorinated tin oxide
DSCs	dye-sensitized solar cells
TCO	transparent conductive oxide
PCE	power conversion efficiency
CPDT	cyclopentadithiophene
TD-DFT	time-dependent-density functional theory
MCR	multivariate curve resolution
TA	transient absorption
TiO <sub>2</sub>	titanium dioxide/titania
spiro-OMeTAD	2,2',7,7'-tetrakis-(N,N-di-p-methoxyphenyl-amine)-9,9'-spirobifluorene
tBP	4-tert-butylpyridine
Li-TFSI	lithium bis (trifluoromethanesulphonyl) imide salt
Al <sub>2</sub> O <sub>3</sub>	aluminium oxide/alumina
AM 1.5 G	air mass 1.5 global
Ag	silver
J <sub>sc</sub>	short circuit current density
V <sub>app</sub>	applied voltage
V <sub>oc</sub>	open circuit voltage
FF	fill factor
P <sub>inc</sub>	incident light irradiance

$I_{\text{MPP}}$	current at maximum power point
$V_{\text{MPP}}$	voltage at maximum power point
EQE	external quantum efficiency
$q$	elementary charge
$\hbar$	Plank's constant
$P_{\text{in}}$	light intensity
IQE	internal quantum efficiency
UV-Vis	ultraviolet to visible wavelength range
$\text{FeCl}_3$	iron(III) chloride
Lupasol <sup>®</sup>	polyethylenimines; adhesion promoter
BASF	chemical company
PIA	photoinduced absorption spectroscopy
LED	light-emitting diode
$P$	power density
$c$	the speed of light
$A$	absorbance
PL	photoluminescence
BBO	Barium Borate
CCD	charge-coupled device
TAS	transient absorption spectroscopy
OPA	optical parametrical amplifiers
YAG	yttrium-aluminium-garnet
$\text{YVO}_4$	yttrium vanadate
NIR	near-infrared
PMIMA	perylene mono-imid mono-anhydride

TMIMA	terylene mono-imid mono-anhydride
QMIMA	quaterylene mono-imid mono-anhydride
KOH	potassium hydroxide
Z907	Acronym for a Ru based dye: cis-Bis(isothiocyanato)(2,2'-bipyridyl-4,4'-dicarboxylato)(4,4'-di-nonyl-2'-bipyridyl)ruthenium(II)
Ru	ruthenium
IC	internal conversion
ISC	intersystem crossing
vr	vibrational relaxation
HOMO	highest occupied molecular orbital
LUMO	lowest occupied molecular orbital
EMR	electromagnetic radiation
BO	Born-Oppenheimer
MC	metal-centered transition
LC	ligand-centered transition
LMCT	ligand-to-metal charge transfer
MLCT	metal-to-ligand charge transfer
FRET	Förster resonance energy transfer
GSB	ground state bleaching
SE	stimulated emission
PIA	photoinduced absorption
KLM	Kerr lens mode-locking
CPA	chirped pulse amplification
Ti:Sa	titanium-sapphire
ZnO	zinc oxide

HTM	hole transporter material
TCO	transparent conductive oxide layer
D- $\pi$ -A	donor- $\pi$ bridge-acceptor
PDI	perylene diimide
TDI	terrylene diimide
QDI	quaterrylene diimide
PEDOT	Poly(3,4-ethylenedioxythiophene) poly(styrenesulfonate)
P3HT	Poly(3-hexylthiophene-2,5-diyl)
EFA	evolving factor analysis



## 10. LIST OF FIGURES

- Figure 1-1. A variety of applications of dye-sensitized solar cells in electronics and building: tablet manufactured by G24 Innovation and Logitech (top left), flexible dye-sensitized solar cells by G24 innovation (top right), and building-integrated photovoltaics by Fraunhofer (bottom).
- Figure 2- 1.  $\sigma$  and  $\pi$  bonds in a benzene ring.
- Figure 2- 2. Jablonski diagram illustrating electronic states of a molecule (singlet excited states  $S_n$  or triplet states  $T_n$ ) and transitions between those states.
- Figure 2- 3. Electronic transition represented as vertical line between two potential energy diagrams of ground ( $\psi$ ) and excited state ( $^*\psi$ ) as a function of the internuclear separation distance ( $Q$ ). The Franck-Condon principle states that an electronic transition is faster than a nuclear transition due to the difference in mass of electron and nuclei.
- Figure 2- 4. Transition in a two discrete energy level system, namely induced absorption, spontaneous emission, and stimulated (induced) emission.
- Figure 2- 5. The Stark effect on different energy levels by relation of dipole moment with external electric field.
- Figure 2- 6. Marcus theory: the potential energy curves of an electron transfer reaction are represented as harmonic oscillators as a function of nuclear coordinate.  $i$  and  $f$  stand for initial state and final state, respectively. A small electronic coupling value of  $|V_{DA}|^2$  compared to the reorganization energy in non-adiabatic electron transfer reactions (a), and different electronic situation depending on the relation between the energy barrier and activation energy,  $\Delta G^\ddagger$  (b).
- Figure 2- 7. Schematic diagram of (a) electron transfer, (b) Dexter and (c) Förster energy transfer.
- Figure 2- 15. A schematic diagram of signals obtained from transient absorption spectroscopy.
- Figure 2- 9. A schematic diagram of generation of mode-locked pulses having different frequencies (a) and a laser resonator using gain and loss medium in a cavity mode (b).
- Figure 2- 10. Passive mode-locking using a Kerr lens to allow only focused light to pass through.
- Figure 2- 11. Process of chirped pulse amplification of a femtosecond laser pulse.

- Figure 2- 12. A schematic diagram of supercontinuum white light generation.
- Figure 2- 13. Different exciton radii of Wannier and Frkel excitons due to the different dielectric permittivity of the material.
- Figure 2- 14. Working principle of solid-state dye-sensitized solar cells. A: absorption of a photon, B: a dye's excited state decay, C: Injection of electrons, D: recombination between injected electrons with oxidized dye molecule, E: reduction process of a dyes' oxidized state, and F: D: recombination between injected electrons with a oxidized hole conductor
- Figure 3-1. Time-temperature profile of the sintering process for two layers. A mesoporous titania layer after doctor blade coating in blue, and an insulating metal oxide layer in red.
- Figure 3-2. Molecular structure of spiro-OMeTAD (a), Li additive ion salt (b), and tert-butylpyridine (tBP) (c).
- Figure 3-3. Schematic structure of a solid-state dye-sensitized solar cell: FTO as an anode, compact titania layer, mesoporous metal oxide layer as an electron acceptor, sensitized dye as a photon harvesting system, hole conductor for dye regeneration, and silver as a cathode.
- Figure 3-4. Spectral irradiance at air mass (AM) 1.5 global solar conditions.
- Figure 3-5. Schematic diagram showing how the band positions shift according to the applied voltage.
- Figure 3-6. (a) Changes in absorption of oxidized dye FH303 created by adding 5 mM anhydrous iron(III) chloride solution. Ratios are based on volume percent; (b) Changes in absorption of ID889 due to anion formation under Lupasol and UV illumination treatment.
- Figure 3-7. Schematic illustration of photoinduced absorption spectroscopy.
- Figure 3-8. Working rinciple of a streak camera system.
- Figure 3-9. Schematic of the transient absorption spectroscopy setup.
- Figure 3-10. Chemical structures of PMIMA (n=0), TMIMA (n=1), and QMIMA (n=2) with anhydride group (left) and as potassium salts of the dicarboxylic acids (right).
- Figure 3-11. Chemical structure of the perylene dye ID889.

Figure 3-12. Molecular structures of the series of CPDT building block dyes, FH224 (a), FH231 (b), FH233 (c), and FH303 (d).

Figure 3-13. Molecular structure of the ruthenium complex Z907.

Figure 4-1. Chemical structures of PMIMA (n=0), TMIMA (n=1), and QMIMA (n=2) with anhydride group (left) and as potassium salts of the di-carboxylic acids (right) used in solution measurements.

Figure 4-2. Potential binding configurations of maleic acids on TiO<sub>2</sub> surface: (a) bidentate bridging and (b) monodentate mode. Atoms in blue originate from titanium dioxide surface and atoms in black come from maleic acid anhydride.

Figure 4-3. The HOMO and LUMO energy levels of anhydride-PMIMA (black solid), TMIMA (red solid), and QMIMA (blue solid) and of di-carboxylic acids of the dye molecules (dotted) calculated by density functional theory calculation

Figure 4-4. Normalized absorption/emission spectra of 0.1 mM PMIMA (black), TMIMA (red), and QMIMA (blue) dyes in toluene solution as anhydrides (a) and after ring opening (b).

Figure 4-5. Normalized fluorescence decay of PMIMA (black) and TMIMA (red) in toluene solution. Di-carboxylic acid PMIMA and TMIMA dye solutions are represented as gray and orange, respectively. The decays (solid lines) of anhydride and di-carboxylic dye solutions follow a single exponential.

Figure 4-6. Normalized absorption and emission spectra of 0.1 mM solutions of anhydride (a) PMIMA and (b) TMIMA in toluene (TLN) and dichlorobenzene (DCB). Black and red lines represent anhydride PMIMA and TMIMA in TLN and gray and orange lines show anhydride PMIMA and TMIMA in DCB, respectively.

Figure 4-7. Normalized absorption and photoluminescence spectra of (a) di-carboxylic acids PMIMA dye solution in TLN (black) and DCB (gray), and of (b) di-carboxylic acids TMIMA dye solution in TLN (red) and DCB (orange)

Figure 4-8. Normalized photoluminescence decays of 0.1 mM di-carboxylic acid PMIMA in TLN (black) and DCB (gray), and of 0.1 mM di-carboxylic acid TMIMA in TLN (red) and DCB (orange). The solid lines correspond to mono-exponential fits.

- Figure 4-9. Steady-state absorption spectra of PMIMA-(black), TMIMA-(red), and QMIMA-(blue) sensitized titania films.
- Figure 4-10. Normalized absorption and emission spectra of dye molecules adsorbed on titania in the presence and absence of Li salts. (a) PMIMA on titania (black) and after application of Li cation (gray); (b) TMIMA on titania (red) and with Li cation (orange); (c) QMIMA on titania (blue) and with Li cation (light blue).
- Figure 4-11. Normalized PL decays of PMIMA (black) and TMIMA (red) on titania, and the decays of PMIMA (gray) and TMIMA (orange) after application of Li cations. Solid lines represent stretched-exponential fits.
- Figure 4-12. Steady-state absorption spectra of (a) PMIMA, (b) TMIMA, (c) QMIMA dye cations, and (d) spiro-OMeTAD cations after addition of a 10 mM FeCl<sub>3</sub> solution.
- Figure 4-13. Quasi-steady-state PIA absorption spectra (a) of the dyes adsorbed on titania, (b) of the dyes on titania after application of Li-TFSI, and (c) of a device-like sample when PMIMA (black), TMIMA (red), and QMIMA (blue) dyes are used. The inset: PIA spectra of a device-like sample using Z907 (green) compared to the rylene dyes.
- Figure 4-14. J-V curves of the dye-sensitized solar cells measured under AM1.5G solar illumination (a) and corresponding EQE spectra (b) using PMIMA (black), TMIMA (red), and QMIMA (blue) dyes.
- Figure 5-1. Molecular structure of the perylene monoimide derivative dye ID889 and the HOMO/LUMO energy levels of the dye.
- Figure 5-2. Absorption and emission spectra of (a) 0.1 mM ID889 in toluene and (b) of Sample 1 (red), 2 (orange), 4 (black), and 5 (gray).
- Figure 5-3. Absorbance spectrum of dye-sensitized titania film (black), dye anion (red), and dye cation (blue) with an arbitrary offset.
- Figure 5-4. J-V characteristics of ID889-sensitized solid-state DSC measured under 100 mWcm<sup>-2</sup> AM 1.5 G solar intensity and (b) corresponding EQE spectra as a function of wavelength.
- Figure 5-5. Quasi-steady-state photoinduced absorption (PIA) spectra of ID889 dye excited with a 530 nm LED: ID889 on TiO<sub>2</sub> (black, Sample 4), ID889 on TiO<sub>2</sub> with Li salt (gray, Sample 5), and ID889 on TiO<sub>2</sub> with all additives and a hole conductor, having a

complete-device structure (light gray, Sample 6). Red-dotted line represents the absorption of dye cations obtained from steady-state absorption measurement.

Figure 5-6. (a) Normalized absorption and emission spectra of 0.1 mM ID889 solutions in toluene (TLN, black) and dimethylsulfoxide (DMSO, red) solvent; (b) Decay of the PL in dye solutions of TLN (black) and DMSO (red) obtained from Streak Camera measurements and decay with lifetimes of 6.5 and 2.9 ns for TLN and DMSO, respectively. The solid lines correspond to stretched exponential fits.

Figure 5-7. Short delay (ps-ns) broadband transient absorption spectra of ID889 solution (a) in TLN and (b) in DMSO in the visible spectral region at delay time of 1 ps (red), 3 ps (orange), 30 ps (green), and 3000 ps (purple). The pump fluence are  $37.56 \mu\text{J cm}^{-2}$  at 510 nm for both measurements. Two blue lines represent the PL spectra of each sample.

Figure 5-8. Early time dynamics of the exciton-induced absorption at different wavelength regions: 780-820 nm for ID889 TLN solution (black) and 800-840 nm for ID889 DMSO solution (red).

Figure 5-9. (a) Normalized photoluminescence (PL) decay of ID889 on alumina without application of Li cations (Sample 1, black scatter) and fitting (red solid line) with a lifetime of 3.2 ns. PL decay of ID889 on alumina with Li cations (Sample 2, red squares) and fitting (black solid line) with a lifetime of 1.4 ns. Lifetimes are obtained from a stretched exponential function. (b) Time-resolved photoluminescence measurement of ID889 adsorbed on  $\text{TiO}_2$  layer (Sample 4, black) and with Li cations (Sample 5, gray). The lifetimes were determined to be 54 and 52 ps for Sample 4 and 5, respectively.

Figure 5-10. The charge distribution of the HOMO (left) and of the LUMO (right) calculated from TD-DFT.

Figure 5-11. Short delay (ps-ns) broadband TA spectra of Sample 1 (a) and of Sample 2 (b) at delay times of 1 ps (red), 3 ps (orange), 30 ps (green), and 3000 ps (purple). The pump fluence at 510 nm is  $6.4 \mu\text{J cm}^{-2}$  for the visible and  $25.8 \mu\text{J cm}^{-2}$  for the near infrared measurements in Sample 1. For Sample 2 fluence is  $5.9 \mu\text{J cm}^{-2}$  for the visible and  $24.2 \mu\text{J cm}^{-2}$  for the near infrared measurements. Two blue lines represent the PL spectra of each sample.

Figure 5-12. (a) Normalized decay dynamics (long-delay measurement) of CT state absorption signal between 875 nm and 925 nm in Sample 2 with different pump fluences:  $5.9 \mu\text{J cm}^{-2}$  (black),  $12.3 \mu\text{J cm}^{-2}$  (gray),  $66.7 \mu\text{J cm}^{-2}$  (light gray), and  $83.3 \mu\text{J cm}^{-2}$  (white).

Inset: The dynamics of the PIA signal from Sample 1, 2, and 5 probed at a wavelength between 875 and 925 nm. (b) Normalized decay dynamics (long-delay measurement) of the dye cation's absorption between 830 nm and 850 nm in Sample 5 with different pump fluences: 5.5  $\mu\text{J cm}^{-2}$  nJ (dark red), 30.1  $\mu\text{J cm}^{-2}$  (red), 50.5  $\mu\text{J cm}^{-2}$  (pale red) and 80.7  $\mu\text{J cm}^{-2}$  (pink). Inset: The dynamics of the PIA signal from Sample 4 in long-delay measurements, showing weaker fluence dependence.

Figure 5-13. TA spectra on the femto- to nano-second timescale and PL spectra of Sample 4 (a) and of Sample 5 (b) at delay times of 1 ps (red), 3 ps (orange), 30 ps (green), and 3000 ps (purple). The pump fluence at 510 nm is 18.5  $\mu\text{J cm}^{-2}$  in the visible and 36.0  $\mu\text{J cm}^{-2}$  in the NIR for Sample 4 and 18.5  $\mu\text{J cm}^{-2}$  in the visible and 25.0  $\mu\text{J cm}^{-2}$  in the NIR for Sample 5. Two blue lines represent the PL spectra of each sample. Insets: TA spectra of Sample 4 and Sample 5 in the visible normalized to a minimum value of each spectrum.

Figure 5-14. Normalized decay dynamics (ps-ns) of the dye cation absorption observed between 830 and 850 nm in ID889 on titania (Sample 4, red) and in ID889 on titania plus Li cations (Sample 5, black). The solid lines correspond to stretched exponential fits for Sample 4 and 5.

Figure 5-15. Long delay (ns - sub-ns) broadband TA spectra of Sample 4 (a) and of Sample 5 (b) with delay times of 1 ns (red), 100 ns (orange), 1  $\mu\text{s}$  (green), and 100  $\mu\text{s}$  (purple). Excitation at 532 nm and energy density of 4.9  $\mu\text{J cm}^{-2}$  in the visible and 6.2  $\mu\text{J cm}^{-2}$  in the NIR for Sample 4 and of 4.9  $\mu\text{J cm}^{-2}$  in the visible and 7.5  $\mu\text{J cm}^{-2}$  in the NIR for Sample 5.

Figure 5-16. Broadband TA spectra of (a) ID889 on  $\text{TiO}_2$  with Li-TFSI/tBP/spiro-OMeTAD (complete device structure, Sample 6) and (b) ID889 on  $\text{TiO}_2$  with tBP/spiro-OMeTAD (Sample 7) on short-delay time scale (ps - ns) at delay times of 1 ps (red), 3 ps (orange), 30 ps (green), and 3000 ps (purple). The insets: The spectra in the visible normalized to the maximum value of each spectrum. The pump fluence at 510 nm is 5.75  $\mu\text{J cm}^{-2}$  for the visible and 23.3  $\mu\text{J cm}^{-2}$  for the infrared measurements in Sample 6 and 14.8  $\mu\text{J cm}^{-2}$  for the visible and 11.3  $\mu\text{J cm}^{-2}$  for the infrared measurements in Sample 7.

Figure 5-17. Normalized decay dynamics (short-delay measurement) of the oxidized spiro-OMeTAD's absorption between 1400 - 1430 nm in Sample 6 (closed triangle) and 7 (open triangle) with pump fluences 23.3  $\mu\text{J cm}^{-2}$  for Sample 6 and 11.3  $\mu\text{J cm}^{-2}$  Sample 7.

- Figure 5-18. (a) Long delay (ns-sub-ms) broadband TA spectra of Sample 6 (a) and of Sample 7 (b) with delay times of 1 ns (red), 100 ns (orange), 1  $\mu$ s (green), and 100  $\mu$ s (blue). Excitation at 532 nm and energy density of 45.2  $\mu$ J cm<sup>-2</sup> in the visible and 51.7  $\mu$ J cm<sup>-2</sup> in the NIR for Sample 6 and of 52.7  $\mu$ J cm<sup>-2</sup> in the visible and 70.0  $\mu$ J cm<sup>-2</sup> in the NIR for Sample 7.
- Figure 5-19. Normalized decay dynamics (long-delay measurement) of the oxidized hole conductor's absorption between 1400 – 1430 nm in Sample 6 (a) and Sample 7 (b) with different pump fluences.
- Figure 5-20. (a) Short delay (ps-ns) broadband transient absorption spectra of ID889 blend sample (Sample 8) at delay times of 1 ps (red), 15ps (green), 300 ps (blue), and 3000 ps (purple). The pump fluence at 510 nm is 33.8  $\mu$ J cm<sup>-2</sup> in the visible and 45.4  $\mu$ J cm<sup>-2</sup> in the NIR. The inset: Normalized TA spectra of Sample 8 (black gradients) and of Sample 3 (red gradients) at delay times of 1 ps, 15 ps, and 4.5 ns as color becomes pale. (b) Decay dynamics between 1400 – 1430 nm of Sample 3 (red) and 8 (black) normalized at the delay time of 0.
- Figure 5-21. Normalized steady-state absorption of cationic (dotted red)/anionic (dotted black) dye molecules and normalized TA spectra of Sample 8 (solid black), 5 (solid red), and 3 (solid blue).
- Figure 5-22. (a) Spectra of the exciton (solid) and the charges (dotted) in Sample 4 (blue), 5 (red), and 6 (black) obtained from MCR analysis using the TA data and (b) kinetics of exciton from Sample 4 (blue), 5 (red), and 6 (black).
- Figure 6-1. Molecular structures of FPH 224, 231, 233, and 303 (a), and the HOMO levels measured by cyclic voltammetry (b).
- Figure 6-2. Normalized absorption and emission spectra of 0.1 mM FPH224 (panel a, black), 231 (panel b, red), 233 (panel c, blue), and 303 (panel d, green) in the less polar solvent TLN (dark) and in more polar solvent THF (pale).
- Figure 6-3. Photoluminescence decay transient of 0.1 mM FPH224 (black), 231 (red), 233 (blue), and 303 (green) solutions in a polar solvent (darker lines, THF) and in a less polar solvent (lighter lines TLN). The solid lines correspond to stretched-exponential fits.
- Figure 6-4. Normalized absorption and emission spectra of FPH224 (panel a), 231 (panel b), 233 (panel c), and 303 (panel d) adsorbed on titania in the presence (black, red, blue, and green lines) and absence (gray, pink, sky blue, yellow-green lines) of Li cations.

- Figure 6-5. Normalized photoluminescence decay of (a) FPH224 (black), 231 (red), 233 (blue), and 303 (green) on alumina in the absence (full) and presence (hollow) of Li-TFSI, and (b) FPH224, 231, 233, and 303 on titania in the absence (full) and presence (hollow) of Li-TFSI.
- Figure 6-6. Photoluminescence decay curves of (a) FPH224 (black), 233(blue), and 303 (green) on Al<sub>2</sub>O<sub>3</sub> (solid lines) and on TiO<sub>2</sub> (dashed lines), and of (b) dye molecules on TiO<sub>2</sub> in the absence (dashed lines) and presence (dotted lines) of Li cation.
- Figure 6-7. (a) J-V curves of solid-state DSC using FPH224 (black), 231 (red), 233 (blue), 303 (green), and Z907 (purple) measured under 100 mWcm<sup>-2</sup> AM 1.5 G solar intensity and (b) external quantum efficiency of each device.
- Figure 6-8. Quasi-steady-state photoinduced absorption spectra of FPH224 (black), FPH231 (red), FPH233 (blue), and FPH303 (green) adsorbed on TiO<sub>2</sub> (a), of the four dye molecules on TiO<sub>2</sub> after application of Li cations (b), and in device-like structures (c). The samples were excited at 530 nm with high power LED.
- Figure 6-9. Short delay (ps-ns) broadband TA spectra of FPH224 on TiO<sub>2</sub> (a), of FPH224 TiO<sub>2</sub> after application of Li cations (b), and of FPH224 on TiO<sub>2</sub> with Li-TFSI/tBP/spiro-OMeTAD (complete device structure) at delay times of 3 ps (red), 30 ps (orange), 300 ps (green), and 3 ns (purple). The pump fluence at 520 nm is 5.5 μJ cm<sup>-2</sup> for the visible and 7.0 μJ cm<sup>-2</sup> for the near infrared measurements. The two blue lines represent the PL spectra of each sample.
- Figure 6-10. Long delay (ns – μs) broadband transient absorption spectra of (a) FPH224 on TiO<sub>2</sub>, and (b) FPH224 on TiO<sub>2</sub> after addition of Li-TFSI, and (c) FPH224 device-like structure in the visible and the NIR spectral region at delay times of 1 ns (red), 100 ns (orange), 10 μs (green), and 100 μs (purple). The samples were excited at 532 nm with a pump fluence of 7.2 μJ cm<sup>-2</sup> for the visible and 8.0 μJ cm<sup>-2</sup> for the NIR measurements.
- Figure 6-11. (a) Fluence dependence of the kinetics between 850 - 900 nm in FPH224 on TiO<sub>2</sub> with the Li-TFSI additive. The inset: Fluence dependence on FPH224 adsorbed on TiO<sub>2</sub> at the same wavelength region. (b) Long delay recombination dynamics of the photoinduced absorption probed at the wavelength regions between 850 – 900 nm in FPH224 on TiO<sub>2</sub> (black), in FPH224 on TiO<sub>2</sub> with Li-TFSI salts (dark grey), and in FPH224 device-like structure (light grey).
- Figure 6-12. TA spectra on the femto- to nano-second timescale and PL spectra of FPH233 on TiO<sub>2</sub> (a), of FPH233 on Al<sub>2</sub>O<sub>3</sub> (b), of FPH233 on TiO<sub>2</sub> after addition of Li cations (c),



and of a FPH233 device-like sample (d) at delay time of 3 ps (red), 30 ps (orange), 300 ps (green), and 3000 ps (purple). The pump fluence at 510 nm is  $5.5 \mu\text{J cm}^{-2}$  in the visible and  $7.0 \mu\text{J cm}^{-2}$  in the NIR.

- Figure 6-13. Long delay (ns –  $\mu\text{s}$ ) broadband transient absorption spectra of (a) FPH233 on  $\text{TiO}_2$ , and (b) FPH233 on  $\text{TiO}_2$  after addition of Li-TFSI, and (c) FPH233 device-like structure in the visible and the NIR spectral region at delay times of 1 ns (red), 100 ns (orange), 10  $\mu\text{s}$  (green), and 100  $\mu\text{s}$  (purple). The samples were excited at 532 nm with a pump fluence of  $7.2 \mu\text{J cm}^{-2}$  for the visible and  $8.0 \mu\text{J cm}^{-2}$  for the NIR measurements.
- Figure 6-14. (a) Fluence dependence of the kinetics between 850 - 900 nm in FPH233 on  $\text{TiO}_2$  with Li-TFSI additive. The inset: Fluence dependence on FPH233 adsorbed on  $\text{TiO}_2$ . (b) Long delay recombination dynamics of the photoinduced absorption of dye cations probed at the wavelength regions between 850 – 900 nm in FPH224 on  $\text{TiO}_2$  with Li-TFSI salts (blue) and in FPH224 device-like structure (light blue).
- Figure 6-15. TA spectra on the femto- to nano-second timescale of FPH231 on  $\text{TiO}_2$  (a), of FPH231 on  $\text{Al}_2\text{O}_3$  (b), of FPH231 on  $\text{TiO}_2$  with Li cations (c), and of the FPH231 device-like structure sample (d) at delay times of 3 ps (red), 30 ps (orange), 300 ps (green), and 3000 ps (purple). The pump fluence at 510 nm is  $5.5 \mu\text{J cm}^{-2}$  in the visible and  $7.0 \mu\text{J cm}^{-2}$  in the NIR.
- Figure 6-16. (a) Kinetics of the dye cations in FPH224 and 233 with (darker)/ without (paler) Li cations in the short-time delay TA measurements. The kinetics are averaged for FPH224 (black) and 233 (blue) between 850 – 900 nm and between 850 – 900 nm, and those for FPH224 (grey) and 233 (sky blue) with Li cations are taken from 900 – 950 nm and 900 – 950 nm, respectively. (b) Kinetics of the dye cations in FPH231 on  $\text{TiO}_2$  (red, 1150 – 1170 nm), in FPH231 on  $\text{TiO}_2$  with Li (dark red, 1120 – 1150 nm), and kinetics of spiro-cations (purple, 1480 – 1500 nm).
- Figure 6-17. (a) Transient absorption kinetics of dye cations monitored between 1150 – 1170 nm in FPH231 on  $\text{TiO}_2$ . Inset: the kinetics of dye cations between 1120 – 1150 nm in FPH231 on  $\text{TiO}_2$  with Li cations. (b) Transient absorption kinetics of a solar cell probed between 1480 – 1500 nm where the spiro cations dominate the photoinduced absorption.
- Figure 6-18. TA spectra on the femto- to nano-second timescale and PL spectra of FPH303 on  $\text{TiO}_2$  (a), of FPH303 on  $\text{Al}_2\text{O}_3$  (b), of FPH303 on  $\text{TiO}_2$  with Li-TFSI (c), and of a FPH303 solar cell (d) at delay times of 1 ps (red), 3 ps (orange), 30 ps (green), and

3000 ps (purple). The pump fluence at 510 nm is  $5.7 \mu\text{J cm}^{-2}$  in the visible and  $7.2 \mu\text{J cm}^{-2}$  in the NIR. Two blue lines in panel (a) and (c) represent the PL spectra of each sample.

Figure 6-19. Transient absorption kinetics of (a) FPH303 on  $\text{Al}_2\text{O}_3$  (solid green), of FPH303 on  $\text{TiO}_2$  (olive scatter), and of FPH303 on  $\text{TiO}_2$  with the application of Li-TFSI monitored between 1150 – 1200 nm where the dye cations absorb strongly, and of (b) the FPH303 device-like sample monitored between 1450 – 1500 nm.

Figure 6-20. Intensity dependence measurement of FPH303 on  $\text{TiO}_2$  with Li cations for the wavelength between 1150 – 1200 nm. The inset: Intensity dependence measurement of FPH303 on  $\text{TiO}_2$  for the same wavelength.

Figure 6-21. Transient absorption kinetics of (a) dye cations measured with samples of the dye adsorbed on  $\text{TiO}_2$  after addition of Li cations and of (b) spiro cations in the solar cell-like samples. FPH224, 231, 233, and 303 are represented in black, red, blue, green lines, respectively. The inset shows the dynamics of spiro cations in long-time delay measurements.

Figure 7-1. Schematic diagram representing factors that affect the power conversion efficiency.